Banded iron formations, pyritic black shale, and gold deposits: A re-evaluation

---

by

Jeffrey Alan Steadman
B.S., M.S. (Geology)

Submitted in fulfillment of the requirements for the degree of
Doctor of Philosophy

UNIVERSITY
OF TASMANIA

October 2015

Declaration of originality

This thesis contains no material which has been accepted for the award of any other degree or diploma in any tertiary institution and, to the best of my knowledge and belief, contains no copy or paraphrase of material previously published or written by another person, except where due reference is made in the text of the thesis, nor does the thesis contain any material that infringes copyright.

Signature: Date: 6-10-15

Authority of access

This thesis may be made available for loan and limited copying in accordance with the Copyright Act of 1968.

Signature: Date: 6-10-15

Statement regarding published work

The publishers of the papers comprising Chapters 2, 3, 4, and 5 hold the copyright for those contents; access to those materials should be sought from the journals *Precambrian Research* and *Economic Geology*. The remaining non-published content of the thesis may be made available for loan and limited copying in accordance with the Copyright Act of 1968.

Signature: Date: 6-10-15

Statement of co-authorship

The following people and institutions contributed to the publication of work undertaken as part of this thesis:
1. Jeffrey A Steadman (CODES [ARC Centre of Excellence in Ore Deposits], University of Tasmania)
2. Ross R Large (CODES, University of Tasmania)
3. Sebastien Meffre (CODES, University of Tasmania)
4. Stuart W Bull (CODES, University of Tasmania)
5. Garry J Davidson (CODES, University of Tasmania)
6. Paul H Olin (CODES, University of Tasmania)
7. Jay Thompson (CODES, University of Tasmania)
8. Leonid Danyushevsky (CODES, University of Tasmania)
9. Daniel D. Gregory (CODES, University of Tasmania)
10. Ivan Belousov (CODES, University of Tasmania)
11. Elena Lounejeva (CODES, University of Tasmania)
12. Trevor R. Ireland (Research School of Earth Sciences [RSES], Australian National University)
13. Peter Holden (RSES, Australian National University)

Paper details and authors' roles

Paper 1 (Located in Chapter 2)
Age, origin, and significance of nodular sulfides in 2680 Ma carbonaceous black shale of the Eastern Goldfields Superterrane, Yilgarn Craton, Western Australia
Jeffrey A Steadman (candidate), Ross R Large, Sebastien Meffre, and Stuart W Bull

Candidate was the primary author and with author 2, author 3 and author 4 contributed to the idea, its formalisation and development
Author 2 and author 3 assisted with refinement and presentation
Authors 2 and 4 offered assistance in the field
Author 3 provided assistance in the laboratory

Paper 2 (Located in Chapter 3)
Paragenesis and composition of sulfides, oxides, and silicates in the Randalls BIF-hosted gold deposits, Eastern Goldfields Superterrane, Yilgarn Craton, Western Australia: Implications for the timing of ore deposit formation and constraints on possible gold sources
Jeffrey A Steadman (candidate), Ross R Large, Garry J Davidson, Stuart W Bull, Jay Thompson, Trevor R. Ireland, and Peter Holden

Candidate was the primary author and with author 2, author 3, author 4, author 5, author 6, and author 7 contributed to the idea, its formalisation and development
Authors 2, 3, and 4 assisted with refinement and presentation
Authors 2 and 4 provided assistance in the field
Authors 5, 6, and 7 assisted in the laboratory

Paper 3 (Located in Chapter 4)
Syn-sedimentary, diagenetic, and metamorphic pyrite, pyrrhotite, and marcasite at the Homestake BIF-hosted gold deposit, South Dakota, USA: Insights on ore genesis from LA-ICP-MS trace element and sulfur isotope studies
Jeffrey A Steadman (candidate), Ross R Large, Trevor R. Ireland, and Peter Holden

Candidate was the primary author and with author 2, author 3, and author 4 contributed to the idea, its formalisation and development
Author 2 and Stuart W Bull (secondary advisor) assisted with refinement and presentation
Authors 3 and 4 assisted in the laboratory (SHRIMP S isotopes)

Paper 4 (Located in Chapter 5)
Syn-sedimentary to early diagenetic gold in black shale-hosted pyrite nodules at the Golden Mile deposit, Kalgoorlie, Western Australia
Jeffrey A Steadman (candidate), Ross R Large, Sebastien Meffre, Paul H Olin, Leonid V Danyushevsky, Daniel D Gregory, Ivan Belousov, Elena Lounejeva, Trevor R Ireland, and Peter Holden

Candidate was the primary author and with author 2, author 3, and author 4 contributed to the idea, its formalisation and development
Authors 2, 3, 4, and 5 assisted with refinement and presentation
Authors 4, 6, 7, 8, 9, and 10 assisted in the laboratory

We the undersigned agree with the above stated 'proportion of work undertaken' for each of the above published (or submitted) peer-reviewed manuscripts contributing to this thesis:

Signed: _

Ross R Large
Supervisor
School of Physical Sciences
University of Tasmania

Date: 6/10/15

Signed: _____

Leonid Danyushevsky
Head of Discipline, Earth Science
School of Physical Sciences
University of Tasmania

Date: 6/10/15

Acknowledgements

For the work at Lucky Bay (Chapter 2) and Randalls (Chapter 3), I would like to thank Chris Cairns (former Managing Director, Integra Mining Pty Ltd.) and Terry Brown (former General Manger for Project Development, Integra Mining) for permission to carry out these projects. Special thanks to Karsten Gömann and Sandrin Feig (Central Science Laboratory [CSL], University of Tasmania) for help with the SEMs and the microprobe. Thanks also to Christine Cook (CSL, University of Tasmania) for analyzing sulfide separates for S isotope measurements. Leonid Danyushevsky, Sarah Gilbert, and Sebastien Meffre are thanked for their input, suggestions, and expertise with the laser ablation system at CODES. And last, but not least: many thanks to all the fieldies and geologists at Mt. Monger field station; I could not have done this work without you!

The project at Homestake (Chapter 4) was graciously supported by the staff at SURF (Sanford Underground Research Facility) in Lead, South Dakota. Special thanks to Jaret Heise (Science Director, SURF) for permission to carry out research on the archived drill core and for logistical support. Discussions with former Homestake geologists Tom Trancynger, John Scheetz, and Kathy Hart were of immense value. We are also indebted to Prof. Colin Paterson (South Dakota School of Mines and Technology) for his expertise on Homestake geology and his hospitality. The lead author is also grateful to Mark Fahrenbach at the South Dakota Geological Survey and the legendary Black Hills field geologist Jack Redden for a productive one-day field excursion around the north-central Black Hills. The laser staff at CODES were indispensible to the success of this project; thanks especially to Leonid Danyushevsky, Sarah Gilbert, Sebastien Meffre, Marcel Guillong, and Ian Little. François Robert is thanked for providing permission to publish this work on behalf of Barrick Mining Company. Finally, we wish to thank the Editor of *Economic Geology*, Larry Meinert, and associate editor Paul Spry, plus reviewers John Ridley and Robert Frei for their critical suggestions. These greatly improved the quality of this manuscript.

For the work on the Golden Mile (Chapter 5), I wish to thank the Editor of *Economic Geology*, Larry Meinert, and reviewers Neil Phillips, Iain Pitcairn, Cam McCuaig, Katy Evans, Shaun Barker, and an anonymous reviewer from *Economic Geology*, all of whom provided valuable comments and criticisms that have greatly helped in improving the final version of this manuscript. Thanks also to Drs. Karsten Goëmann and Sandrin Feig (CSL, UTas) for their assistance with the Hitachi SU70 FESEM. SDG.

When I was nearing the end of my Master's degree and had plans for doing a PhD, I had no intention of leaving the United States. However, a good word about CODES was put in by my Master's advisor, Paul Spry (himself not only Australian but Tasmanian - Lindisfarne born and raised!), so I applied for a scholarship. Four short years later, here I am at the end of it all.

The biggest thanks go to my primary supervisor Ross Large, whose fountain of ideas, insight, and optimism is never-ending. I was pretty wet behind the ears when I got to Hobart, and I am oh-so-grateful that he stuck with me to the end.

Running a close second to Ross are my secondary supervisors, Stuart Bull and Garry Davidson, who provided chapter feedback and support when Ross was busy or away (which was more often than I preferred!).

I also want to thank Sebastien Meffre, because he was like a fourth supervisor to me, though his name was never on any official university paperwork as such. So much of my laser work (particularly

the Pb isotope studies with sulfides) would never have made it as far as it did with his guidance and expertise. Merci beaucoup.

I would be remiss in not tipping my figurative hat to all the students and staff who have come and gone in my four years here as a student; all of them provided a helping hand, a word of encouragement, or constructive criticism at various times in various places.

Paul George (digital graffiti) and June Pongratz (CODES thesis designer extraordinare) were invaluable in navigating all things Adobe-related. June was especially indispensible in finalizing this printed work.

Abstract

Banded iron formations (BIF) are predominantly Precambrian sedimentary rocks composed of alternating layers of iron-rich minerals (commonly hematite and magnetite, but also siderite, chlorite, and grunerite) and silica-rich minerals (e.g., quartz or chert) in which the Fe content of the entire rock is at least 15 wt. %. Although typically thought of as strictly Fe resources, such as in the world-class Archean-Proterozoic Pilbara Craton of NW Australia, some BIF are associated with non-Fe ore resources, including (but not limited to) gold deposits in greenstone terranes. Due to fluctuations in ocean and atmospheric chemistry, BIF are commonly interbedded with pyritic black shales, which are regarded as waste material in Fe deposits but nonetheless are of great scientific interest (as are BIF) and potentially play a role in the creation of some gold resources (recent research has suggested that black shales are a source of Au and As in sediment-hosted gold deposits). The source of gold in these BIF, or more accurately, in BIF that host gold deposits, is a contentious issue in historical and modern economic geology. Over the past 40 years, debate in the economic geology community has revolved around whether the gold now in such deposits was an original part of the iron formation, or if it was introduced from an external, distant source. Less attention has been paid to the sources of As, Ag, and Te in these deposits, but as they commonly co-exist with gold in ore zones, determining their provenance is of relevance in assessing the origin of sediment-hosted and greenstone-hosted gold deposits.

In this thesis, black shales are investigated as the source of gold, arsenic, and tellurium at two BIF-hosted gold districts, Randalls (Australia) and Homestake (USA). The primary tools used in this investigation were petrography, textural analysis, whole-rock XRF, optical and scanning electron microscopy, and laser ablation inductively-coupled plasma mass spectrometry (LA-ICP-MS). In particular, sulfides associated with the BIF-gold ores (e.g., pyrite, pyrrhotite, and arsenopyrite) and 'background' sulfides in non-BIF rocks a short distance from the ore zones were analyzed using laser ablation imaging and spot methods to determine their trace element contents and zonation (especially their Au, As, Ag, and Te concentrations). Special attention was paid to fine-grained, carbonaceous and sulfidic (meta) sedimentary rocks, or black shales, as these are widely acknowledged to be excellent source material for sediment-hosted gold, nickel, and copper deposits.

The Archean Randalls district (including Lucky Bay) is located in the southern Eastern Goldfields Superterrane, one of several crustal fragments that make up the Archean-Proterozoic Yilgarn Craton. The Yilgarn is one of the most gold-rich areas in the world, containing an estimated 9500 t (270 million ounces [Moz]) of Au. The Randalls district is located in the Belches Basin, one of several so-called 'Late-Stage Basins' in the Eastern Goldfields, and contains three BIF-hosted gold deposits (Cock-Eyed Bob, Maxwells, and Santa-Craze). Other styles of gold mineralization do occur in the area, such as the Daisy Milano deposit (quartz-vein lodes in altered basalts) and the Imperial-Majestic deposits (possible intrusion-related gold systems).

The >40 Moz (1300 t Au) Paleoproterozoic Homestake BIF-hosted deposit (the largest of its kind in the world) is located in the Black Hills dome of western South Dakota, which consists of an Archean-Proterozoic metasedimentary/metaigneous core flanked by Phanerozoic sediments; the current geologic architecture of the Black Hills was created during the 80–40 Ma Laramide orogeny, which formed the Rocky Mountains. Numerous felsic and alkalic intrusions were emplaced in all Precambrian and Phanerozoic units during this time, some of which are present in the Homestake mine area. These are

commonly pyrite-bearing.

At Randalls, the ore host BIF is enveloped by km-thick quartz- and feldspar-rich turbidites, with very little shale (and virtually no carbonaceous black shale). However, 10 km west of Cock-Eyed Bob is the Lucky Bay prospect, which contains abundant carbonaceous, fine-grained, and sulfidic (meta) black shale. This unit contains several types of pyrite, including pyrite nodules that are orders-of-magnitude more enriched in Au (0.1–2 ppm), As (500–10,000 ppm), Ag (1–100 ppm), and Te (0.5–50 ppm) than average crustal background levels. Other elements enriched in the Lucky Bay nodules are Co (500–1000 ppm), Ni (500–1000 ppm), Cu (100–500 ppm), Zn (50 ppm), Se (10–50 ppm), Mo (1–5 ppm), Sb (100–200 ppm), Hg (1000–2000 counts per second), Tl (0.5–10 ppm), Pb (500–1000 ppm), and Bi (20-50 ppm). Structural relationships observed in drill core and under the microscope suggest that these nodules are pre-metamorphic and pre-deformation, as evidenced by the 'wrapping' of bedding around the nodules. Pressure shadows containing quartz, mica, and a second generation of pyrite (plus sphalerite and chalcopyrite) also point to pre-deformational (likely syn-sedimentary or early diagenetic) growth.

Likewise, fine-grained (<0.5 mm diameter) anhedral pyrite and larger (up to 5 mm), partially recrystallized pyrite nodules in metamorphosed black shale at Homestake also have high amounts of Au (up to 0.5 ppm, average 0.3 ppm), As (up to 10,000 ppm), Ag (~10 ppm), Te (~10 ppm), and the other ore-associated elements noted above for pyrite nodules at Lucky Bay, though not quite at the same level as those nodules. This is likely due to the greater intensity of metamorphism (lower-middle amphibolite facies) experienced by lithologies at the Homestake deposit and surrounds, which recrystallized and partially converted the pyrite to pyrrhotite; pyrite at Lucky Bay (lower-middle greenschist facies) was spared this same fate. Furthermore, whole-rock analyses of the pyrite-bearing lithologies at Homestake show that the unit contains levels of V, Ag, Mo, Cu, and Zn on par with anomalous carbonaceous black shale (as published in the literature).

Lead isotopes of the pyrite nodules and the diagenetic pyrites from both localities appear to reinforce the claim that these pyrites did indeed form early in the history of the sedimentary units that host them. However, whereas Pb-Pb model ages of the Lucky Bay nodules are within error of the U-Pb depositional age, those from Homestake are hundreds of millions of years younger than the established intrusive, crystallization and depositional ages for all Proterozoic rock types in the Black Hills, suggesting that Pb loss and isotopic resetting had a major effect on minerals and rocks in and around Homestake. Futhermore, Pb isotope systematics of the eastern Yilgarn Craton are complex, such that two pyrites of otherwise different generations (i.e., sedimentary vs. ore-stage pyrite) can have Pb isotope compositions within error of each other. These aspects of the pyrite Pb isotope data from Lucky Bay and Homestake are here presented as caveats, not insurmountable obstacles, to the study and understanding of Pb isotope systematics in sulfides.

The sulfides within ore zones at both deposits do not contain the same high levels of trace elements, nor (with rare exceptions) do the amounts of the trace elements they have rival the levels of concentration seen in the various sedimentary pyrites outside the ore zone. At Randalls, pyrrhotite and arsenopyrite (the two major ore sulfides) are enriched in Co (up to 2000 ppm), Ni (up to 250 ppm), Se (up to 60 ppm), Mo (up to 50 ppm), Ag (up to 15 ppm), Sb (up to 200 ppm), and Te (up to 500 ppm). Certain elements, such as Mo and Te, are enriched only in arsenopyrite, while the rest are enriched at similar levels in both sulfides (furthermore, Te and Mo are more highly enriched in ore-stage arsenopyrite at Randalls than any other sulfide studied in this work). Arsenopyrite and pyrrhotite from Homestake (again the dominant ore zone sulfides) contain Co (50–1000 ppm), Ni (50–500 ppm), Se (100–200 ppm), Mo (10–100 ppm), Sb (50–500 ppm), Pb (1–100 ppm), and Bi (0.1–100 ppm). Many of the trace elements in the Randalls sulfides are strongly zoned, whereas the Homestake sulfide trace elements are more (but not completely) homogenized; as with the sedimentary pyrite above, this is interpreted to reflect higher metamorphic conditions attained at Homestake (lower-middle amphibolite facies) compared to

Randalls (upper greenschist facies), which would lead to the expulsion of most trace impurities, or at least the erasure of original zonation.

This work demonstrates that certain trace elements, including those most commonly associated with sediment-hosted and greenstone-hosted gold deposits, were concentrated in upper-crustal siliciclastics during sedimentation or early diagenesis (that is, prior to later events that gave rise to sediment-hosted and greenstone-hosted gold deposits), and particularly in syn-sedimentary to early diagenetic pyrite. This research also has the potential to address metal source issues in some very large orogenic gold resources around the world: for example, an extension of the work completed here was conducted at the world-class, ~60 Moz dolerite-hosted Golden Mile Au district in Kalgoorlie, ~60 km NW of Lucky Bay and Randalls. Despite the overwhelming abundance of basalt, komatiite, and dolerite, three separate black shale layers are present in the district as interflow sediments between the mafic/ultramafic volcanic flows. All three units (Kapai Slate, Oroya Shale, and Black Flag Group shale) contain pyrite nodules with very similar internal and external textures to those at Lucky Bay. The likenesses between these nodules' textures and the Lucky Bay nodules' (including deformed bedding around the nodules) indicate that those at the Golden Mile are diagenetic, not hydrothermal.

LA-ICP-MS geochemical studies of the Golden Mile pyrite nodules reveals differences between the nodules from each formation, but also consistent characteristics. One of these, the Oroya Shale, contains diagenetic pyrite nodules with very similar textures to those from Lucky Bay, but the amount of Au and other trace elements contained in these nodules is significantly higher (e.g., up to 10 ppm Au dissolved in the pyrite structure). Given the abundance of this trace element-enriched pyrite in black shales (~5–10 vol. %), and the thickness and extent of this rock type at Lucky Bay (~7 km^3), Homestake (~12 km^3), and the Golden Mile (~3 km^3), it is at least conceivable that a portion of the gold ore (plus As, Ag, and Te, in their various forms) now in the banded iron formations (and, by extension, the Golden Mile Dolerite) was sourced from the black shale units within the same succession (i.e., the stratigraphic footwall or hangingwall to the ore host).

Table of contents

List of figures and tables

Chapter 1

Introduction

Banded iron formations (BIF) are sedimentary rocks composed of intercalated beds, layers, or laminae of Fe-rich and Fe-poor minerals (Fe-rich: magnetite, hematite, siderite, and/or chlorite; Fe-poor: chert, quartz and/or carbonate), in which the iron content is at least 15 wt % (Bekker et al., 2010). They are dominantly Precambrian, although deposition of ironstone (Fe-rich sedimentary lithology containing appreciable P but lacking chert or quartz) occurred in the Paleozoic (Bekker et al., 2010). Iron formations (not including ironstone) are subdivided into four facies: silicate, oxide, carbonate and sulphide (Fig. 1.1; James, 1954), however, recent research (Bekker et al., 2010) has narrowed the classification from four to three, noting that sulphide-facies iron formation, as originally described, is actually pyritic carbonaceous black shale. Furthermore, BIF have been grouped into two classes broadly based on depositional setting (Gross, 1980): Algoma-type iron formations formed in close association with mafic volcanism, resulting in interlayered basaltic flows and iron formation. Rare earth element (REE) geochemistry studies on Algoma-type BIF suggest a deep ocean environment, away from cratonic influence, and consequently most iron formations of this type are not areally extensive (~ tens of km^2). Superior-type iron formations are commonly interbedded with carbonates, quartz arenites, and black shales, indicating a relatively shallower, more cratonic depositional setting. As a result, they cover large areas (~ hundreds of km^2) and can contain huge tonnages of Fe (10^{14} Mt at 15% Fe, in some cases; Bekker et al., 2010).

Iron formations of all types (including ironstones) are economically important for their high Fe content, especially those which have experienced post-depositional 'upgrading' to Fe ore (≥56% Fe). Some BIF have additional economic value, particularly those associated with ore-grade concentrations of Au. Gold deposits hosted in silicate-, oxide-, and/or carbonate-facies iron formation, either Algoma or Superior-type, are considered to be a subset of the orogenic lode gold deposit class, which contains 25% of the world's known gold resource (Goldfarb et al., 2005). These deposits are found almost exclusively within volcanosedimentary sequences of late Archaean age (2.7–2.5 Ga), except for the Homestake deposit, South Dakota, USA, which is believed to be Paleoproterozoic (~1.75 Ga). None are known to exist from the Phanerozoic. Due to the comparatively small volume of iron formations (including Superior-type BIF), total gold content in these deposits is typically low compared to other types of orogenic lode gold systems hosted in greenstone belts (<1 million ounces versus >10 million ounces, on average; Table 4.1), but locally they can be relatively gold- and sulphide-rich, especially near shear zones and fractures developed during deformation and/or metamorphism. Two opposing ideas have been developed to explain this association. Rye and Rye (1974), followed by a series of independent papers (Anhaeusser, 1976; Hutchinson, 1976; Fripp, 1976), proposed that gold and sulphides were formed at the same time as the host iron formation or shortly following (i.e., syngenetic), and then experienced minor remobilisation during deformation (Fig. 1.2a). In contrast, Phillips and Groves (1983) and Phillips et al. (1984) maintained that the gold and associated minerals were late (i.e., epigenetic), introduced by metamorphic fluids during deformation of the iron formation (Fig. 1.2b). The epigenesis model requires hydraulic fracturing of competent layers in the BIF during deformation, allowing Au-bearing fluids to infiltrate the otherwise impermeable iron formation. Researchers favouring this model believe that

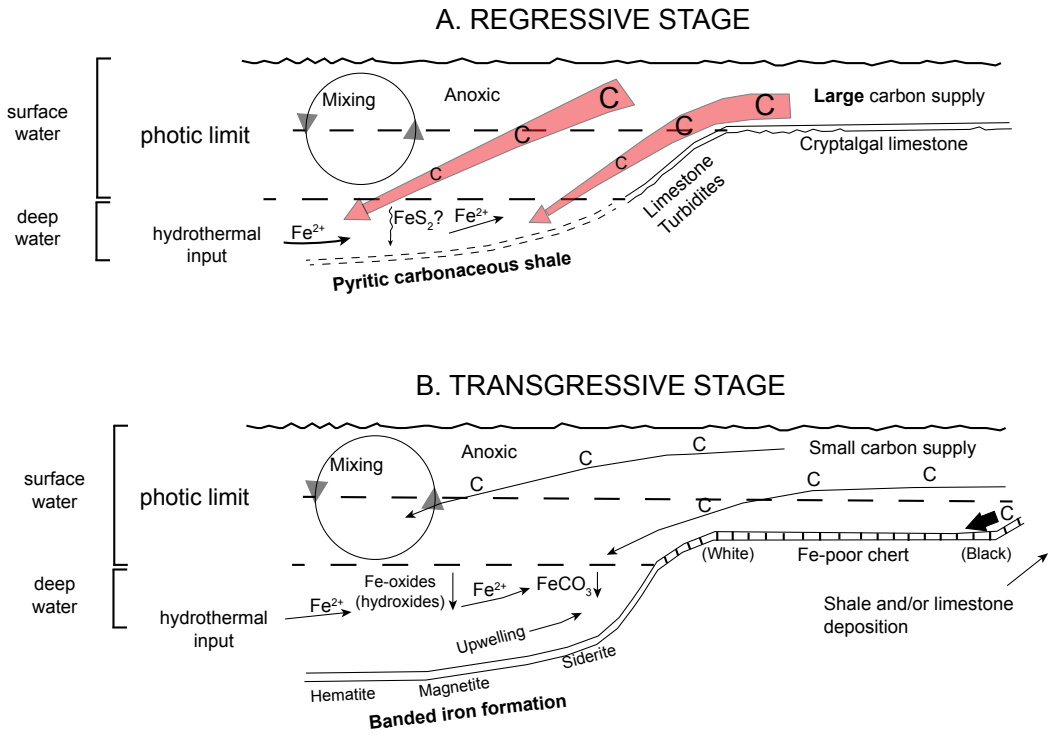

Figure 1.1 Schematic model for iron formation deposition. **A**. During regressive sea level stages, pyritic carbonaceous shale (formerly 'sulfide-facies' IF) is deposited in the abyssal plain due to the position of the photic zone (deep shelf floor), leading to a high organic C supply. **B**. In a transgressive stage, the photic zone is significantly above the deep shelf floor and the amount of organic C delivered to the abyssal plain is reduced, allowing for the deposition of iron formation and chert. Figure from Klein (2005).

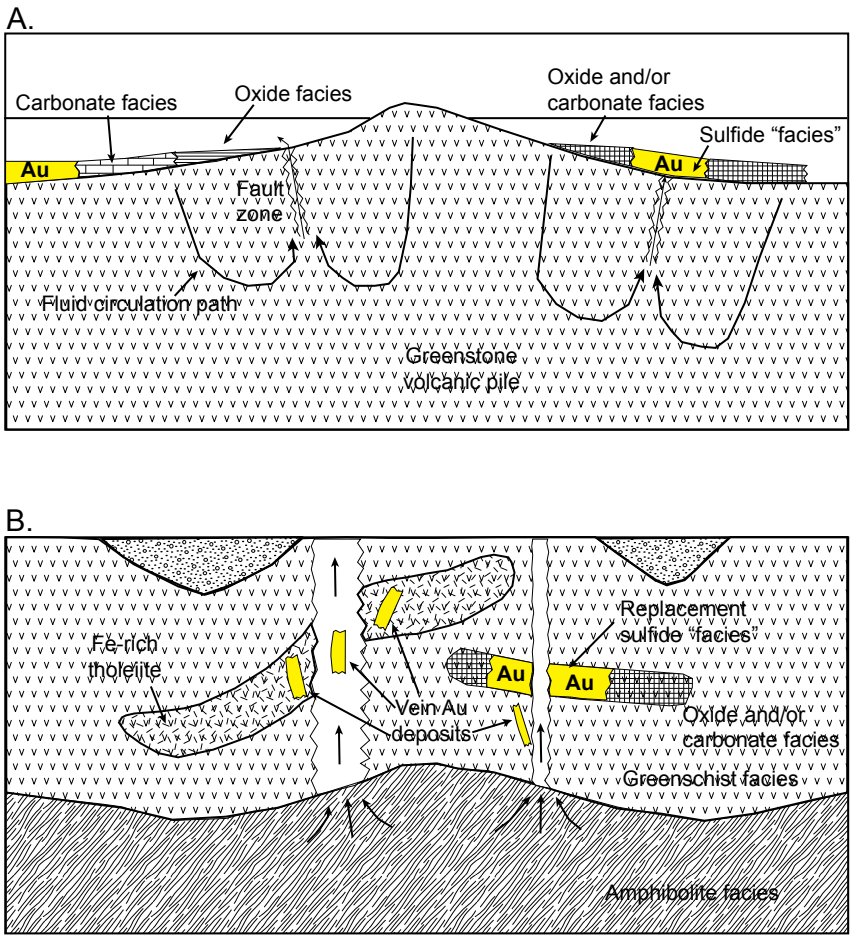

Figure 1.2 Contrasting models for the formation of gold deposits in BIF. **A.** The original 'syngenetic' model, proposed by Fripp (1976) for Archean BIF-gold systems in Zimbabwe. This model requires circulation of seawater through the metavolcanic pile, with faults serving as fluid pathways. These fluids leach the greenstones, depositing iron formation on the seafloor, with facies controlled by distance from the vent (oxide-facies proximal, sulfide-facies and Au distal). **B**. The 'epigenetic' model, first proposed by Phillips et al. (1984). Here, Au and associated ore elements are leached from amphibolite-facies rocks at depth and transported via shear zones and faults to favorable depositional horizons, such as BIF or Fe-rich tholeiites. Where the fluids intersect these lithologies, Au and sulfides are precipitated, replacing the host rock. Figures are from Phillips et al. (1984).

gold was carried in solution as thiocomplexes (e.g., $Au[HS]_2^-$) in the fluids that created and filled the fractures (Groves et al., 2003; Goldfarb et al., 2005). Reaction of the sulphur in the fluids with the iron in BIF (magnetite, hematite, siderite, and/or chlorite) caused the formation of pyrite, which dramatically reduced the availability of H_2S in the fluid and facilitated the precipitation of gold, either in the pyrite crystal structure or as native gold.

Phillips et al. (1984) was a watershed paper that clearly demonstrated the selective replacement of magnetite by pyrrhotite adjacent to syn-metamorphic, cross-cutting, Au-bearing quartz-pyrrhotite veins at the Water Tank Hill deposit near Mt. Magnet, Western Australia (Fig. 1.3A, B). The authors observed similar structures in other BIF-hosted gold deposits in Australia and Africa, and concluded that these features represented the main ore-forming mechanism. Numerous studies on iron formation-hosted gold deposits since the publication of Phillips et al. (1984) have echoed this hypothesis (e.g., Fyon et al., 1986; Groves et al., 1987; Caddey et al., 1991; Bullis et al., 1994; Hammond and Moore, 2006; Ribeiro-Rodrigues et al., 2007; Andrianjakavah et al., 2007; Frei et al., 2009). Consequently, nearly all of these deposits are now thought to be products of epigenetic processes, similar to the more common (and larger) vein- and shear-hosted orogenic gold deposits in greenstone terranes (altered volcanic rocks containing chlorite and/or epidote), near which the former are ubiquitous (Goldfarb et al., 2005).

Some iron formation-hosted gold deposits are still regarded as syngenetic despite the plethora of research articles to the contrary. The best-studied example of syngenetic BIF-hosted gold mineralization is the Kolar deposit (and surrounding lodes) in southern India (Siva Siddaiah and Rajamani, 1989; Siva Siddaiah et al., 1994). Kolar actually contains gold in mafic volcanic-hosted quartz-carbonate veins as well as banded iron formation lodes, but there are significant differences in the chemistry of these two ore types such that two separate modes of origin are advanced for each one. Syngenesis is argued for the BIF-hosted gold-sulphide ores on the basis of rare earth element (REE) patterns in the iron formation, which are similar to metalliferous hydrothermal fluids emanating from vents on the seafloor at or near spreading centres (Fig. 1.4A). On the other hand, the REE profiles of the quartz-carbonate vein lodes indicate derivation from more evolved, light rare earth (LREE)-enriched and heavy rare earth (HREE)-depleted metamorphic fluids, which would have been introduced during fracturing and deformation of the metavolcanic pile (Fig. 1.4B). Pari, a small iron formation-hosted gold deposit in the Quadrilátero Ferrífero (Iron Quadrangle) of Brazil, is also considered to be syngenetic (Vial et al., 2007), and is apparently the only such among the nine other known Archaean BIF-hosted gold deposits of this district.

The work of Kerswill (1993; 1996) represents another formidable challenge to the epigenetic models of the past 30 years. He focused on BIF-hosted gold deposits in Canada, where he formed two separate deposit classes: stratiform and non-stratiform (also called vein-type). Some of the studied deposits have features of both types in them; these he termed hybrid BIF-gold deposits. It was his considered opinion, based upon extensive and detailed mapping of several BIF-hosted gold mines in Canada, that most deposits of this type start off with a significant 'syngenetic' component, whereby many ore components (e.g., Au, Ag, and S) were already present in the host iron formation (or units immediately around the BIF and/or interlayered with it) before the deposit formed. Later, during hydrothermal ore creation (presumably related to deformation and/or metamorphism of the pile), these components would have been remobilized on a relatively small scale (e.g., 1-10 m), concentrating with other, possibly external ore metals in structurally prepared sites and forming reefs, lodes, and/or stockwork systems.

Recent research on the timing of gold emplacement in certain sediment-hosted orogenic gold deposits (Large et al., 2007; Meffre et al., 2008; Chang et al., 2008; Large et al., 2009; Thomas et al., 2011; Large et al., 2011, 2013; Pasava et al., 2013) has shown that gold and a characteristic assemblage of elements (Co, Ni, Cu, As, Se, Mo, Ag, Sb, Te, Tl, Pb, and Bi) are pre-concentrated in first-generation, syngenetic/early diagenetic pyrite and remobilized during later metamorphism and deformation. This 'two-stage' hypothesis was developed through the use of a laser microprobe mated to an inductively-

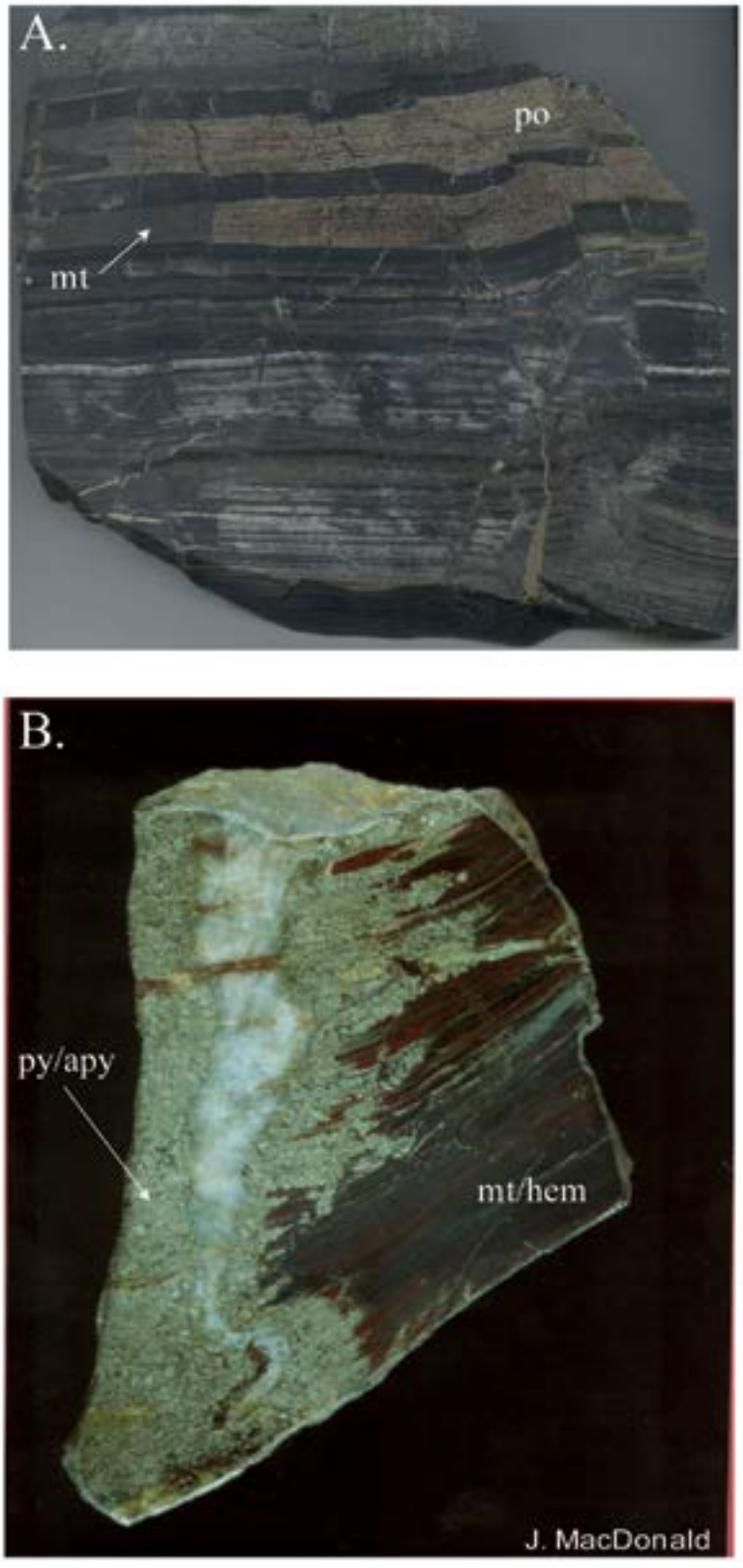

Figure 1.3 Sulphide replacement of original oxide-facies BIF. **A**. Sample from the Water Tank Hill deposit, near Mt. Magnet, Western Australia. Pyrrhotite (po) replaces magnetite (mt) adjacent to quartz veins (not seen in this picture). **B**. Sample from the King Solomon's Pillars area, near Geraldton, Ontario, Canada. Pyrite and arsenopyrite (py/apy) can be seen bleeding out laterally from the quartz vein, which is cutting across the primary layering of magnetite and hematite (mt/hem) at a high angle. Unlike the sample in A, this replacement texture is destructive of the original fabric.

coupled plasma-mass spectrometer (ICP-MS) that allows for precise spot analyses (25-40 μm wide) of pyrite via laser ablation (LA). The LA-ICPMS system measures trace metal content (typically 30–35 elements) for one specific area in the crystal. An element 'map' for a given pyrite grain can thus be created by overlaying the pyrite surface with a virtual grid and ablating sets of parallel lines along the same; an example is shown in Figure 1.5 (from Large et al., 2009). The end result is the full history of gold paragenesis. In the case of pyrite-dominant systems, gold remains in pyrite (either in solution or as nanoparticles) at low temperatures (~250–300°C), but with increasing metamorphic grade, pyrite is converted to pyrrhotite, thereby releasing gold, arsenic, tellurium, and other trace metals to the surrounding rock matrix and metamorphic fluid (Fig. 1.6A–C; Buryak, 1982; Large et al., 2009; Tomkins, 2010; Thomas et al., 2011; Large et al., 2011). This allows the gold to be concentrated in fold hinges and other structurally favourable sites during deformation. LA-ICP-MS imaging has the potential to be extremely useful in the epigenesis versus syngenesis debate regarding iron formation-hosted gold deposits. One indication of promise is provided by a sample of distal silicate-facies iron formation from the Kolar goldfields, which shows gold and VAMSNAZ enrichment in the lepidocrocite (Fe)-rich mesobands but little to no such in the chert mesobands (Fig. 1.7; Large, 2010). This lends strength to the syngenetic hypotheses of Siva Siddaiah and Rajamani (1989) and Siva Siddaiah et al. (1994) for the iron formation-hosted lodes in the Kolar goldfields, and calls for more testing, especially within BIF-hosted gold districts that are widely believed to be epigenetic.

The purpose of this research is to re-evaluate the epigenetic model of ore formation for two iron formation-hosted gold districts, Homestake (USA) and Randalls (Australia), using iron formation and pyritic black shale from the mines (in the case of Homestake) as well as samples of pyritic black shale from the Lucky Bay gold prospect, 10 km W of the Randalls district. Further work on the trace element character of pyrite within the black shale facies has been carried out on one other, non-BIF-hosted orogenic gold deposit, the Golden Mile (Australia). The primary method of analysis has been the laser ablation (LA-ICPMS) imaging technique previously described to determine the trace element contents and zonation within the diagenetic pyrite and iron-rich mesobands of the iron formations and surrounding lithologies, with particular interest in gold and the ore-forming trace element suite. These deposits were selected on the basis of their differing metamorphic grades, with Homestake having the highest metamorphic grade (lower amphibolite facies) and Randalls being the lowest grade district (maximum upper greenschist facies). This spectrum of metamorphic conditions is necessary for unravelling the evolution of these ores. Testing this model at the selected sites (as well as at the Golden Mile greenstone-hosted orogenic Au deposit) has hopefully provided a clearer paragenetic sequence of gold mineralization in BIF-hosted systems than currently exists. Lead isotopes in pyrite (Meffre et al., 2008), conventional and SHRIMP sulfur isotope studies, and whole-rock geochemical analyses have complimented the LA-ICPMS results and help construct a more robust framework for understanding the origins of iron formation-hosted gold ores. Research questions answered in this study include:

- Is gold originally concentrated in pyritic carbonaceous shale ('sulfide-facies BIF') only, as previous workers suggest, or has it been concentrated in oxide, silicate, and/or carbonate-facies BIF, as well?

- Do arsenic (As) and tellurium (Te) display enrichment in unaltered iron formations, or are they introduced from an external source?

- Are pyritic black shales in orogenic gold camps realistic sources of gold for these deposits, in a geodynamic (structural, hydrogeologic) sense?

- Is the now 25-year-old epigenetic model for BIF-hosted gold deposits still applicable to the majority of known districts?

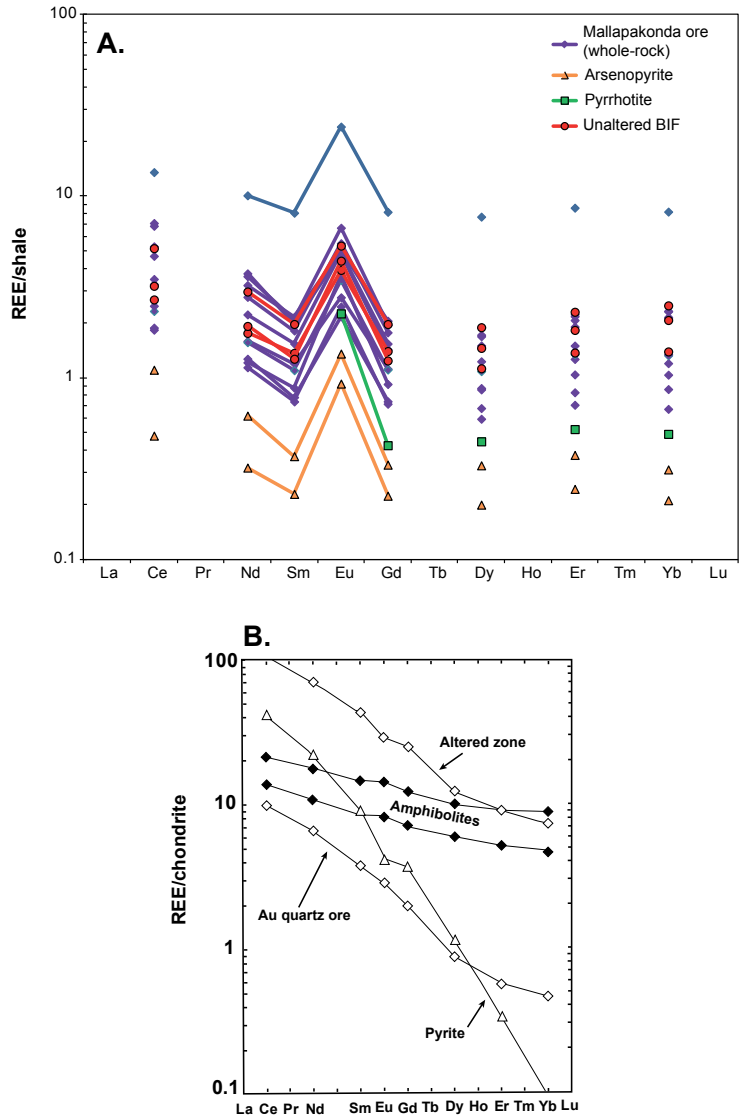

Figure 1.4 Rare-earth element (REE) profiles of gold-sulfide lodes, sulphide separartes, barren iron formation, and gold-bearing quartz-carbonate veins in amphibolite from the Kolar district, India (firgures from Siva Siddaiah et al., 1994). **A.** REE patterns of gold-sulfide lodes, individual sulphide minerals, and barren BIF are remarkably similar (positive Eu anomaly, no LREE/HREE fractionation). This suggests that the unmineralized and mineralized BIF formed from the same, hot (≥300°C), reduced fluid. **B.** In contrast, the REE profiles of the amphibolites and amphibolite-hosted, auriferous quartz-carbonate veins are much different, showing high LREE/HREE ratios and no Eu anomaly, which indicates that these lithologies were deposited from a late, possibly metamorphic, fluid rich in LREE and depleted in HREE.

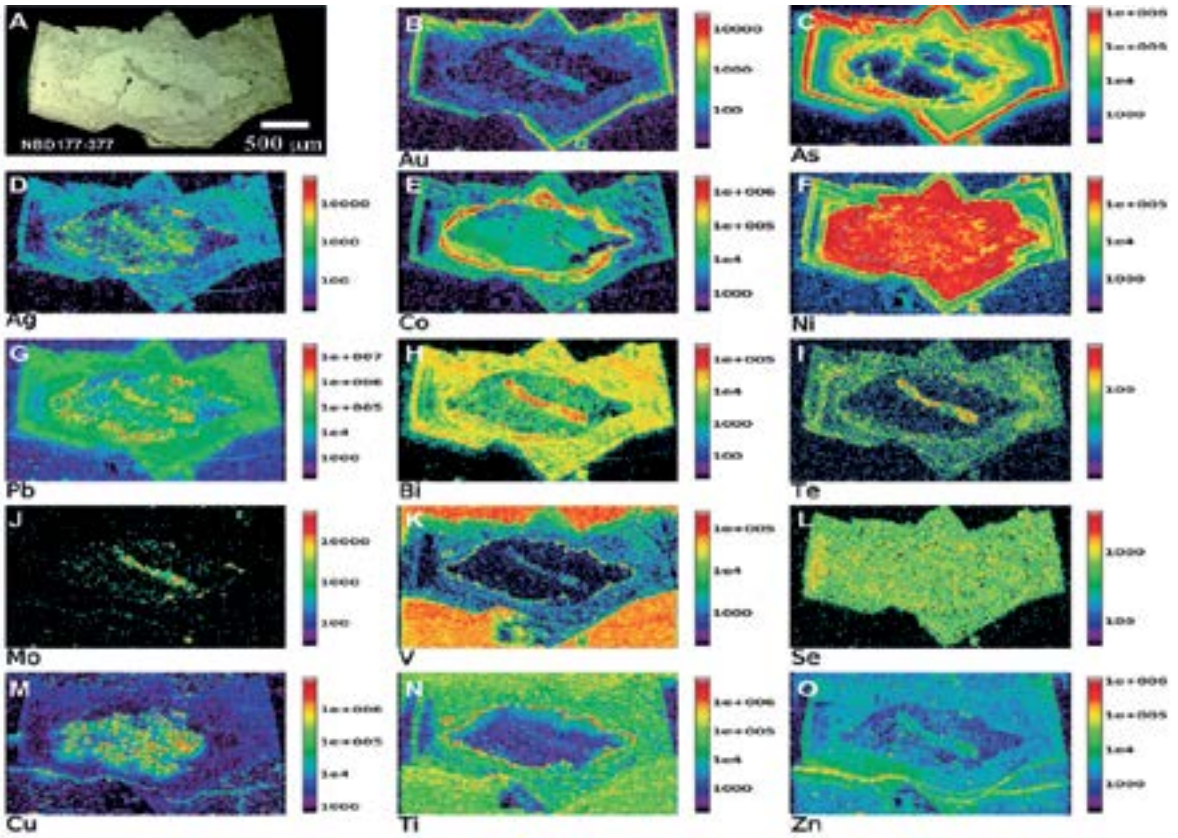

Figure 1.5 Series of maps showing trace element concentrations (in counts per second) in pyrite from Bendigo, Australia, produced by LA-ICPMS imaging techniques developed at CODES, University of Tasmania (figure from Large et al., 2009). Gold shows a bimodal distribution in this sample, with the tubular core and the outermost rim both containing relatively high amounts of Au compared to all other pyrite types in this image. This indicates a multi-stage process for Au enrichment at Bendigo, and also showcases the power of LA-ICPMS technology in unraveling ore-forming processes.

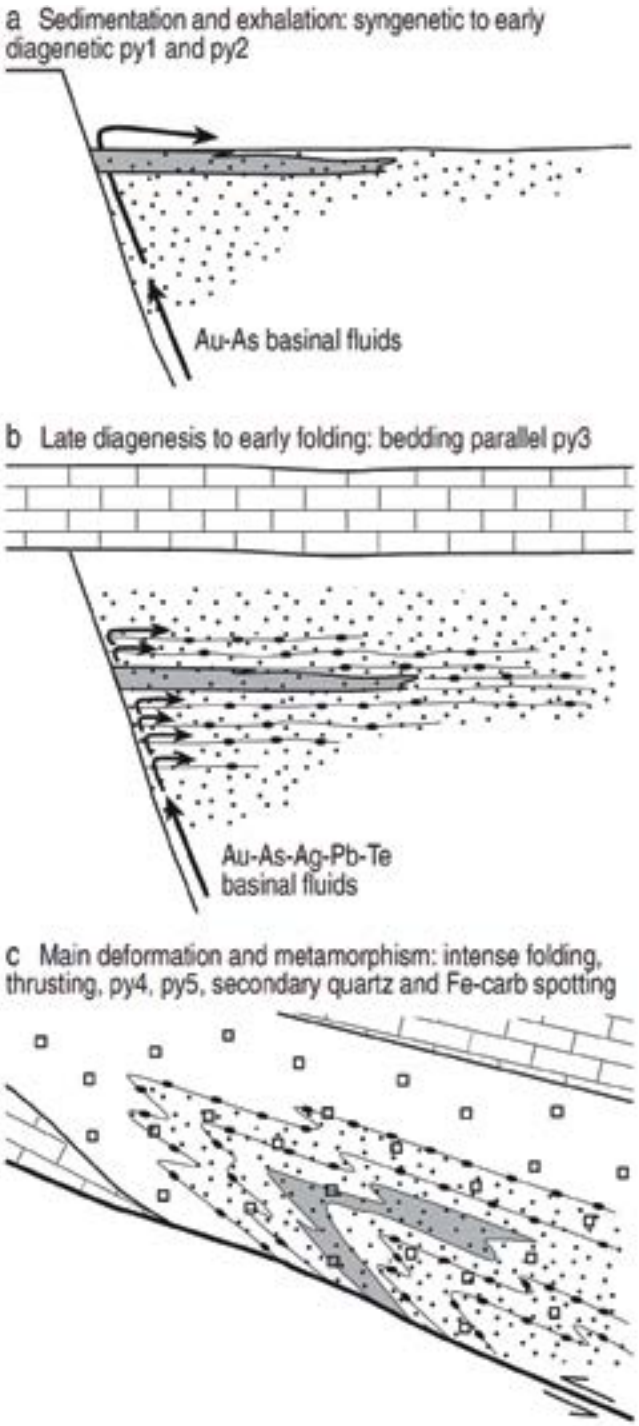

Figure 1.6 Model of formation for Sukhoi Log, Russia (figure from Large et al., 2007), which can be applied to other sediment-hosted Au deposits (see Large et al., 2009, 2011; this study). **A.** Gold and As are preconcentrated in carbonaceous, fine-grained sediments during sedimentation and early diagenesis. **B.** Other elements, such as Ag, Te, Pb, as well as Au and As, are added during late diagenesis/incipient folding. **C.** The deposit is then 'created' during the main period of deformation and metamorphism, when diagenetic pyrite is converted to pyrrhotite, which causes release of all elements contained within the pyrite (as microinclusions or within the crystal lattice). These elements (including Au) migrate to structurally favorable sites of deposition (e.g., anticlinal fold hinges).

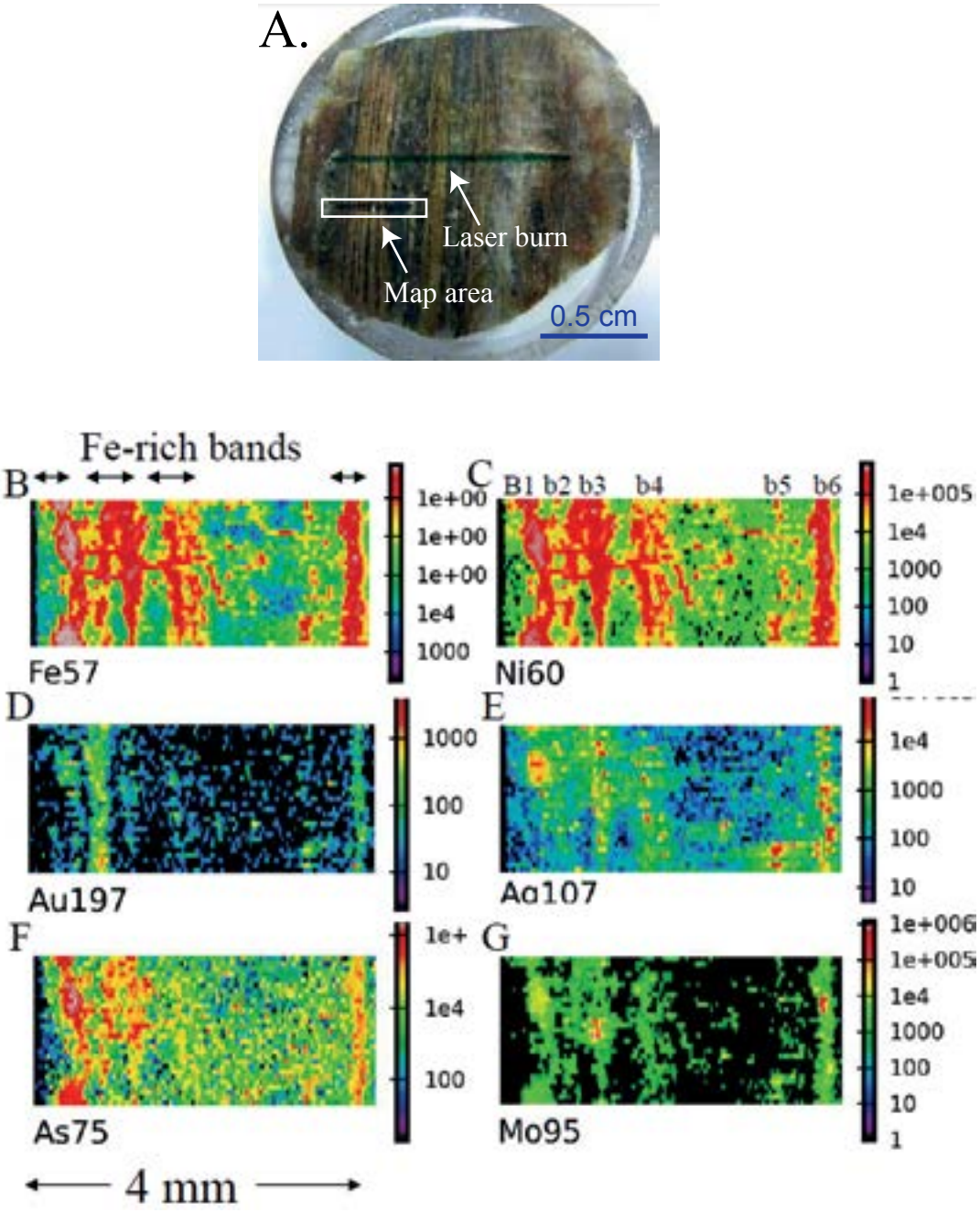

Figure 1.7 **A.** LA-ICPMS image of silicate-facies BIF from the Kolar district, India (figure from Large, 2010). The map encompasses several Fe-rich bands (**B**; bands numbered b1-b6 from left to right; Fe present as lepidocrocite [FeO(OH)]), which is also enriched in Ni (**C**). **D.** Au (especially b2 and b6). **E.** Ag. **F.** As (Si bands also contain As). **G.** Mo. The map area is 4 mm by 1.7 mm.

At the University of Tasmania, each PhD student in the Earth Sciences department has the option of writing their thesis in the traditional format or as a series of published papers (minimum of three). I opted for the second choice, and thus this thesis is structured as a series of four papers: Chapter 2 (published 2013 in *Precambrian Research*) covers the trace element and Pb isotope geochemistry of pyrite nodules from Lucky Bay (~10 km W of Randalls). Chapter 3 (published 2014 in *Precambrian Research*) deals with the geology of the Randalls BIF-hosted gold deposits. Chapter 4 (to be re-submitted to *Economic Geology* following corrections) is on the trace-element and Pb isotope geochemistry of pyrite in Homestake BIF-gold deposit, and Chapter 5 (published 2015 in *Economic Geology*) is on the geochemistry of diagenetic and ore-stage pyrite at the Golden Mile deposit. Finally, Chapter 6 is the synthesis/conclusions of the preceding chapters, which ties them all together.

Chapter 2

Age, origin, and significance of nodular sulfides in 2680 Ma carbonaceous black shale of the Eastern Goldfields Superterrane, Yilgarn Craton, Western Australia

Published in ***Precambrian Research****, 2013, v. 230, p. 227-247*

Abstract

Sulfide nodules composed of pyrite occur within black shales in the Lucky Bay area of the Bulong Domain, Eastern Goldfields Superterrane, Yilgarn Craton, Western Australia that correlate with the Neoarchean Black Flag Group. Detailed petrography reveals a variety of shapes and textures, from spherical to ovoid and zoned to uniform. Some nodules have recrystallized, resulting in a later generation of pyrite. All have been affected by post-depositional metamorphism, as evidenced by pressure shadows containing quartz±mica±carbonate assemblages. LA-ICP-MS analyses show that these nodules are enriched in a range of trace elements, including Co, Ni, Cu, Ag, Sb, Te, Au, Tl, Pb, and Bi. Gold and Te concentrations range from 0.3–1 ppm and 10–50 ppm, respectively. The Black Flag Group equivalents stratigraphically and structurally underlie a younger basin east of Lucky Bay that contains turbidites, sandy debris flows and BIF, the latter of which hosts several gold deposits at Randalls, 60 km SE of Kalgoorlie. It is likely that the lateral equivalents of the nodular sulfide-bearing black shale originally occurred stratigraphically beneath what is now the ore horizon at Randalls. Given its anomalous Au and Te content, this lithology is a potential contributor of gold to the BIF-hosted gold deposits of the Randalls Goldfield, as well as other similar gold resources elsewhere in the Eastern Goldfields Superterrane.

2.1 Introduction

Nodules or concretions composed of base metal sulfides, particularly iron sulfides, are a common feature in fine-grained sediments deposited in marine basins. Nodular sulfides have also been reported from some carbonaceous chondrites, where their mineralogy is quite complex and exotic relative to terrestrial sulfide nodules (Rubin, 1993; Lin and El Goresy, 2002; Weisberg et al., 2006; Lehner et al., 2008). The morphology of sedimentary sulfide nodules is quite diverse, ranging from near spherical to ellipsoid (the latter often due to post-depositional compaction and deformation) and zoned or unzoned internally (Melezhik et al., 1998). Their textures and mineralogy are just as varied and can include finely intergrown marcasite and pyrite; aggregated framboidal pyrite; fine-grained marcasite with septarian cracks infilled by calcite; intergrown galena and chalcopyrite (Jowett et al., 1991); and intergrown pyrite, pyrrhotite, and carbonate (Melezhik et al., 1998).

Nodular sulfides in Archean and early Proterozoic black shale sequences appear to be no less abundant than those in Phanerozoic sequences, but their occurrences are not as well-reported (Melezhik et al., 1998). In the Mesoarchean Witwatersrand Supergroup of South Africa, pyrite nodules have been reported from the Coronation Formation in the West Rand Group below the major gold reefs (Guy

et al., 2011). In the Neoarchean Yilgarn Craton of southern Western Australia, sulfide nodule-bearing black shale (the Kapai Slate) occurs in the Kambalda Ni-Cu sulfide district (Bavinton, 1981) and the St. Ives orogenic Au district (Gregory, unpub. data), while at Mount Charlotte (Au), graywackes belonging to the Black Flag Group contain pyrite nodules up to ~1 cm in diameter (Mueller and Muhling, 2013). Further to the north, in the Archean-Proterozoic Pilbara Craton of northern Western Australia, nodular sulfide-bearing horizons have been documented in the Mount McRae Shale and Whaleback Shale of the Brockman Supersequence (Krapež et al., 2003). The latter two sequences are also intimately associated with banded iron formation. Proterozoic examples of black shale sequences containing nodular sulfides occur, for example, in the ~2000 Ma Pilgujärvi ('Productive') Formation of NW Russia (Melezhik et al., 1998), the ~2000 Ma Poorman Formation and ~1880 Ma Nahant Formation, northern Black Hills, South Dakota, USA (Steadman, unpub. data), the 1325 Ma Newland Formation, Belt Supergroup, Montana, USA (Strauss and Schieber, 1990), and in the shale host rocks to the ~600 Ma Sukhoi Log Au deposit (Large et al., 2007).

Fine-grained, carbonaceous, sulfidic black shale such as that reported here from Lucky Bay is often spatially associated with orogenic gold deposits of all ages around the world (e.g., St. Ives, Australia; Sukhoi Log, Russia; Bendigo, Australia; Kumtor, Kyrgyzstan; and Muruntau, Uzbekistan). Prevailing models for the formation of these gold reserves typically involve syn- or post-orogenic timing of ore deposition and a deep-seated fluid and metal source (Groves et al., 1998; Goldfarb et al., 2005). Recent work by Large et al. (2007; 2009; 2011) and Thomas et al. (2011) on sulfide paragenesis in four sediment-hosted orogenic gold deposits around the world counters the latter component of the reigning paradigm by presenting evidence to suggest the mineralizing fluids and metals may be relatively locally derived (i.e., sourced from the surrounding sediments, which are fine-grained, often carbonaceous and sulfidic). In the deposits studied by these authors, fine-grained carbonaceous sediments containing pyrite and/or pyrrhotite are common to abundant in and around the ore zone, and in these lithologies a multi-stage history of pyrite growth, dissolution, and re-growth is preserved. At Sukhoi Log, fine-grained bedding-parallel pyrite nodules and clusters of micro-euhedra, with a large, diverse trace element inventory (including Au, Ni, Ag, and As) and a broad range in S isotope values, were interpreted to be early diagenetic, while coarser-grained pyrite with subhedral to euhedral crystal shapes and comparatively minor trace element enrichments (i.e., low Au, As, Ni, and Ag) was interpreted as metamorphic or hydrothermal (Large et al., 2007; Chang et al., 2008). Lead isotope analyses of the various pyrite types showed that the early diagenetic pyrite contained the least radiogenic Pb, which supported the paragenetic classifications (Meffre et al., 2008). A complete history of gold paragenesis in the deposit, from sedimentation to ore-formation, was thus developed using detailed petrography, whole-rock XRF, and LA-ICPMS trace element and Pb isotope analyses on individual pyrite generations. A similar multi-faceted geochemical approach has been applied to this study, elucidating the paragenesis of pyrite nodules contained within the carbonaceous black shale at the Lucky Bay gold prospect, and bolstering the arguments put forth in Large et al. (2009; 2011) concerning the origins of sediment-hosted gold resources, which in this case are associated with BIFs.

2.2 Geological context

2.2.1 Regional geology – stratigraphy and geochronology

The Lucky Bay prospect is located approximately 70 km SE of Kalgoorlie (~35 km E of Kambalda) in the Eastern Goldfields Superterrane (Fig. 2.1A). The Eastern Goldfields Superterrane (EGS) is a Neoarchean granite-greenstone terrain composed of five NNW-trending arc fragments, termed the Kalgoorlie, Gindalbie, Kurnalpi, Burtville, and Yamarna Terranes (Fig. 2.1B). Each terrane has its own history, complete with intermediate to felsic volcanic rock packages defined by unique volcanic facies, age, and geochemistry (Swager, 1997; Barley et al., 2008). Nevertheless, the development of

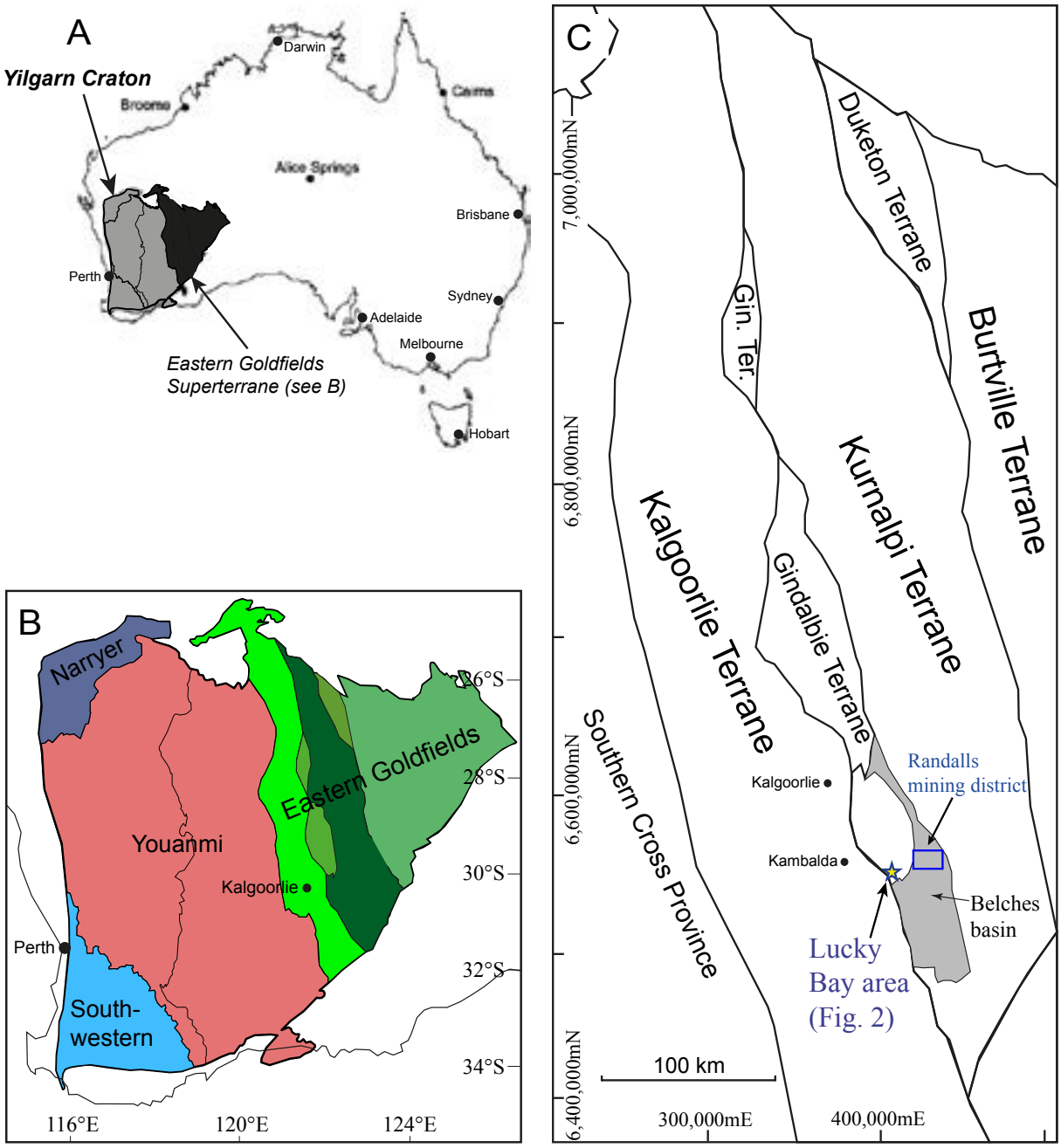

Figure 2.1 **A**. Map of Australia showing location of the Yilgarn Craton; the Eastern Goldfields Superterrane is in black (redrawn after Krapež et al., 2008). **B.** The Yilgarn Craton (after Czarnota et al., 2010), composed of two provinces (Narryer and Southwestern) and two superterranes (Youanmi and Eastern Goldfields). **C**. Schematic representation of the Eastern Goldfields Superterrane (after Krapež et al., 2008). The blue box (SE region of map) represents the Randalls BIF-Au district, while the star indicates the location of the Lucky Bay area.

the individual terranes was at least partially linked in time and space. Squire et al. (2010) highlight the fact that most of the volcano-sedimentary successions comprising the EGS were created during four separate magmatic pulses, at 2940, 2810, and 2760 Ma, and a protracted episode from 2715–2655 Ma (all ages approximate). During these periods, the arc fragments-turned-terranes were physically separate, explaining the relatively minor differences now preserved in the rock record. At ca. 2660 Ma they amalgamated, and by ~2645 Ma were sutured to the preexisting proto-continent (Fig. 2.1B, C).

SHRIMP and LA-ICP-MS measurements of magmatic and detrital zircon from numerous successions in the EGS have played a key role in elucidating the tectonostratigraphic architechture

of the Yilgarn Craton (e.g., Krapež et al., 2000, 2008; Kositcin et al., 2008; Krapež and Pickard, 2010; Squire et al., 2010). These and other research papers provide detailed accounts of the construction of the several sequences contained within each terrane; a summary of the successions in the youngest magamatic episode (2715–2655 Ma) is provided here. The rocks produced during this magmatic pulse are the dominant representatives of Neoarchean volcanism and sedimentation in the Kalgoorlie, Gindalbie and Kurnalpi Terranes. Krapež and Pickard (2010) divide the event into two main stages in each of the three Terranes, with slight differences in timing and petrochemistry. The second stage of Episode 4 is best represented by the Kalgoorlie Sequence, a ~6 km-thick pile of predominantly felsic clastic rocks that stratigraphically overlie the Kambalda Sequence in the Kalgoorlie Terrane. The Kalgoorlie Sequence is also called the Black Flag Group, which includes the Spargoville, Black Flag, and White Flag Formations (Fig. 2.3; Krapež et al., 2000; Swager et al., 1992). These three components of the Black Flag Group/Kalgoorlie Sequence are comprised of varying amounts of rhyolitic/dacitic lavas, volcaniclastic breccias/sandstones, turbidites, and carbonaceous shale. The maximum depositional age of the Kalgoorlie Sequence is constrained by two ages: 2692±4 Ma and 2686±3 Ma (both 2σ). The first date is a U-Pb zircon age for the Kapai Slate, an interflow sedimentary unit (including sulfidic black mudstone) within the upper Kambalda Sequence (Claoué-Long et al., 1988). The second date, also a U-Pb zircon age, is from a dacite clast within the basal Black Flag Group (Spargoville Formation; Krapež et al., 2000). The minimum depositional age is believed to be 2658±3 Ma (2σ), which was obtained from a felsic intrusion (Mt. Shea porphyry, Kositcin et al., 2008) that cross-cuts the Black Flag Group south of Kalgoorlie (sample SHD-9, Krapež et al., 2000). Squire et al. (2010) placed the minimum depositional age of the Kalgoorlie Sequence at ~2670 Ma, based on the texture, composition, and zircon age of a sample of sandstone they collected from the upper Kalgoorlie Sequence. This sample (LB212 in their paper) came from a very thick package of quartz-rich sandstone at St. Ives containing volcanic quartz and exhibiting a tight distribution of U-Pb ages (2670–2660 Ma). These characteristics are unlike those of the underlying (and older) Kalgoorlie Sequence units, which are more feldspar- and mafic clast-dominant. Squire et al. (2010) therefore maintain that the felsic intrusion dated by Krapež et al. (2000; sample SHD-9) is more likely to be a constraint on the minimum depositional age of the overlying Merougil Group (see 'Discussion' for more detail on this issue).

2.2.2 Regional geology – deformational and metamorphic history

Blewett et al. (2010), building upon the previous work of Swager (1997), presented a new framework for understanding the deformational events that occurred in the Eastern Goldfields Superterrane (EGS) during the late Archean. They highlighted five main structural events ($D_{1\text{-}5}$), of which D_1, D_2, D_3, and D_4 are of greatest relevance to this paper. D_1 ('D_E' in Swager, 1997) was the longest-lived of the five, commencing ~2810 Ma and ending at approximately 2670 Ma. It was an episode of east-northeast extension, primarily responsible for the volcanism and deposition associated with the Kambalda and Kalgoorlie Sequences in the Kalgoorlie Terrane (and correlatives in the Gindalbie and Kurnalpi Terranes) as well as the strong NNW-trending structural fabric of the entire Eastern Goldfields Superterrane. The subsequent D_2 event (ENE–WSW compression; ~2668 Ma) formed a weak fabric and open, upright folds in pre-2670 Ma units across the Superterrane. D_3 (ENE–WNW extension) began at around 2665 Ma in the Kalgoorlie Terrane. This second extension event created the depo-centers for granitic detritus shed off the basement domes, which are now the so-called "Late-Stage" basins, the final products of Neoarchean sedimentation in the Eastern Goldfields Superterrane. One of these late basins, the Belches Basin, is host to the Randalls BIF-gold district. The last episode, D_4 ('D_2' in Swager, 1997), is separated by Blewett et al. (2010) into two stages: stage 4a commenced with a second ENE–WSW compressive regime, similar to D_2, which tightened earlier-formed F_2 and F_3 folds and initiated thrusting to the WSW along major NNW-trending faults. D_{4a} also produced tight folding in the Late-Stage Basin sediments. Localized areas of high strain developed in units at the margins of granite domes. Stage 4b

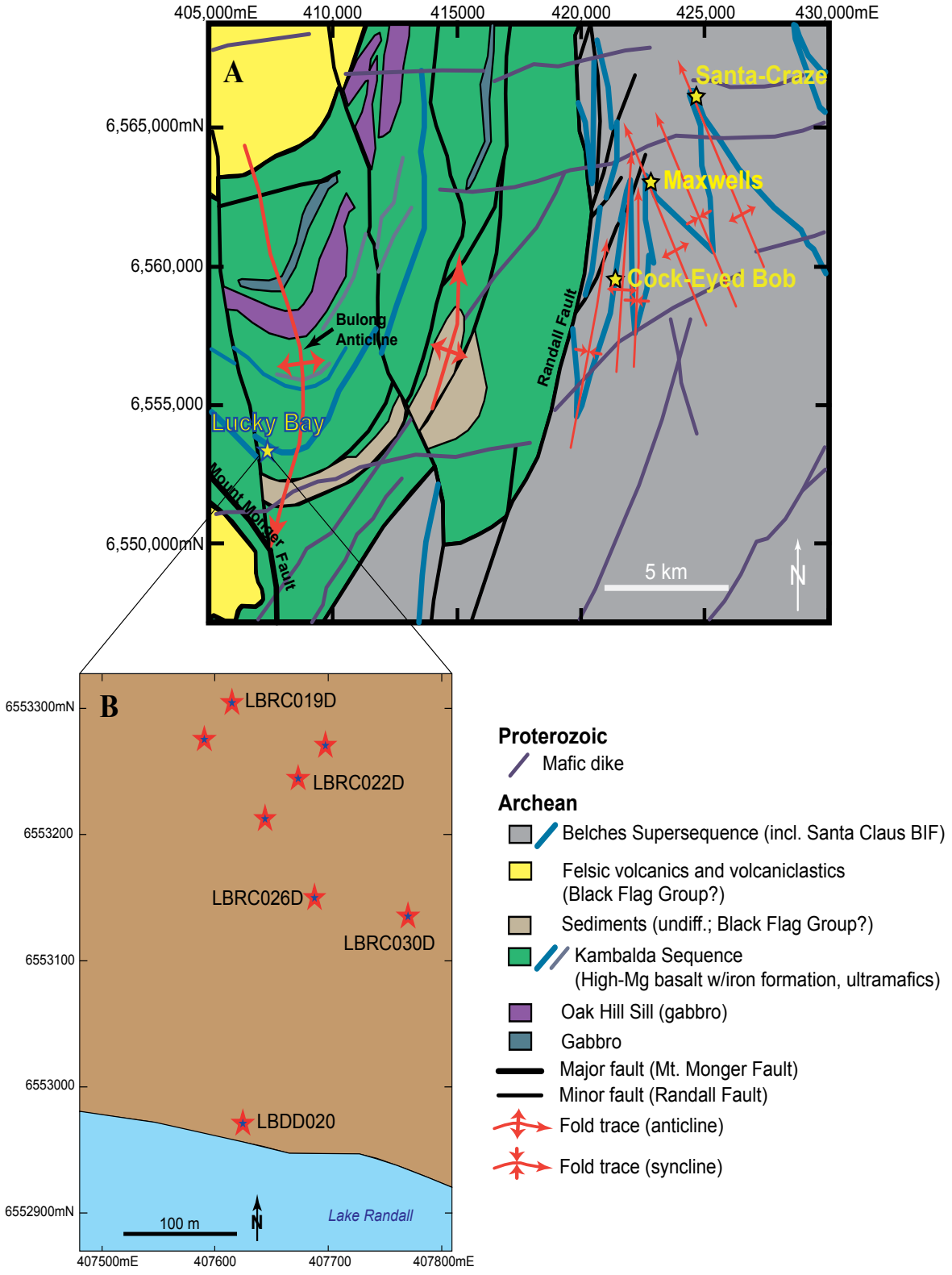

Figure 2.2 **A.** Bedrock geology map of Lucky Bay and the surrounding area, including the Belches Basin and Randalls BIF-Au district deposits (redrawn after Painter and Groenewald, 2001). The Lucky Bay sedimentary sequence is enveloped by greenstone successions (mainly basalt) which belong to Kambalda Sequence correlatives. Lucky Bay is west of the Randall fault, which is the boundary between the Gindalbie Terrane and the younger Belches basin, which contains the Belches Supersequence. Although Lucky Bay appears to sit within a thick succession of basalt, the dominant local lithology is fine/medium-grained turbidite, with only minor igneous horizons. **B.** Local map of the Lucky Bay prospect. Stars indicate drill holes sampled, and drill holes mentioned are labeled. Drill lines run SW-NE, perpendicular to stratigraphy.

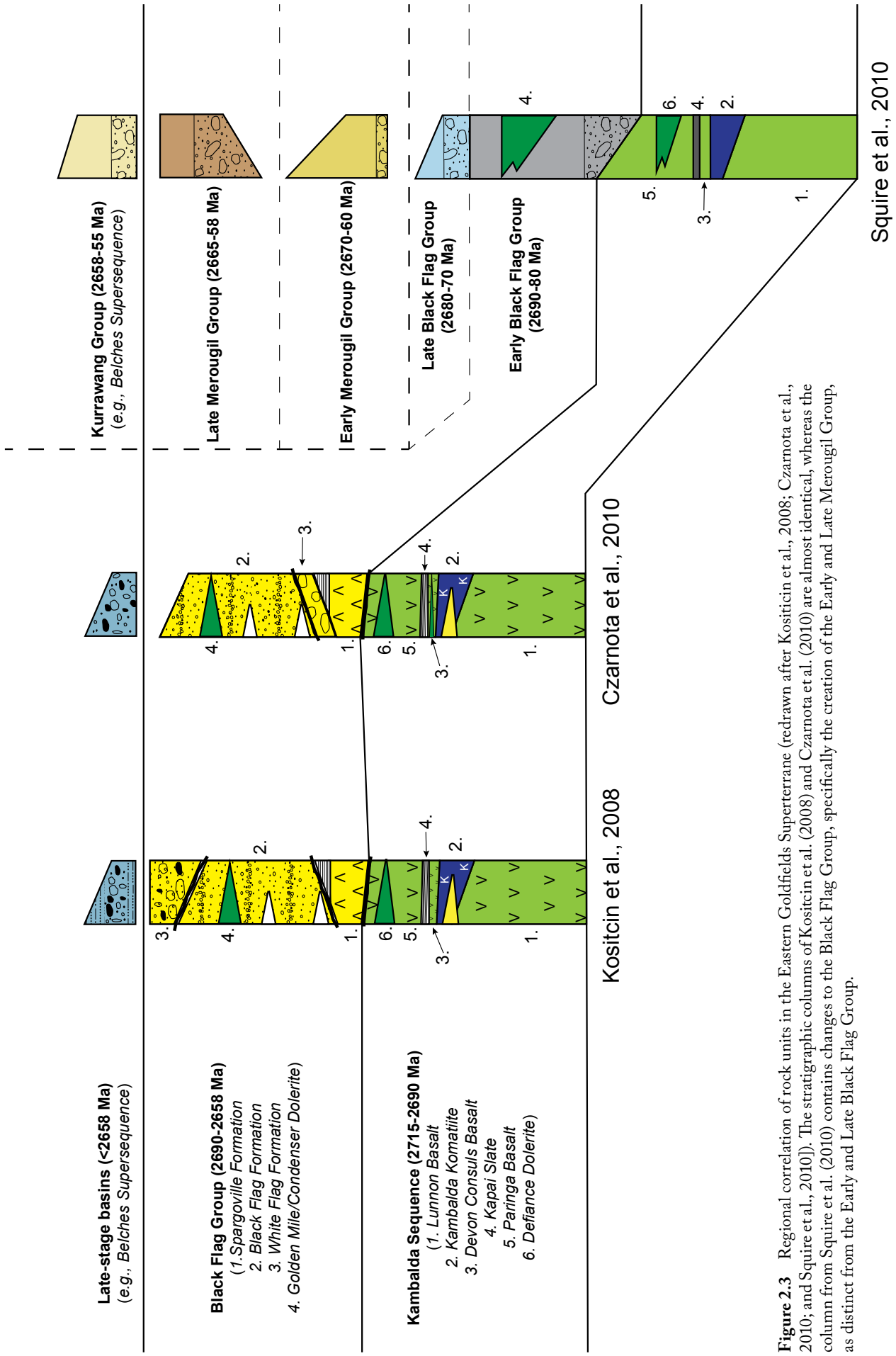

Figure 2.3 Regional correlation of rock units in the Eastern Goldfields Superterrane (redrawn after Kositcin et al., 2008; Czarnota et al., 2010; and Squire et al., 2010]). The stratigraphic columns of Kositcin et al. (2008) and Czarnota et al. (2010) are almost identical, whereas the column from Squire et al. (2010) contains changes to the Black Flag Group, specifically the creation of the Early and Late Merougil Group, as distinct from the Early and Late Black Flag Group.

marked a change from the accordion-like extension and compression cycles of $D_{1–4a}$ to sinistral strike-slip movement along the major terrane-bounding faults. Thrust faulting to the NW and SE (part of D_1 in Swager, 1997; see his Fig. 11B) also took place in the hinge zones of SE- and NE-plunging domes and anticlines at this time.

The metamorphic history of the Eastern Goldfields Superterrane is also quite complex. Goscombe et al. (2009) defined five periods of metamorphism, labeled M*a*, M1, M2, M3a, and M3b. Only event M2 will be discussed here, as it is the most regionally pervasive of the five and thus affected nearly all units in the eastern Yilgarn Craton, including those at Lucky Bay. The M2 stage (2685–2665 Ma) is considered to be a hybrid 'regional-contact' episode of metamorphism, in which the elevated thermal gradients that existed throughout the Yilgarn during M2 were largely the result of widespread, voluminous granite intrusion. These granites, which today form the majority of the rock mass in the eastern Yilgarn (60–65 %), are high-Ca and Th-enriched, and are thought to be the products of high-pressure melting of basalt (Champion and Cassidy, 2007). The high Th was particularly responsible for the granites driving regional metamorphism across the entire craton. The 'contact' metamorphic portion of the M2 period is due to the fact that metamorphic temperatures increase with proximity to a (high-Ca) granite dome. M2 mineral assemblages range from sub-greenschist to mid-amphibolite facies temperatures (350–620°C) at low pressures (3.5–5.0 kb).

2.3 Lucky Bay geological context

2.3.1 Stratigraphy and geochronology

The location of the Lucky Bay prospect is shown in Figure 2.2A. Figure 2.2B shows the detail of diamond drilling in the immediate area; stars indicate holes sampled for this study. There is no outcrop at Lucky Bay, and fresh bedrock is not recoverable in drill core until at least 70 m below the surface. This complicates the three-dimensional understanding of the geology, but all sampled drill core in this study were oriented and structural measurements taken. The local stratigraphy is dominated by fine- to medium-grained turbidites with well-preserved sedimentary structures (e.g., load casts, soft-sediment deformation, and graded bedding), medium- to coarse-grained, massive to thickly-bedded sandy debris flows, magnetitized shale (shale partly replaced by magnetite), chert, and fine-grained carbonaceous black shale with disseminated, laminated, and nodular sulfides, and interbedded siltstone/sandstone layers (Figs 2.4, 2.5). In drill hole LBDD020, there is also a 35 m-thick intermediate igneous unit (andesite or dacite) with black shale (containing nodular sulfides) above the unit and metamorphosed carbonate-bearing siltstone/mudstone and minor exhalative sulfide (pyrrhotite) lithologies below it. Petrographically, the intermediate igneous unit is dominated by twinned plagioclase (albite) phenocrysts in an altered, fine-grained groundmass (Fig. 2.6A, B). It has been cross-cut by quartz-K-feldspar veins, is brecciated in places, and exhibits a moderate foliation. Fine-grained tourmaline (Fig. 2.6C) is present in the quartz-K-feldspar veins, suggesting a granitic source for the alteration fluids (A.J. Crawford, personal communication). These characteristics, coupled with the stratigraphic columns and rock descriptions of Krapež et al. (2000), Painter and Groenewald (2001), and Kositcin et al. (2008), suggest the unit is probably a correlative of the Spargoville Sequence of the Kalgoorlie Terrane (Black Flag Group; Krapež et al., 2000).

Thin (≤ 5 m), relatively unaltered and undeformed feldspar-phyric intermediate dikes intrude the Lucky Bay sedimentary sequence in some drill holes. These dikes contain large plagioclase and k-feldspar phenocrysts in a very fine-grained quartz/feldspar groundmass, and are cross-cut by quartz-carbonate veins. Phaneritic quartz is present, but in lesser amounts than the feldspar phenocrysts. The dikes are weakly foliated, suggesting that they formed pre-deformation, which would have occurred ca. 2650 Ma or later.

No geochronological data have been published for rocks in the immediate vicinity of the Lucky Bay prospect, although three lithologies in the greater area were dated via SHRIMP by Nelson (1995)

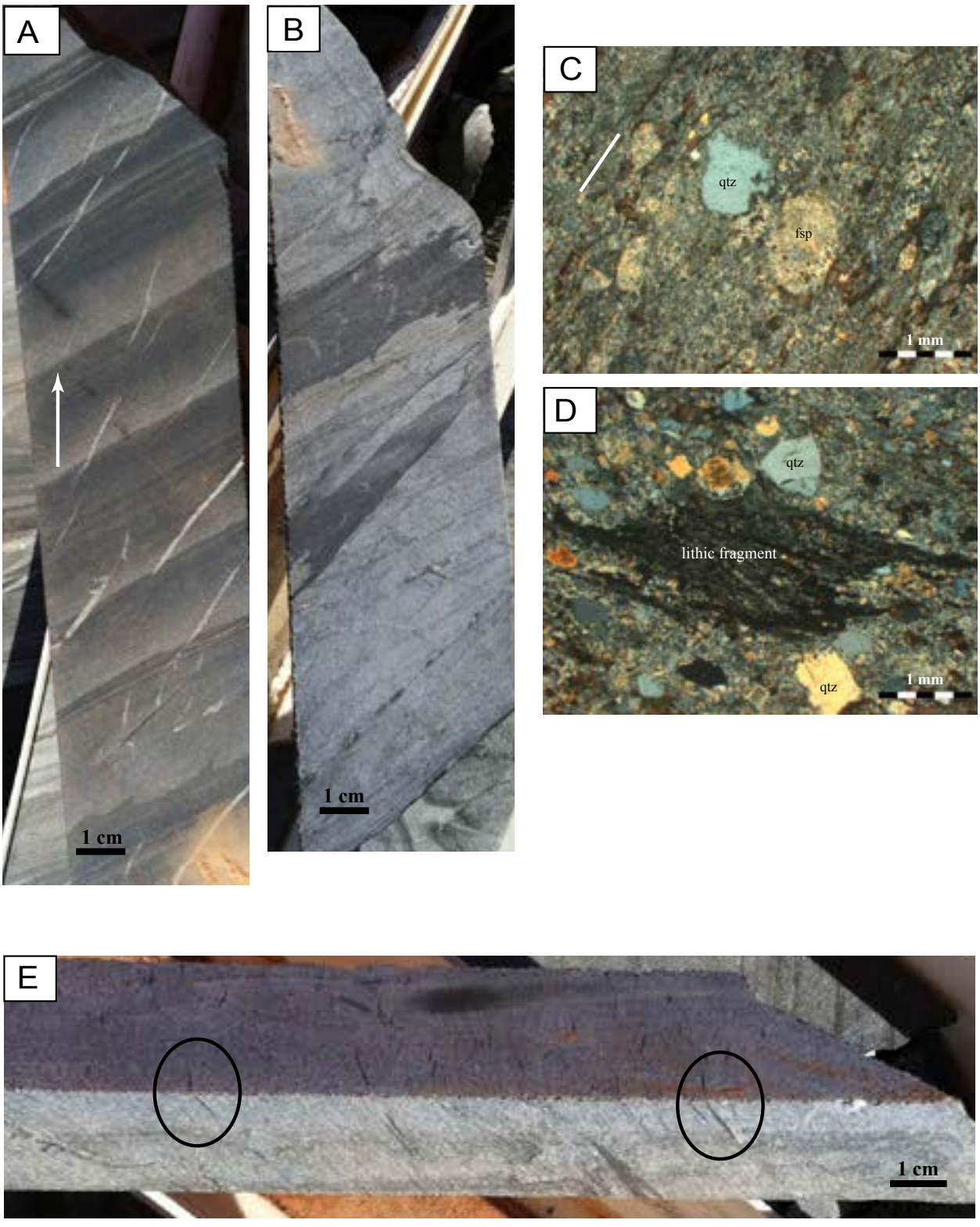

Figure 2.4 **A.** Fine-grained turbidite displaying well-preserved graded bedding (tops indicated by white arrow). Late carbonate veinlets cut across the sample at a low angle. **B.** Coarser-grained turbiditic sandstone from the same drill hole as the sample in A, but with a more pronounced structural fabric. Sedimentary structures have been obliterated. **C.** Representative photomicrograph of 26D-120.8, a sandy debris flow collected for detrital zircon dating. Quartz and feldspar dominate, the latter having a grungy appearance due to sericite alteration. The groundmass appears to be quartz-feldspar rich, as well. White line in left side of photo traces the structural fabric. **D.** Lithic fragment (black shale) in sandstone from DD020-151.5, surrounded by quartz and feldspar grains in a quartz-feldspar matrix. Such clasts are common in sandstones from Lucky Bay. **E.**Sandy debris flow from LBRC030D. Note how the lithic fragments (black; circled) are aligned parallel to the foliation (coming out of the page).

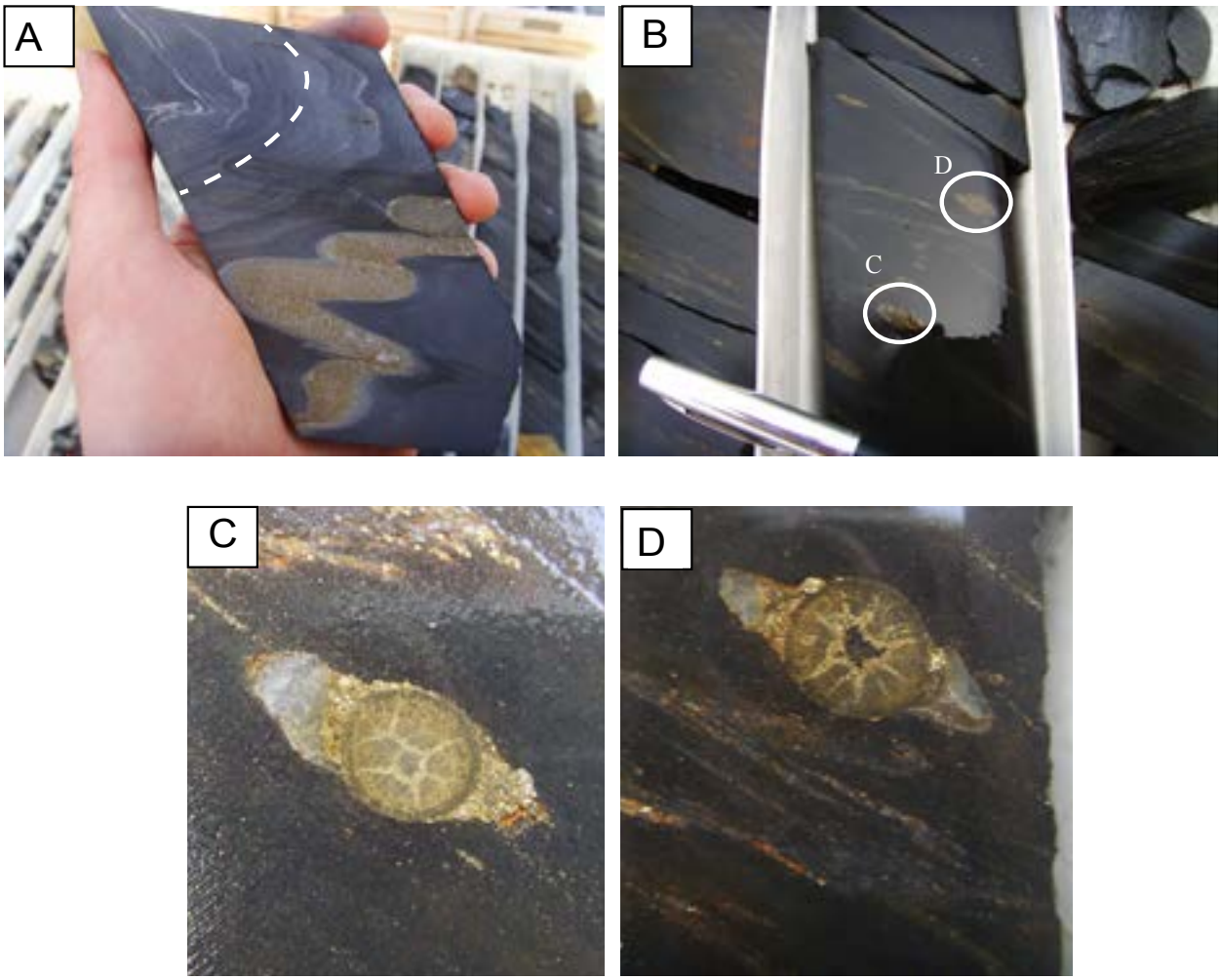

Figure 2.5 Black shale hand samples. **A.** Folded black shale with interbedded siltstone/sandstone, which has been pyritized. **B.** Less deformed black shale sample with two pyrite nodules (circled). **C.** Pyrite nodule. Note the pattern of the late pyrite and its resemblance to syneresis cracks, suggesting an early formation for the fractures. **D.** Pyrite nodule. Unlike nodule C, the core of this nodule is apparently occupied by the wall rock, which is a definite indication of early formation.

and three more by Kositcin et al. (2008). The units studied by Nelson (1995) are felsic to intermediate intrusions that cover a range of Neoarchean ages (~2700–2670 Ma), the youngest of which (2672±12 Ma, 2σ) intrudes the Bulong Anticline ~20 km north of Lucky Bay. Kositcin et al. (2008) sampled three sandstones from two different localities in the Bulong Anticline, one of which is approximately 17 km NNW of Lucky Bay. Maximum depositional ages indicated by detrital zircon U-Pb ages for the feldspar-rich sandstones at this locality were 2702±5 and 2708±5 (both 2σ).

2.3.2 Lucky Bay – structural and metamorphic history

The Lucky Bay prospect sits just on the western limb of the doubly-plunging Bulong Anticline, near the hinge zone on its southern margin (Fig. 2.2). The Bulong Anticline formed during D_2 compression, which involved east-directed thrusting of an older (~2700 Ma), mafic-ultramafic succession over a younger (2672±12 Ma), calc-alkaline package currently exposed in the core of the anticline. The entire block was then truncated by <2660 Ma Late Basin sediments (Penny Dam Conglomerate and Belches Supersequence), and re-thrust eastward during D_{4a} re-compression along the Emu Fault (Swager, 1997). Macroscale upright F_2 folds developed in all Bulong Anticline rock units during D_2, and F_2 folds near major NNW-trending faults (e.g., Emu and Mount Monger Faults) were tightened during D_{4a} as a result of renewed thrusting (Blewett et al., 2010). Although all rocks at Lucky Bay have been deformed,

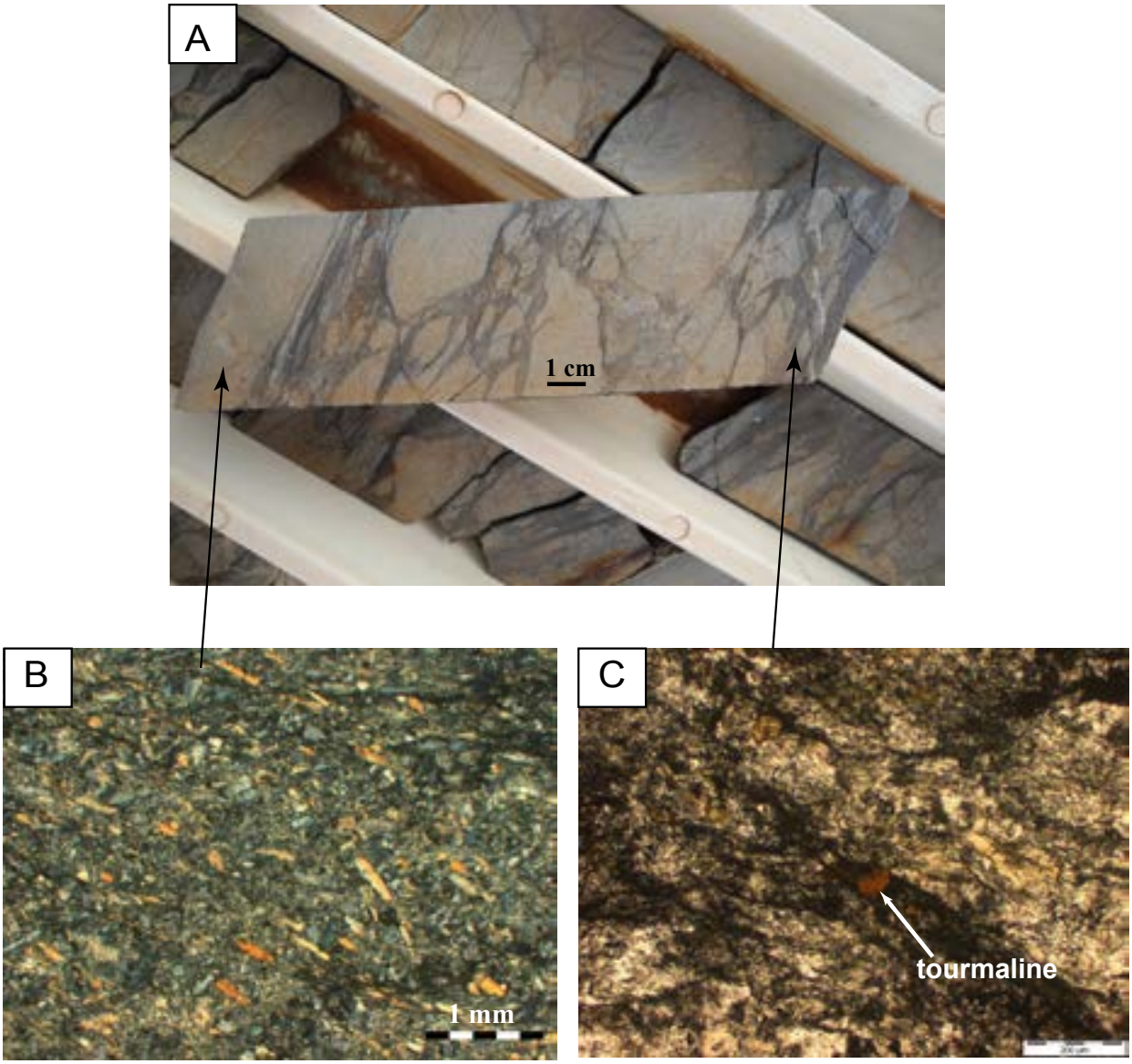

Figure 2.6 The andesite/dacite. **A**. Hand sample of brecciated and foliated andesite/dacite in drill hole LBDD020. **B**. Photomicrograph of the relatively "unaltered" parts of the unit, which have abundant, often twinned plagioclase (albite) phenocrysts in a fine-grained groundmass. **C**. Photomicrograph of tourmaline (brown, hexagonal grains) in quartz-feldspar-altered sections of the andesite/dacite.

the degree of deformational intensity varies. Structural fabrics in the fine- to medium-grained turbidites display a wide range of development, from nearly non-existent to strong, penetrative fabrics, often within a few tens of meters of each other in the same drill hole (Fig. 2.4A, B). Structural fabrics in the sandy debris flows are somewhat more cryptic, but the lithic fragments often present in these units highlight the foliation (Fig. 2.4D, E).

The Lucky Bay succession was metamorphosed to at least the middle greenschist facies (biotite zone; ~350°C) during M2, which converted original Fe-rich mudstone to chlorite phyllite with biotite porphyroblasts. No high-Ca/high-Th granitoid is known in this area, which explains the absence of higher-T assemblages in Lucky Bay lithologies. The sulfides in the carbonaceous black shale appear to have been shielded somewhat from the effects of deformation, which has been taken up by phyllosilicate minerals, leading to textural preservation of most of the pyrite. Fine-grained tourmaline has also been reported from the black shale, which suggests the presence of evolved hydrothermal fluids; coarse-grained pyrite and sphalerite are also associated with this mineral.

2.3.3 Description and textures of sulfide nodules

All nodules in the studied samples are composed of pyrite and exhibit a wide range of sizes, shapes, and textures. Nodule shape in 19D-171.2 is round to oblong with metamorphic pressure shadows containing quartz, mica, and a second generation of pyrite that is much coarser-grained (Fig. 2.7A, B). Some of the nodules, particularly the oblong or non-spherical ones, contain silicate inclusions (Fig. 2.7B, C). A moderately well-developed foliation is present in thin sections from 19D-171.2. This fabric is displaced around nodules, indicating that they formed prior to deformation (Fig. 2.7A–C). Elsewhere in 19D-171.2, significantly smaller nodules occur around which the foliation is displaced, yet their character appears to be different to the big ones. These 'miniature' concretions are composed of aggregates of very fine pyrite, whereas such texture is not seen in the larger examples.

Nodules from sample DD020-124.2 are different to those in 19D-171.2, most notably in the thick (1–5 mm) rinds of pyrite that form the outermost zone of growth. The interior zones of DD020-124.2 nodules are similar to those from 19D-171.2 (i.e., fine-grained pyrite) although some are sufficiently coarse-grained as to allow for etching with dilute nitric acid to reveal the internal structure. Figure 2.7E, F shows the result of etching in one nodule, which clearly shows the presence of two distinct textures. Both the pale yellow, cubic sulfide and the yellow brown, acicular/"star"-shaped sulfide, are pyrite, though the crystal shape suggests the acicular pyrite was once marcasite. This exact style of pyrite-pyrite (marcasite) intergrowth is not repeated in all samples, but based on the etching of some of the other nodules it is believed that they have comparable relationships. There is also a band of mixed silicate-carbonate-sulfide in between the pyrite (marcasite) outer zone and the interior "main body" of the nodule in DD020-124.2 (Fig. 2.8A, B), indicating fluctuations in fluid chemistry during nodule formation.

A third style of nodule is found in sample 22D-184.4 (Fig. 2.8C). This type is larger (≥1 cm) and apparently more deformed than the nodules in the other two samples. There is also a higher proportion of carbonate intergrown with pyrite in this nodule and in others from this drill hole, particularly in the outer zones (Fig. 2.8C). A defining characteristic of the nodule in 22D-184.4 is its "exploded" appearance, which is caused by the infiltration of coarse-grained, euhedral, gangue inclusion-poor pyrite veins (Fig. 2.8C). The growth pattern of this nodules is less obvious than the two described previously (e.g., no readily discernable growth zones), but it appears to have been originally spherical. Due to deformation, however, it now has a "bean"-shaped outline (i.e., flattened from the top and bottom but bulging at the sides). Some of the other pyrite nodules from this drill hole are rounder (Fig. 2.5C) and appear to have inclusions of the host shale in their cores (Fig. 2.5D).

2.4 Analytical methods

2.4.1 Zircon preparation and analysis

One sample (26D-120.8) of sandy debris flow from drill hole LBRC026D was selected for detrital zircon U-Pb geochronology. Approximately 200 g of sample was crushed using a hydraulic crusher and milled for 5–10 seconds in a chrome steel ring mill to make it pass through a 400-μm sieve. The entire rock pulp was then emptied into a clean gold pan and repeatedly washed and sifted to concentrate the heavy minerals. This fraction was transferred to a watch glass for microscopic determination of the presence or absence of zircons. The heavy mineral separate in sample 26D-120.8 contains hundreds of detrital zircons, which were easily visible under the microscope, along with pyrite, magnetite and ilmenite. The zircon-bearing fractions were dried for 24 hours in an oven set to 50°C. A hand-held Fe-B-Nd magnet was then passed over the dried fractions to remove the magnetic heavy minerals (e.g., magnetite and ilmenite). Zircons were hand-picked using a binocular scope and mounted on double-sided sticky tape in several separate rectangular domains. A 2.5 cm-diameter hollow mold was fitted around the domains, and epoxy glue was poured into this mold on top of the zircons. A total of approximately 100 zircons

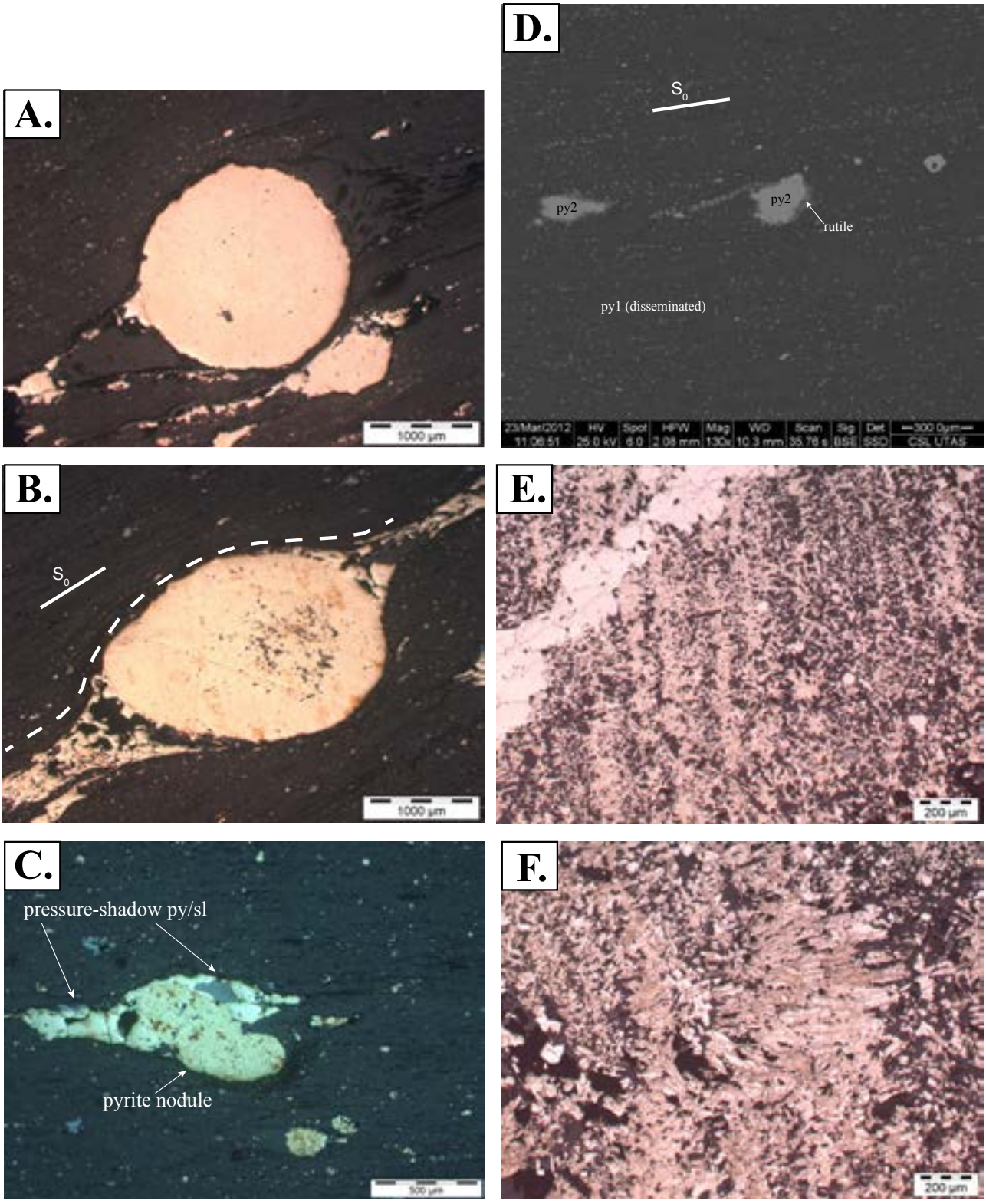

Figure 2.7 Sulfide photomicrographs. **A.** Pyrite nodule from 19D-171.2, exhibiting a nearly spherical outline together with metamorphic pressure shadows containing pyrite and quartz. **B**. An oblong (or "egg"-shaped) nodule from the same sample. Bedding (S0/S1) wraps around the nodule, indicating that nodule growth occurred pre-deformation. Also note the increased amount of matrix inclusions in the core of the nodule relative to the nodule in A. **C.** A strongly-deformed nodule that displays pressure shadows containing mostly pyrite and sphalerite. Silicate (matrix) inclusions are relatively abundant in this nodule, as well. **D.** SEM back-scattered electron image of 19D-171.2. Fine-grained, euhedral pyrite is truncated by later subhedral pyrite mantled by rutile (dark gray). The later pyrite and rutile probably grew during metamorphism, which may have been synchronous with deformation. **E.** First image of an etched nodule from DD020-123.5, showing pale yellow and blocky pyrite intergrown with a darker brown, more acicular pyrite that was probably once marcasite. A vein of late pyrite cross-cuts the nodule in the upper left of the image. **F.** Second image of the same nodule, showing the same texture but with better detail.

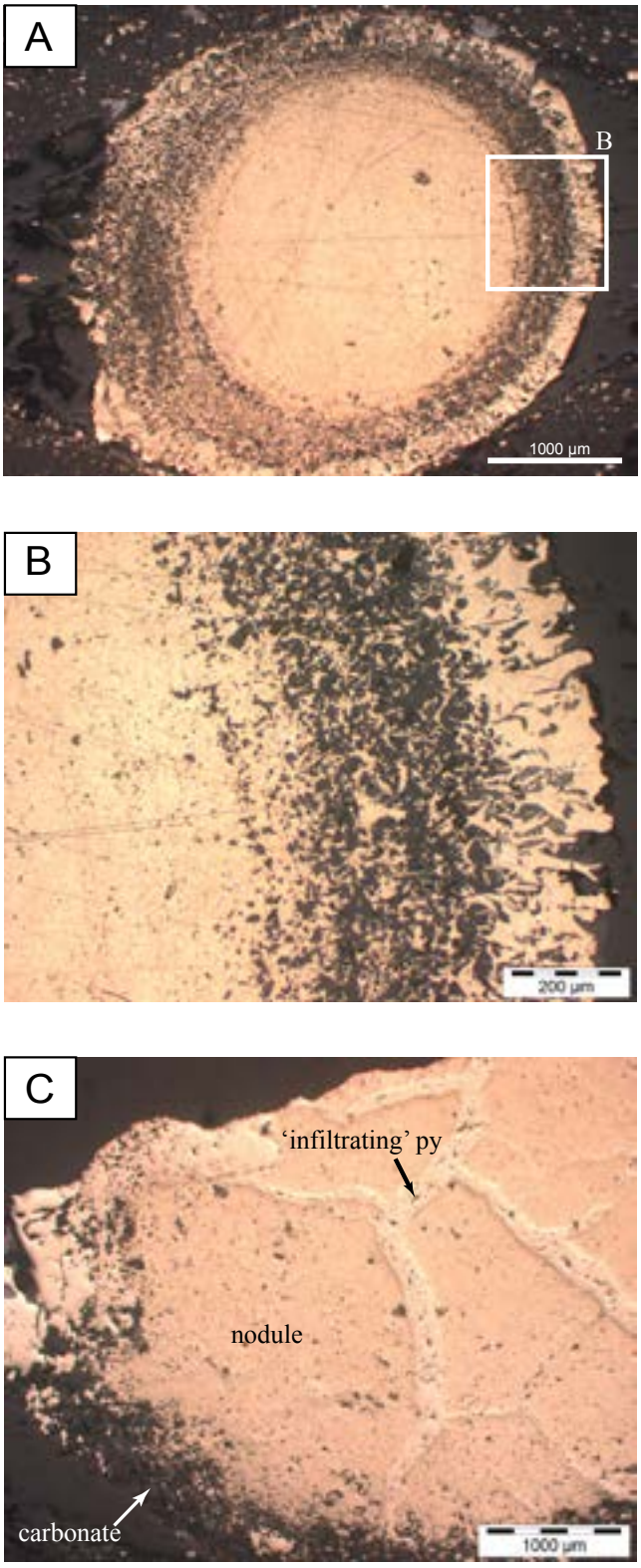

Figure 2.8 Sulphide photomicrographs. **A.** A large nodule from DD020-124.2. **B.** Close-up of the outer rim, along with the middle band of silicate-carbonate-pyrite. **C.** Nodule in 22D-184.4. Note the intergrown carbonate (arrow) and the infiltrating network of later pyrite.

were mounted in epoxy and, once the epoxy had set (~12 hours), polished with clean sandpaper and a clean lap wheel. The mount was then washed in distilled water using an ultrasonic bath, dried, and set in a vacuum chamber until the analytical session.

The laser method employed here is similar to that used in Sack et al. (2011), which is a derivative of the methods used at the Australian National University (Harris et al., 2004; Bryan et al., 2004; Campbell et al., 2006), Macquarie University (Jackson et al., 2004), and the University of Melbourne (Paton et al., 2010). Instrumentation for this study consisted of a Resonetics M50 ablation cell and a 193-μm Coherent Ar-F gas-charged excimer laser microprobe coupled to an Agilent 7500cs/ce quadrupole ICP-MS at CODES, University of Tasmania, Hobart, Australia. Downhole fractionation, instrument drift, and mass bias correction factors for Pb/U ratios in zircons were calculated using two analyses on the primary standard (91500; Weidenbeck et al., 1995) and one analysis each on the secondary standards (TEMORA 1 – Black et al., 2003; GJ1 – Jackson et al., 2004; Mud Tank – Black and Gulson, 1978), analyzed at the beginning of each session and after every 12 unknown zircons (or every ~30 minutes) using the same spot size and conditions used on the sample. The correction factor for the $^{207}Pb/^{206}Pb$ ratio was calculated using three medium-size (32 μm) spots on NIST 610, which were run at the same time as the primary and secondary standards, and corrected using the values suggested by Baker et al. (2004).

Seventy-five analyses were completed on 72 zircons (most analyses were one spot per grain, but a few zircons were ablated twice to measure core-rim differences). All reported dates are $^{207}Pb/^{206}Pb$ ages, with no correction for common Pb. Each analysis on the zircons began with a 30-second background measurement, followed by a further 30 seconds of analysis when the laser was turned on. Zircons were sampled with 32-micron spots, using the laser at 5 Hz and an energy density of approximately 2 J/cm^2. A flow of He carrier gas (0.5 l/min) transported ablated particles out of the chamber to be mixed with Ar gas en route to the plasma torch. Elements measured were ^{49}Ti, ^{90}Zr, ^{146}Nd, ^{178}Hf, ^{202}Hg, ^{204}Pb, ^{206}Pb, ^{207}Pb, ^{208}Pb, ^{232}Th, and ^{238}U, with each element being measured for 5 (Zr, Nd, Hf, and Th) or 10 (Ti, Hg, ^{204}Pb, and U) milliseconds, except for ^{206}Pb, ^{207}Pb, and ^{208}Pb, which were analyzed for 30, 30, and 15 milliseconds, respectively. Total quadrupole sweep time was 0.16 seconds. Data reduction was based on the method outlined in detail in Meffre et al. (2008), which is similar to that described in Black et al. (2004) and Paton et al. (2010).

2.4.2 Nodule trace element and Pb isotope analysis via LA-ICP-MS

Five samples of nodule-bearing black shale were selected from the drill cores sampled. A 2.54 cm-round "chip" was then drilled out with a hollow diamond-bit drill, set in epoxy, and the surface of the mount was polished to facilitate petrographic examination and laser ablation of the nodules. All laser ablation analyses of nodule trace element content and Pb isotope composition were obtained at CODES, University of Tasmania using a New Wave 193 nm Nd-YAG solid-state laser microprobe coupled to an Agilent 7700 quadrupole ICP-MS. The method is described in detail in Danyushevsky et al. (2011); a summary is provided here. The laser microprobe is equipped with an in-house, fast-response small-volume ablation cell boasting <1-s response time and <2-s washout delay. Ablation was performed in an atmosphere of pure He (0.7 l/min). The aerosol carried by the He gas was immediately mixed with Ar (1.23 l/min) after exiting the cell and then passed through a pulse-homogenizing device before hitting the torch inside the ICP-MS.

Daily optimization of the ICP-MS took place to maximize sensitivity toward mid- to high-mass isotopes (a.m.u. ranging from 130–240). Production of molecular oxide species (e.g., $^{232}Th^{16}O/^{232}Th$) and doubly charged ionic compounds (e.g., $^{124}Ce^{2+}/^{140}Ce^{+}$) was kept to <0.2%. No correction was needed for the analyte signal intensities caused by the presence of these interfering species, as they occurred at low levels. Each analysis was run in time-resolved mode, which involves sequential peak cycling through the mass spectrum.

Nodule trace element analyses were performed by ablating spots 50 μm in diameter, repeating at a

rate of 5 Hz for 60 seconds (300 blasts per spot); laser energy density was maintained between 3.5 and 4.5 J/cm^2. Total analysis time was 90 seconds, which included a 30-second background measurement (i.e., laser on but shutter closed) and a 60-second ablation period (i.e., shutter open). Element acquisition times were controlled by element type: major silicate/carbonate elements (e.g., Na, Mg, Al, Si, Ca, and Mn) were set at 0.005 seconds, along with S; minor silicate/carbonate elements (e.g., Zr, Ba, and U) at 0.01 seconds, along with Fe and As; transition metals (e.g., Co, Ni, Zn, and Mo) at 0.02 seconds; Te and Pt at 0.05 seconds; Au at 0.1 second; and all other elements at 0.02 seconds, for a total of 39 elements and a collector sweep time of 0.8 seconds.

Data reduction was done according to standard procedures (Longerich et al., 1996), using Fe as the internal standard. The primary standard was a Li borate fused glass of a pyrite or sphalerite mixture developed at CODES (STDGL2b2; Danyushevsky et al., 2011). This was analyzed once every 90 minutes with a 100-µm beam size at a frequency of 10 Hz to correct for instrument drift.

Nodule imaging consisted of ablating a set of parallel lines arranged in a grid across a given sample, such that the space between the individual lines was the same as the line diameter. Spot size varies depending on the size and type of grain analyzed – e.g., a small beam diameter (e.g., 10 or 15 µm) is suitable for smaller pyrites (≤ 500 µm) with intricate chemical zonation. Due to the large size of the nodules (> 1mm diameter), the laser beam diameter was set to 47 µm and the lines were rastered at a speed double that of the beam diameter (i.e., 94 µm/s), operating at a rate of 20 Hz. Thus, each position on the nodule was ablated 20 times, contributing 10 consecutive pixels to the image. The end result is an unprocessed effective resolution equaling the beam size (47 µm, in this case). Each individual sweep of the quadrupole forms a single pixel in the image (~20 µm x ~20 µm), assuming a sweep time of ~0.2 seconds and an image speed of 94 µm/s. Samples were ablated to a depth of approximately 5 µm, estimated from the depth of a single blast (0.5 µm) multiplied by the number of blasts in a single spot (10).

A set of 36 elements was chosen for imaging, with acquisition time for most elements set to 0.002 seconds. Certain elements of interest were analyzed for longer periods, such as Se (0.005 s), Sb (0.01 s), and Au (0.02 s). Total sweep time was ~0.2 s. A 15-second delay was factored in at the end of each line to allow for cell washout. Background levels and instrument drift were measured before and after each image. Nodule maps were designed to finish within a 60-minute time window (i.e., between 30 and 90 minutes total run time) to diminish the effect of sensitivity drift in the ICP-MS on the image. Image processing involved applying a median filter to remove artifacts, subtraction of background from filtered counts, replacement of filtered counts below background values with the standard deviation value for that element, and the production of a logarithmic color-scale image for each element. Interference of the signal of the unknown caused by sample "splatter", or re-deposition of ablated material on the surface, was kept to a minimum by pre-ablating each line. Some elements, such as gold, are nonetheless prone to re-deposition, which can be seen as a halo of elevated counts around a grain of free gold that the laser has passed over.

The laser method employed for Pb isotope measurements in pyrite/marcasite was similar to both the trace element and zircon U-Pb methods, and is based on those described in Guillong et al. (2003), Meffre et al. (2008) and Woodhead et al. (2009). Equipment used for analyses included the 193-µm New Wave Nd-YAG solid-state laser and Agilent 7700 quadrupole ICP-MS housed at CODES, University of Tasmania. Instrument drift and mass bias correction factors were calculated using two analyses on the primary standard (NIST 610; values from Baker et al., 2004), analyzed every ~45 minutes. Results were checked using the 700380 pyrite standard (Woodhead et al., 2009) and an additional in-house pyrite (Chatree). Each analysis on the unknowns began with a 10-second background (laser off) measurement, followed by 50 seconds of data acquisition with the laser turned on. The nodules were sampled with 25–100 µm spots (depending on the amount of Pb in a given area) at 10 Hz and an energy density of 2 J/cm^2. A flow of He carrier gas (0.8 l/min) moved particles out of the ablated crater to be mixed with

Ar gas and introduced into the plasma torch. Elements measured were ^{57}Fe, ^{65}Cu, ^{75}As, ^{197}Au, ^{202}Hg, ^{204}Pb, ^{206}Pb, ^{207}Pb, ^{208}Pb, ^{232}Th, and ^{238}U, each for 5 ms with the exception of ^{204}Pb (10 ms). Such short counting times enhance the signal quality of the ratios (Guillong et al., 2003). Another innovation that has improved signal quality at the CODES laser facilities is in addition of a particle filter to the laser/chamber interface. The filter consists of a tygon tube wrapped four times around a 10 mm-diameter cylinder (i.e., a pen lid), which serves to eliminate spikes in the signal caused by large particles that flash in the plasma for a few milliseconds and cause one isotope to be elevated above the others. The device removes ~75% of the spikes and leaves 90–95% of the unfiltered count rates intact (Guillong et al., 2003).

The mass spectrometer was tuned to maximize detection of the heavy masses. Data reduction was done after the methods of Meffre et al. (2008), Woodhead et al. (2009), using the Isoplot software (Ludwig, 2003).

2.4.3 LA-ICP-MS trace element image processing

An additional step in the imaging method described above converts the mass spectrometer count rates to concentrations (parts-per-million, or ppm). The conversion factors were calculated using (1) the count rates on the STDGL2b2 standard (Danyushevsky et al., 2011) relative to Fe; (2) the average count rate of Fe on the given pyrite nodule; and (3) the stochiometric Fe value for pyrite (46.55 wt. %). The conversion factors are applied to each pixel for each element in each image. This simple conversion tends to slightly underestimate major and trace element concentrations in silicate minerals and the matrix around the nodules, but produces accurate concentrations for the pyrite. Instrumental drift corrections were not necessary as very little drift was observed during the analytical runs.

2.5 Results

2.5.1 Zircon U-Pb geochronology

The mineral separate from the sandy debris flow has a morphologically diverse suite of zircons. Crystals range from large, doubly terminated prisms to small, well-rounded grains. Most contain growth zones, which are especially visible on CL images (Fig. 2.9A, 1–4). Archean zircons are notoriously prone to Pb loss and common Pb gain (from the surrounding rock matrix) as a result of radiation damage through time, caused by U and Th decay. This results in a metamict zircon crystal. Many of the zircons in 26D-120.8 are metamict, but not all such grains were thrown out of the data set used to calculate the maximum depositional age. Only those with a high degree of alteration (i.e., significant Pb loss or disturbance) were cast out (black bins in Fig. 2.9B). Twenty-nine analyses on 28 zircons were obtained to determine the age of sample 26D-120.8 (Fig. 2.9A, B); of the 29 spots, 11 were rejected due to large Pb loss resulting from metamict zones. The weighted mean age of the remaining 18 zircons is 2679±11 Ma (2σ), with a mean standard weighted deviate (MSWD) of 0.93. A further 47 analyses on 44 other zircons in the same mount were run, and these were added to the preexisting 29 to create a probability density plot containing 76 zircon ages (Fig. 2.9B). Over half of all zircons analyzed in 26D-120.8 fall within the 2680–2700 Ma age bracket, regardless of morphology. The few zircons with old ages (e.g., >3000 Ma) were also those with greatest Pb loss, so the reported ^{207}Pb/^{206}Pb ages should not be taken as representative of the true age of the crystal.

2.5.2 LA-ICPMS analyses: imaging

The three pyrite nodules mapped by LA-ICP-MS show similar zonation patterns and trace element characteristics to that described by Large et al. (2009).

19D-171.2: This sample comes from a drill hole (LBRC019D) on the NE end of the Lucky Bay prospect. Laser ablation imaging shows that the nodule in 19D-171.2 is characterized by a uniform trace element composition, with little zonation except for subtle variations in some elements from core to rim

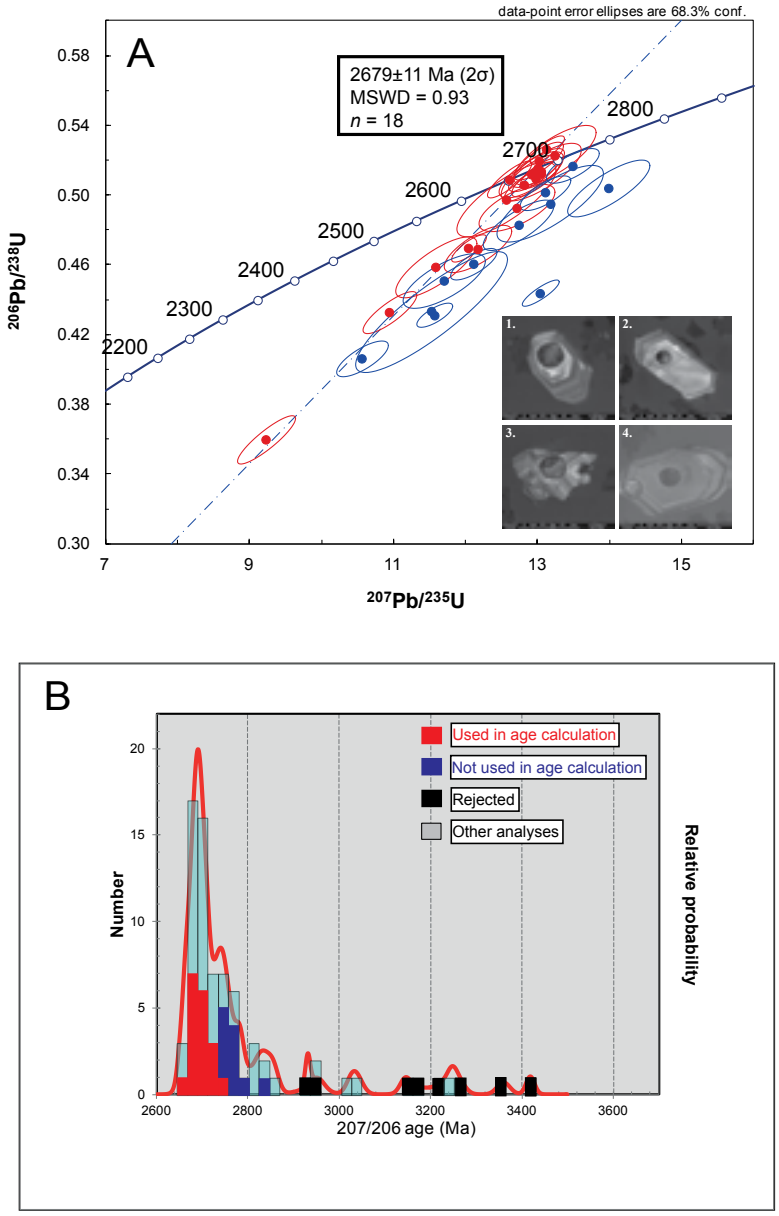

Figure 2.9 **A.** U-Pb concordia diagram of detrital zircons from the Lucky Bay area. Red symbols indicate those analyses used for the age calculation; blue symbols are analyses that were not used for the sample age calculation. Inset photos (1-4) are CL images of analysed zircons. **B.** Histogram showing age populations in sample 26D-120.8. Of the 75 zircons analysed, three had 207/206 ages younger than 2670 Ma, which might suggest a younger maximum depositional age for 26D-120.8 than that proposed (2679±11 Ma), one closer to the currently accepted maximum depositional age for the Belches Supersequence (~2664 Ma: Krapež et al., 2000). However, the 1σ error bars on these grains are large (~5-10 million years), which likely means that the actual age is older (i.e., ≥2670 Ma). Furthermore, a >2670 Ma maximum depositional age fits better with published age data for the Kambalda and Kalgoorlie Sequences west of Lucky Bay in the Kalgoorlie Terrane (Krapež et al., 2008; 2010; Squire et al., 2010). The sedimentologic character of the Lucky Bay sequence is also more similar to the fine-medium-grained Kalgoorlie Sequence (Black Flag Group), rather than the medium-coarse-grained turbidites and BIF of the Belches Supersequence.

(Fig. 2.10). Overall the nodule contains elevated Co (up to 1000 ppm), Ni (300–1000 ppm), Cu (up to 300 ppm), As (1000–5000 ppm), Se (5–50 ppm), Ag (5–20 ppm), Sb (50–100 ppm), Te (20–50 ppm), Pb (500–1000 ppm), and Bi (20–50 ppm), as well as above-background Au (~500 ppb). The trace element suite present in the nodules contrasts with that of the metamorphogenic pyrite located in the pressure shadows. These later pyrites have lower trace element contents overall, and are enriched only in Se and Ni relative to the nodules (Fig. 2.10). The Zn and Cu enrichments in the pressure shadow pyrite are due

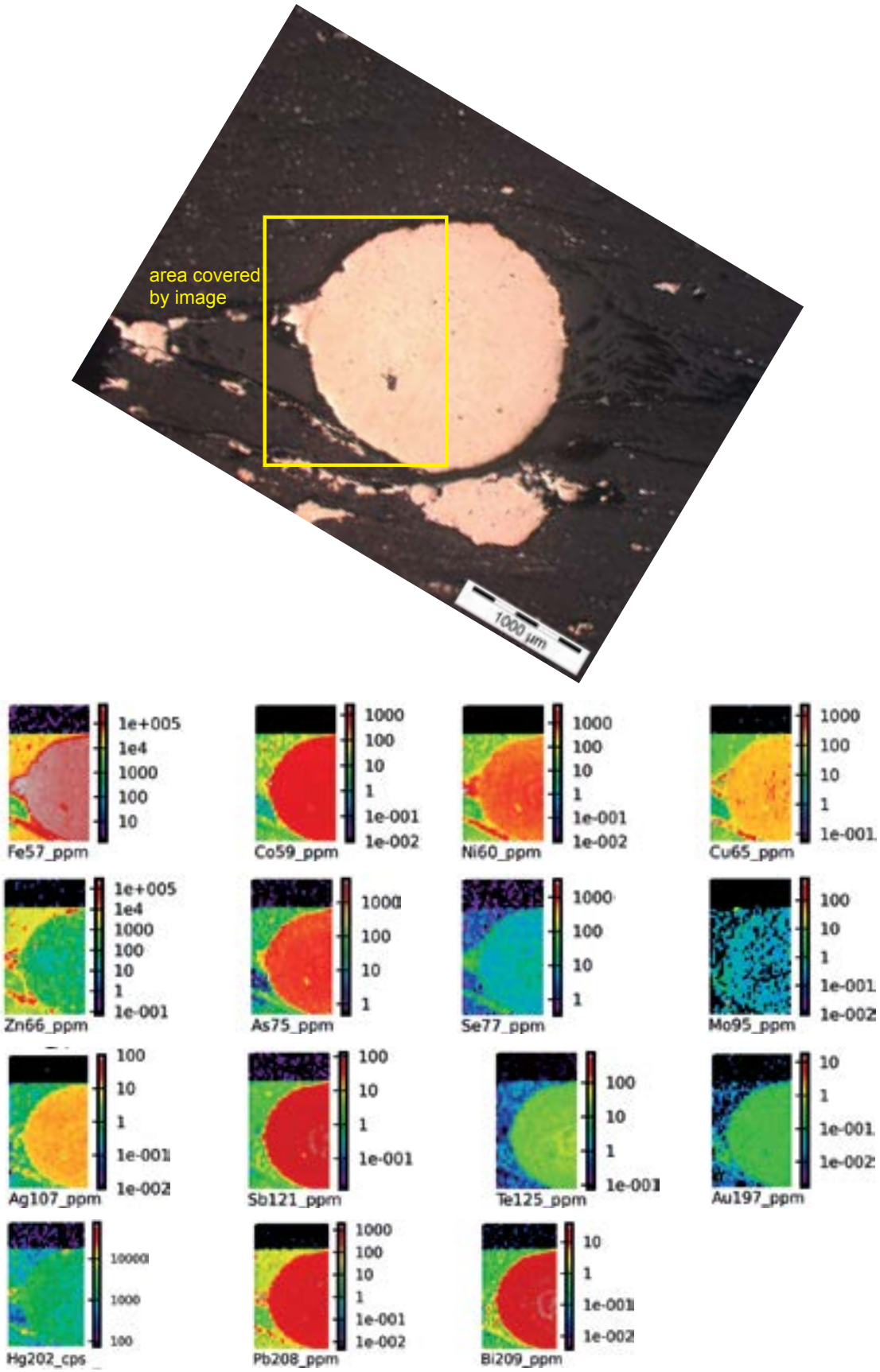

Figure 2.10 LA-ICP-MS image of 19D-171.2. The Lucky Bay sequence includes tens of meters of black shale with nodular pyrite. Nodules from 19D-171.2 contain low-level Au (~300 ppb) and a suite of trace elements (Co, Ni, Cu, Zn, As, Ag, Te, Sb, Hg, Pb, and Bi). The high Ag/Au ratio (~20; see Fig. 2.14C) and preferential concentration of other elements (especially Mo) within the nodule indicate that it most likely formed during early diagenesis.

to the presence of small sphalerite and chalcopyrite grains intergrown with the metamorphogenic pyrite.

DD020-124.2: This sample is from a drill hole (LBDD020) on the SW end of the Lucky Bay prospect. Half of a single nodule from DD020-124.2 was imaged. Like the nodules from sample 19D-171.2, those from DD020-124.2 are enriched in a suite of elements, including Au (~1 ppm) and As (>1000 ppm). Element zonation is more pronounced and complex in this nodule relative to those from 19D-171.2 (Fig. 2.11). The nodule can be divided into an inner, middle, and outer zone. The inner zone has two parts, composed of a core area of trace element-enriched pyrite surrounded by an outer rim of pyrite with similar amounts of most trace elements except for greater Co (>1000 ppm), Ni (500 ppm), As (5000 ppm), Ag (10 ppm), Sb (>100 ppm), Te (50 ppm), Pb (1000 ppm), and Bi (20–30 ppm) than the interior. The concentration levels of these trace elements are similar in the outermost zone of pyrite/sphalerite intergrowths, but drop off significantly in the interstitial silicate-carbonate-sulfide band. Mercury is also present in the outermost rim, presumably related to the presence of sphalerite.

22D-184.4: This sample is from the same general area as 19D-171.2, but was taken from a different drill hole (LBRC022D). The 1-inch round mount has only one nodule, which takes up a significant portion of the surface area and contains cross-cutting pyrite veins. Laser ablation mapping of approximately one-half of the nodule reveals that the two types of pyrite (the nodule and the veins) have considerably different trace element characteristics (Fig. 2.12). The nodule is enriched in Co, Ni, Sb, Te, Pb, Bi, and Au relative to the vein pyrite, whereas the vein pyrite is at least an order of magnitude richer in As and Cu than the nodule but nearly an order of magnitude less enriched in all other trace elements, including Au. The vein pyrite also contains individual micro- or nano-scale particles of chalcopyrite and galena. The presence of Au nanoparticles is inferred by examining the time-resolved LA-ICPMS line charts which recorded unusually high Au counts above background; Figure 2.13 shows one such line. Although the Au spike is not very large, it is significantly above both the background values and the low-level Au present within the nodule itself. The Cu-rich (red) and Pb-rich spots (red) in the image also correspond to spots of relatively low Fe, consistent with the presence of small chalcopyrite and galena inclusions. Neither type of pyrite in this sample is zoned with respect to elemental concentrations.

2.5.3 LA-ICPMS analyses: spots

Spot data were obtained on pyrite nodules in three samples: 19D-171.2, DD020-124.2, and 22D-184.4. For sample 19D-171.2, twenty-six spots were drilled on two nodules (16 on one, 10 on the other). Fourteen spots were drilled on the large nodule in DD020-124.2, and 17 spot analyses were obtained from the very large nodule in 22D-184.4 (13 on the core pyrite and four on the late-stage pyrite). In order of trace element magnitude, the nodules contain As (670–2850 ppm), Ni (370–820 ppm), Co (290–1415 ppm), and Au (0.1–1.1 ppm; Table 2.1). The spot data confirm the imaging results, but also highlight additional characteristics of the trace element contents of the nodules. On a bi-variate plot measuring Co versus Ni (Fig. 2.13a), the three nodules analyzed show positive correlations, but each one has a different amount of Co and thus a different Co/Ni ratio. In contrast, they have roughly the same Ni content. Likewise in Au-Te space, the nodular pyrite in all samples exhibits a positive correlation between these elements, differing only in total Au (Fig. 2.14B). The nodules also contain positive Au-Ag (Fig. 2.14C) and Sb-As ratios (not shown). However, the late, cross-cutting pyrite in 22D has no correlation between Au and Te, Au and Ag, or Sb and As, and the positive Co/Ni ratio of the nodules has also been altered in the later pyrite.

2.5.4 Pb isotopes

Lead isotopes were analyzed by quadrupole LA-ICP-MS, as described above. Figure 14A, B shows the $^{207}Pb/^{206}Pb$ and $^{208}Pb/^{206}Pb$ data for nodular and metamorphogenic pyrite in the three different samples (19D-171.2, 22D-184.4, and DD020-124.2). Most of the points cluster between 2700–2600 Ma, with one data point at ~2500 Ma and two at ~2800 Ma; all points have 1σ error ellipses (68.3 % confidence).

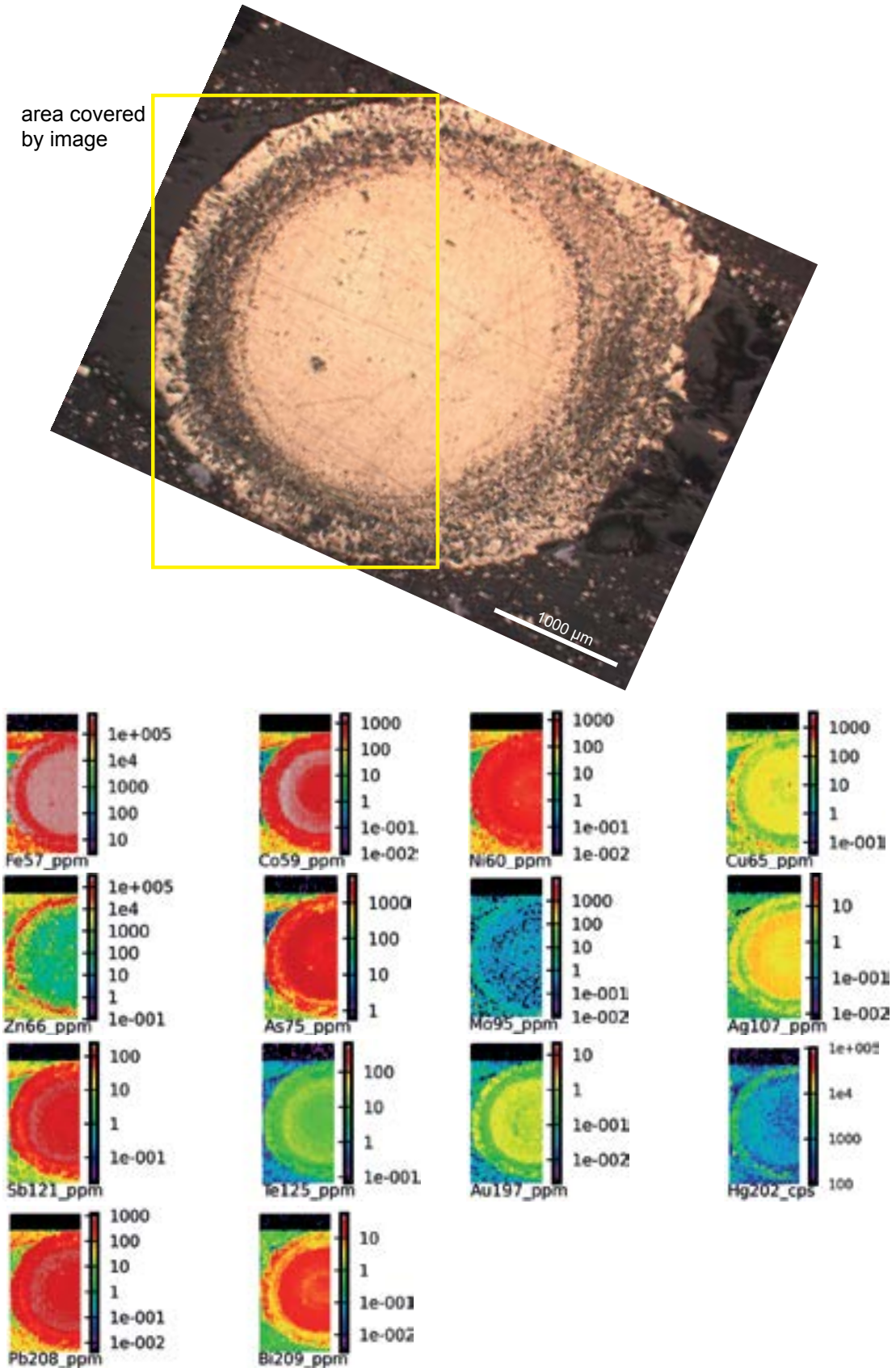

Figure 2.11 LA-ICP-MS image of DD020-124.2. Unlike the nodule in 19D-171.2, this one is concentrically layered, containing a zone of matrix-sulfide intergrowths between the inner and outer pyrite-rich zones. A clear internal chemical zonation is evident with regard to Co, Ni, As, Ag, Sb, Te, Pb, and Bi. Mercury is present in the rim of the nodule, contained mostly in sphalerite intergrown with pyrite there.

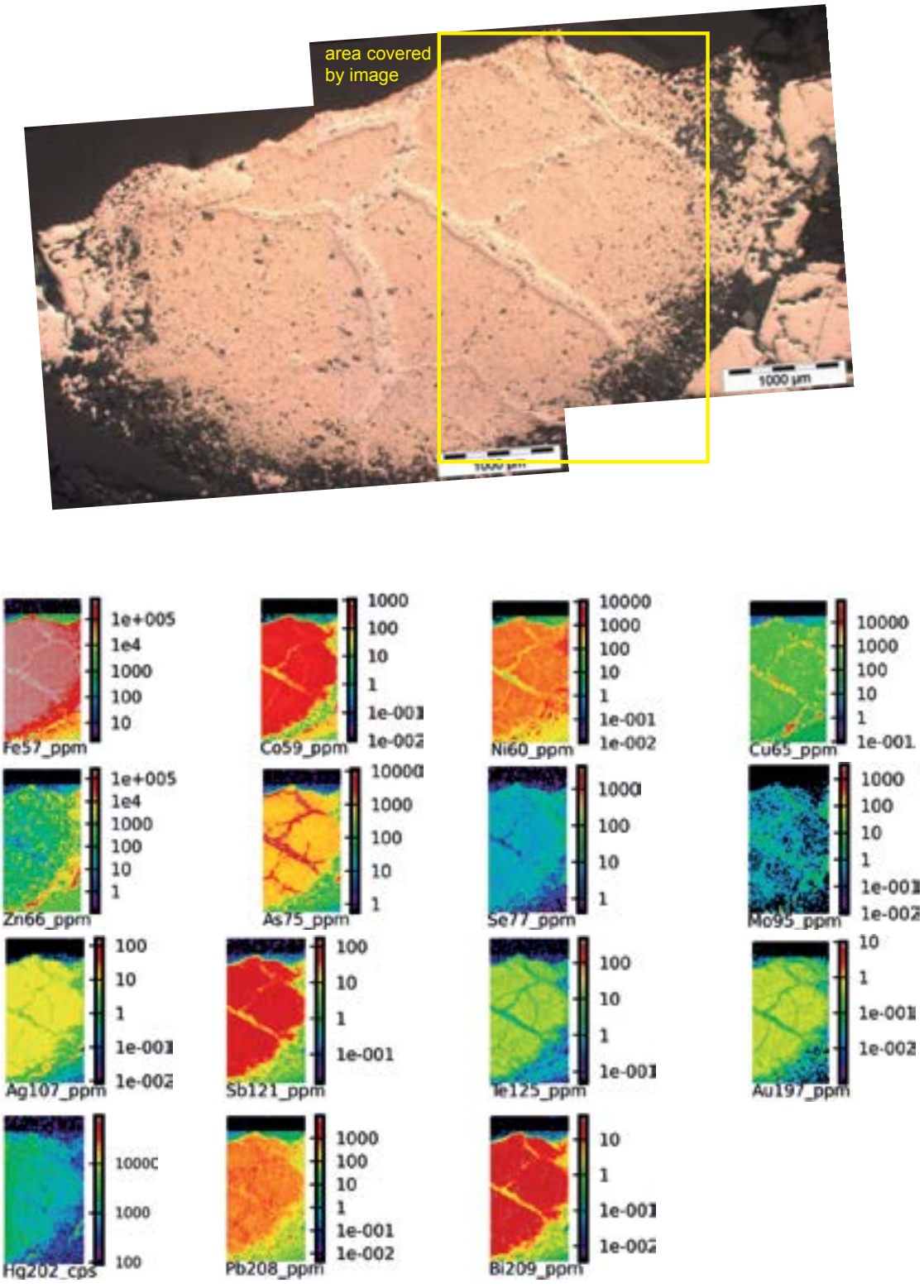

Figure 2.12 LA-ICP-MS image of 22D-184.4. This is a large, deformed (flattened) nodule that has been intruded by later pyrite containing higher As and Mo but lower Co, Ni, Ag, Sb, Te, Au, Pb, and Bi. Later pyrite also exists in the pressure shadows surrounding the nodule. Free gold grains are present near the edge of the nodule, as can be seen on the time-resolved laser tabcharts (Figure 2.13). Low levels of Hg are present within the nodule, as well.

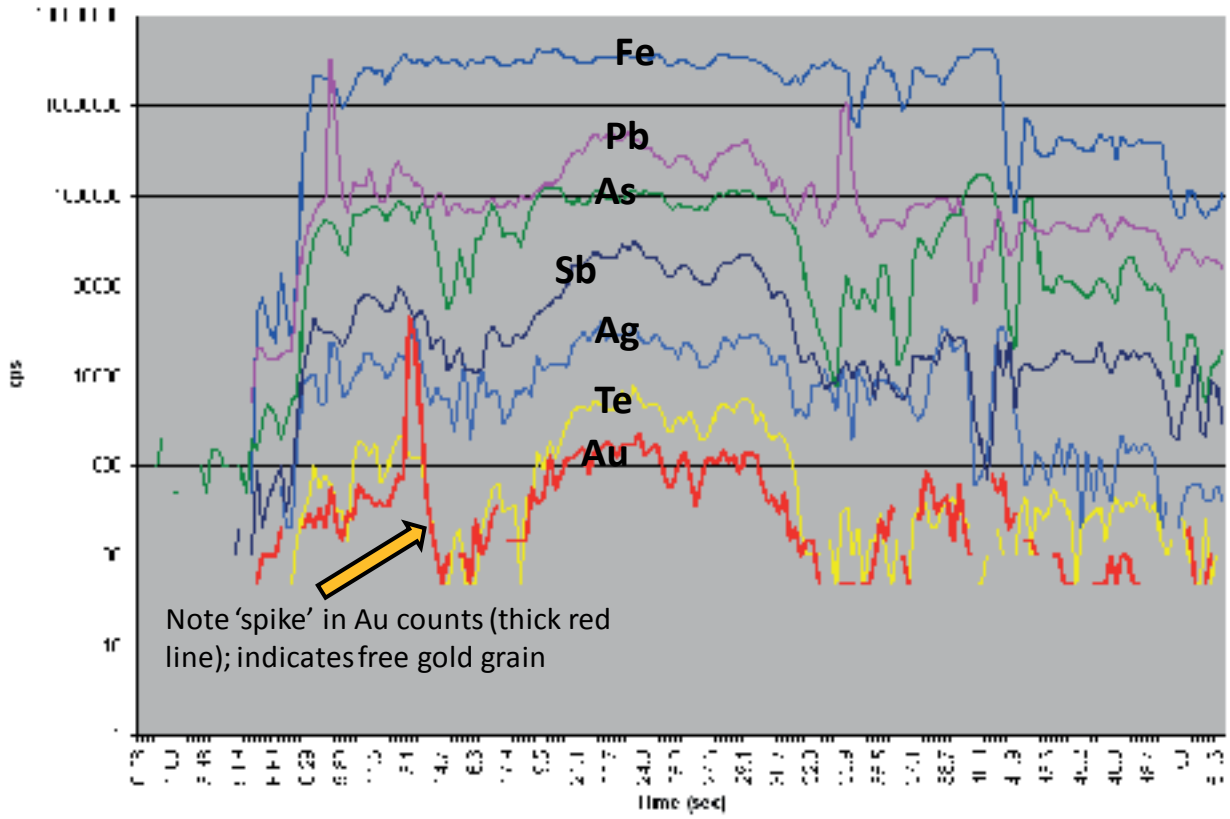

Figure 2.13 Time-resolved laser line from the previous image (Fig. 2.12). The spike in gold counts above both background and nodule count values indicates that a small native gold grain is present.

Table 2.1 Average trace element abundances (ppm) in nodular and associated pyrites

	Co	Ni	Cu	As	Se	Mo	Ag	Sb	Te	Au	Tl	Pb	Bi
19D-171.2A	773	622	232	1313	9	0.4	14	79	28	0.2	0.8	586	23
19D-171.2B													
rim	621	564	172	1006	10	0.7	9	58	21	0.17	1	472	17
core	400	371	123	666	5	0.6	8.6	41	15	0.16	1.5	305	13
DD020-124.2	1415	369	135	2854	10	0.6	7	147	21	1.1	0.8	535	13
22D-184.4													
nodule pyrite	290	817	211	1097	10	0.4	10	90	20	0.5	9	512	28
vein pyrite	65	195	2341*	8953	4	1.8	8	23	2	0.1	2	452	4

* ccp inclusions

In DD020-124.2, spots were drilled in the rims of the nodules as well as the cores, while in 19D-171.2 and 22D-184.4 spots were drilled in the cores, rims, and pressure shadow pyrites. 22D-184.4 also contains the network of infiltrated pyrite within the nodule, which was also analyzed. Little difference in the Pb isotope ratios exists between the core and rim pyrite in DD020-124.2, whereas a significant difference in Pb isotope signals was recorded in the nodular and pressure-shadow metamorphic pyrites of 19D-171.2 and 22D-184.4 nodules. Only a minor difference in ratios was detected between nodular pyrite and the later 'infiltrating' pyrite in 22D-184.4. Almost all of the data in the 207/206 diagram plot above the normal crustal Pb growth curve of Stacey and Kramers (1975), indicating that the local $^{238}U/^{204}Pb$ ratio (μ) around Lucky Bay is enriched relative to the average crustal value. The nodule 208/206 ratios are also above the Stacey and Kramers growth curve (Fig. 2.15B), further indicating a shallow crustal Pb source. Except for the three outliers in Figure 2.15A, B (all metamorphic pyrite with low total Pb), the data trend off the growth curve on an apparent isochron at ~2700 Ma, with Pb from nodules in 19D-171.2 being the oldest of the sample set.

2.6 Discussion

2.6.1 Correlation of the Lucky Bay sequence with the Black Flag Group

The maximum age of 2679±11 Ma (2σ) based on LA-ICP-MS analysis of detrital zircons from the sample of sandy debris flow from Lucky Bay fits well with previously published U-Pb ages for the Black Flag Group (Krapez et al., 2000; Krapež and Hand, 2008; Kositcin et al., 2008; Squire et al., 2010). The dominance of fine- to medium-grained turbidites in the Lucky Bay succession, the presence of carbonaceous shale, and the relative paucity of igneous lithologies are also permissive of correlation

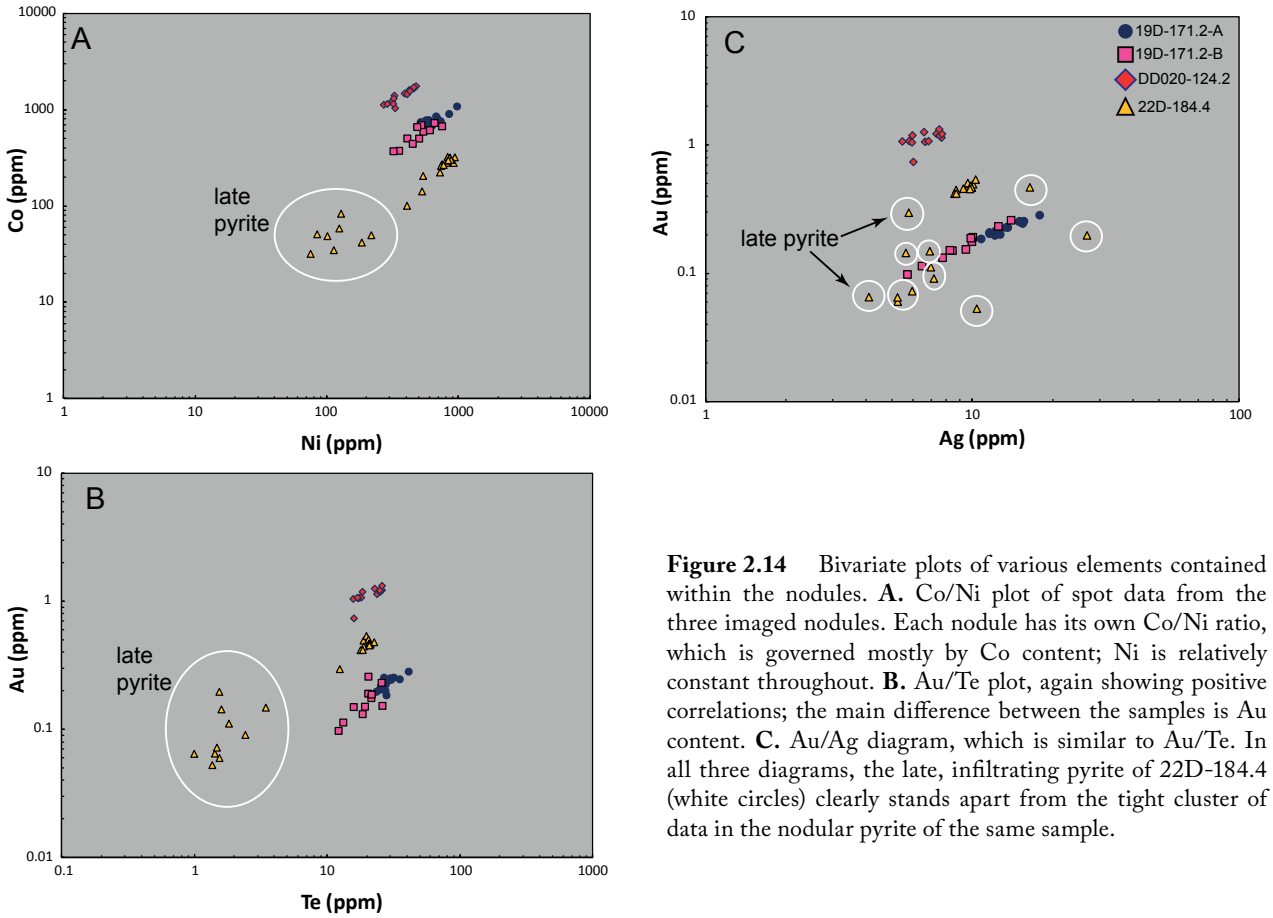

Figure 2.14 Bivariate plots of various elements contained within the nodules. **A.** Co/Ni plot of spot data from the three imaged nodules. Each nodule has its own Co/Ni ratio, which is governed mostly by Co content; Ni is relatively constant throughout. **B.** Au/Te plot, again showing positive correlations; the main difference between the samples is Au content. **C.** Au/Ag diagram, which is similar to Au/Te. In all three diagrams, the late, infiltrating pyrite of 22D-184.4 (white circles) clearly stands apart from the tight cluster of data in the nodular pyrite of the same sample.

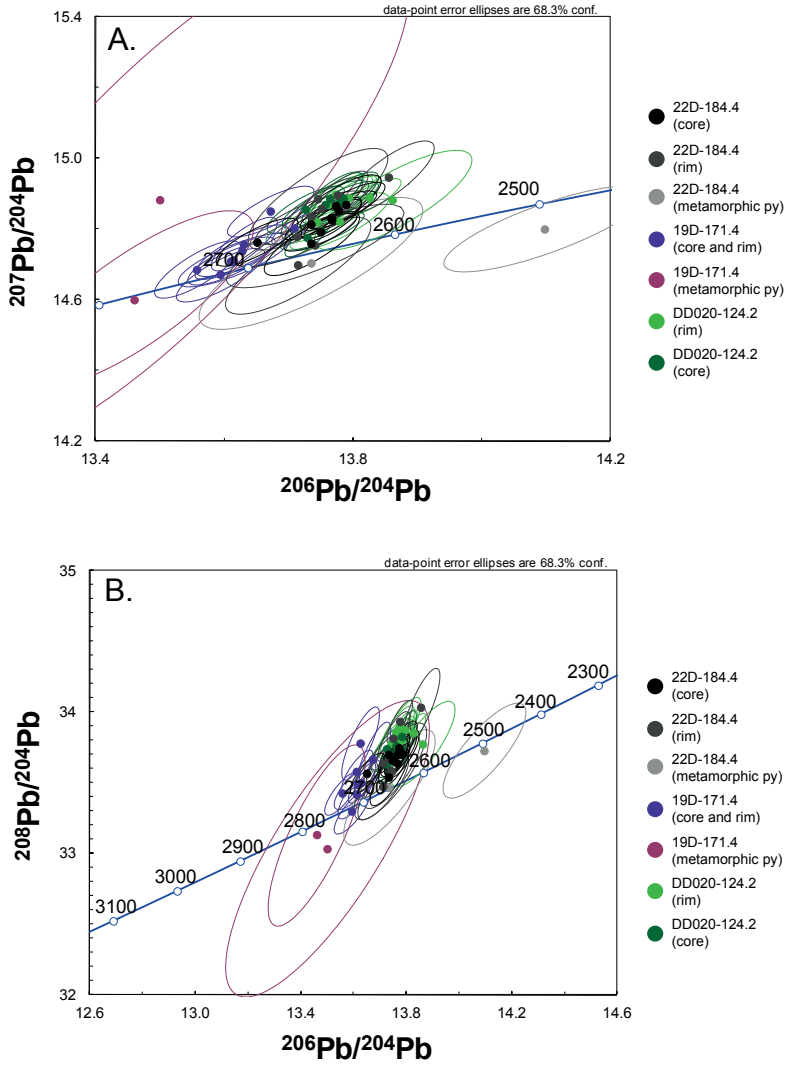

Figure 2.15 Pb isotope diagrams. **A.** Lucky Bay uranogenic (207/206) Pb isotopes in pyrite. **B.** Thorogenic (208/206) pyrite Pb isotopes.

Figure 15.

of the Lucky Bay succession with the Black Flag Formation of the Kalgoorlie Terrane, also called the Killaloe Formation (SE Kambalda Domain) and Mount Kirk Formation (Norseman; Krapež et al., 2000). On the other hand, the andesite in drill hole LBDD020 has a character similar to that of the dacite belonging to the Spargoville Sequence of the Kalgoorlie Terrane, near Kambalda and Kanowna Belle (Krapež et al., 2000; Kositcin et al., 2008; Squire et al., 2010), and the fact that this unit is overlain by carbonaceous black shale containing sulfide concretions in LBDD020 suggests that Spargoville correlates are the bedrock to the Lucky Bay prospect (the Spargoville dacite is overlain by black shale at Kambalda).

Debate exists on the topic of what should and should not be called the Black Flag Group. Krapež and Hand (2008) defined the Kalgoorlie Sequence (Black Flag Group) as a series of four ~8 million-year-long cycles, each separated by uplift, granite intrusion, and erosion. The oldest began at ~2690 Ma, and the youngest ended at ~2658 Ma. This model has been called into question by Squire et al. (2010), who point out that the four cycles of Krapež and Hand (2008) do not appear to correlate with (1) previously-established work which defined two major periods of felsic magmatism in the eastern Yilgarn (2685 and 2665 Ma; Campbell and Hill, 1988); (2) the three orogenic episodes that occurred at this time (D_1–D_3; Blewett et al., 2010); or (3) the timing of mafic magmatism (2680 Ma – Golden Mile Dolerite and correlatives; Squire et al., 2010). The revised Black Flag Group of Squire et al. (2010) has a

maximum age of 2690 Ma and a minimum age of 2670 Ma, and is divided into only two stages – Early and Late (Fig. 3). We believe that the volcano-sedimentary sequence at Lucky Bay is sufficiently old (<2680 Ma) to be placed in the Black Flag Group, regardless of which model best describes the tectonic, sedimentary, and structural history of the eastern Yilgarn Craton.

2.6.2 Textural similarities with other nodular sulfide-bearing sequences

Detailed petrographic and S isotope work on Paleoproterozoic sulfide concretions in NW Russia by Melezhik et al. (1998) defined four stages of nodular sulfide growth: (1) early diagenetic pyrite-pyrrhotite, (2) middle diagenetic pyrrhotite, (3) late diagenetic pyrite-pyrrhotite, and (4) catagenetic (i.e., post-diagenetic but pre-metamorphic) pyrite-pyrrhotite and pyrrhotite-only. While the mineralogy of their sulfides is different to those discussed here (e.g., the Lucky Bay nodules are virtually pyrrhotite-free), the parallels between their early diagenetic textures and those in the Lucky Bay samples are compelling.

2.6.3 Significance of nodule trace element content

The style of trace element enrichment revealed in the nodules by LA-ICPMS analyses (e.g., high Co, Ni, Mo, Ag, As, Te, Pb, Sb, Hg, Bi, and elevated Au, with a Ag:Au ratio of ~10) is suggestive of an early diagenetic timing of formation, based on analogies with previous studies (e.g., Large et al., 2007, 2009). Pyrite which forms early in the rock history (i.e., syn-sedimentary or early diagenetic) is likely to contain significant amounts of the redox-sensitive trace elements (e.g., Zn, As, Ni, and Mo), whereas hydrothermal or metamorphic pyrite is typically poor in these elements, except for As, Ni, and Co (Large et al., 2007, 2009, 2011).

The variance in Co/Ni ratios of the nodules in different samples seems to suggest that the Co/Ni ratios of the diagenetic fluids in equilibrium with the nodules were slightly different at each stratigraphic level in the shale, despite being part of the same overall succession. This also argues against a metamorphic origin for the nodules. A metamorphic fluid would likely have produced nodules with near-identical trace element profiles, independent of stratigraphic position. The order-of-magnitude decrease in trace element content (except for As) in the late cross-cutting pyrite of 22D left trends in the remaining nodule surprisingly undisturbed, a fact that highlights the robustness of the nodular pyrite against wholesale chemical change during late diagenesis and metamorphism.

2.6.4 Sources of Pb in sulfide nodules

The nodule Pb isotope data fit well with the other trace element analyses in supporting an early diagenetic origin for the concretions, although there are differences among the three samples. The average 207/206 and 208/206 ratios of the three nodules (Fig. 2.16A, B) illustrate these differences clearly. The spread of data in Figure 2.16A, B imply at least two different sources of Pb at the three sites of deposition: a less-radiogenic source (represented by data from 19D-171.2) and a more-radiogenic source (the data from 22D-184.4 and DD020-124.2). Sources of Pb for the three nodules were high-μ and high-κ, as evidenced by the position of the data relative to the growth curves on both plots. On the 207/206 diagram (Fig. 2.15A), the ore field Pb growth curve of Cumming and Richards (1975) fits the data best (isochron at ~2700 Ma), but only if $\mu = 10.75$. The crustal Pb growth curve of Stacey and Kramers (1975) is a poor fit to the data at $\mu = 9.74$, and higher values fit even less well. On the other hand, the Stacey and Kramers curve ($\mu = 9.74$) fits the data best in thorogenic (208/206) space, although the isochron on this diagram places the least radiogenic Pb at >2700 Ma (~2730 Ma). Higher μ vales for both growth curves on the 208/206 diagram result in even older formation ages for the Lucky Bay black shale that are not geologically reasonable (e.g., 2800 Ma).

Perhaps most intriguing is the geographical distribution of these data: as mentioned previously, 19D-171.2 and 22D-184.4 come from two separate drill holes less than 100 m apart, in essentially the same stratigraphy (fold-thickened carbonaceous black shale), whereas DD020-124.2 comes from a drill

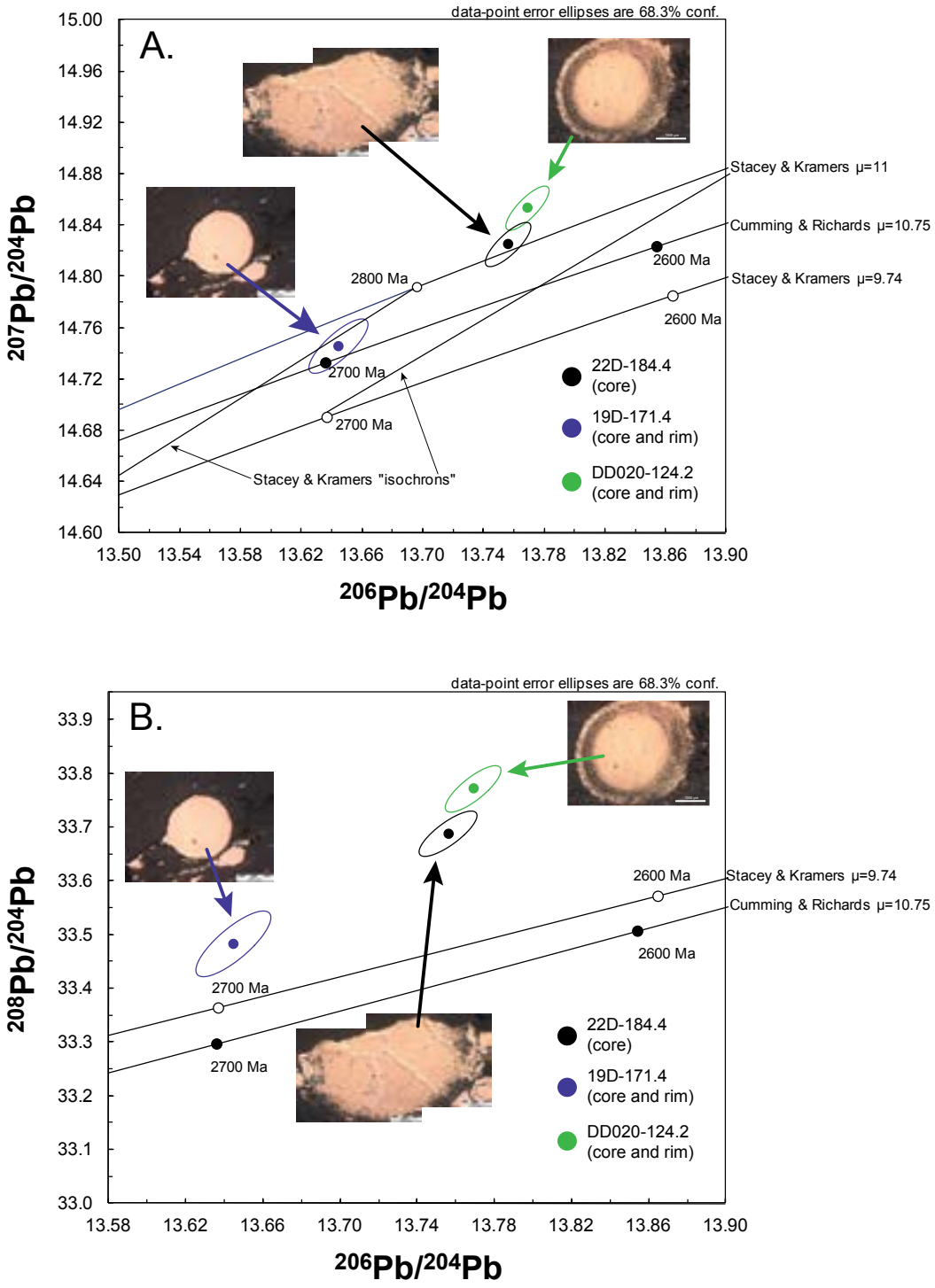

Figure 2.16 Average Pb isotope (207/206 and 208/206) diagrams for the nodules, excluding the metamorphic pyrites from 22D-184.4 and 19D-171.4. **A.** 207/206 data. **B.** 208/206 data.

hole at the other end of the section line, in somewhat different rocks (andesite and C_{org}-poor mudstone/siltstone along with nodule-bearing black shale), >300 m away from either of the other two holes. One might therefore expect the Pb isotope ratios to be similar between 19D-171.2 and 22D-184.4, given the commonality in rock type and location, yet this is not the case – the ratios in DD020-124.2 are more like those in 22D-184.4 (Fig. 2.16A, B). A possible explanation for the discrepancy between 19D-171.2 and 22D-184.4 is the varying amount of deformation and recrystallization experienced by the two samples. The second generation of pyrite that cuts through the nodule in 22D-184.4, and which is absent from 19D-171.2, may have introduced a second, more radiogenic, type of Pb that disturbed the original Pb ratios in the nodule but left the other trace elements unaffected. The similarity in 207/206 and 208/206 ratios between 22D-184.4 and DD020-124.2 indicate that these may have formed from or were contaminated by a radiogenic Pb source, but not necessarily the same source. One possible Pb source might be the voluminous, high-Ca and high-Th granitoids that were intruded into the greenstones between 2685 and 2665 Ma. The maximum depositional age of ~2680 Ma for the Lucky Bay sequence therefore makes it possible that the high-Ca granites may have contributed some Pb (and Th) to the sediments.

Regardless of the obvious differences in Pb sources, they are all 'old' Pb (i.e., Neoarchean), and the early (diagenetic) formation of these sulfide concretions is beyond a reasonable doubt. Uranium concentrations in the nodules are low (30–70 ppb) and measured Pb is relatively high (100s of ppm), which makes U/Pb ratios very low (~10 x 10^{-6}), so even when corrected for in-situ U decay, Pb-Pb ratios within the nodules remain essentially unchanged from the initial ratios (Table 2.2). These data bolster our assumption that the measured Pb-Pb ratios in the nodules are initial ratios, and are not produced from or significantly modified by in-situ U decay. A metamorphic origin for the nodules can also be ruled out; if the nodules were metamorphic in origin, a single, homogenous Pb isotope signal might be expected, given the widespread, voluminous granitic magmatism that occurred coincident with regional deformation in the Lucky Bay area (regional deformation commenced ~2660 Ma). These plutons almost certainly had their own Pb isotope character that would have overprinted any locally-derived signal in the country rock. We believe that the sulfide nodules in this study likely began as marcasite (or marcasite after pyrite), but during metamorphism they converted to pyrite, which left the original structure intact. The nodules subsequently experienced minor deformation and metamorphism, as evidenced by the oblong nature of some of the nodules, the change in orientation of the layering enveloping them, and the presence of the second generation of pyrite rich in As, Se, and Ni, but depleted in all other trace elements.

2.6.5 Regional black shale-gold deposit correlations in the Eastern Goldfields Superterrane and other greenstone terranes

Tomkins (2010) modeled the release of sulfur during metamorphism in a variety of lithologies that are commonly associated with gold deposits in greenstone belts, and found that pyrite-bearing carbonaceous metasediments (black shale) are the most favorable source rock (metamorphic H_2S production from a given volume of black shale is often 10–100 times greater than that of mafic greenstones). In particular, the presence of multiple black shale horizons within a regional volcano-sedimentary package seems to be ideal. As pressure and temperature increase during prograde regional metamorphism, the rocks pass through a sulfur liberation 'window' that occurs at moderate temperatures and low pressures (450–550°C and 0.3–1.0 GPa for pelites). This P–T range also coincides with the terminal stability of hydrous minerals such as chlorite. When pyritic black shale horizons are present in the regional rock succession, the pyrite in those units converts to pyrrhotite, thereby releasing sulfur (and potentially considerable quantities of trace metals, especially As and Au) to the metamorphic fluid. Should deformation be simultaneous with pyrite desulfidation and chlorite breakdown in the regional sedimentary-volcanic sequence, the fluid becomes sufficiently mobile to scavenge large quantities of H_2S, As, and Au from pyrite breakdown, which in time may lead to the formation of a gold deposit, if it encounters a suitable

Table 2.2 U-corrected initial Pb in Lucky Bay pyrite nodules

Analysis	Current values		$^{206}Pb/^{204}Pb$	$^{207}Pb/^{204}Pb$	$^{208}Pb/^{204}Pb$	^{204}Pb (moles/tonne)	^{206}Pb (moles/tonne)
	^{206}Pb (ppm)	Pb (mole/tonne)					
Oldest (19D-171.2)	533	2.587378641	13.645	14.746	33.483	0.041151806	0.561516391
Intermediate (DD020-124.2)	515	2.5	13.769	14.853	33.771	0.039436531	0.543001593
Youngest (22D-184.4)	510	2.475728155	13.756	14.825	33.687	0.039130811	0.538283437

	Current values		^{238}U (ppm)	^{238}U (mole/t)	$^{238}U/^{206}Pb$	$^{238}U/^{204}Pb$	^{235}U (mole/t)
	^{207}Pb (moles/tonne)	^{208}Pb (moles/tonne)					
Oldest (19D-171.2)	0.606824529	1.377885915	0.03	0.00012605	9.23785E-06	0.00012605	9.14204E-07
Intermediate (DD020-124.2)	0.585750793	1.331811083	0.027	0.000113445	8.23919E-06	0.000113445	8.22783E-07
Youngest (22D-184.4)	0.580114274	1.318199633	0.069	0.000289916	2.10756E-05	0.000289916	2.10267E-06

	$^{235}U/^{207}Pb$	$^{235}U/^{204}Pb$	Time of deposition T (Ma)	Decay constants		Initial ratios	
				λ_{238}	λ_{235}		
Oldest (19D-171.2)	1.50654E-06	2.22154E-05	2700	1.54E-10	9.71E-10	13.645	14.746
Intermediate (DD020-124.2)	1.40466E-06	2.08635E-05	2700	1.54E-10	9.71E-10	13.769	14.853
Youngest (22D-184.4)	3.62458E-06	5.37344E-05	2700	1.54E-10	9.71E-10	13.756	14.824

structural trap.

Several world-class orogenic gold deposits are intimately associated with pyritic black shales, including Muruntau (Morelli et al., 2007), Sukhoi Log (Large et al., 2007), and multiple deposits in the Bendigo-Ballarat goldfields (Glasson and Keays, 1978; Large et al., 2009; Thomas et al., 2011). These deposits are also As-rich, a fact not surprising given that black shale usually contains much more As than other rock types (e.g., 10–100 times more than mafic greenstones; Tomkins, 2010). Furthermore, fluid inclusion studies on orogenic gold deposits have demonstrated that the ore fluids were likely high in CO_2; these data are supported by the widespread carbonate alteration surrounding many orogenic gold camps. A mantle source for the carbon-in-carbonate has been invoked in the past (Groves et al., 1988), but given the high average C_{org} content of black shales, their proximity to known gold deposits, and the negative $\delta^{13}C$ values recorded in the carbonate alteration, these lithologies should not be discounted as a possible source of carbon for ore-forming fluids.

Although the Eastern Goldfields Superterrane is dominated by greenstone-granitoid complexes, and most of the gold contained in the Superterrane is hosted by these rocks, there are black shale sequences present in several of the gold camps (e.g., the Kapai Slate at St. Ives and Golden Mile; carbonaceous shale/siltstone of the Black Flag Group at Kanowna Belle and Mount Charlotte). Given the fertility of black shales in the other districts, it is theoretically possible that a portion of the gold budget in the greenstone-dominant Eastern Goldfields Superterrane was originally sourced from these nearby sulfide-rich sediments.

2.6.6 Lucky Bay shale as a contributing source of gold to the Randalls BIF-Au district

The Randalls district, a collection of three separate Au deposits hosted in a folded BIF unit (Fig. 2.2; Newton et al., 1998; Roberts et al., 2004), is approximately 20 km east of Lucky Bay. The host BIF is part of the Belches Supersequence, which occupies the late-stage Belches Basin (Fig. 2.1C; Krapež et al., 2008). Tectonic reconstructions of the eastern Yilgarn Craton suggest that lateral equivalents of the Black Flag Group (including the nodular sulfide-bearing black shale) were likely present where and when the Belches Supersequence was deposited (Krapež et al., 2008; Czarnota et al., 2010). In such a scenario, the medium- to coarse-grained turbidites and BIF of the Belches Supersequence were deposited directly on top of the succession containing the gold-anomalous black shale equivalents. This spatial relationship could have been a key factor during orogenesis and granite intrusion, the latter event presumably leading to metamorphism of the Black Flag equivalents and the liberation of gold and arsenic from the black shales, as well as contact metamorphism of the Belches Supersequence near intrusive centers (Painter and Groenewald, 2001). Fluids exsolving from the granite bodies would have acquired gold and arsenic as they passed through the black shales on their way to the BIF horizons, so in this way, gold may have been contributed from the nodule-bearing black shales at Lucky Bay to BIFs that make up the Randalls Goldfield.

2.7 Conclusions

The maximum depositional age of the rocks hosting the Lucky Bay gold prospect is constrained to 2679±11 Ma (2σ) by detrital zircon U-Pb geochronology. This age constraint suggests that the sequence is correlative with the Black Flag Group, which makes the area younger than Kambalda, St. Ives, and Golden Mile but older than the turbidites and debris flows of the Randalls district. Several lines of geological and geochemical evidence support an early timing of formation (i.e., early diagenesis) for sulfide concretions in carbonaceous black shale at the Lucky Bay prospect. Bedding wraps around the nodules, and they have obviously been affected by deformation during orogenesis (e.g., recrystallization of pyrite, non-spherical outlines, and quartz-pyrite-mica pressure shadows). Trace element mapping via

LA-ICP-MS reveals a large and diverse suite of chalcophile elements present within the nodules (e.g., Co, Ni, As, Ag, Te, Pb, Bi, and Au), a common feature of early diagenetic pyrite worldwide. Lead isotope analyses also suggest a Neoarchean timing of formation (~2700 Ma) and a shallow crustal Pb source for the sulfide concretions. The source of Au at Randalls is presently unresolved, but given (1) the anomalous concentrations of Au in the sulfide concretions at Lucky Bay (~0.5–1 ppm), (2) the amount of Au-enriched pyrite in the black shale sequence (~10%), (3) the thickness of the unit (~50 m), and (4) the likelihood of this succession underlying the Belches Basin prior to deformation and granite intrusion, the carbonaceous black shale at Lucky Bay may have contributed some of the gold now present in the BIF-lode gold deposits of the Randalls district.

Chapter 3

Paragenesis and composition of ore minerals in the Randalls BIF-hosted gold deposits, Yilgarn Craton, Western Australia: Implications for the timing of deposit formation and constraints on gold sources

Published in ***Precambrian Research****, v. 243, p. 110-132*

Abstract

The Randalls district comprises three individual gold deposits — Cock-Eyed Bob, Maxwells, and Santa-Craze — hosted in the same unit of banded iron-formation (BIF) in the southern Eastern Goldfields Superterrane, Yilgarn Craton, Western Australia. The iron formation is a silicate/oxide-facies unit with overprinting sulfides, and has undergone metamorphism (upper-greenschist facies) and deformation (two generations of folds). The gold deposits are hosted in two structural locations: hinge zones of anticlinal folds (e.g., Santa-Craze and Maxwells) and overturned, steeply-dipping limbs of anticlinal folds (e.g., Cock-Eyed Bob). Gold dominantly occurs as inclusions of native gold and/or electrum within or around pyrrhotite, magnetite, and arsenopyrite.

The earliest mineral assemblage preserved in the banded iron formation at Randalls is banded magnetite-quartz. Magnetite in all forms has elevated Mg, Al, Ti, V, Mn, Cr, Zn, and W, but very low Ni compared to other BIF globally. Pyrrhotite, the most abundant sulfide, is restricted to ore zones and occurs as laminae, 'blebs', and veinlets, all of which have replaced magnetite. Some pyrrhotite in the hydrothermally altered BIF (especially in near-surface samples) has been re-sulfidized to pyrite. Trace elements associated with pyrrhotite include Co, Ni, Ag, Sb, and Pb. Large, coarse-grained arsenopyrite overgrows the pyrrhotite-defined foliation; it is enriched in Co, Ni, Sb, and Te, but contains very little 'invisible' gold (<0.01 ppm Au), unlike arsenopyrite in many orogenic Au systems globally (commonly ≥ 0.1 ppm Au).

Petrographic studies of several mineralized BIF from Randalls reveal that pyrrhotite and arsenopyrite are associated with Fe(-Ca) amphibole, which grew during contact metamorphism caused by granite plutons. This spatial sulfide-amphibole relationship indicates that gold mineralization likely occurred during granite intrusion, consistent with prior studies on Randalls. The trace element characteristics of the sulfides show that they were not inherited from replaced magnetite. Further, these characteristics suggest that the fluid from which sulfides crystallized was not indigenous to the BIF, and that this S-rich fluid either contained S in abundance originally, or interacted with a lithology/lithologies that were rich in S before reaching the BIF. Black shale containing diagenetic nodular pyrite occurs in the upper Black Flag Group, which unconformably underlies the Belches Supersequence at depth (~3 km). The trace element composition of nodular pyrite from this unit fits well with the trace element characteristics of the BIF pyrrhotite and arsenopyrite, and the nodular pyrite contains an average of 0.5 ppm Au.

However, the nodular pyrites have an average $\delta^{34}S$ value of 5.6‰ (n = 13), which contrasts markedly with the $\delta^{34}S$ average of pyrrhotite, pyrite and arsenopyrite in mineralized BIF (0.8‰, n = 17). Thus, a definitive source of gold, arsenic, silver, and tellurium in the Randalls system remains elusive, although we would contend that the upper Black Flag Group should be considered as a possible metal and S source in areas of the Yilgarn where it forms a thick substrate to ore camps.

3.1 Introduction

The majority of Precambrian gold deposits may be divided into two groups — Witwatersrand-type and orogenic (i.e., structurally controlled)-type — which, combined, account for much of Earth's accessible gold endowment. The orogenic category is further subdivided into sediment-hosted and greenstone (altered mafic volcanics)-hosted. A variant of the sediment-hosted subclass is the banded iron-formation (BIF)-hosted gold deposit group, members of which are commonly small and subeconomic. One exception to this general rule is the Homestake BIF deposit (South Dakota, USA), which contained over 40 million ounces (Moz) of gold (Caddey et al., 1991).

The Randalls orogenic (structurally controlled) Au district, Western Australia (~0.6 Moz total contained Au, Integra Mining Pty Ltd, 2011; Figs 3.1, 3.2), is one of the few gold camps globally where banded iron-formation (BIF) is the primary ore host. Other orogenic gold districts (both sediment- and greenstone-hosted) have BIF in the regional stratigraphic sequence but it is not the principal host to the ore (e.g., Sunrise Dam, Western Australia). The banded iron-formation at Randalls includes oxide (magnetite) and silicate (chlorite) facies, and a replacement sulfide 'facies' (pyrrhotite and arsenopyrite) is localized in or near the individual gold deposits. The latter lithology contains the majority of the gold budget.

BIF-hosted gold deposits, although small in size and number, have been the subject of much research and a protracted debate for nearly a century. For example, the origin of Homestake has been reviewed numerous times since the early 1900s (Paige, 1923; Gustafson, 1933; Noble, 1950; Rye and Rye, 1974; Caddey et al., 1991). Several papers published in the 1970s (e.g., Fripp, 1976; Anhaeusser, 1976; Hutchinson, 1976) argued for a syngenetic origin of all BIF-hosted gold deposits worldwide, drawing analogies between banded iron-formations and seafloor exhalites. The following decade marked a departure from this mode of thinking towards a metamorphic-hydrothermal, or 'epigenetic', formation model, in which the iron formations were simply efficient chemical traps for migrating metal- and H_2S-rich fluids (Phillips et al., 1984; Groves et al., 1987). This model has remained the paradigm in academic and exploration literature.

Syngenesis has been revived and revised in recent years for certain sediment-hosted orogenic gold resources (e.g., Large et al., 2007, 2009, 2011; Thomas et al., 2011). In the deposits studied by these authors, gold and other associated trace elements (e.g., As, Te, Bi, Ag, and Pb) were found to be incorporated into synsedimentary/early-diagenetic pyrite in fine-grained, carbonaceous sediments (i.e., black shale). Later generations of pyrite, interpreted to be late diagenetic/early metamorphic, had orders-of-magnitude smaller concentrations of gold in the pyrite structure, but often contained inclusions of native gold and/or precious-metal tellurides. These textures were interpreted to reflect a multi-stage process of gold enrichment, from pre-concentration in the early pyrite, to release and upgrading in structurally favorable zones during metamorphism and/or deformation, facilitated by the pyrite-to-pyrrhotite conversion at deeper levels in the basin.

This paper discusses the syngenesis versus epigenesis origin of the Randalls deposits, but the main aim is to evaluate the source of metals and sulfur from the textures and chemistry of the oxide-sulfide assemblages of BIF within the ore envelope, using various techniques. Constraints on the depositional age of the sequence hosting the BIF are also addressed, for comparison with previous detrital zircon

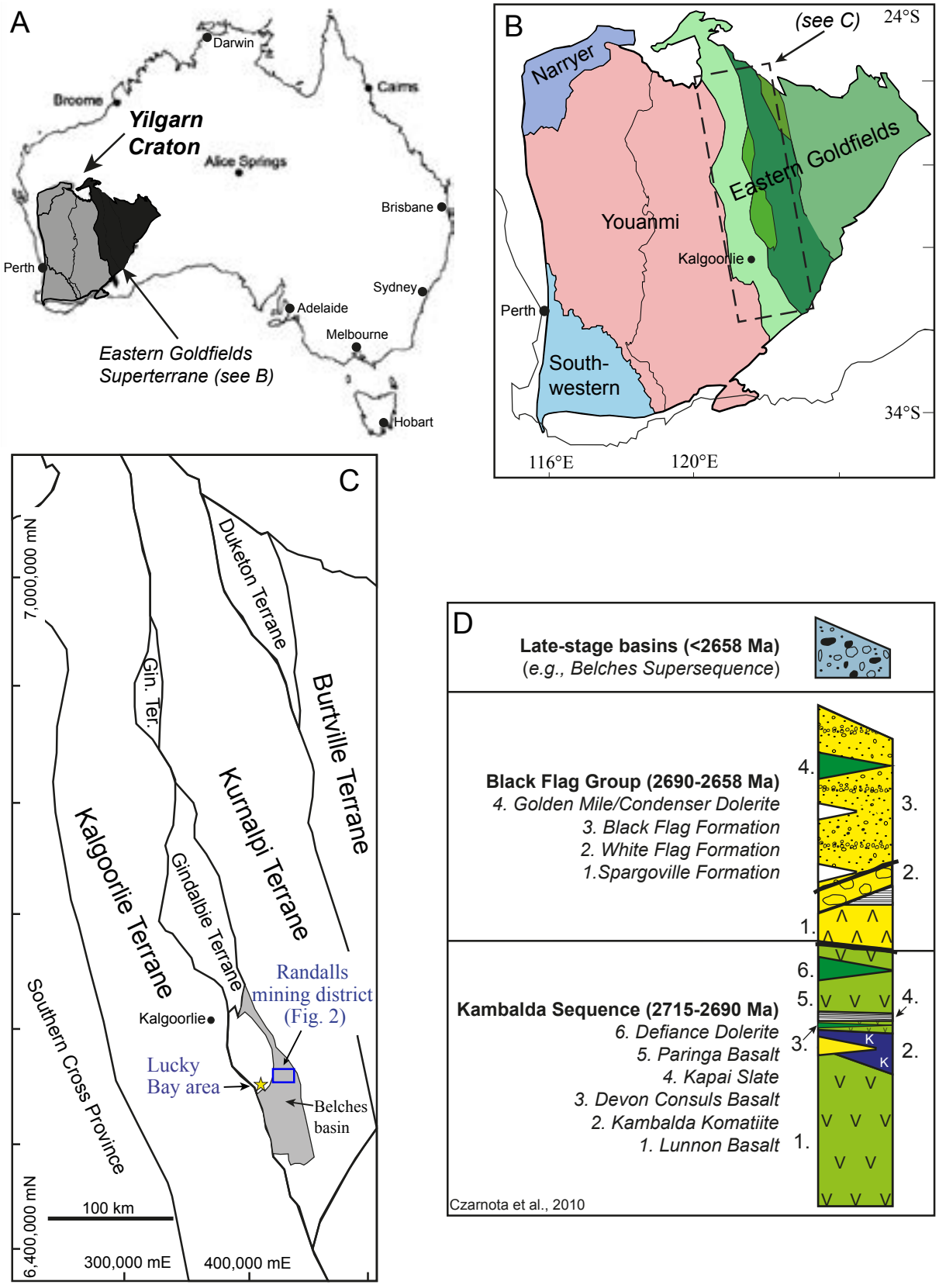

Figure 3.1 **A.** Map of Australia showing location of the Yilgarn Craton; the Eastern Goldfields Superterrane is in black (modified after Krapež et al., 2008). **B.** The Yilgarn Craton (after Czarnota et al., 2010), composed of five provinces (Narryer, Murchison, Eastern Goldfields, Southern Cross, and Southwestern). **C.** Schematic representation of the Eastern Goldfields Superterrane (after Krapež et al., 2008). The blue box (SE region of map) represents the area included in the Randalls mining district. **D.**Regional stratigraphy of the Eastern Goldfields (redrawn from Czarnota et al., 2010), showing the chronological position of the Belches Supersequence relative to the Kambalda Sequence and Black Flag Group. The Belches basin is entirely occupied by the Belches Supersequence, while most of the Kalgoorlie, Gindalbie, and Kurnalpi terranes (shown in 'C') are comprised of the Kambalda Sequence and Black Flag Group, and correlates to these lithostratigraphic packages.

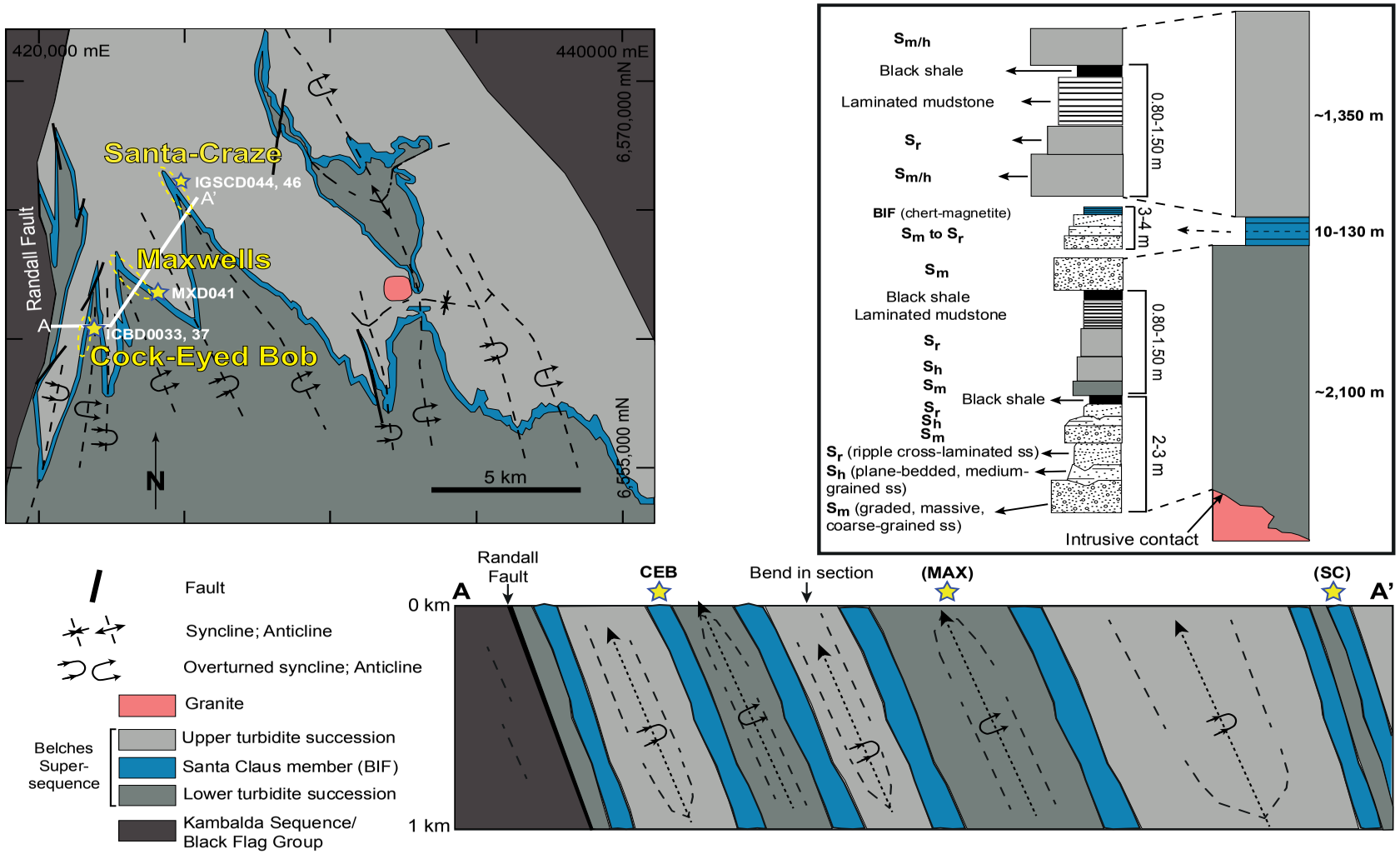

Figure 3.2. A) Map of the Belches basin (after Krapež et al., 2008, and Painter and Groenewald, 2001), which includes the three deposits comprising the Randalls mining district. Two of the three deposits (Santa-Craze and Maxwells) occupy the hinges of F_4 folds (refolded F_3 folds; Krapež et al., 2008). Cock-Eyed Bob is located on the western limb of the westernmost F_4 fold, adjacent to the Randalls Fault, a syn-amalgamation sinistral strike-slip fault separating the Belches Supersequence from the Minerie Sequence. Dashed ovals are rough pit outlines, while stars represent location of sampled drill holes. **B)** Graphic log of the Belches Supersequence (redrawn after Krapez et al., 2008). The Randalls BIF (Santa Claus member) separates a lower and upper sequence of turbidites, consisting of repeated coarse-grained, massive sandstone to fine-grained, ripple cross-laminated sandstone facies (S_m-S_h-S_r); laminated mudstone and black shale can also be present. The Santa Claus member (Randalls BIF) also contains S_m-S_h-S_r fining-upward sequences, with oxide-facies BIF instead of laminated mudstone/black shale at the top. The intrusive contact noted on the log is not seen in the Randalls area. **C)** Generalized cross-section of the western Belches basin. All F_4 anticlines and synclines are overturned to the east-northeast; consequently, all units dip steeply east-northeast.

geochronology studies that focused on the southern (stratigraphically lower) portion of the Belches Basin (e.g., Krapež et al., 2000). Sulfur isotope analyses on both BIF-hosted sulfides and pyritic black shale from the Lucky Bay gold prospect (~15 km west of the Randalls district; Steadman et al., 2013), are used to evaluate sulfur sources. The Lucky Bay area was chosen because it does not have the same metamorphic history as the Belches Basin; rather, the maximum P-T conditions there were somewhat lower (lower-middle greenschist facies; Goscombe et al., 2009) compared to the Belches Basin. Furthermore, Steadman et al. (2013) maintained that the Lucky Bay black shale horizon correlates with the Black Flag Group shale/greywacke sequence at the Golden Mile and St. Ives gold camps, which means it is slightly older (~10 Ma; Squire et al., 2010) than the Belches Supersequence. These authors also postulated that distal correlates of the Lucky Bay shale underlie the Belches basin at depth, in keeping with the tectonic reconstruction of Czarnota et al. (2010), providing a potential source of S, CO_2, and metals to the Randalls deposits.

3.2 Regional Geology

Swager (1997), Krapež et al. (2008), Czarnota et al. (2010), and Pawley et al. (2012) provide detailed accounts of the geologic framework of the Eastern Goldfields Superterrane. A brief summary of their papers is given below.

The Eastern Goldfields Superterrane is an amalgamation of five ancient volcanic arcs (now referred to as terranes; Fig. 3.1) that were sutured together to form one giant superterrane (Eastern Goldfields) at about 2660–2650 Ma. The Superterrane has a protracted tectonic history involving multiple cycles of magmatism, uplift, erosion, and sedimentation, the products of which have largely escaped preservation or are concealed beneath younger (but still Archean) rocks. The exception is the package of rocks formed during the youngest cycle, which makes up the overwhelming majority of lithologic units (including the Black Flag Group (BFG)) exposed in the Eastern Goldfields.

The Black Flag Group is a thick (~4000 m; Krapež and Hand, 2008; Krapež and Pickard, 2010) sequence of volcaniclastic siltstones, sandstones, conglomerates, and shales (this latter lithology comprises ~15% of the overall Group; Krapež and Pickard, 2010) that overlie all other lithologies in the Eastern Goldfields, with the exception of the late-stage basins (see below). The BFG is separated into an Early and Late sequence (Squire et al., 2010). Maximum depositional age of the Early BFG, as determined by detrital zircon U-Pb geochronology, is ~2690 Ma (Squire et al., 2010; Krapež and Pickard, 2010). Late Black Flag deposition is assumed to have commenced later than dolerite intrusion in the Kalgoorlie and St. Ives areas (i.e., after 2680 Ma; Squire et al., 2010). Steadman et al. (2013) analyzed detrital zircon from coarse grained sandstone interbedded with carbonaceous and pyritic black shale at the Lucky Bay gold prospect (Fig. 3.1C), and obtained an age of 2679 ± 11 Ma (2σ), similar to that of the Late Black Flag Group and the Golden Mile/Condenser Dolerite.

The Belches Basin is one of several so-called 'Late-Stage' basins that formed after the cessation of volcanic activity in the Eastern Goldfields Superterrane ca. 2660 Ma, where it adjoins the Kurnalpi and Gindalbie Terranes (Fig. 3.1). Tectonostratigraphic reconstruction of the Eastern Goldfields Superterrane by Czarnota et al. (2010) shows that the Belches Supersequence (Krapež et al., 2008) most likely deposited on top of Black Flag Group rocks, which formed the floors of graben blocks during D_3 extension. The >3600 m-thick Belches Supersequence is dominated by sandstone, which grades into mudstone over intervals of varying thickness. Krapež et al. (2008) identified two successions of sandstone, separated by a horizon of banded iron formation (maximum thickness 130 m; Fig. 3.2B), which is the focus of this paper. Each succession is ~1500 m thick, and sedimentary structures are generally well-preserved.

The first geochronologic study of the Belches Basin was by Krapež et al. (2000), who collected

a lower-succession sandstone sample from an outcrop on Mt. Belches, ~10 km south of the Randalls district. Their SHRIMP U-Pb detrital zircon age of 2664 ± 4 Ma represents a maximum depositional age for at least the lower succession of the Belches Supersequence. Later sequence stratigraphy by Krapež et al. (2008) suggested that, despite the differences in sedimentary facies between the upper and lower successions, and the so-called 'condensed section' (i.e., BIF) that separates them, the Belches Supersequence was likely deposited entirely within their 'Stage I' of Late-Stage Basin development. Detrital zircon age spectra for the Belches Supersequence should therefore be homogeneous regardless of sample location; this statement is tested with new data presented in section 3.5.2 (see below).

The Belches Supersequence has been multiply folded, beginning with regional D_4 compression following the regional D_3 extension that created the late-stage basins (Squire et al., 2010; Blewett et al., 2010). The east-trending, open F_3 folds that formed during D_3 were folded again during D_{4a} and D_{4b} compression, which resulted in NNW-trending F_4 anticlines and synclines that characterize the present day geometry of the units comprising the Belches Supersequence, particularly the banded iron formation (Fig. 3.2A).

At about 2660 Ma, the Belches Supersequence was intruded by several granitic plutons, including the Kiaki Monzogranite, a two-feldspar and two-mica granite which outcrops in the southern portion of the structural basin, ~50 km from Randalls (Painter and Groenewald, 2001). This pluton and others concealed at depth induced contact metamorphism in the surrounding sediments, particularly the mudstones. At the same time, granitoid bodies were intruding the rest of the Eastern Goldfields Superterrane (including the Black Flag Group at Lucky Bay); this regional event is the 'M3' of Goscombe et al. (2009), characterized by greenschist-facies assemblages (e.g., biotite and/or amphibole) in rocks distal to intrusions, and amphibolite- to possibly granulite-facies assemblages (e.g., staurolite and clinopyroxene) proximal to the intrusions.

3.3 Local Geology

In the Randalls district, all three subunits of the Belches Supersequence are present, but the only one which is named is the banded iron formation (the Santa Claus member; Painter and Groenewald, 2001; Figs 3.2, 3.3). The three gold deposits hosted by the Santa Claus member in the Randalls district are (from E to W): Cock-Eyed Bob (1.7 Mt @ 3.4 g/t Fig. 3.3), Maxwells (2.6 Mt @ 3.8 g/t), and Santa-Craze (4.3 Mt @ 2.2 g/t; Fig. 3.3). The latter two deposits are located in anticlinal fold hinges, while Cock-Eyed Bob is hosted by the western limb of the westernmost F_4 anticline (Fig. 3.3A). The anticlines are overturned to the west, resulting in right-way-up stratigraphy on the eastern limbs of folds and overturned bedding on western limbs.

The Santa Claus member is 10–130 m thick, and in the Randalls area it consists of two to three horizons of laminated chert-magnetite-amphibole rock that represent the tops of graded sandstone-mudstone packages (Newton et al., 1998; Roberts et al., 2004; Krapež et al., 2008; Fig. 3.2B). In the individual deposits, parts of the chert-magnetite-amphibole BIF have been sulfidized to chert-pyrrhotite/arsenopyrite-amphibole BIF, especially adjacent to quartz-carbonate veins. Laminations are on the mm- to cm-scale within the BIF, while both the mudstones and sandstones are massively bedded (0.5–1 m). The latter two lithologies may also contain magnetite of metamorphic (mudstones) or detrital (sandstones) origin.

The ore zones of the three main deposits are characterized by abundant quartz-chlorite-ankerite veins, which are mostly restricted to the competent Santa Claus member (Newton et al., 1998; Roberts et al., 2004). The member is sulfidized adjacent to these veins, and most of the gold is located in sections of altered wall rock, not in the veins themselves. The veins dip 25–40° SW throughout the district (Roberts et al., 2004; Fig. 3.3). Two fault sets are present in the deposits: a NW–NNW brittle-ductile group with reverse movement; and a later, NNE–ENE, brittle-ductile set with dextral movement (Newton et al., 1998; Roberts et al., 2004; Fig. 3.3). Gold mineralization is localized around sites of brittle failure in the

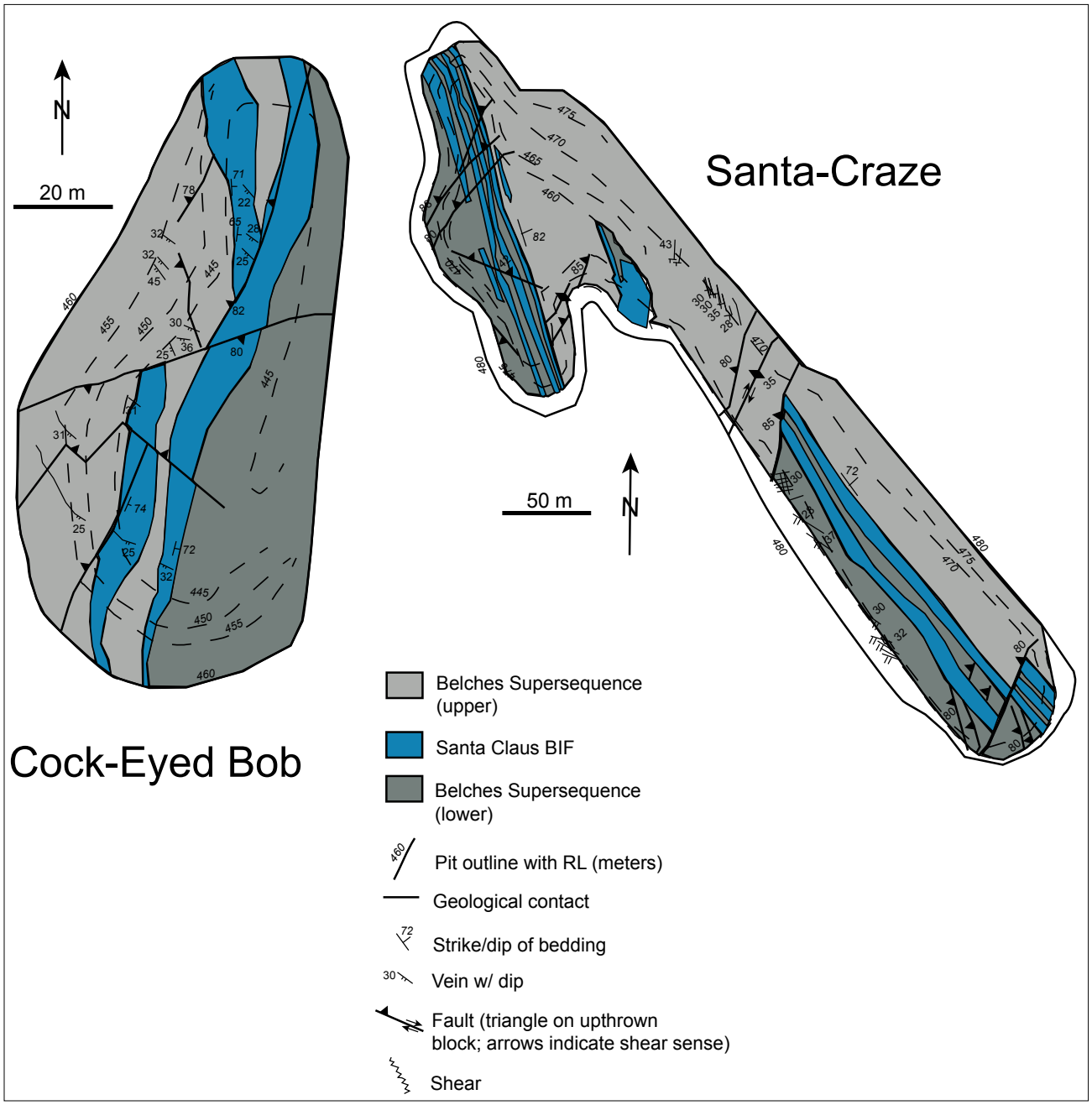

Figure 3.3. Schematic geology of the Cock-Eyed Bob and Santa-Craze open pits (modified after Roberts et al., 2004).

BIF (Roberts et al., 2004).

The Belches turbidites and banded iron formation at Randalls have been contact metamorphosed to at least upper greenschist-facies, evidenced by the presence of metamorphic biotite and/or Ca-Fe amphibole in the muddier sections of the turbidites as well as in the BIF. Biotite porphyroblasts also occur in the sandstones. All mudstones in the Belches Supersequence have been converted to chlorite-rich rocks (with or without biotite and magnetite porphyroblasts; Fig. 3.4A), whereas originally mud-rich laminae in the sandstones are now completely biotitized. The presence of these minerals, and the absence of higher-T phases such as staurolite, indicates that the Randalls district is relatively distal to any granite intrusion that may exist at depth in this part of the basin (Painter and Groenewald, 2001). Deformation experienced by the Belches units at Randalls during D_4 was low-strain, which permitted the preservation of most original sedimentary structures (e.g., trough cross beds, flame structures, load casts, and graded bedding; Fig. 3.4A).

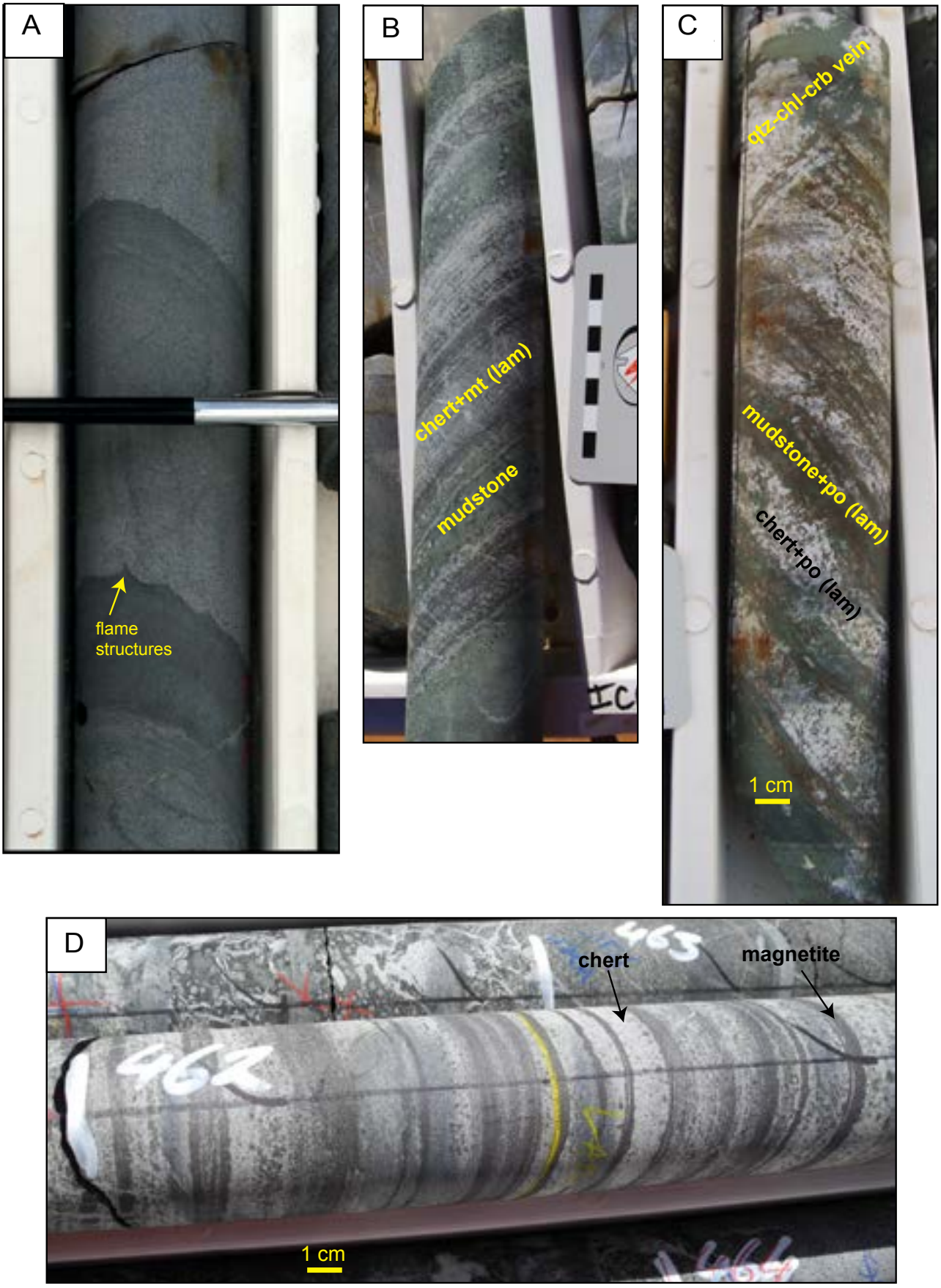
A
flame
structures
B
chert+mt (lam)
mudstone
C
qtz-chl-crb vein
mudstone+po (lam)
chert+po (lam)
1 cm
D
chert
magnetite
1 cm

3.4 Analytical Methods

3.4.1 Sampling strategy

Sample material collected for this study was restricted to recent (within 6–12 months) drill core, mostly to minimize effects of surface weathering and alteration of primary minerals by meteoric water; all sample data, including location information, is recorded in Table 3.1. One potential drawback associated with relying solely on drill core is a lack of spatial context: underground workings at Cock-Eyed Bob were not operational at the time of investigation, while both Maxwells and Santa-Craze are exclusively open-pit operations — the latter is also not currently in production. Open pit exposures naturally provide the necessary spatial context, but the high degree of weathering in most near-surface Western Australia outcrops, coupled with logistical hurdles, negated site visits of sufficient duration to be useful.

While all drill core sampled were fresh, there was a bias in drill collar location: all of the holes sampled were drilled in known ore zones, due to the fact that all holes drilled in the vicinity of the deposits were put there to test the viability of mineralization along strike from historic workings. We therefore cannot comment with certainty on the sedimentary mineralogy and geochemistry of the BIF, which is likely metamorphosed to at least middle greenschist facies across the entire basin (Painter and Groenewald, 2001).

Table 3.1 Randalls sample list

Name	Drill hole	Easting	Northing	Azimuth	Depth (m)
CB33-145	ICBD0033	421510	6560040	270	145
CB33-147.3	"	"	"	"	147.3
CB33-173.62	"	"	"	"	173.62
CB37-159	ICBD0037	421571	6560225	270	159
CB37-161.9	"	"	"	"	161.9
CB37-164.1	"	"	"	"	164.1
CB37-179.5	"	"	"	"	179.5
CB37-180	"	"	"	"	180
MX41-130.3	MXD041	423790	6561232	230	130.3
MX41-317	"	"	"	230	317
SC44-16	IGSCD044	424689	6565261	240	16
SC44-17	"	"	"	"	17
SC44-117	"	"	"	"	117
SC44-118	"	"	"	"	118
SC46-126	IGSCD046	424690	6565260	210	126

Figure 3.4 (opposite) A. Well preserved flame structures (bottom) and graded bedding (middle) in turbidite from the upper succession of the Belches Supersequence, Santa-Craze (pen for scale), drill hole IGSCD051. Mud-rich sections are now almost 100% chlorite (green color) with small (~1 mm or less) biotite porphyroblasts. Original shale fragments in sand-rich sections have also been converted to biotite. **B.** Typical interbedded mudstone (green) and laminated quartz-magnetite rock (white-dark gray) of the Santa Claus BIF member, Cock-Eyed Bob (drill hole ICBD0037). Large (1–3 mm) magnetite porphyroblasts (dark spots) pepper the mudstones. **C.** Same unit, but here the magnetite has been sulfidized to pyrrhotite (drill hole ICBD0037). Alternating quartz-pyrrhotite layers (white) and chlorite-pyrrhotite layers (green) are clearly visible. A quartz-chlorite vein truncates the layering near the top of the photo. **D.** Banded quartz-magnetite BIF from Santa-Craze (drill hole IGSCD051, wedge 1).

3.4.2 Microscopy & electron microprobe analysis

Numerous thin sections and polished mounts, representing all three deposits, were examined in detail using transmitted and reflected light microscopy. Scanning electron microscopy (SEM) was also used to supplement the transmitted and reflected light work with enhanced mineral identification capabilities. Two different SEMs were used: a FEI Quanta 600 MLA environmental (E) SEM and a Hitachi SU-70 field emission (FE) SEM. The latter machine is calibrated using standards, which allows for semi-quantitative mineral chemistry analysis. Both instruments are housed at the Central Science Laboratory (CSL), University of Tasmania.

Electron microprobe analyses of amphibole were also undertaken at the CSL, using a CAMECA SX100 equipped with 5 tunable wavelength-dispersive spectrometers, operating with beam energy of 15 keV, a beam current of 10 nÅ, and a beam diameter of 10 μm. The primary standard was the Smithsonian Kakanui hornblende (Jarosewich et al., 1980).

3.4.3 Zircon analyses

The methods of zircon separation and analysis used in this study are nearly identical to those used in Steadman et al. (2013), which were derived from Sack et al. (2011) and references therein. One sample of coarse grained sandstone from Santa-Craze (SC46-163) was selected for detrital zircon U-Pb geochronology. Approximately 200g of sample was crushed using a hydraulic crusher, then milled for 5–10 seconds in a chrome steel ring mill, or until the sample passed through a 400-μm sieve. Zircons were separated from the rest of the pulverized rock mass via panning; the total number of zircons found in this separate was about 50. These grains were then set in epoxy, and after the epoxy hardened, the mount was washed in an ultrasonic bath, dried for 12 hours, and placed in a sealed vacuum chamber until analysis.

Laser ablation-ICPMS instrumentation used for this study included a Resonetics M50 ablation cell and a 193 nm Coherent ArF gas-charged excimer laser microprobe, coupled to an Agilent 7500cs/ce quadrupole ICPMS at CODES (University of Tasmania). The primary zircon standard was 91500 (Weidenbeck et al., 1995), and secondary standards were TEMORA 1 (Black et al., 2003), GJ1 (Jackson et al., 2004), and Mud Tank (Black and Gulson, 1978). All reported ages (with one exception) are $^{207}Pb/^{206}Pb$ ages with no correction for common Pb. Data reduction was done according to the methods outlined in Black et al. (2003) and Paton et al. (2010), using the Isoplot software of Ludwig (2003).

3.4.4 LA-ICPMS trace element analyses

Eleven samples of banded iron formation were selected from drill cores representing all three deposits. A 2.54 cm-wide round piece of drill core was then taken for polished mount preparation. All laser ablation analyses of BIF sulfides and oxides were conducted at CODES, University of Tasmania, using a New Wave 193 nm Nd-YAG solid-state laser microprobe for sulfides, and a Coherent 193 nm ArF gas-charged excimer laser microprobe for oxides (this laser is the same as that used for zircon U-Pb work). The former instrument is coupled to an Agilent 7500 cs/ce quadrupole ICPMS, while the latter is connected to an Agilent 7700 quadrupole ICPMS. Detailed descriptions of the laser methods employed during this study can be found in Danyushevsky et al. (2011), Thomas et al. (2011), and Steadman et al. (2013). Data reduction was performed according to the standard procedures laid out in Longerich et al. (1996), using Fe as the internal standard element.

3.4.5 Sulfur isotopes

Thirteen powdered sulfide separates from sulfidized BIF (7 pyrrhotite, 4 arsenopyrite, and 2 pyrite) and 13 separates from 13 diagenetic pyrite nodules (one analysis per nodule) within black shale from the Lucky Bay gold prospect, ~10 km SW of Cock-Eyed Bob (Steadman et al., 2013), were obtained using

tungsten carbide drill bits of various diameters (300–1000 μm) and a foot pedal-operated dental drill. The latter were chosen as representatives of the regional basin S signature, given their early timing (late diagenesis) and their host rock's inferred correlation with the Black Flag Group, thought to underlie the Belches Basin at depths > 3 km (see section 3.2). Approximately 1 to 2 mg of each mineral was analyzed for $\delta^{34}S$ on an Isoprime100 mass spectrometer coupled to an Elementar varioPYROcube elemental analyzer at the Central Science Laboratory, University of Tasmania. Reference standards were NBS-123 (17.13‰), IAEA-SO-5 (0.75‰), NBS-127 (20.45‰), Soufre de Lacq (16.76‰) and IAEA-S-3 (–31.27‰). Error variations for the standards were within 0.3‰. Values are reported relative to the Canyon Diabolo Troilite (CDT).

Four additional in-situ S isotope analyses were performed on a single pyrite grain in a sample of sulfidized BIF from Cock-Eyed Bob via SHRIMP-SI at the Research School of Earth Sciences, Australian National University. Laser mounts like the ones used for LA-ICP-MS analyses were gold-coated and placed under vacuum for 24 hours prior to introduction into the sample chamber. Analyses were performed with a 10 kV and 2.5 nÅ Cs+ focused primary beam using an average spot size of 27 μm. Each spot was rastered for 30 seconds before analysis to remove surface impurities; total analysis time was approximately 6.5 minutes. The reference sulfide was Balmat pyrite ($\delta^{34}S$ = 15.1 ± 0.2 ‰; Crowe and Vaughan, 1996; Williford et al., 2011).

3.5 Results

3.5.1 Overview of BIF samples

In hand sample, 'unaltered' BIF (i.e., those with no sulfides) display mm-scale chert-magnetite laminae separated by massive green mudstone every 3–4 cm (Fig. 3.4B), as well as cm- to decimeter-thick intervals of banded quartz-magnetite rock (Fig. 3.4D). Euhedral magnetite porphyroblasts are readily visible in the massive mudstone layers, also (Fig. 3.4B). Sulfidized portions of the Randalls BIF preserve the original sedimentary banding in most cases, but the Fe-oxide mineralogy has been changed wholesale to Fe-sulfides (pyrrhotite), especially adjacent to quartz-chlorite-Fe carbonate veins (Fig. 3.4C); pyrrhotite is present in both chert and mudstone layers.

3.5.2 Petrographic and SEM description of major BIF minerals not exclusively related to ore

The following two sections are a series of detailed accounts of the minerals in these BIF, their relationships to each other and (where applicable) the gold ore. A paragentic chart graphically depicting the timing of each mineral is presented at the end of the second section (see 3.5.3 below).

Magnetite

In unmineralized BIF (i.e., those without gold and sulfides), magnetite is the earliest preserved non-silicate/non-carbonate mineral. Textures in some samples suggest hematitic precursors, but in most samples any inherited hematite crystal habits have been destroyed by recrystallization during metamorphism (see 'Discussion' for more on precursor BIF minerals). Magnetite occurs in two main styles: (1) banded magnetite intergrown with carbonate and/or silicate minerals (e.g., calcite, quartz, and chlorite; Fig. 3.5A); and (2) euhedral to subhedral porphyroblasts (Fig. 3.5B). The latter variety is particularly plentiful in chlorite-dominant BIF layers (iron 'metashale'; see Roberts et al., 2004). Magnetite porphyroblasts also core some amphibole rosettes.

In ore and the ore envelope, various stages of magnetite replacement by pyrrhotite, arsenopyrite, and/or pyrite are preserved in the BIF. Below are possible reactions suggested by Qian et al. (2010) and Corkhill and Vaughan (2009) that describe this process:

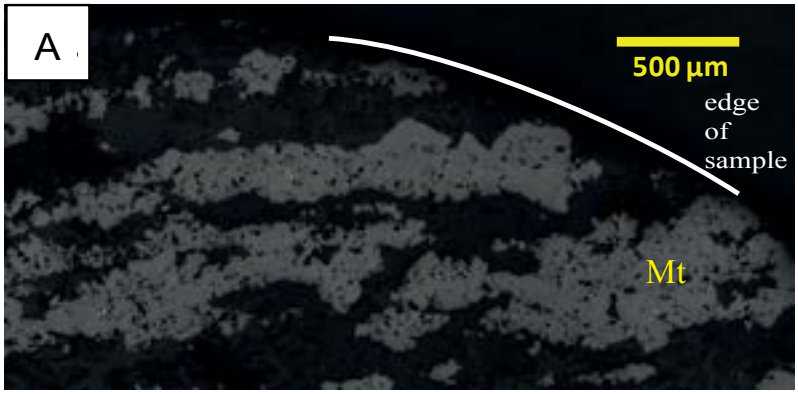
A
500 µm
edge
of
sample
Mt

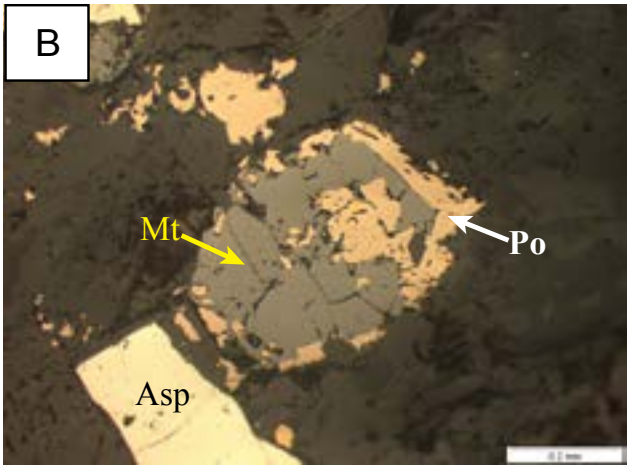
B
Mt
Po
Asp

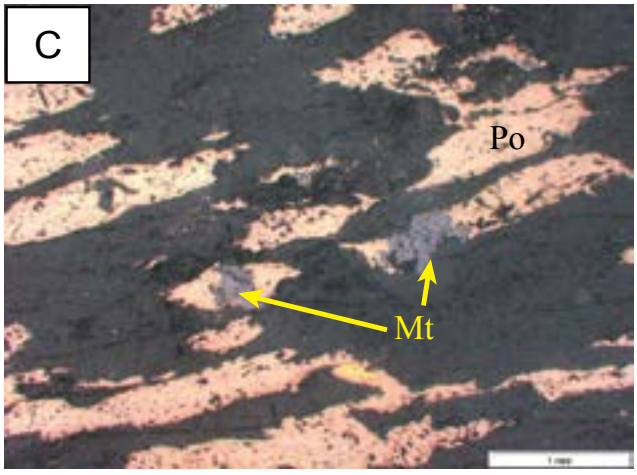
C
Po
Mt

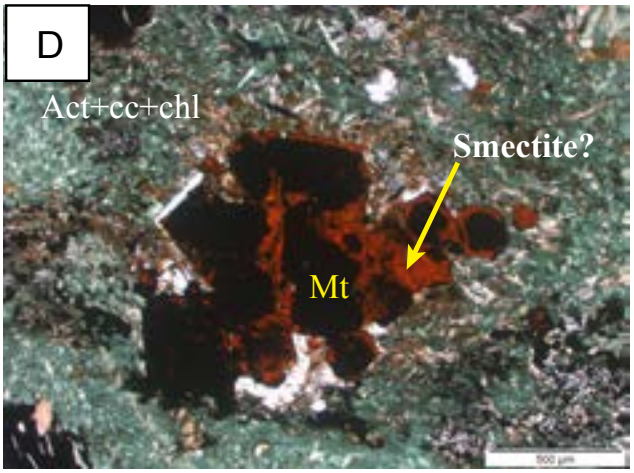
D
Act+cc+chl
Smectite?
Mt

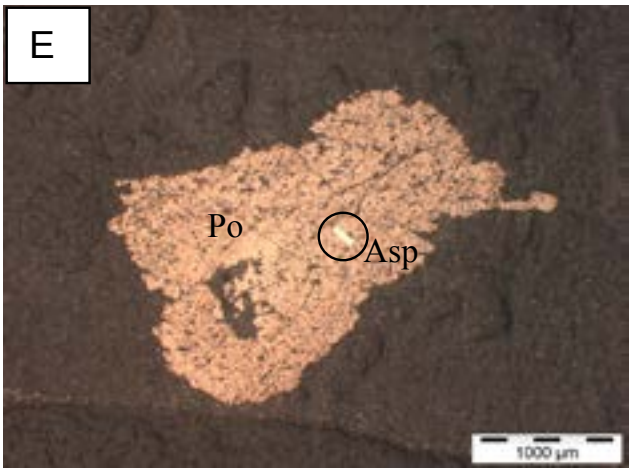
E
Po
Asp
1000 µm

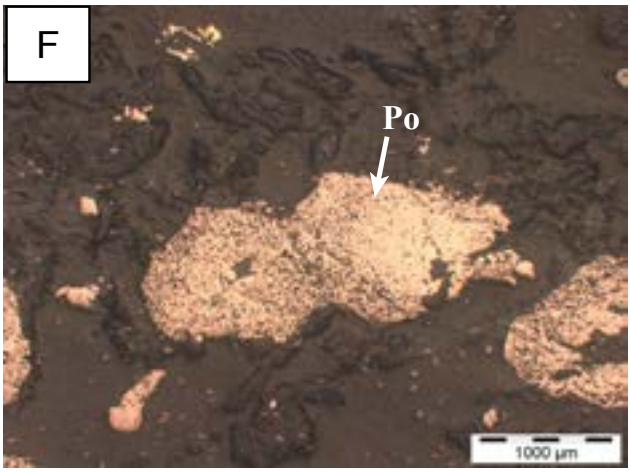
F
Po
1000 µm

$$Fe_3O_4 + 3HS^- + 3H^+ \Rightarrow 3FeS + 3H_2O + 1/2O_2 \quad (1)$$
$$Fe_3O_4 + 3H_2S + 3H_3AsO_3 \Rightarrow 3FeAsS + 5/2H_2O + 1/4O_2 \quad (2)$$
$$Fe_3O_4 + 6H_2S + O_2 \Rightarrow 3FeS_2 + 6H_2O \quad (3)$$

In surface samples from Santa-Craze (those <100 m deep), magnetite has been partly altered to hematite and iron oxyhydroxide, mainly near fractures.

Banded magnetite layers are intergrown with quartz, chlorite, carbonate, and apatite. In one banded magnetite sample from the Cock-Eyed Bob ore envelope, a grain of electrum was found in a fractured magnetite crystal. Small amounts of pyrrhotite were also found nearby, indicating this sample had been exposed to hydrothermal gold- and sulfur-bearing fluids, despite being on the fringe of the main Cock-Eyed Bob ore zone.

Within-ore magnetite from Cock-Eyed Bob (CB33-145A) is expressed as porphyroblast relics which are variably altered to a reddish-brown mineral with shrinkage cracks (Fig. 3.5D). SEM and probe investigations suggest the mineral is an Fe-rich clay belonging to the smectite group, possibly ferrosaponite [$Ca_{0.3}(Fe^{2+}, Mg, Fe^{3+})_3(Si, Al)_4O_{10}(OH)_2 \bullet 4H_2O$]. These porphyroblasts occur within domains of fine-grained actinolite needles and calcite with chlorite-rich layers.

Quartz

Quartz comprises the majority of the silicate-rich BIF bands in all samples, occurring as grains ~10 μm in diameter. It also occurs in the chlorite-rich bands, but in those areas the grains have cores containing very fine-grained chlorite or sericite. The cause of this texture is unclear. Quartz is also a major component of the ore zones, specifically in the form of quartz-carbonate-chlorite veins. These cross-cut and destroy the primary layering and mineralogy.

Chlorite

The dominant Fe-bearing silicate in the Randalls BIF is chlorite. Felted masses of chlorite ('Fe-metashale'; Roberts et al., 2004) lend a distinct green hue to hand samples and thin sections. Chlorite in the Randalls BIF is Fe-rich (ripidolite; average 41 wt % FeO at Santa-Craze; 36–40 wt % FeO at Maxwells; Roberts et al., 2004), and the literature suggests that it resulted from the metamorphism of precursor Fe-rich clay minerals, such as greenalite [$(Mg,Fe)_6Si_4O_{10}(OH)_8$; Krapež et al., 2003; Pecoits et al., 2009]. Chlorite breaks down to biotite and amphibole in areas where metamorphic temperatures and/or pressures exceeded terminal chlorite stability during prograde metamorphism (Newton et al., 1998).

Figure 3.5 (opposite) Photomicrographs of magnetite, pyrrhotite, arsenopyrite, and pyrite. **A.** Laminated magnetite-quartz BIF (CB37-159A). This is interpreted to be the earliest preserved mineralogical assemblage in the Santa Claus BIF member at Randalls. Note euhedral magnetite overgrowths on preexisting magnetite laminae. **B.** Magnetite porphyroblast partially destroyed and pseudomorphed by pyrrhotite, adjacent to an arsenopyrite grain (SC44-18). This is a clear indication that all magnetite was formed before S-rich fluids infiltrated the unit. **C.** Individual chlorite-rich BIF band with large 'streaks' of pyrrhotite aligned parallel to the dominant strain field (CB37-161.9). This texture is not common in the Randalls district, due to the relatively low-strain style of deformation that occurred in the Belches Basin. Two magnetite porphyroblasts are also present, in various stages of breakdown. **D.** Magnetite porphyroblasts in actinolite-calcite-chlorite domains, surrounded by a chlorite matrix (CB33-147.3). The magnetite porphyroblasts are altered to a brown-red clay mineral, possibly Fe-rich smectite. **E.** Large, anhedral 'blebby' pyrrhotite porphyroblast (CB37-179.5). This style of pyrrhotite is relatively common in certain sections of chlorite-rich BIF, where it overgrows the foliation, indicating a relatively late timing of formation. Note the small arsenopyrite crystal in the center of the porphyroblast. **F.** 'Blebby' pyrrhotite porphyroblast with hexagonal outline (CB37-180), indicating that it may be the high-temperature polymorph of pyrrhotite, which has hexagonal structure.

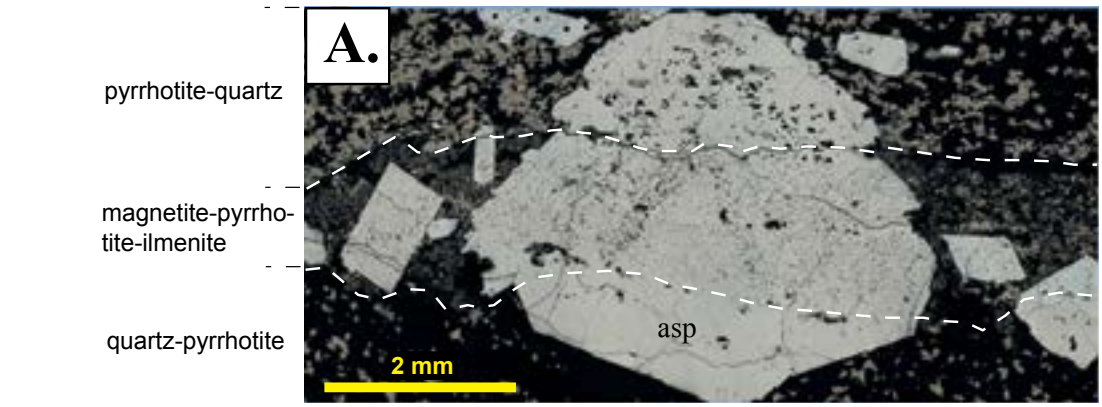
A.
pyrrhotite-quartz
magnetite-pyrrho-
tite-ilmenite
quartz-pyrrhotite
asp
2 mm

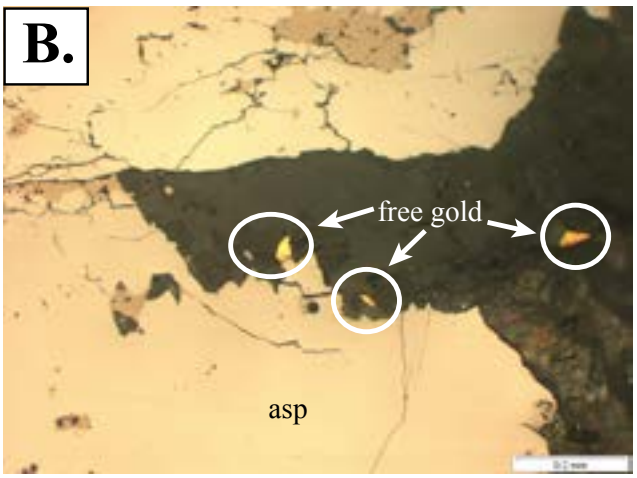
B.
free gold
asp

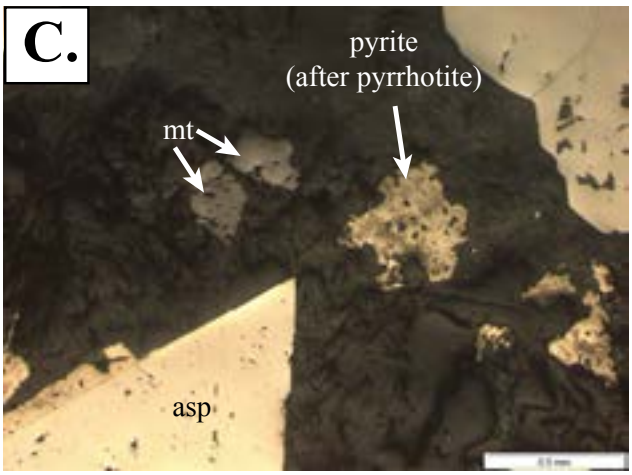
C.
pyrite
(after pyrrhotite)
mt
asp

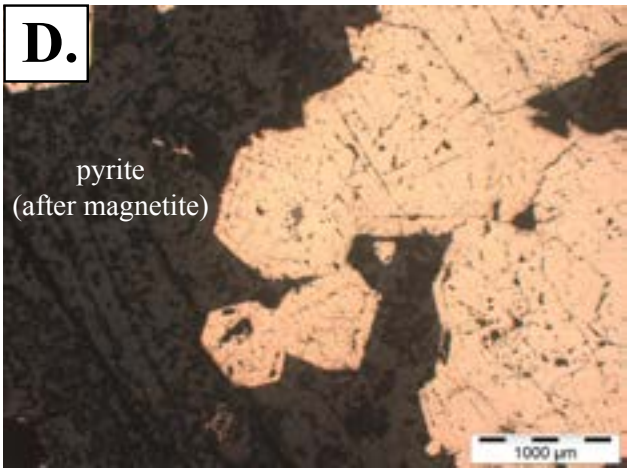
D.
pyrite
(after magnetite)
1000 µm

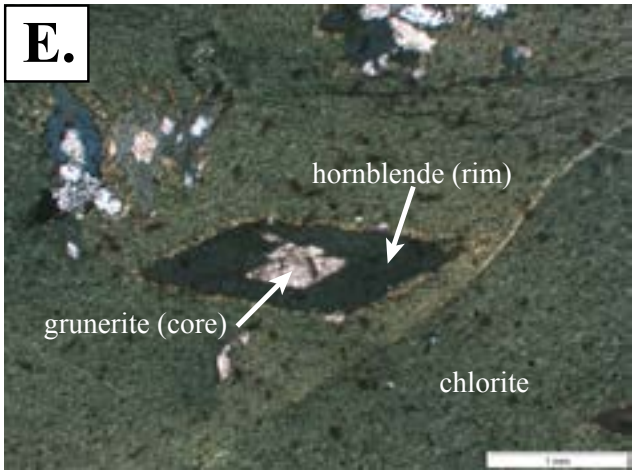
E.
hornblende (rim)
grunerite (core)
chlorite

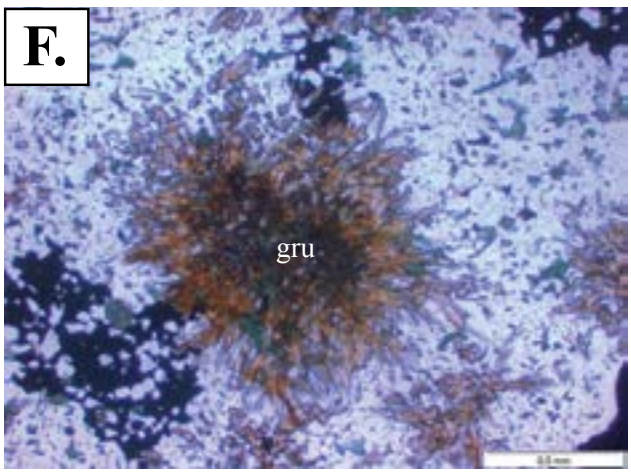
F.
gru

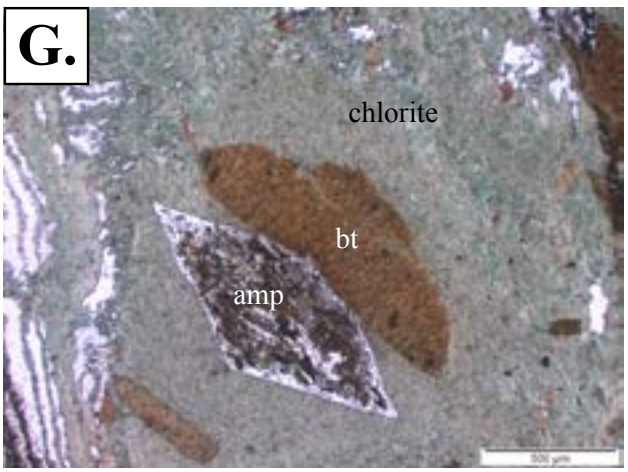
G.
chlorite
bt
amp

Amphibole

In unmineralized areas, at least three types of amphibole are present in the iron formations: grunerite, actinolite and hornblende ('blue-green' amphibole). Grunerite forms the cores to large (~2–5 mm) amphibole porphyroblasts in chlorite-rich bands, whereas hornblende forms the outer zones of these crystals (Fig. 3.5E). Both minerals are interpreted to be metamorphic products of chlorite. Grunerite also forms rosettes centered on magnetite or pyrrhotite grains (the latter has commonly replaced precursor magnetite in these instances; Fig. 3.5F). Other minerals in similar rosettes include chlorite and calcite, which are retrograde. Grunerite can be associated with chlorite, calcite, and siderite in chlorite-rich BIF samples; there, it forms rims around irregular chlorite grains, indicating that chlorite contributed to grunerite growth. Actinolite comprises irregular domains in chlorite-rich samples, where it is associated with calcite, magnetite, and grunerite. Most amphiboles are late in the prograde paragenesis, as they have replaced porphyroblastic magnetite, and some have been retrogressed to chlorite, quartz, and pyrrhotite (Fig. 3.5G).

The zoned grunerite-hornblende crystals in CB37-161.9 and CB37-173.62 are compositionally distinct: grunerite in the cores and in the rosettes contains ~31 wt % Fe and hornblende ~20 wt % Fe (ferro-tschermakite; Table 3.1).

Carbonate

Carbonate minerals in either mineralized or unmineralized Randalls BIF are relatively scarce (≤ 5% of all minerals in the unit). The major carbonate mineral in these rocks is calcite, which exists in three main forms: (1) as calcite or calcite-quartz veins cross-cutting original layering; (2) as part of the selvage surrounding grunerite rosettes; and (3) as ill-defined patches within chlorite- and pyrrhotite-rich BIF, where it has undergone partial replacement by siderite. Ankerite/ankerite-quartz veins also cross-cut layering in certain sections, particularly in ore zones.

Apatite

Apatite is not present in all observed BIF; however, apatite does occur as discontinuous micro-laminae in magnetite-rich BIF sections from the Cock-Eyed Bob ore envelope. The apatite laminae also contain monazite as intergrowths and inclusions. We interpret the laminated apatite to be an early (diagenetic?) phase, based on its association with the magnetite laminae. Apatite also exists as subhedral to euhedral grains in square-shaped domains composed of quartz, chlorite, and magnetite (Steadman, unpub. data).

Figure 3.6 (opposite) Photomicrographs continued. **A.** Extended-view image illustrating spatial relationships between arsenopyrite, pyrrhotite, and magnetite in the Santa Claus BIF member at Randalls (SC44-117). The large arsenopyrite crystal in the center of the images has overgrown three bands: (1) pyrrhotite-quartz (note inclusions of pyrrhotite in arsenopyrite); (2) magnetite-pyrrhotite-ilmenite (ubiquitous ilmenite grains in all arsenopyrite crystals); and (3) quartz-pyrrhotite. **B.** Free gold grains adjacent to a large (>5 mm) arsenopyrite megacryst (MX41-130.3B). Gold deportment at Randalls is dominantly elemental Au or electrum, and can be associated with either arsenopyrite or pyrrhotite. **C.** Surface BIF sample (~16 meters below current ground surface; SC44-16) illustrating pyrrhotite that has been resulfidized by SO_4-bearing groundwater. Magnetite and arsenopyrite remain unaffected. **D.** Pyrite after magnetite (note crystal shape and remnant magnetite at the core of the center grain; MX41-317). **E.** Amphibole porphyroblast in chlorite (after shale) layer, displaying characteristic compositional zoning (grunerite in the core, hornblende in the rim; CB33-173.62). The hornblende is ferro-tschermakite. Plane polarized light. **F.** Grunerite rosette, with a selvage of chlorite (SC44-118). Many rosettes are cored by magnetite, magnetite-pyrrhotite, or pyrrhotite. Plane polarized light. **G.** Retrogressed amphibole adjacent to a biotite porphyroblast, in a chlorite-rich BIF (CB33-145A). The amphibole is now quartz-chlorite-calcite, suggesting it was hornblende, originally.

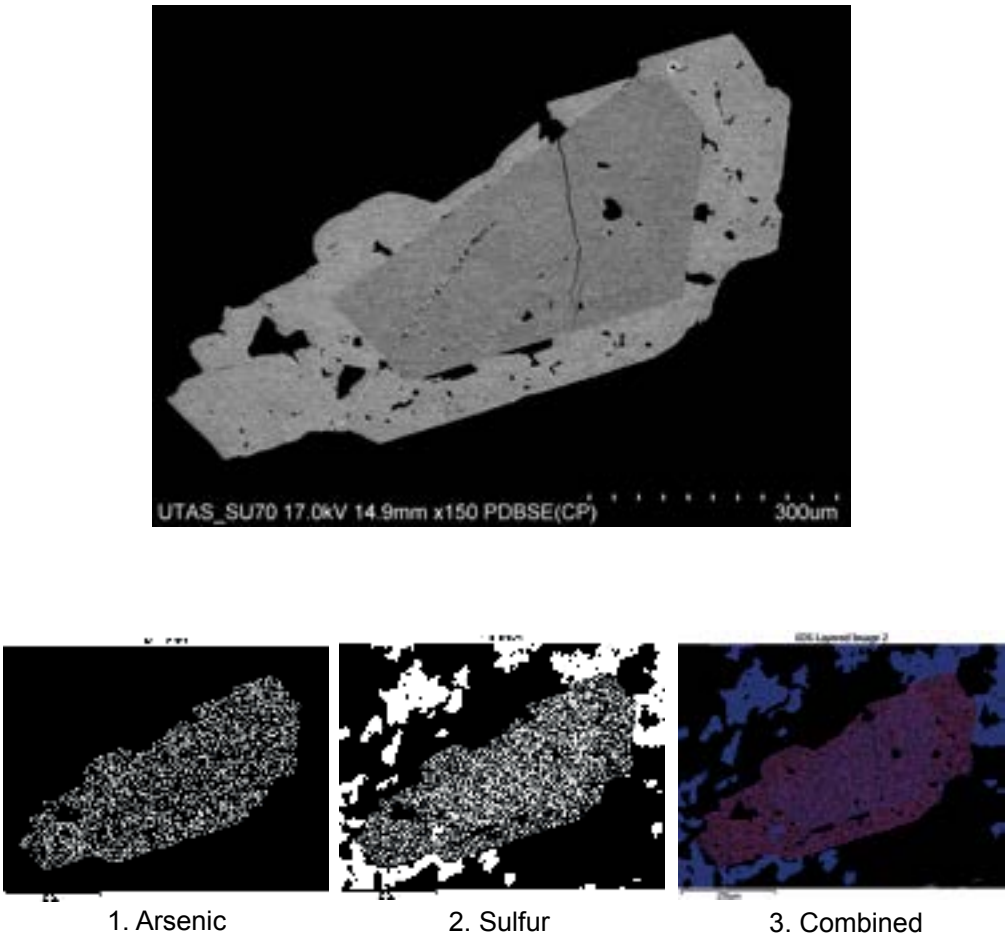

Figure 3.7 SEM scanning electron image and x-ray map showing As and S zonation in arsenopyrite from Santa-Craze (SC44-117). Both As and S vary by 1–2 wt % between the two zones of the crystal. Interestingly, the S zonation is more clearly defined than the As zonation, despite sulfur's lower atomic weight. The other bright spots on the S image are pyrrhotite crystals.

3.5.3 Petrographic and SEM description of major BIF minerals — Ore mineralogy

Pyrrhotite

Pyrrhotite typically pseudomorphs magnetite, (e.g., Fig 3.4B), yielding a euhedral appearance, which is unusual for this mineral (in deformed rocks, pyrrhotite is mainly aligned with the dominant foliation; Fig. 3.4C). In areas where magnetite has been consumed, small ilmenite grains that appear to have been exsolved from magnetite dot the samples in and around pyrrhotite or arsenopyrite crystals. Their long axes are generally oriented parallel to the principal foliation. Pyrrhotite also occurs as large 'blebs' with numerous matrix inclusions (Fig. 3.4E). Some of these blebs have distinct 'cubic' or hexagonal outlines (Fig. 3.4F), which suggests that they may be hexagonal pyrrhotite. Other blebs (as in Fig. 3.4E) that appear to be of the same generation have no defined shape, and have overgrown the preexisting foliation. In several samples, pyrrhotite has also replaced magnetite laminae; relict magnetite grains are common in these bands.

Pyrrhotite-bearing sections of the Randalls BIF are mainly associated with ore-grade gold mineralization (1.5 g/t Au cutoff). In one sample dominated by banded pyrrhotite-quartz/chlorite-carbonate (probably banded magnetite-quartz/chlorite-carbonate, originally), numerous grains of

electrum are concentrated in small domains within the pyrrhotite bands (see 'LA-ICPMS imaging' below). Small grains of chalcopyrite are associated with pyrrhotite in all samples, and some pyrrhotite grains appear to contain exsolved chalcopyrite. Like magnetite, some pyrrhotite crystals form the core to amphibole rosettes, suggesting the latter mineral formed at the expense of both magnetite and pyrrhotite. However, some pyrrhotite-cored amphibole rosettes have relict magnetite, indicating that magnetite was sulfidized by pyrrhotite before or during amphibole growth (Fig. 3.5F; opaques in photo are pyrrhotite).

Arsenopyrite

Arsenopyrite has overgrown magnetite and pyrrhotite and regularly transgresses the foliation (Fig. 3.5A). Arsenopyrite crystals in the Randalls BIF samples are characteristically megacrystic euhedra, and almost all of them are fractured. Inclusions of pyrrhotite are abundant, and in many samples pyrrhotite appears to have been resistant as the arsenopyrite grew around it (Fig. 3.5A); however, rare pyrrhotite veinlets cross-cut arsenopyrite in other samples, indicating a close timing relationship between these two minerals. Lesser amounts of magnetite are present as inclusions within arsenopyrite, but in one sample (SC44-117) ilmenite inclusions are ubiquitous (Fig. 3.5A). SEM analyses reveal two strongly chemically defined stages of arsenopyrite growth, most notably in terms of core-rim As and S variations (Fig. 3.7). A 'patchy' zonation of As and S is present in the interior regions of other crystals. Trace element concentrations in arsenopyrite mimic the major element zonation in some instances (see 'laser imaging' below). Free gold and/or electrum are commonly associated with arsenopyrite, either as inclusions or just outside arsenopyrite grains in the BIF matrix (Fig. 3.5B).

Pyrite

All preserved pyrite in the Randalls BIF is paragenetically late. Some pyrite is interpreted to be re-sulfidized pyrrhotite, especially in near-surface samples, whereas others appear to have partially replaced magnetite. The crystal shape of the former pyrite type mimics the surrounding pyrrhotite crystals (i.e., anhedral; see Fig. 3.5C), whereas pyrite-after-magnetite is euhedral to subhedral (ostensibly mimicking the precursor magnetite; Fig. 3.5D).

Gold

Nearly all gold at Randalls exists as native gold or electrum inclusions within quartz, carbonate, pyrrhotite, arsenopyrite, magnetite, and chlorite; the invisible gold content of magnetite, pyrrhotite, and arsenopyrite is negligible (max ~200 ppb; see section 3.5.3). Gold grains range in size from <1 to 30 μm, and exhibit a wide variety of shapes, from rounded to angular. Some occupy fractures in sulfide or oxide phases, whereas others exist alone in quartz or carbonate, typically near other sulfides or oxides. A paragenetic sequence chart for all minerals is shown in Figure 3.8.

3.5.4 U-Pb geochronology of detrital zircon from Belches Supersequence sandstone

Detrital zircons from SC46-163 vary greatly in size, shape and zonation, as revealed by cathodoluminescense (CL; Fig. 3.9A, 1–4), but these morphological differences did not seem to control which age group each zircon belonged to. Forty-four analyses on 44 zircons (one spot per grain) were obtained from SC46-163; of the 44, 22 were rejected from the data set for one or more reasons (e.g., high U, extensive Pb loss, high common Pb, or a combination of these). Such a high percentage of defective zircons per population is common for Archean samples due to their age, which facilitates more structural damage through U decay than younger zircons (Squire et al., 2010). The remaining 22 zircons that define the youngest valid age peak yielded a weighted mean age of 2646 ± 5 Ma (2σ; MSWD = 1.1), which is taken as the maximum age of deposition of SC46-163 and, by extension, the upper Belches

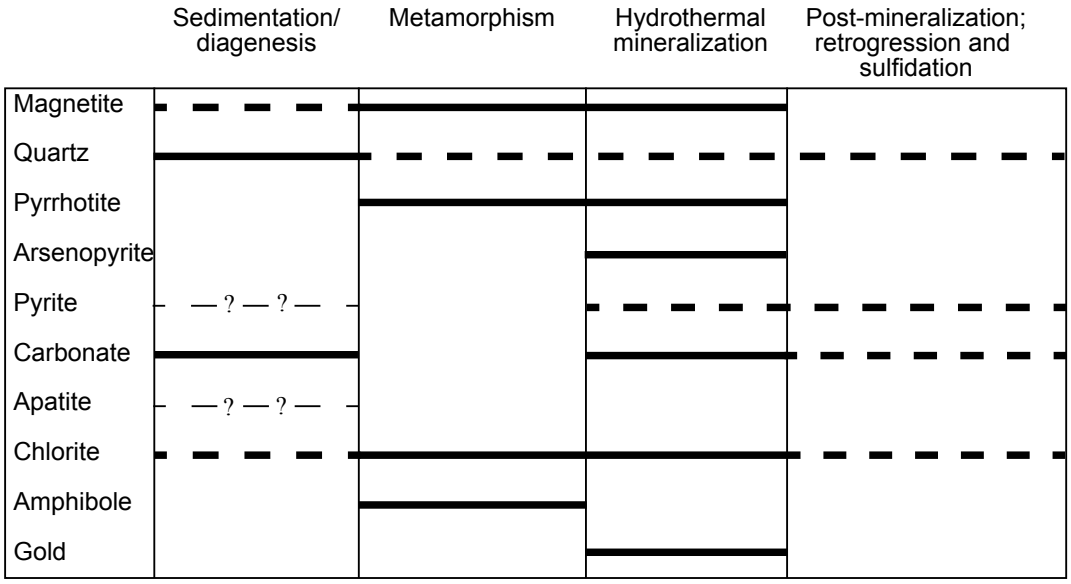

Figure 3.8 Paragenetic chart for minerals in the Santa Claus BIF member at Randalls. The post-mineralization box includes retrogression of prograde amphibole to chlorite-carbonate assemblages and sulfidation of magnetite and pyrrhotite to pyrite.

Supersequence. This result is significantly younger than the maximum depositional age of 2666±5 Ma (2σ; n = 48) determined by Krapež et al. (2000) for a sample of lower Belches sandstone south of the Randalls district (their 'KU-3'). That age was later revised to 2663±6 Ma (2σ) by Krapež and Pickard (2010). Individual detrital zircons from SC46-163 have fairly clustered ages, with none exceeding 2800 Ma and few younger than 2630 Ma, again unlike the results of lower Belches Supersequence samples analyzed by Krapež et al. (2000) and Squire et al. (2010). Zircons from SC46-163 with <2600 Ma ages are mostly high-U grains that have extensive Pb loss, indicating that their ages are not real. These have therefore been removed from our probability plot (Fig. 3.9B).

3.5.5 Trace element content of Randalls sulfides and oxides: Imaging

Two pyrrhotite and two arsenopyrite crystals, taken from all three Randalls deposits, were imaged to determine (1) their gold concentrations; (2) the presence or absence of any trace element zonation; and (3) any relationships between gold and other trace elements. Below are the results.

CB37-179.5 ('blebby' pyrrhotite)

LA-ICP-MS mapping of one of the large pyrrhotite 'blebs' in Cock-Eyed Bob sample CB37-179.5 revealed internal zonation with respect to Zn, Sb, Ag, Tl, Pb, Bi, and U, in that the rim is slightly more enriched in these elements than the core (Fig. 3.10). However, Ni, Co, and Se are uniformly distributed throughout the crystal. No Au is present within the pyrrhotite structure, and no free gold appears to be associated with this pyrrhotite, either. Cobalt is roughly an order of magnitude more abundant than Ni, which is atypical of pyrrhotite elsewhere at Randalls (see below).

CB37-164.1-C (laminated pyrrhotite with free gold/electrum)

Figure 3.11 contains an image of gold-bearing banded pyrrhotite-quartz-chlorite iron formation from the same drill hole and deposit as the previous image (Fig. 3.10). The laser map was run across parts of two separate pyrrhotite bands, with a chlorite-quartz band dividing them; only the upper pyrrhotite band contained the gold. While the specific trace elements present in pyrrhotite are nearly identical between the two pyrrhotite bands (apart from obvious differences in Au, Ag, and Te), the concentration

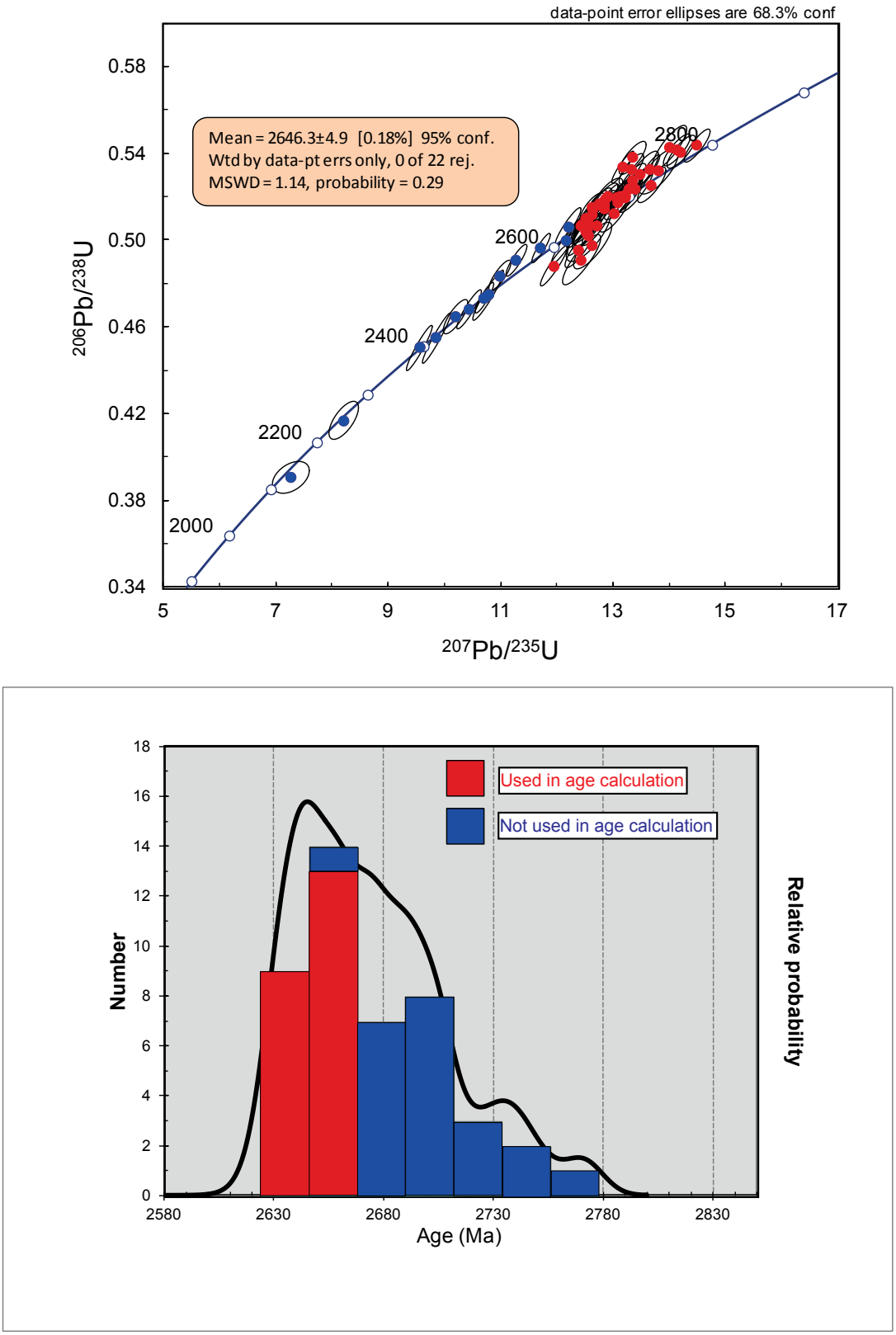

Figure 3.9 A. U-Pb concordia plot of detrital zircons from Santa-Craze. Red symbols indicate analyses used in the age calculation; blue symbols were other zircons/analyses not used for this purpose. The four photos in the bottom right hand portion of the diagram are CL images of selected analyzed zircons. **B.** Histogram of zircons in SC46-163 with little to no Pb loss. Zircons with 207/206 ages younger than ~2630 Ma had high U (>500 ppm), significant Pb loss, or both. This resulted in spuriously young ages for these crystals; consequently, these were not plotted.

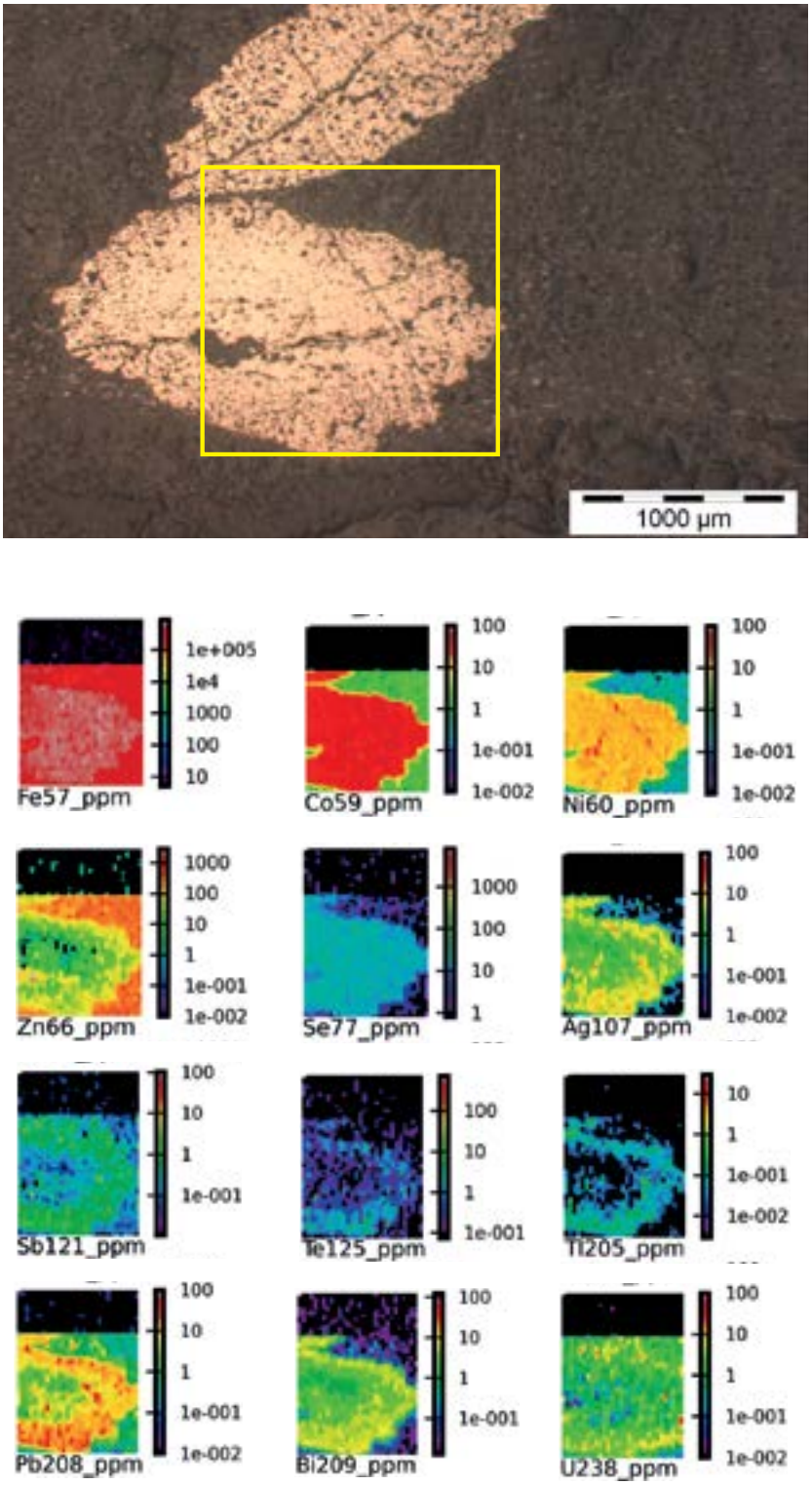

Figure 3.10 LA-ICP-MS image from CB37-179.5 (Cock-Eyed Bob), showing trace element contents and distribution in 'blebby' pyrrhotite. Cobalt, Ni, and Se are uniformly distributed throughout the crystal, but other elements display preferential concentration in different zones. Zinc, Ag, Sb, Te, Tl, Pb, Bi, and U are elevated in the rim of the pyrrhotite, whereas the core is relatively depleted in these elements.

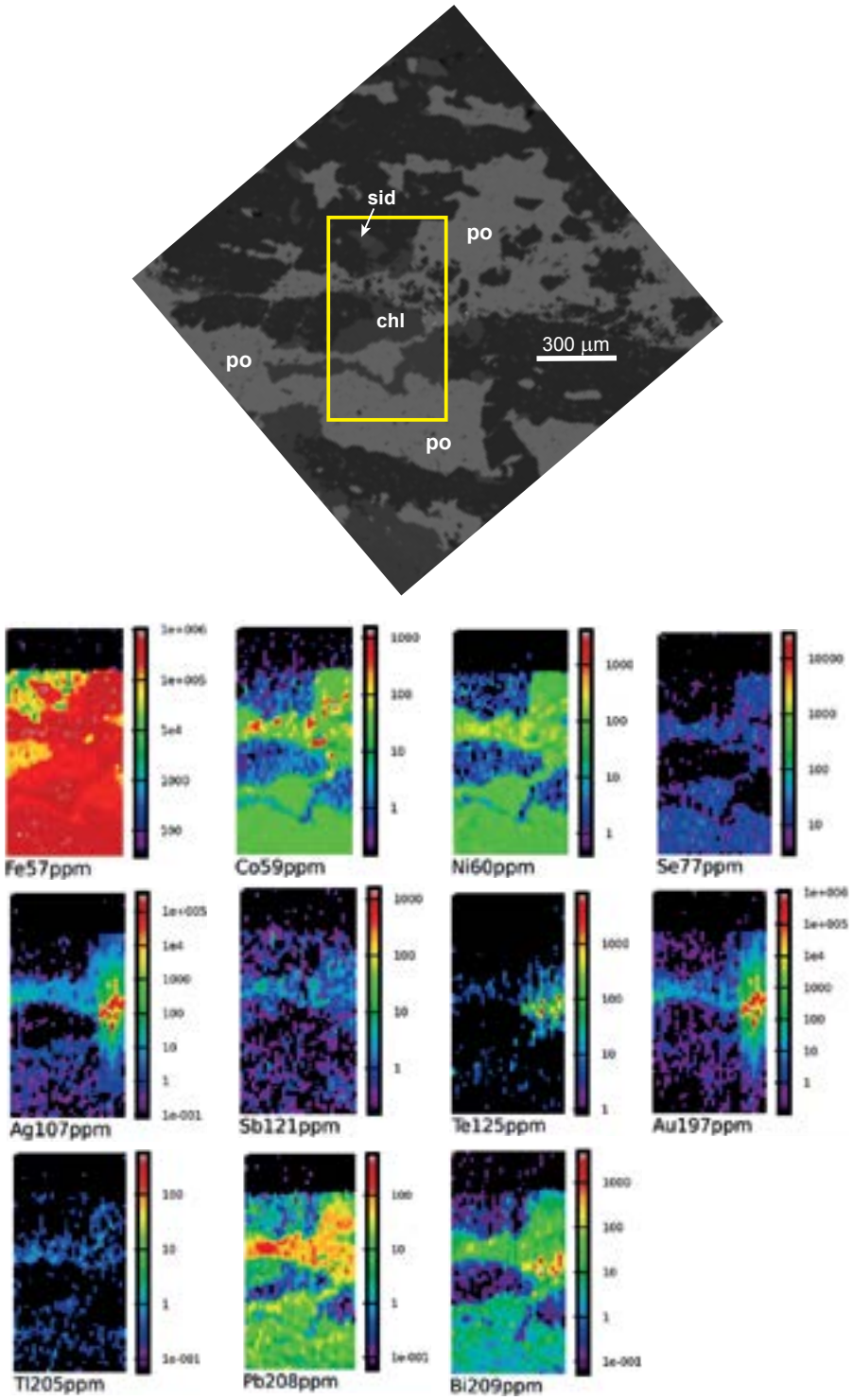

Figure 3.11 LA-ICP-MS image of pyrrhotite containing grains of gold/electrum (CB37-164.1-C; Cock-Eyed Bob). Pyrrhotite laminae are intergrown with chlorite-quartz laminae, along with minor siderite. There are multiple trace element associations in this sample: (1) all pyrrhotite in this image contains elevated Co, Ni, Se, Pb, and Bi; (2) Silver, Sb, and Tl, while present in both the upper and lower pyrrhotite bands, are clearly more enriched in the upper band, apparently due to the presence of free gold/electrum; (3) Tellurium and Bi are strongly enriched around the native Au/electrum inclusions; and (4) Lead and Bi concentrations between the two pyrrhotite bands vary by a factor of at least two, with the upper band having more Pb and Bi, presumably because of the presence of gold. Cobalt 'spikes' are also present, but SEM reconnaissance revealed no Co-bearing phases. The cause of these spikes remains unclear.

of these elements display a bimodal distribution: the upper, gold-bearing pyrrhotite band has higher overall Co, Ni, Sb, Pb, and Bi than the lower, Au-barren band. Selenium, as in the previous image, is uniformly distributed in both pyrrhotite bands, regardless of Au content. Spikes in Co concentrations (red-white dots) are noted in the upper band, but the cause of these anomalies is unclear, since no Co-bearing phase was identified by reflected light or scanning electron microscopy.

SC44-117 (Santa-Craze arsenopyrite)

Arsenopyrite from Santa-Craze has a Co-Ni-Sb-Te-Se±Au trace element signature. Antimony, Te, and Se are enriched in the cores but depleted in the rims, while Co and Ni are depleted in the cores but enriched in the rims (Fig. 3.12). Small amounts of Au appear to be dissolved in the structure of the crystal (0.1–0.5 ppm); a gold grain may be present on the edge of the arsenopyrite (green-blue dot on image, corresponding to ~10 ppm Au). Lead and Bi are excluded from the crystal structure of arsenopyrite, concentrating on the rims or along fractures, although the light blue colors on the Bi image indicate slight enrichment in the crystal. The zonation of Co and Ni in this crystal mimics that of As and S (compare Fig. 3.12 with Fig. 3.7), whereas Sb-Te-Se zonation is slightly different. Some pyrrhotite is present in this map, which contain Co, Ni, Pb, Bi, and a little Se.

MX41-130.3B (Maxwells arsenopyrite)

Trace-element systematics in arsenopyrite at Maxwells are mostly the same as those in arsenopyrite from Santa-Craze, with some exceptions (Figs 3.12 and 3.13). The key difference between the Maxwells grain and the one from Santa-Craze is the Mo-Te zonation. Individual bands of high Mo alternate with bands of relatively high Te in this arsenopyrite. Antimony seems to follow Mo in the upper portions of the crystal (near the edges), but unlike Mo, Sb is enriched throughout the rest of the grain. Co and Ni are present in the main portion of the arsenopyrite grain, albeit at low levels (~10 ppm), but higher values occur in the barely-developed rim on the lower right-hand side of the grain. This rim is also an area of relatively low Sb (~10 ppm vs. ~100 ppm in the interior). Like arsenopyrite from Santa-Craze, Pb and Bi are mostly excluded from the crystal structure, forming concentrated zones around the edges. Pyrrhotite and chalcopyrite inclusions are also present in this grain (the high Pb areas inside arsenopyrite and high Ni zones outside arsenopyrite). Dissolved Au in the arsenopyrite structure is close to the detection limit (0.1–0.5 ppm), but free gold appears to be associated with at least one of the pyrrhotite inclusions (areas of ~10 ppm Au in the middle of the arsenopyrite).

3.5.6 Quantitative multi-element LA-ICP-MS analyses of sulfides and oxides

Quantitative trace element analyses of pyrrhotite, magnetite, and arsenopyrite confirm the information acquired during LA-ICP-MS imaging. Magnetite in all forms (disseminated, laminated, or porphyroblastic) contains trace Mg (34–203 ppm), Ca (172–812 ppm), Al (1440–2000 ppm), Zn (27–46 ppm), Cr (26–123 ppm), Ti (817–2828 ppm), V (44–650 ppm), and Mn (107–144 ppm); all data in Table 3.2; also see Figure 3.14A. Nickel (2–4 ppm) and Co (~1 ppm) are anomalously low compared with Ni and Co contents of magnetite in the literature (e.g., Singoyi et al., 2006; Dupuis and Beaudoin, 2011).

Pyrrhotite has trace Ni (85–189 ppm), less Co (13–35 ppm), and also contains small amounts of Ag (0.23–1.51 ppm), Te (0.05–3 ppm), Pb (2–12 ppm), and Bi (1–10 ppm; Table 3.2, Fig. 3.14B). Gold is likewise very low (max 0.02 ppm), only rising above the detection limit where a free gold inclusion has been ablated down-hole.

Arsenopyrite from Randalls is strongly enriched in Te (up to 500 ppm in one analysis; average 30–145 ppm) but less so in Sb (50–111 ppm) and Se (21–33 ppm) compared to arsenopyrite in the literature (Thomas et al., 2011; Deol et al., 2012). Small amounts of Ag (0.03–2 ppm) and Au (0.1–0.2 ppm) are present. Cobalt concentrations (134–640 ppm) are an order of magnitude higher than Ni

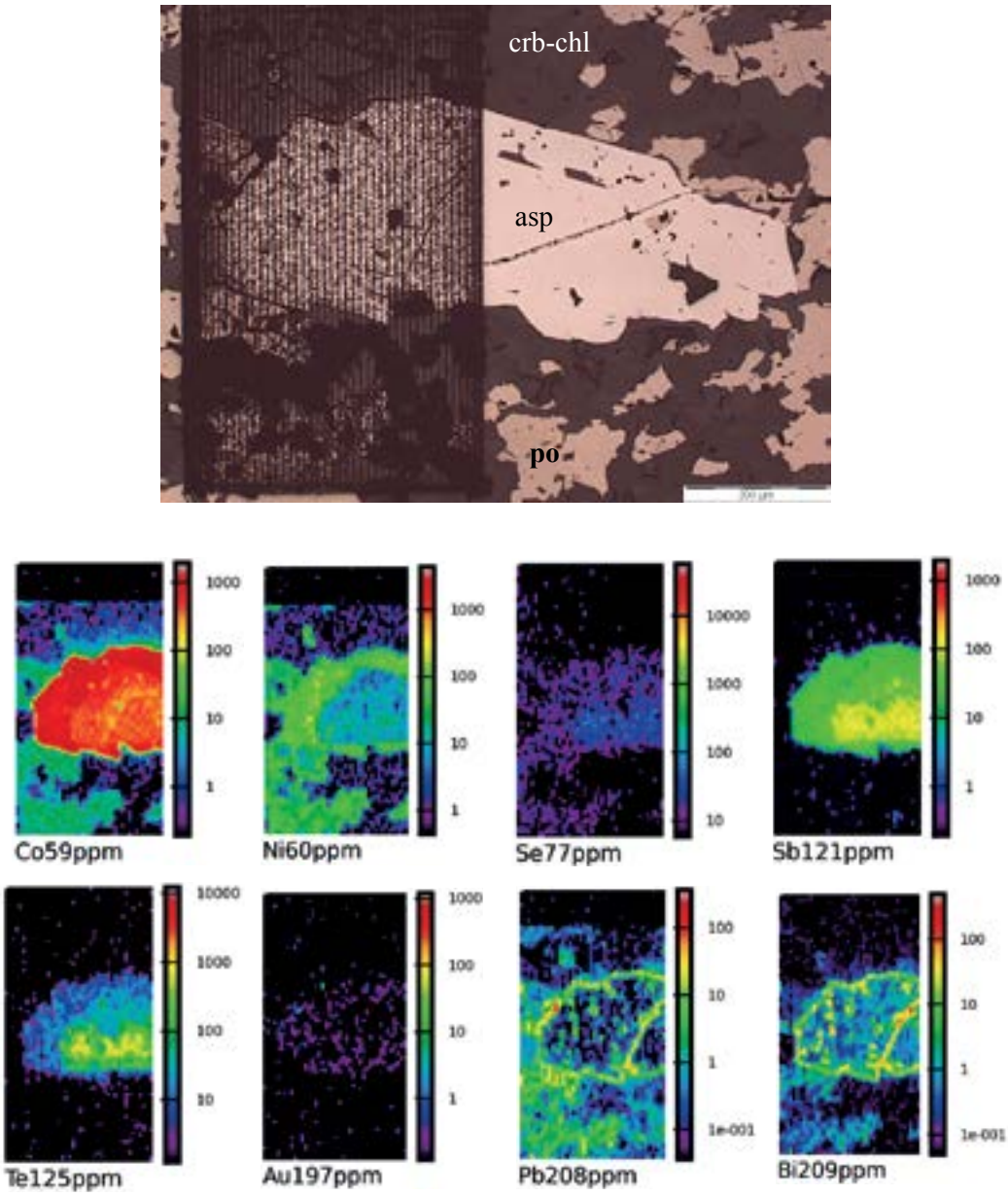

Figure 3.12 LA-ICP-MS image of arsenopyrite from SC44-117 (Santa-Craze). Like the pyrrhotite in Figure 9, element distribution varies within the crystal. Selenium, Sb, and Te define an early core, which is enveloped by a second phase containing siginificantly less Se, Sb, and Te, while also being poor in Co and Ni. In the rim of the crystal, Se, Sb, and Te concentrations continue to drop, which Co and Ni are an order of magnitude higher.

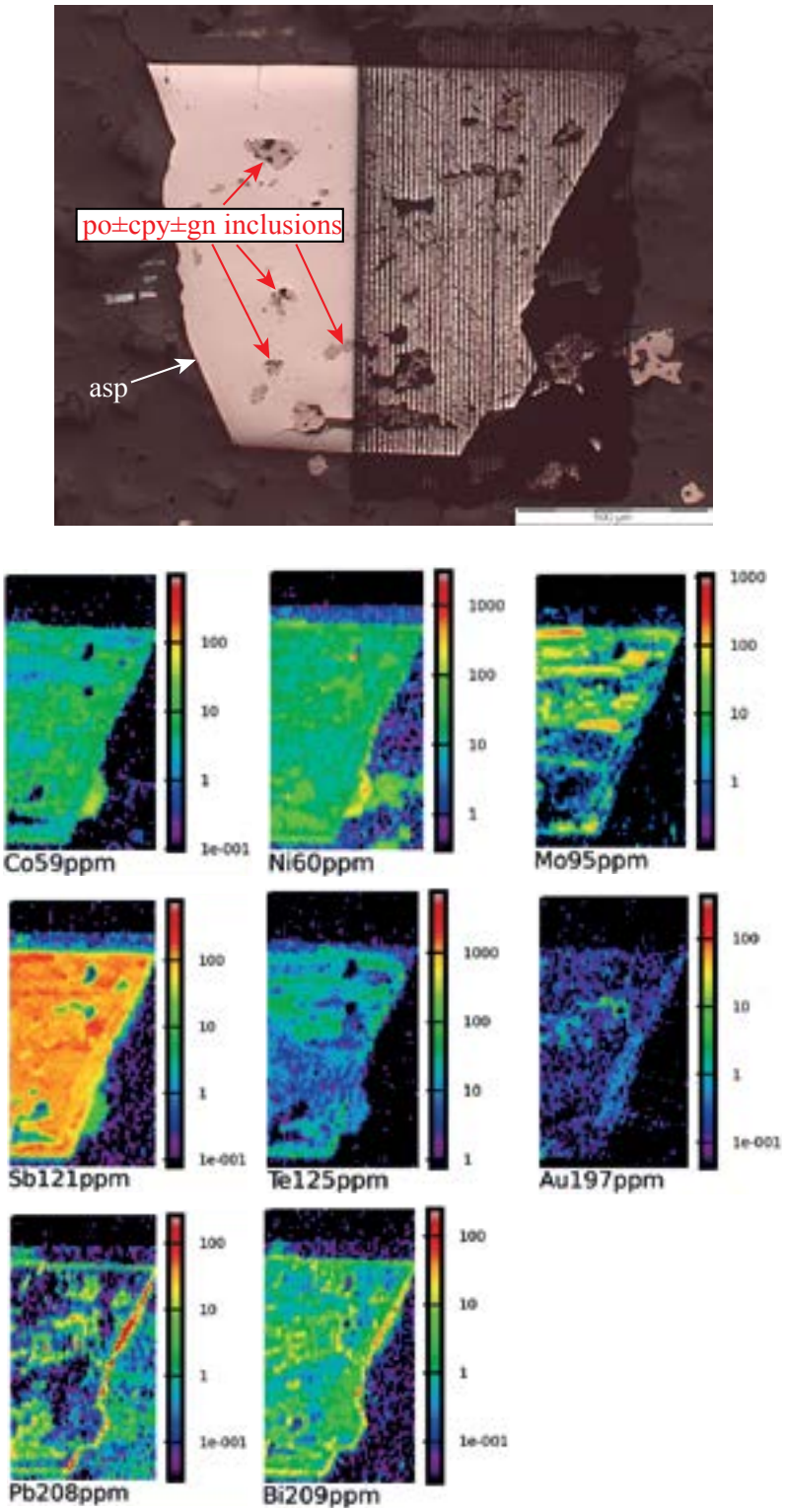

Figure 3.13 LA-ICP-MS image of arsenopyrite from MX41-130.3B (Maxwells). Unlike arsenopyrite from Santa-Craze, this grain exhibits well-defined zones of alternating Mo and Te enrichment, and does not contain as much Co and Ni. However, like the others, Pb and Bi are confined to the edges and fracture networks within the crystal. Gold in solid solution is present but negligible (~0.01 ppm). Antimony seems to follow Mo in some areas, but it is also widespread throughout. A rim has just started to develop on the right-hand side of the main crystal; this rim is enriched in Co and Ni but depleted in Sb and contains little to no Mo.

Table 3.2 Average trace element abundances (ppm) in magnetite, pyrrhotite, and arsenopyrite

Magnetite												
CB33-148.06	Mg	Al	Sc	Ti	V	Cr	Mn	Co	Ni	Zn	Ga	Ca
	203	1746	1	2828	650	123	107	1	4	27	13	812
CB37-164.1-A	Mg	Al	Sc	Ti	V	Cr	Mn	Co	Ni	Zn	Ga	Ca
	34	1443	1	817	44	26	137	1	2	31	11	172
CB37-164.1-B	Mg	Al	Sc	Ti	V	Cr	Mn	Co	Ni	Zn	Ga	Ca
	88	2015	2	2712	267	55	144	1	3	46	12	451
Pyrrhotite												
CB37-164.1-C	Co	Ni	Se	Ag	Sb	Te	Au	Pb	Bi			
	35	103	22	2	0	1	0.02	12	4			
MX41-130.3B	Co	Ni	Se	Ag	Sb	Te	Au	Pb	Bi			
	13	189	31	0.2	0.05	0.2	bdl	2	0.5			
SC44-117	Co	Ni	Se	Ag	Sb	Te	Au	Pb	Bi			
	18	85	18	1	0.03	0.05	bdl	5	1			
Arsenopyrite												
MX41-130.3B	Co	Ni	Se	Mo	Ag	Sb	Te	Au	Pb	Bi		
	134	45	33	15	0.03	111	30	0.2	1	3		
SC44-18	Co	Ni	Se	Mo	Ag	Sb	Te	Au	Pb	Bi		
	281	44	21	1	2	50	75	0.2	27	13		
SC44-117	Co	Ni	Se	Mo	Ag	Sb	Te	Au	Pb	Bi		
	640	28	26	2	0.2	69	145	0.1	2	5		

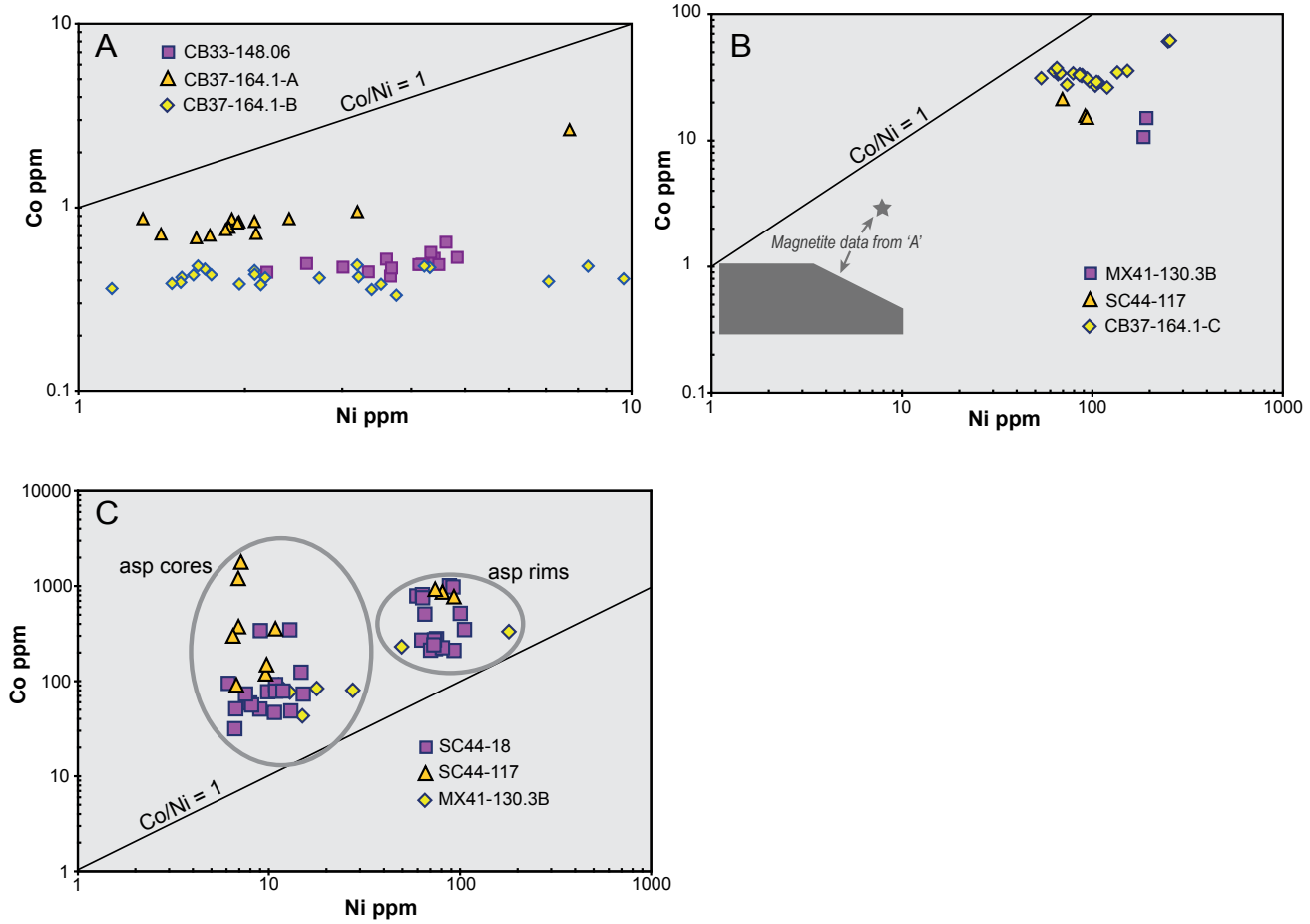

Figure 3.14 Cobalt-Nickel diagrams. **A.** Magnetite data. All magnetite data plot below the 1:1 line and define flat to slightly positive Co-Ni trends. The Co content of these magnetites is also not as variable as their Ni content. **B.** Pyrrhotite data. All pyrrhotite plot below the 1:1 line, suggesting sedimentary precursor minerals or lithologies. Pyrrhotite from CB37-179.5 (shown in Fig. 3.8) is not plotted on this diagram. Note that Co and Ni contents of pyrrhotite are roughly an order of magnitude greater than Co and Ni contents of magnetite. **C.** Arsenopyrite data. Cores and rims of arsenopyrite are clearly defined on this plot, but regardless of position, all data plot above the 1:1 line, indicating igneous affinities. Cobalt concentrations are commonly an order of magnitude greater than those in pyrrhotite.

(28–45 ppm), consistent with laser mapping data (Fig. 3.14C). Molybdenum varies between districts, with the highest values (15 ppm) recorded from Maxwells arsenopyrite, which ties in with Mo data in the LA-ICP-MS map of Figure 3.13. Lead and Bi values are low and variable, likely caused by very minor galena inclusions within arsenopyrite.

3.5.7 Sulfur isotopes

The $\delta^{34}S$ isotope values of all pyrite, pyrrhotite and arsenopyrite separates from Cock-Eyed Bob (n = 10), Maxwells (n = 4), and Santa-Craze (n = 3) exhibit a narrow range of –1.8 to 2.6‰, with a mean of 0.8‰ (n = 17; Fig. 3.15). Such a tight distribution, and its proximity to 0‰, is common for ore-stage sulfides in Archean orogenic Au deposits across the globe (Rye and Rye, 1974; McCuaig and Kerrich, 1998; Groves et al., 2003; Hodkiewicz et al., 2009). Pyrite has the smallest $\delta^{34}S$ spread (1.23 to 2.06‰; n = 6). All pyrrhotite analyses (except one) have negative $\delta^{34}S$ values, yielding a total range of –1.8 to 1.9‰ (n = 7). Arsenopyrite (n = 4) displays both positive and negative $\delta^{34}S$ values as well (SC44-16 yielded $\delta^{34}S$ = 2.6‰, while SC44-17 had $\delta^{34}S$ = –1.7‰).

The average $\delta^{34}S$ of thirteen pyrite nodules (one analysis per nodule) in black shales from four drill holes at Lucky Bay is 5.6‰, with a median of 5.4‰, both of which are significantly ^{34}S enriched compared to the 0.8‰ average for the Randalls sulfides. Most individual nodules had positive $\delta^{34}S$ between 2–10‰, with only one near-zero per mil analysis (0.5‰).

3.6 Discussion

3.6.1 Implications of detrital zircon U-Pb ages in the Belches Supersequence

The 2646 ± 5 Ma (2σ) age obtained via detrital zircon analyses of the Belches sandstone sample SC46-163 illustrates that a major difference in depositional age exists between the upper and lower sections of the Belches Supersequence. This age also serves as a minimum age for the Santa Claus member BIF, and is among the youngest published for all Late-Stage Basins. Krapež and Pickard (2010) attributed the presence of ≤2650 Ma depositional ages in other Late-Stage Basins north of the Belches Basin to nearby ~2650 Ma granites, but no such rocks are exposed in any part of the Belches Basin (Painter and Groenewald, 2001). Furthermore, a change in provenance between the lower and upper sections is apparent, as the probability density peak for SC46-163 is relatively narrow, with no 'old' zircons (i.e., >3000 Ma) as in the lower Belches (Krapež et al., 2000, 2008; Krapež and Pickard, 2010). These two features raise questions about the age and nature of other Late-Stage Basin successions in the Eastern Goldfields. Squire et al. (2010) sampled the Kurrawang Formation and the Pottarroo Turbidite in the Kalgoorlie Terrane (Fig. 3.1), and noted the difficulties in constraining depositional ages for these units (e.g., no cross-cutting intrusions and only an inferred disconformable contact between the older Early Merougil Group and the other two units). Both the Kurrawang Formation and the Pottarroo Turbidite were considered temporal equivalents to the Belches Supersequence by Squire et al. (2010), based on similarities in detritus composition and zircon ages. However, the age obtained in this study for the upper Belches is outside the margin of errors for both the Kurrawang and Pottarro Turbidite, and the very old zircons present in the Kurrawang Formation (i.e., >3500 Ma) are not present in our sample of upper Belches material. Our work indicates that Late-Stage Basin sedimentation was continuous in the Belches Basin to at least ~2650 Ma, which places constraints on the timing of gold mineralization (and metamorphism?) at Randalls.

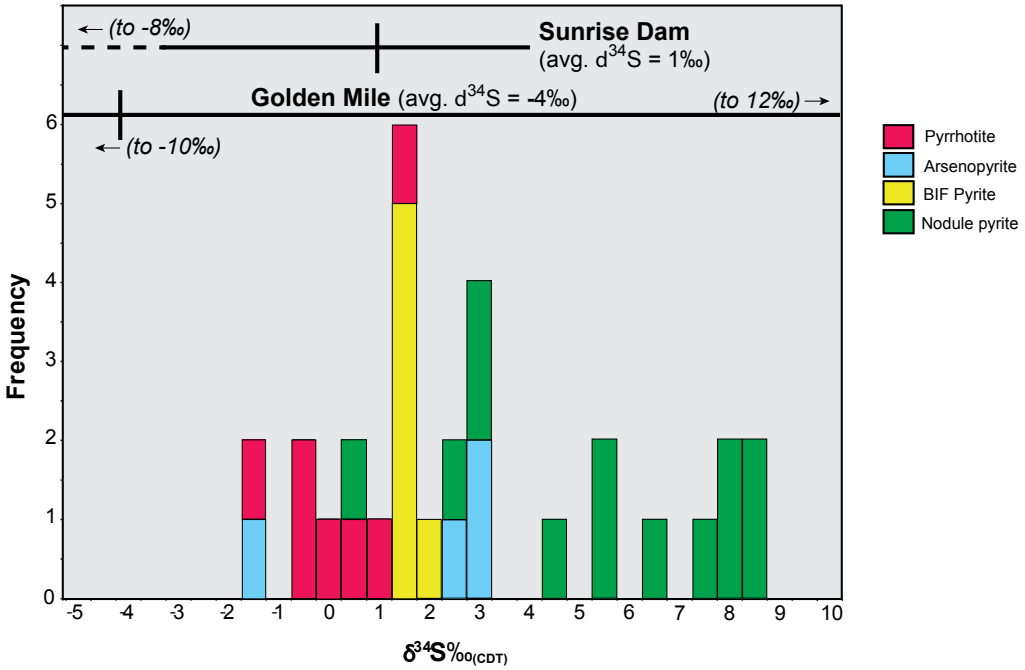

Figure 3.15 Sulfur isotope histogram. Golden Mile and Sunrise Dam data from Hodkiewicz et al. (2009).

3.6.2 Precursor BIF minerals and lithology at Randalls

Magnetite is the earliest preserved Fe-bearing phase in the BIF paragenesis at Randalls, but Krapež et al. (2008) suggest that siderite was the primary Fe phase before it was replaced by magnetite. They base this on analogy with Hamersley BIF textures, where magnetite has clearly replaced not only siderite but also hematite, both of which formed during early diagenesis (Krapež et al., 2003; Ayres, 1972; Morris, 1980; Pecoits et al., 2009). Magnetite-after-siderite textures do not exist in the Randalls BIF; instead, siderite-after-calcite is present in some samples from Cock-Eyed Bob, as described earlier, and individual grains of siderite occur within pyrrhotite-chlorite-quartz laminae, mainly intergrown with quartz and chlorite.

Krapež et al. (2008) also surmise that many so-called banded iron formations of Archean and Proterozoic age are actually metamorphosed sideritic shales, given the presumed widespread availability of siderite (i.e., reduced assemblages) in the global ocean during the Precambrian Era. While this may indeed be the case at many Precambrian BIF localities, this argument is unclear for Randalls. Randalls BIF magnetite lacks carbonate replacement textures, but on the other hand, one possible origin for ferric calc-silicates is a carbonate + silica prograde metamorphic reaction (e.g., Klein, 1973). We propose that magnetite was precipitated during late diagenesis/burial metamorphism, likely forming from $Fe(OH)_3$ or hematite (by analogy with Bekker et al., 2010), and was recrystallized during metamorphism associated with granite intrusion ca. 2650 Ma. The magnetite porphyroblasts in chlorite-rich sections would have also likely grown at this time, followed by grunerite.

3.6.3 Ore stage BIF minerals and lithology at Randalls

Phillips et al. (1984) described sulfide replacement textures in BIF from sites in Australia and southern Africa, and concluded that replacement of magnetite or hematite by pyrite or pyrrhotite (i.e., sulfidation) was the dominant method of gold precipitation in those deposits because it destabilized Au-thiocomplexes in the ore fluids. Their observations and proposed model were later supported by other researchers in North America (e.g., Macdonald and Fyon, 1986, following on from Macdonald, 1983) and, more recently, in India (Ajjanahalli; Kolb et al., 2004), South Africa (Hammond and Moore, 2006), and Madagascar (Andrianjakavah et al., 2007). Our work also reinforces the conclusions of Phillips et al. (1984), with textures like those seen in CB38-159.5 (pyrrhotite after magnetite) and SC44-18

(pyrrhotite after magnetite) defining a clear paragenetic sequence for this process. In the former example, micro-inclusions of electrum and nano-inclusions of precious-metal tellurides are present in pyrrhotite or in silicates.

3.6.4 Significance of oxide and sulfide trace element chemistry; elements associated with gold

Magnetite

Magnetite at Randalls is very low in Ni (Figs 3.13B, 3.14A; Table 3.2) compared to BIF from other localities (Dupuis and Beaudoin, 2011). Nickel contents of BIF have been used to track changes in atmospheric oxygen through geologic time (Konhauser et al., 2009), implying that most BIF (especially Archean examples) have high Ni. This feature is presumably related to the erosion of voluminous Ni-rich tholeiite, olivine-rich basalt, and/or komatiite, all three of which were abundantly generated in the Archean due to elevated mantle temperatures (Berry et al., 2008; Barley et al., 1998). Komatiites and Ni-rich tholeiites are widepsread in the Eastern Goldfields Superterrane, but no such lithologies are currently present at the surface near Randalls. The low Ni content of the Randalls magnetite suggests that komatiites and/or Ni-rich tholeiites were either not exposed proximal to the site of BIF deposition, or they had been eroded before deposition of BIF commenced. Additionally, if Krapez et al.'s (2008) contention about the origins of some Precambrian BIF is accurate (i.e., that they are metamorphosed sideritic shales and thus not anomalously high in Ni), this may also help explain why magnetite in the Randalls BIF is so Ni-poor.

Pyrrhotite

Pyrrhotite trace element characteristics at Randalls are similar to pyrrhotite from other sediment-hosted orogenic gold systems (e.g., high Co and Ni with Co/Ni < 1; elevated Ag, Te, Pb, and Bi; and little to no Au in solution; Large et al., 2007; Thomas et al., 2011), but overall the concentrations of these elements are lower at Randalls than elsewhere (e.g., pyrrhotite from Sukhoi Log [n = 24] and Bendigo [n = 63] contain mean Ni values > 500 ppm and mean Co values > 40 ppm, whereas Randalls pyrrhotite averages <200 ppm Ni and 30 ppm Co [n = 29]). The absence of early (syn-sedimentary or diagenetic) pyrite in the BIF precludes investigation of the pyrite-to-pyrrhotite metamorphic reaction, a common feature in orogenic gold deposits (Large et al., 2007; Thomas et al., 2011; Tomkins 2010, 2013; Gaboury, 2013). However, nearly all pyrrhotite analyzed in this study plot beneath the 1:1 line in Co-Ni space (Fig. 3.14B). This is a characteristic of pyrrhotites that have grown at the expense of pyrites in shales (Large et al., 2007; Thomas et al., 2011), indicating that these pyrrhotites have replaced pre-existing minerals of sedimentary origin (i.e., conversion of diagenetic pyrite or magnetite to pyrrhotite during contact metamorphism). The only pyrrhotites that do not exhibit this behavior are the 'blebs' in CB37-179.5, which have an order of magnitude more Co than Ni (Fig. 3.10). These overgrow the pre-existing foliation and are thus interpreted to be post-kinematic. Pyrrhotites in other styles of deposits globally display very different characteristics: for example, Co and Ni data in pyrrhotites from the Flin Flon VHMS deposit, Canada, have no preferred trend on a standard bivariate plot (Rae and Davidson, unpub. data, 2001), while the same elements in pyrrhotites from Norilsk and the Bushveld Complex display characteristics similar to those of sediment-hosted gold deposits, despite having a purely magmatic genesis (D. Hutchinson, unpub. data, 2011). In light of these data, conclusions about ore-forming processes that rely solely on pyrrhotite trace element studies must be regarded with caution.

Arsenopyrite

Trace element studies of arsenopyrite in orogenic gold systems are few compared to trace element studies

on pyrite, likely due to the latter's more common occurrence in such deposits and its typically close association with gold. However, three recent studies (Morey et al., 2008; Sung et al., 2009; Deol et al., 2012) on arsenopyrite from several different orogenic gold districts have provided useful information about some aspects of the mineral's geochemical characteristics, which in turn have helped us constrain interpretations of our arsenopyrite data.

One of the most noticeable differences between arsenopyrite in the earlier studies and arsenopyrite at Randalls is our finding of a lack of 'invisible' gold (gold dissolved in the mineral structure). Arsenopyrite studied by Morey et al. (2008) contained several ppm Au; arsenopyrite analyzed by Sung et al. (2009) had very high levels of invisible gold (up to 5767 ppm); and arsenopyrite studied by Deol et al. (2012) had invisible gold contents ranging from 0.3–10 ppm. By contrast, maximum dissolved Au in arsenopyrite from the Randalls deposits is 1.6 ppm, with an average of 0.13 ppm (Table 3.2); the overwhelming gold expression in the Randalls district is both as inclusions of native gold or electrum. This feature becomes more intriguing considering the similarity in major element zonation between Randalls arsenopyrites and those from the Yilgarn Craton orogenic gold districts studied by Morey et al. (2008) and Sung et al. (2009). Three possible explanations for the lower amounts of invisible gold at Randalls are (1) arsenopyrite formed during the later stages of gold deposition, such that the ore-forming fluids were low in Au; (2) gold deposition occurred after arsenopyrite crystallization, or (3) native gold and arsenopyrite crystallized simultaneously (cf. Cathelineau et al., 1989). Alternatively, since gold solubility in arsenopyrite apparently decreases with increasing temperature (Cathelineau et al., 1989; Wagner et al., 2007; Morey et al., 2008), the relative lack of 'invisible' gold in the Randalls arsenopyrites may indicate that temperatures were sufficiently high to exsolve most of the gold originally held within the arsenopyrite crystal structure. Had this happened in the Randalls district, other trace elements would likely have been flushed out as well (Morey et al., 2008), and the fact that this apparently did not occur (Figs 3.11, 3.12) suggests that temperatures were either below levels that would lead to significant diffusion of trace metals (including gold) out of arsenopyrite, or that one or more of the three scenarios above more accurately describe conditions at the site of ore deposition.

3.6.5 Sulfide sulfur sources

Ore-related pyrites from orogenic gold deposits in the Eastern Goldfields Superterrane typically have mean $\delta^{34}S$ values between –4 and +4 ‰ (Hodkiewicz et al., 2009, and references therein). Our very small sample set for deeper Belches Basin sedimentary (i.e., Black Flag Group) pyrite (n = 13; Steadman, unpub. data) indicates that if these sediment sources had been leached and formed the sole S source under reducing conditions, the ore deposits would have $\delta^{34}S$ ~5–6‰; this is not the case (Randalls BIF pyrite has $\delta^{34}S$ of 1.2–2.0 ‰, n = 6).

Studies on the $\delta^{34}S$ characteristics of ore-related pyrrhotite and/or arsenopyrite in the Eastern Goldfields or elsewhere in the world are not as numerous as pyrite studies, but those published (Arias et al., 1998; Palin and Xu, 2000; Wagner et al., 2004; Neumayr et al., 2008) contain valuable information about the redox state of the fluid(s) that deposited gold and other trace metals (e.g., Ag, Bi, Te, Pb, and Sb) and provide a more complete picture of the mineralizing system in orogenic and other gold deposits. The redox state of orogenic fluids is very important, as it can control sulfide $\delta^{34}S$ values (e.g., Hodkiewicz et al., 2009; Neumayr et al., 2008). However, our pyrrhotite-stable assemblages indicate that the $\delta^{34}S$ ratio of sulfides in the Randalls BIF is isotopically heavier than the $\delta^{34}S$ of sulfur in the fluid (i.e., $\delta^{34}S_{po} \sim \delta^{34}S \geq S$), following the relationships established between redox state and $\delta^{34}S_{sulfide}$ by Ohmoto (1972) and later works.

Arias et al.'s (1998) argument that pyrrhotite formation from metamorphically-induced pyrite desulfurization can lead to an isotopically heavy sulfur source in the residual fluid is particularly relevant to this paper, in that we are attempting to test a sulfur link between diagenetic pyrite in the upper Black Flag Group (which underlies the Randalls district at depth) and ore-associated pyrrhotite and

arsenopyrite in the Santa Claus member BIF. The near-zero per mil $\delta^{34}S$ values of pyrrhotite, pyrite (after magnetite), and arsenopyrite in the mineralized BIF at Randalls may reflect pyrite conversion processes similar to those described for the Penedela zone in Spain by Arias et al. (1998), but the average $\delta^{34}S$ of 5.6 ‰ in the diagenetic pyrite nodules from Lucky Bay suggests that the sulfur in the Randalls gold deposits likely came from some other source. This conclusion is analogous to that of Arias et al. (1998) for the ore-stage pyrite in their study, which had $\delta^{34}S$ values several per mil heavier than both diagenetic pyrite and the pyrrhotite that formed from the desulfurization of this pyrite in the surrounding country rock. If the sulfur source of the Lucky Bay diagenetic pyrite nodules and the BIF sulfides was the same, we would expect the average $\delta^{34}S$ values of these minerals to also be the same.

Three possible scenarios arise to account for the significant difference between the two averages: (1) the data set from Randalls is small (n = 13 for Black Flag Group shale, n = 6 for BIF pyrite), and so the average of these analyses may not be fully representative of the district $\delta^{34}S$ average, or the average of black shales in the Yilgarn Craton; (2) the $\delta^{34}S$ signal from the Lucky Bay black shale sequence might have mixed with a magmatic sulfur signal en route to the BIF horizons higher in the stratigraphy, causing the shift to less positive values; and (3) the near-zero per mil $\delta^{34}S$ average at Randalls may simply be due to the fact that the sulfur source there was magmatic or mantle-derived. Mantle and non-arc magmatic sulfur through time have $\delta^{34}S$ of zero per mil (Ohmoto, 1972; Ohmoto and Rye, 1979), which has led to the belief that most sulfides in reduced fluids with $\delta^{34}S$ ~0‰ have a significant component of mantle or magmatic sulfur in their overall sulfur budget.

Variation in $\delta^{34}S$ over short stratigraphic distances occurs at Santa-Craze, as evidenced by the values of arsenopyrite from SC44-16 and SC44-17, which are only 1 meter apart in the same drill hole. The change in $\delta^{34}S$ is significant (~4–5‰), and could be accounted for by different amounts of S from more than one source.

It is clear that further work on the $\delta^{34}S$ systematics of the region is needed before $\delta^{34}S$ can provide an unambiguous indicator of the S source in the Randalls BIF-Au ores. On the basis of our data to date, an origin for the S solely by leaching the deep-seated Black Flag Group sediment sulfur is not likely.

3.6.6 Source of gold and arsenic for Randalls deposits

Modeling of mafic and sedimentary bulk chemistries under varying P-T and redox conditions by Tomkins (2010) illustrates that carbonaceous sediments with disseminated pyrite are an ideal source rock for orogenic gold deposits. Mafic igneous lithologies can also be source rocks, but these are less efficient at forming a deposit than the former, despite their greater volumes in the rock record. Mafic lithologies produce one to two orders of magnitude less H_2S than their sedimentary counterparts during metamorphism, according to Tomkins (2010). As emphasized by Large et al. (2011), mafic igneous lithologies are not good source rocks for As; in fact, black shales are the only crustal rocks which are significant sources for both Au and As. Steadman et al. (2013) undertook a geochemical study of pyrite nodules from black shale belonging to the Neoarchean upper Black Flag Group of Squire et al. (2010). These nodules are enriched (relative to other pyrite types in the same samples) in a suite of trace elements [Co, Ni, Cu, As, Ag, Sb, Te, Au, Pb, and Bi] characteristic of diagenetic pyrite (Large et al., 2007; 2009; Thomas et al., 2011). Nodule-bedding relationships further established an early, probably syn-diagenetic, timing of formation. All this is significant for the Randalls BIF-Au district, because the black shale studied by Steadman et al. (2013) is only ~15 km west of Cock-Eyed Bob in the Lucky Bay area (Fig. 3.1), and tectonostratigraphic reconstructions of the Eastern Goldfields by Czarnota et al. (2010) show that this unit was likely widespread over tens to hundreds of kilometers at the time of its deposition (Fig. 3.16). Following uplift, erosion and folding associated with regional D_2 compression and low-grade regional metamorphism, the upper Black Flag Group was buried during Belches Supersequence sedimentation, and then metamorphosed again by the intrusive post-Belches granite plutons. The metamorphism associated with granite intrusion may have facilitated pyrite nodule breakdown (to

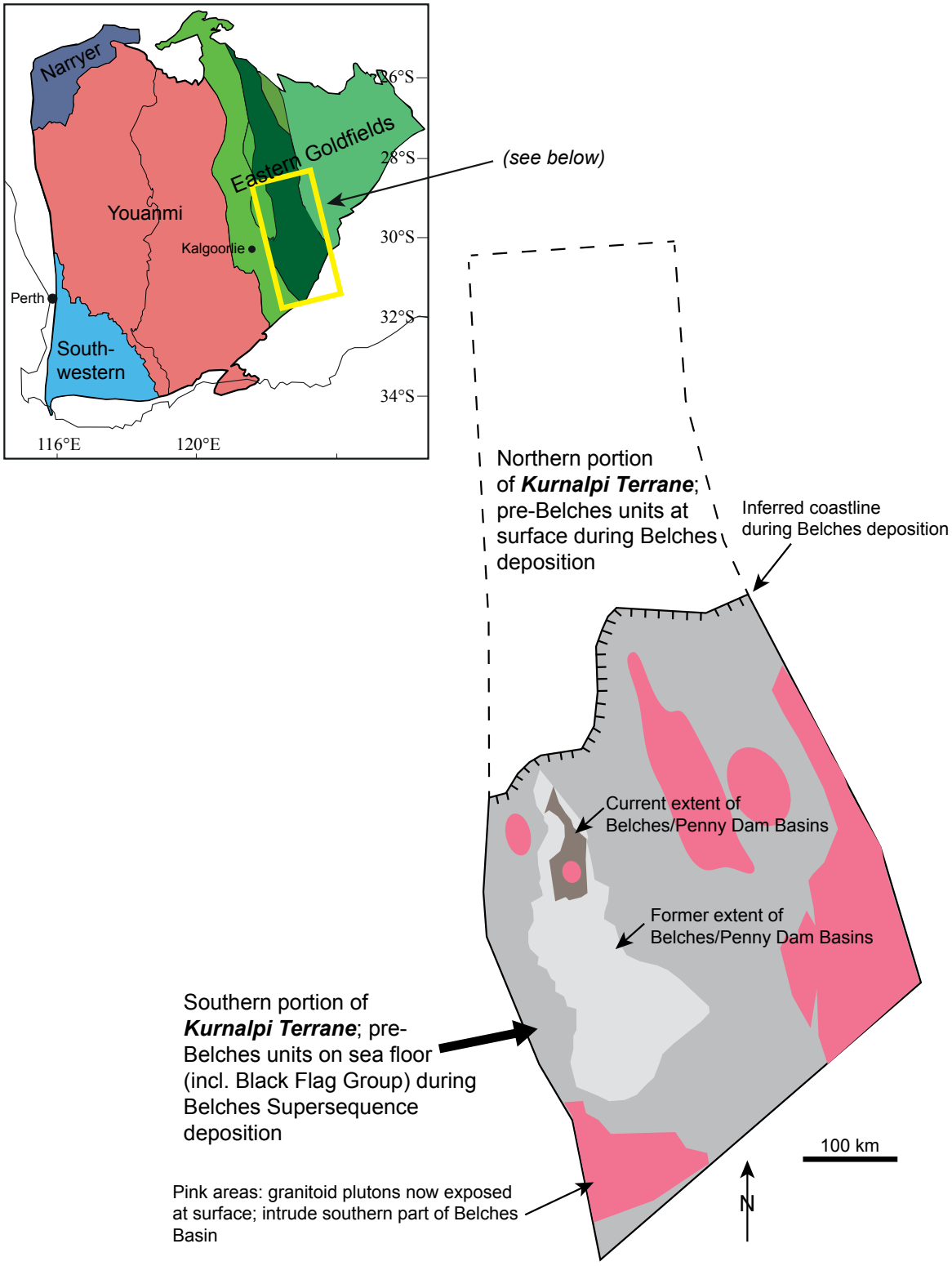

Figure 3.16 Schematic map showing relationship of Belches Basin to the rest of the Kurnalpi Terrane (re-drawn and modified from Krapež et al., 2008). At the time of Belches Supersequence deposition, the lithologies exposed on the surface were likely those of the Black Flag Group and other, older, units (e.g., correlatives to the Kambalda Komatiite, Paringa Basalt, etc.). Some granitoid intrusives may have also been present at this time. The Belches Basin was originally much larger than its current extent; significant amounts of felsic magmatism, uplift, and erosion succeeded in shrinking it down to the preserved remnant.

pyrrhotite) and release of trace elements, especially As and Au, to the metamorphic/hydrothermal fluid (Large et al., 2011).

Mass-balance calculations of background Au and As in the black shale from Lucky Bay support a case for a sedimentary gold (and arsenic) source. The average arsenic and gold contents of the pyrite nodules in the Lucky Bay shale are 1480 ppm and 0.5 ppm, respectively, as determined by LA-ICP-MS. As mentioned in Section 3.2, Krapež and Pickard (2010) estimate that the upper Black Flag Group is ~4 km thick, and approximately 15% of this thickness is carbonaceous black shale. If the black shale contained 1 vol % pyrite nodules with 0.5 ppm Au and 1480 ppm As, and if half of the nodular pyrite recrystallized and converted to pyrrhotite during metamorphism in the Belches Basin, releasing its As-Au budget to the fluid, then 1.03 t of Au and 3034 t of As per cubic kilometre of rock would have been produced (this is apart from any Au and As contained in the very fine-grained, disseminated syn-sedimentary/early diagenetic pyrite that was also released). The Randalls district contains a total of approximately 0.6 Moz Au, which equates to ~18 t Au, requiring approximately 18 km^3 of source material. The district also covers an area roughly 5 x 7 km, meaning a rock sequence ~515 m thick would be needed to source the total gold. This required thickness is well under the total thickness of the black shale in the upper Black Flag Group, and the areal extent is within the range proposed by tectonostratigraphic reconstructions (e.g., Czarnota et al., 2010), suggesting that this unit could have easily been a contributing source, if not the sole source, of gold and arsenic for the Randalls deposits.

The above model is not without deficiencies, most notably in sulfur isotope geochemistry, which evidence does not constrain possible sulfur sources in the fluid(s) that formed the gold deposits in the Randalls district (see sections 3.5.8 and 3.6.5). Future work is needed to resolve this issue.

3.7 Conclusions

3.7.1 Formation of the Santa Claus member (Randalls BIF)

Krapež et al. (2008) interpreted the Santa Claus member as a condensed section, where the chert layers would have formed during diagenesis and their top surfaces would have represented siliceous seafloor hardgrounds, similar to the Hamersley-type BIF (Krapež et al., 2003). While our work was not as focused on the sedimentologic character of the Randalls BIF, we encountered similar lithologic patterns, textures and sedimentary structures to those described by Krapež et al. (2008). However, our findings do not support their speculations about the pre-metamorphic BIF mineralogy (diagenetic siderite; see section 3.6.2 above). Our detrital zircon work also does not support earlier geochronological studies by Krapež et al. (2000) and Krapez and Pickard (2010), in that the maximum depositional ages of the upper and lower sections of the Belches Supersequence are significantly different from each other. Based on previous studies and our own geochronology, we propose that the Santa Claus member BIF was deposited between 2665 and 2650 Ma.

3.7.2 Metamorphism and hydrothermal alteration of the Randalls BIF

At approximately 2660 Ma, the Belches basin was subjected to contact metamorphism as a result of widespread granite intrusion (Champion and Cassidy, 2007); in particular, the Randalls district attained upper greenschist to lower amphibolite facies (~500–550˚C), as evidenced by the presence of biotite and blue-green amphibole (hornblende) in mudrocks and the absence of garnet or staurolite in these same rocks (Goscombe et al., 2009). This history did not occur in the Lucky Bay area 15 km to the west, which allows us to evaluate the pre-metamorphic character of diagenetic pyrite that we contend was metamorphosed below the Randalls area by these granitic intrusions.

3.7.3 Timing and mechanism of gold mineralization at Randalls

Many researchers have promoted the views that gold in Yilgarn orogenic systems has magmatic, mantle,

or igneous-metamorphic sources (Phillips et al., 1984; Groves et al., 1987; Groves et al., 1998; Mueller 1997; Mueller and McNaughton, 2000; Mueller et al., 2004; Mueller and Muhling, 2013). We believe there is a case to be made that systems underlain by thick metamorphosed Black Flag Group pyritic sediments may have either been fully sourced by loss of S and metals from these sediments during granite-related metamorphism, or that these sediments contributed significantly to the metal and sulfur budget of fluids that also saw magmatic, mantle, or igneous/metamorphic sources. A possible model of formation for Randalls would then be: (1) water produced from the breakdown of hydrous minerals (e.g., chlorite) in sedimentary source rocks beneath and within the Belches Basin during granite intrusion, coupled with trace element liberation during pyrite-to-pyrrhotite conversion in these same lithologies, led to a metal- and H_2S-rich solution that was convected upward through the sedimentary pile to the oxidized facies of the Santa Claus BIF at Randalls; and (2) upon reaching the BIF, the reduced H_2S-rich fluid reacted with the oxide-facies (magnetite) BIF, resulting in sulfidation of magnetite to pyrrhotite and consequent destabilization of bisulfide-complexed gold and arsenic, leading to precipitation of free gold/electrum and arsenopyrite.

This chapter has been removed for copyright or proprietary reasons.

Chapter 4

Syn-sedimentary, diagenetic, and metamorphic pyrite, pyrrhotite, and marcasite at the Homestake BIF-hosted gold deposit, South Dakota, USA: Insights on ore genesis from LA-ICP-MS trace element and sulfur isotope studies

Published as: Steadman, J. A., Large, R. R., 2016, Synsedimentary, diagenetic, and metamorphic pyrite, pyrrhotite, and marcasite at the Homestake BIF-hosted gold deposit, South Dakota, USA: insights on Au-As ore genesis from textural and LA-ICP-MS trace element studies, Economic geology, 111, 1731-1752

Chapter 5

Syn-sedimentary to early diagenetic gold in black shale-hosted pyrite nodules at the Golden Mile deposit, Kalgoorlie, Western Australia

*Published August 2015 in **Economic Geology**, v. 110*

Abstract

The Kalgoorlie goldfield (~50 Moz Au produced), famous for its long mining history and diversity of precious-metal telluride minerals, is a world-class Neoarchean Au-Ag-Te district which includes the Golden Mile Super Pit, the largest single gold deposit in the Eastern Goldfields of Western Australia, and the smaller but nonetheless significant Mt. Charlotte deposit, 3 km to the north. The gold ore at Kalgoorlie is of two types – a Au- and Te-rich first stage (Golden Mile, or Fimiston, ore), which constitutes the bulk of the Au endowment, followed by a relatively Te-poor second stage (Mt. Charlotte ore). Fimiston-stage ore is characterized by deformed quartz-carbonate structures termed 'lodes': thin (1-10 cm) zones of quartz/ankerite/gold/telluride-rich vein breccias with haloes of fine-grained pyrite, muscovite, ankerite, and tourmaline. Charlotte-stage ore is primarily hosted by ankerite-pyrite-rich alteration selvages around flat-sided, undeformed bucky quartz veins and is the only ore style present in the Mt. Charlotte mine itself. The primary host unit for both mineralization styles is the Golden Mile Dolerite, one of several dolerite intrusions in the mafic-ultramafic volcanic succession of the Kalgoorlie Terrane.

Along with the large amount of mafic metavolcanics, consistent with typical greenstone belt stratigraphy, the Golden Mile contains at least three fine-grained carbonaceous (meta) black shale units (from oldest to youngest: the Kapai Slate; an unnamed interflow shale near the top of the Paringa Basalt; and black shale forming the base of the Black Flag Group). Each of these units contains varying amounts of syn-sedimentary, diagenetic, and hydrothermal-metamorphic pyrite and pyrrhotite, including well-preserved pyrite nodules. Nodules at the Golden Mile Super Pit vary in diameter from a few mm to several cm, can have several concentric zones of pyrite with internally variant textures, and are commonly deformed into ovoid shapes. There are also horizons of pyrrhotite nodules within certain sections of these units; like their pyrite counterparts, these are commonly concentrically zoned and show evidence of later deformation. Rare examples of thin massive sulfide beds are also present in the interflow shale near the top of the Paringa Basalt.

LA-ICP-MS imaging of pyrite nodules from each of the three black shale units reveals complex (and sometimes spectacular) concentric compositional zonation that parallels the growth zones. Trace element concentrations vary within different nodule bands in a coherent pattern, with Au, Ag, Te, and As typically enriched together in certain zones. Gold content is particularly high in the Paringa Basalt interflow shale nodules, which average 3-4 ppm Au as well as 30-40 ppm Ag, 30-40 ppm Te, and 1,000 ppm As. Samples taken several kilometers to the south (along strike) and west of the Golden Mile of

the Kapai Slate and Black Flag Group shale also contain disseminated and nodular pyrite enriched in Au, Ag, Te, and As at levels comparable to samples of those formations within the deposit. However, in distal samples of the Paringa interflow shale, there is only laminated and nodular pyrrhotite, marked by enrichments in Au, Ag, Sb, Te, Tl, Pb, and Bi relative to a later (and presumably metamorphic) pyrrhotite which cross-cuts and partially replaces the earlier pyrrhotite.

Lead isotope studies of nodules from the three shale units, as well as pyritic ore samples from two separate Fimiston-stage lodes and one Mt. Charlotte-stage lode, have been undertaken to help resolve relative timing issues. Nodular pyrite from each shale formation has a distinct isotopic composition, with the Kapai Slate samples being the least radiogenic, followed by those from the Paringa interflow shale and, lastly, the Black Flag shale. These data result in progressively younger Pb-Pb model ages, in keeping with the established stratigraphic order. In contrast, ore pyrites contain a wide spread of relatively unradiogenic to radiogenic isotopic compositions, partially overlapping with the nodular pyrites.

Sulfur isotope studies (^{32}S, ^{33}S, and ^{34}S) have provided evidence on S source(s) for the nodules and ore-stage pyrites. Whereas the cores of most nodules contain pyrite with negative $\Delta^{33}S$, a signal thought to be derived from seawater sulfate, the rims of the same have positive $\Delta^{33}S$, which may result from photolysis of volcanic SO_2. By contrast, ore-related pyrites (both Fimiston- and Mt. Charlotte-stage) have no or little $\Delta^{33}S$ anomalies.

The shape, internal textures, and distinct trace element enrichment and zonation, apparently little affected by later processes, suggests the nodules are syn-sedimentary to early diagenetic. There is no evidence that gold or other elements have been added to the nodules during hydrothermal ore events; gold, along with many other elements, remains a coherent part of the primary nodule structure. Lead and S isotope studies on the pyrite nodules provide strong supportive evidence of an early marine sedimentary age for the nodules: the Pb isotopes give an age roughly equivalent to progressive sedimentation of the black shale host rocks, and the S isotopes are best explained by marine sulfate being the original S source for the nodules.

The evidence is compelling that there was enrichment of Au-Ag-Te-Hg-As during inter-volcanic sedimentation and diagenesis in the Kapai Slate, the interflow shale near the top of the Paringa Basalt, and Black Flag shale, before the formation of the Fimiston-stage gold-telluride lodes. While we do not have grounds for commenting on the possibility that these shale units contributed to the source of gold in the Golden Mile deposit, the fact remains that syngenetic/diagenetic gold pre-concentration in fine-grained, sulfidic, moderate- to deep-water sediments was likely an on-going process across the Eastern Goldfields between ~2700-2680 Ma.

5.1 Introduction

Sulfide nodules, particularly those composed of pyrite, are commonly (but not exclusively) formed in fine-grained carbonaceous sedimentary rocks (i.e., black shales) during sedimentation or early diagenesis (burial and lithification – Goldhaber, 2003; Rickard, 2012, 2014, and references therein). Those that form in this manner, and which have not been greatly affected by post-depositional processes (e.g., hydrothermal alteration and metamorphic recrystallization), can be reliably employed as proxies to decipher the geochemical nature of the fluids (either seawater or pore waters) from which they precipitated (Large et al., 2014). Archean pyrite nodules can also be helpful, primarily via the minor S isotopes, in determining the redox state of the atmosphere, ocean, and sediment pore waters at the time of nodule formation (Partridge et al., 2008; Marin-Carbonne et al., 2014).

Recent studies on the geochemistry of black shale units around the world (some of them associated with orogenic gold deposits), and the pyrite they typically contain, have shown that this rock type is an excellent source for ore-forming metals, as it contains significant above-crustal average concentrations

of gold as well as As, Te, Ni, Cu, Sb, and Mo (e.g., Ketris and Yudovitch, 2009; Large et al., 2007; 2009; 2011; 2013; Thomas et al., 2011; Jowitt and Keays, 2012; Bardoux, 2013; Bornhorst and Williams, 2013; Pasava et al., 2013). However, most of these studies have focused on post-Archean shale sequences, whereas information on black shale lithologies >2500 Ma is relatively sparse (Rickard, 2014). The eastern Yilgarn Craton, specifically the Eastern Goldfields Superterrane, hosts many fine-grained, carbonaceous and sulfidic (meta)sedimentary units (i.e., black shale) of Neoarchean age, although this fact is not commonly emphasized in the literature (e.g., Steadman et al., 2013 and 2014, but see Bavinton and Keays, 1978; Bavinton, 1981; Bekker et al., 2009; and Fiorentini et al., 2012). Furthermore, due to 1) the volumetric dominance of granitoids and greenstones (basalt and komatiite) over shales in the Eastern Goldfields Superterrane, and 2) the fact that greenstones are the major hosts to gold ores in this area, black shales remain somewhat understudied and underappreciated in the eastern Yilgarn when compared to other Precambrian cratons (e.g., the Pilbara: Krapež et al., 2003; Ono et al., 2003; Kaufmann et al., 2007; Partridge et al., 2008; Scott et al., 2011). Steadman et al. (2013) used LA-ICP-MS techniques to analyze diagenetic pyrite nodules and associated metamorphic/hydrothermal pyrites in black shale belonging to the Black Flag Group from the Lucky Bay gold prospect, ~60 km SE of the Golden Mile deposit, and found that they were highly enriched in ore-forming elements (e.g., Au, As, Ag, and Te) compared to background values. Furthermore, this lithology forms the substrate to a nearby sedimentary basin (Belches) which hosts a gold producing district (Randalls); Steadman et al. (2013; 2014) postulated that the black shale at Lucky Bay may have been leached of some or all its metal budget during metamorphism and granite intrusion, supplying gold to the formation of the BIF-hosted gold ores at the Cock-Eyed Bob, Maxwells, and Santa-Craze deposits.

Pyrite from the Golden Mile and elsewhere around Kalgoorlie has been a focus of trace element, S isotope, and Pb isotope geochemical study for the last 30 years (Phillips et al., 1986a; 1986b; 1988; Browning et al., 1987; Cameron and Hattori, 1987; Clout, 1989; McNaughton et al., 1993; Evans et al., 2006), but in these reports, the type of Golden Mile pyrite chosen for analysis is exclusively ore-related pyrite, particularly from the earliest ore stage (Fimiston). To the best of our knowledge, no in-depth trace element geochemical work has been conducted on other, possibly pre-ore pyrites in interflow shales at the Golden Mile, despite the fact that these pyrites might well carry important information about geochemical conditions before and during the hydrothermal events which created this great resource. One exception to this generality is the Honours thesis of Scantlebury (1983), who did note the presence of pyrite nodules in the Paringa Basalt interflow shale (his "Upper Slates", after Tomich [1959]) and conducted preliminary microprobe work on them. He found them to be high in Au (0.1 wt % in one analysis), Ag, and other elements, and also enriched in certain trace elements relative to the Fimiston-stage ore pyrites. However, he apparently did not proceed further on the topic.

We show here, using LA-ICP-MS trace element, Pb isotope, and S isotope studies, that Au, As, and Te pre-concentration in pyrite and pyrrhotite nodules (and their enclosing black shale host rocks) at the Golden Mile and surrounding region was an on-going synsedimentary process that likely occurred when black shale units were deposited during periods of quiescence in the volcanic eruptive cycle. The Pb isotope evidence from the nodules and ore-stage pyrites also reveals that there were multiple Pb reservoirs in or near the Golden Mile that were tapped at various times. These findings underscore the value of mapping the trace element contents of sulfides (particularly pyrite) in ore districts, and have major implications for gold deposit formation and related exploration models in greenstone terrains.

5.2 Previous Research on the Golden Mile

Since its discovery in 1893, the Golden Mile Au-Ag-Te deposit (Fig. 5.1A-C) has perennially been one of the most studied gold deposits in the world. Early workers (e.g., Lindgren, 1906; Larcombe, 1914; Stillwell, 1931; Gustafson and Miller, 1937) provided details on, and a basic understanding of, the

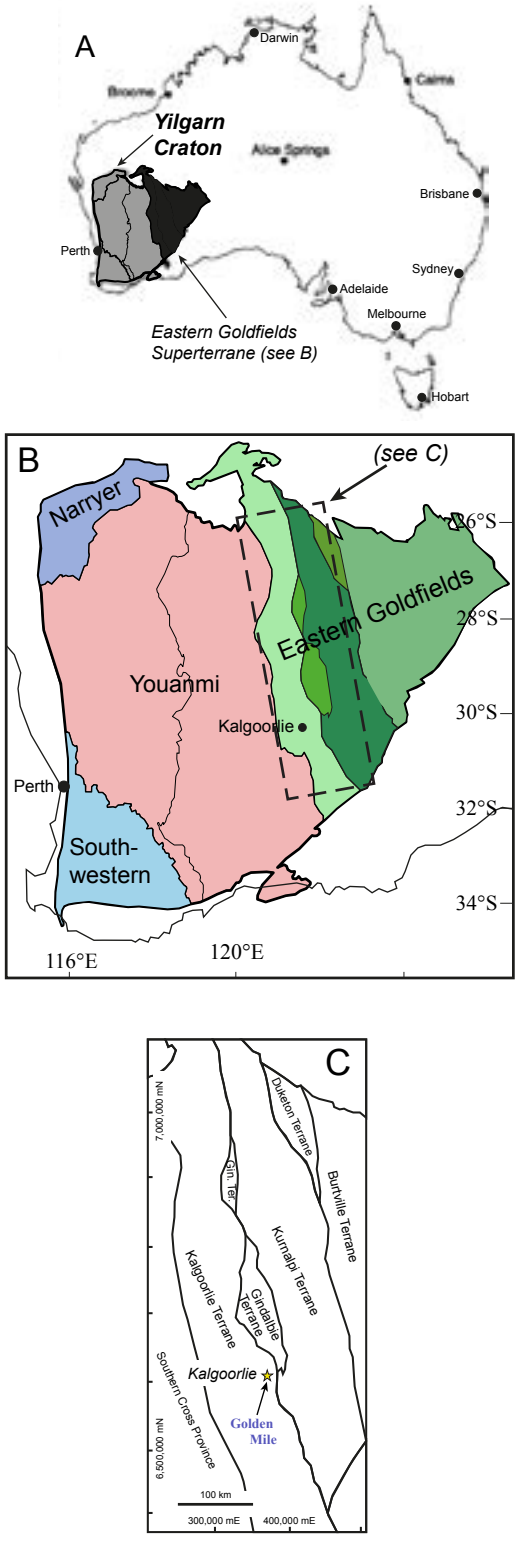

Fig. 5.1 **A**. Map of Australia showing location of the Yilgarn Craton; the Eastern Goldfields Superterrane is in black (modified after Krapež et al., 2008). **B**. The Yilgarn Craton (after Czarnota et al., 2010), composed of five provinces (Narryer, Murchison, Eastern Goldfields, Southern Cross, and Southwestern). **C**. Schematic representation of the Eastern Goldfields Superterrane (after Krapež et al., 2008). The yellow and blue star (southern region of map, near Kalgoorlie) represents the area of the Golden Mile Super Pit.

mineralogy and structure of the ore fields, with most favoring a formational model involving lateral secretion of metals by hydrothermal magmatic fluids from the surrounding country rocks and the Golden Mile Dolerite itself (primary ore host). In particular, the presence of feldspar- and hornblende-phyric porphyry dikes, which either cut (hornblende porphyry) or are cut by (albite porphyry) the first stage of ore (Robert et al., 2005), compelled Gustafson and Miller (1937) to argue a genetic connection between these lithologies and the ore bodies. By the middle 20th century, structural and mineralogical understanding had improved substantially (e.g., Tomich, 1952, 1959; Woodall, 1965; Bartram, 1969; Travis et al., 1971), including the formalization of stratigraphic units (Woodall, 1965; Travis et al., 1971), but the model of origin for the Golden Mile remained essentially the same. However, in the mid-1970s, Tomich (1974; 1976) published a modified 'volcanogenic' model for the deposit, keying on the peculiar ore type locally known as 'Green Leader' ore, and drawing on geological similarities between the Golden Mile and several Au-rich VHMS deposits in the Superior Craton of eastern Canada. His ideas were challenged strongly (Travis and Woodall, 1975), and despite further work by himself (Tomich, 1986) and others (Golding, 1978; Golding and Keays, 1981) that lent some support to this model, it has subsequently been regarded as too interpretive by most researchers familiar with the Golden Mile (Clout, 1989).

Beginning in the 1980s, a new model of formation for the deposit was advanced, based upon metamorphic and structural studies at the University of Western Australia, which posited a deep-crustal (i.e., below the greenschist-amphibolite transition) metamorphic fluid and metal source tapped by large shear zones that precipitated gold into chemically reactive rock packages (e.g., Phillips, 1986; Boulter et al., 1987). This 'orogenic' or metamorphic model has now been applied to many greenstone-hosted deposits around the globe (Groves et al., 1987; 1998; 2003; Goldfarb et al., 2005; Phillips and Powell, 2009; 2010). Later modifications to this model also added the possibility of mantle involvement in the creation of deposits such as the Golden Mile (e.g., Hronsky et al., 2012). Another model proposed in the late 1980s to explain the origin of the Golden Mile involved craton-scale wrench faulting, which presumably propagated to the crust-mantle boundary and transported metals and

fluids to the upper crust via these through-going structures (Mueller et al., 1988).

A PhD thesis on the Golden Mile by Clout (1989) shed new light on certain aspects of the mineralogy and geochemistry of the first-stage ore event (Fimiston) which had been overlooked or not well documented by many previous workers, including the presence of anhydrite veins and banded carbonate and chalcedony cement in brecciated ore zones. These observations led Clout to propose an alternate model of formation for the Golden Mile, one that involved seawater-meteoric±magmatic fluid mixing and/or boiling during the creation of Fimiston ore. Such processes are typically associated with epithermal environments (e.g., Cooke and Simmons, 2000; Simmons et al., 2005), and has led to questions about the true nature of the main Golden Mile mineralization (Gauthier et al., 2004; 2008; Robert et al., 2005; Nixon et al., 2014) which remain unanswered.

5.3 Geologic Context

5.3.1 Regional geology (excluding shales)

The regional geology of the Eastern Goldfields, and particularly the local geology around Kalgoorlie, is well covered in the literature (e.g., Larcombe, 1912; Stillwell, 1931; Gustafson and Miller, 1937; Woodall, 1965; Travis et al., 1971; Phillips, 1986; Clout, 1989; Clout et al., 1990; Swager, 1997; Bateman and Hagemann, 2004; Krapež and Hand, 2008; Krapež et al., 2008; Squire et al., 2010; Vielreicher et al., 2010; Mueller and Muhling, 2013; Tripp, 2013). The Golden Mile is located in the southern portion of the Kalgoorlie Terrane, one of several NNW-trending granite-greenstone belts (formerly volcanic arcs) that comprise the Eastern Goldfields Superterrane (Fig. 5.1C; Czarnota et al., 2010). The Super Pit at the Golden Mile is centered on the NNW-SSE-trending D_1 Golden Mile Fault, which juxtaposes Black Flag Group metasediments and Golden Mile Dolerite (GMD); the latter unit hosts the majority of the gold ore at this deposit (Fig. 5.2A).

There is debate in the literature concerning the emplacement style of the Golden Mile Dolerite: most workers are of the opinion first published in Woodall (1965) and further expounded in Travis et al. (1971), which is that this unit is a differentiated tholeiite sill with chilled margins, a granophyric core, distinct geochemical trends, and disconformable contacts with the surrounding rock units (e.g., see Phillips, 1986; Clout, 1989; Hergt et al., 2000). However, Tomich (1974; 1976; 1986), Golding (1978; 1985) and Nixon et al. (2014) propose an alternative view that maintains the GMD was extruded subaerially, appealing to textures indicative of volcanic processes (e.g., flow-top breccias, pillow lavas with triple-point junctions and vesicles, etc.). Furthermore, the latter authors state that the unit is therefore older than the overlying Black Flag Group metasediments (again using textures as evidence, e.g., rounded cobble- to boulder-sized clasts of GMD in the lower Black Flag Group), whereas the former group argues that the Golden Mile Dolerite was intruded at or near the contact of the Paringa Basalt and Black Flag Group, making the GMD the youngest unit in the district. While this issue is beyond the scope of this paper and extraneous to our data and interpretations, we note that the most recent U-Pb zircon dating of the GMD and Black Flag Group (Tripp, 2013) renders the GMD older than the Black Flag Group by approximately 3 million years (see 'Local geology – Black Flag Group' below).

At the Super Pit, the Devon Consols Basalt (oldest), Paringa Basalt, and Golden Mile Dolerite (youngest) form the majority of the pit walls and floor, their continuity interrupted only by meters-thick metasedimentary interflow units such as the Kapai Slate (at the top of the Devon Consuls Basalt) and an unnamed carbonaceous interflow metashale near the top of the Paringa Basalt, hereafter referred to as the Paringa interflow shale (see below). All lithologic units in the Kalgoorlie Terrane of the Eastern Goldfields were subjected to polyphase deformation and metamorphism; at the Golden Mile, two generations of folds (F_2 and F_4 mesoscale upright folds) are preserved in most units, and maximum P-T

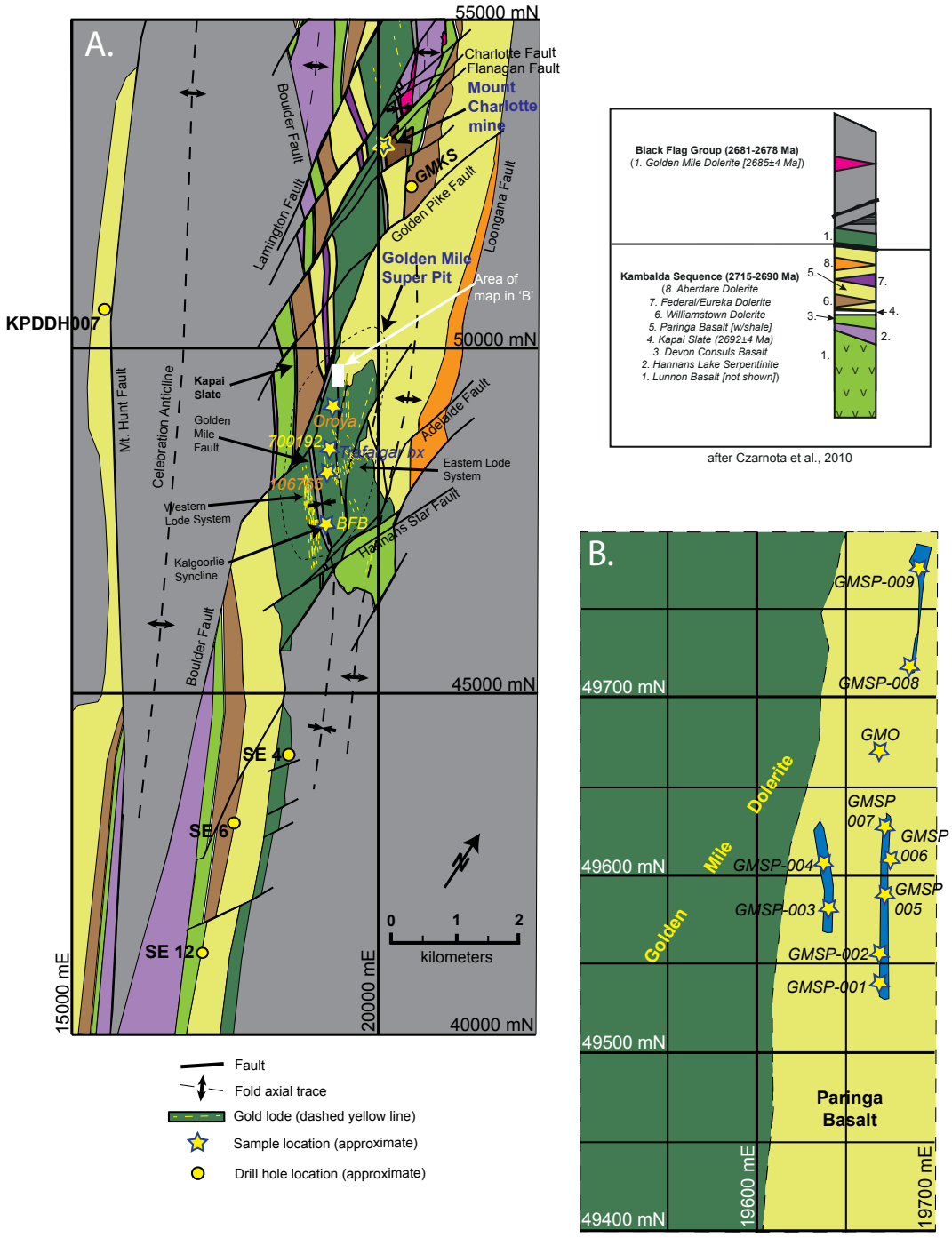

Fig. 5.2 **A**. Geological map of the Kalgoorlie area (after Travis et al., 1971; Clout et al., 1990; and Vielreicher et al., 2010). Stars in the Super Pit area indicate location of samples outside of the inset map in 'B'. Circles indicate the approximate location of drill hole collars. The regional stratigraphy of the Eastern Goldfields (redrawn from Czarnota et al., 2010) is also shown. The quoted Golden Mile Dolerite age of 2685±4 Ma is taken from new U-Pb zircon geochronology undertaken by Tripp (2013). **B**. Map of the specific area of the Super Pit visited for this study. Stars indicate location of 'GMSP' samples from the Paringa interflow shale, plus ore sample 'GMO'.

conditions did not exceed 400˚C at 3.5-4 kb, or middle greenschist facies (Clout et al., 1990; Goscombe et al., 2009).

5.3.2 Local geology - Kapai Slate

The Kapai Slate is easily the best known of the three metasedimentary units examined in this study, having been recognized as a useful marker horizon in the Kalgoorlie Terrane for decades (Woodall, 1965). Although its thickness rarely exceeds 10 meters, it is regionally extensive for hundreds of kilometers in the Yilgarn Craton. In the immediate area around the Golden Mile deposit, it is exposed in the western portions of the Super Pit, with along-strike continuations to the north and south of the pit and town of Kalgoorlie (e.g., there are well-exposed but intensely weathered outcrops near Hannans Lake, approximately 5 km south of Kalgoorlie). The Kapai Slate is notably present in the St. Ives Au district, ~50 km SE of Kalgoorlie near Kambalda, where it is host to minor gold mineralization. In terms of regional stratigraphy, the Kapai marks the boundary between the lower Devon Consuls Basalt and the upper Williamstown Dolerite, and has a U-Pb zircon depositional age of 2692±4 Ma (Claoué-Long et al., 1988).

5.3.3 Local geology - Paringa interflow shale

The unnamed (and never geochronologically dated) black shale near the top of the Paringa Basalt is informally known as the "Oroya Shale" to mine geologists at the Golden Mile. However, since the unit has never been published using this moniker, we have decided to follow convention and not use this term. This unit is thought to be identical with the so-called 'Upper Slates' of the Paringa Basalt, originally defined by Tomich (1959) and studied in some detail by Scantlebury (1983). Much less is known about this unit on a regional scale, but at the Golden Mile, a variant of the Fimiston-stage ore termed "Oroya-style" or "Green Leader" ore (see below for description) is best developed where the Paringa Basalt, Golden Mile Dolerite, and this unit are in contact with each other (Tomich, 1959). Exposures of the Paringa interflow shale at the Golden Mile are particularly prevalent in the eastern sections of the mine due to blasting, but there are also outcrops of it south of the Super Pit, toward Hannans Lake. Its thickness, like the Kapai Slate, rarely exceeds 10 meters.

5.3.4 Local geology - Black Flag Group

The Black Flag Group (BFG) is a thick (>2 km), heterogeneous volcanic-sedimentary succession that stratigraphically overlies nearly every other rock unit in the Eastern Goldfields (Squire et al., 2010; Tripp, 2013). Among its many sub-units is carbonaceous black shale containing pyrite nodules (lots of other sedimentary-diagenetic pyrite styles are preserved, as well). Black shale is particularly prevalent in the lowermost parts of the BFG, where it is commonly tens of meters thick. One of the historic Golden Mile ore bodies, the bonanza-grade Duck Pond Shoot, is thought to have been hosted in altered Black Flag Group shale, though there is some disagreement on this in the literature (see Tomich, 1974; Travis and Woodall, 1975; Tomich, 1976). A depositional age for the shales in the lower Black Flag Group is constrained by a U-Pb zircon crystallization age of 2685±4 Ma for the Golden Mile Dolerite (that is, the shale package is ≤2681 Ma; Tripp, 2013) and a U-Pb zircon crystallization age of 2672±6 Ma for dacitic volcanics overlying the shales (i.e., the shale package is ≥2678 Ma; Tripp, 2013).

5.3.5 Local geology - ore description

The Kalgoorlie goldfield comprises essentially two separate Au mineralization events, each with its own style of ore and, in part, alteration mineralogy – these are the Fimiston (or Golden Mile) lodes and Mount Charlotte quartz vein stockworks (Clout, 1989; Bateman and Hagemann, 2004; McNaughton et al., 2005). The older (and overwhelmingly richer) Fimiston lodes are Te-rich (at least 17 different telluride phases reported; Shackleton et al., 2003; Bateman and Hagemann, 2004) and are associated

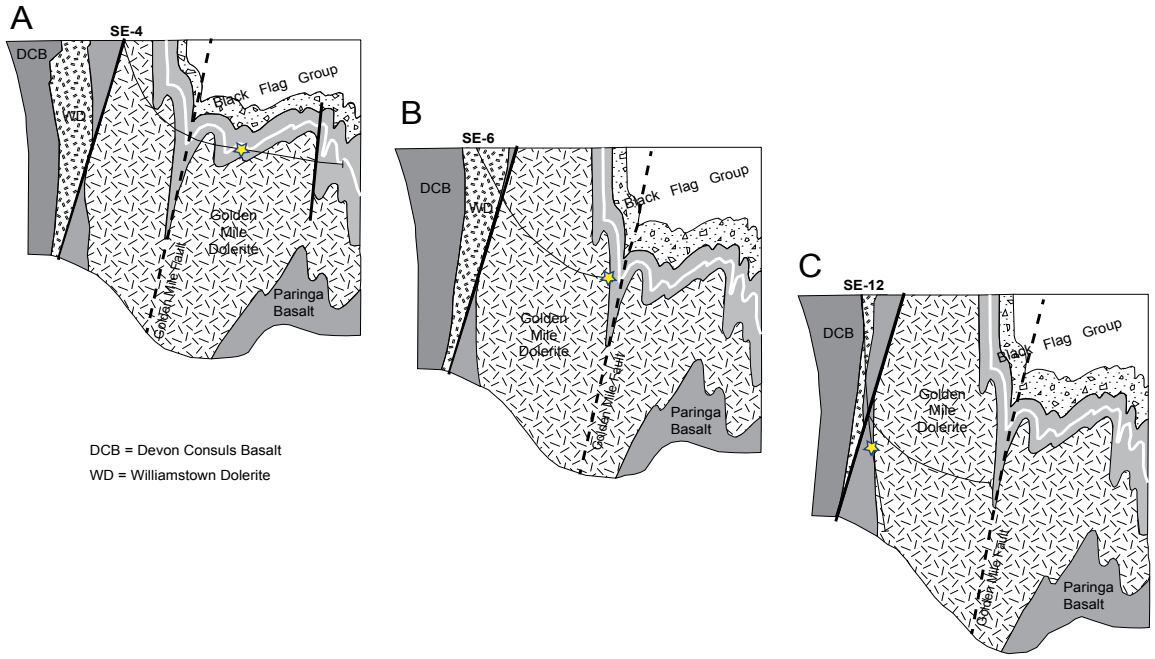

Fig. 5.3 Schematic cross-sections for the South End ('SE') drill holes SE-4, SE-6, and SE-12 (after Travis et al., 1971, and Tripp, 2013). Stars indicate approximate depth for samples taken from each hole. Abbreviations as shown on diagram.

with quartz-ankerite-white mica-pyrite-tourmaline (±siderite±hematite±albite±magnetite±anhydrite±barite±scheelite) alteration; in addition, almost 30% of the gold recovered from this style of mineralization has come from Au-Ag tellurides (Shackleton et al., 2003). Native gold is commonly intergrown with precious-metal tellurides such as coloradoite (HgTe) and calaverite (AuTe), leading to exceptionally high grades in local zones (e.g., ~100,000 g/t Au in the Lake View mine [Duck Pond Shoot] and Oroya Shoot; Clout et al., 1990; Bateman and Hagemann, 2004). An additional defining characteristic of certain Fimiston-stage lodes is the abundance of V-rich muscovite, which lends a distinctive green hue to the host rocks (Nickel, 1977; Scott et al., 2011). Such lodes are referred to as "Green Leader" ore (Tomich, 1959), and are commonly among the richest individual ore bodies in the entire field; the aforementioned Oroya Shoot was one such example: it produced ~2 Moz Au at an average grade of 150 g/t (Tomich, 1986),), while the Duck Pond Shoot, albeit small (<0.5 Moz), ran an average grade of over 1,000 g/t. Some consider this style of mineralization as separate from the Fimsiton/Golden Mile stage, wherein Green Leader ore is termed 'Oroya-style', named after the Oroya Shoot..

The second major stage of Au mineralization in the Kalgoorlie area, and considerably less endowed in gold relative to Fimiston, is the ~250 t Au Mount Charlotte sheeted quartz vein system, named after the Mt. Charlotte mine ~3 km N of the Golden Mile, which formed during D_3 (reactiviation of D_2 fault systems; Clout, 1989; Ridley and Mengler, 2000) and commonly cuts the earlier-formed Fimiston lodes in the Super Pit. The commonly large, flat-sided quartz veins generally have proximal (i.e., within 10 cm of the vein) ankerite-white mica alteration haloes and distal (>10 cm from the vein) chlorite-siderite haloes. Blocky, euhedral pyrite ranging from 1 mm to over 10 mm is ubiquitous in the Mt. Charlotte vein-proximal alteration assemblage. Apart from total Au endowment, one of the major differences between the Mt. Charlotte and Fimiston stages is the comparative lack of Te in the former – less than one percent of the ore mined from Mt. Charlotte has come from Au-Ag tellurides (Mueller and Muhling, 2013). Gold in Mount Charlotte-style lodes is commonly present as native Au inclusions

Table 5.1 Description and location information for sedimentary and ore-stage pyrite/pyrrhotite samples used in this study

Sample	Formation	Age (Ma)	Sulfide	Location	Northing	Easting	RL	Trace Elements	Isotopes
KPD7-272A	Kapai Slate	2692±4	py nod	Somerville (Kal Apt)	50500	15600	120	x	
GMKS-002	Kapai Slate	2692±4	py nod	~2 km N of Super Pit	52419	20381	-272	x	S, Pb
GMSP-001	Paringa int. Shale	2689-2688	py nod	Super Pit, north end	49540	19660	-170	x	S, Pb
GMSP-003	Paringa int. Shale	2689-2688	py nod	Super Pit, north end	49580	19645	-170	x	S, Pb
GMSP-006	Paringa int. Shale	2689-2688	py nod	Super Pit, north end	49615	19670	-170		Pb
GMSP-008	Paringa int. Shale	2689-2688	py nod	Super Pit, north end	49720	19685	-170	x	Pb
GMSP-009	Paringa int. Shale	2689-2688	py nod	Super Pit, north end	49770	19690	-170	x	Pb
BFB-003	Black Flag Group	2681-2678	py nod	Super Pit (Chaffers)	N/A	N/A	N/A		Pb
BFB-004A	Black Flag Group	2681-2678	py nod	Super Pit (Chaffers)	N/A	N/A	N/A	x	S, Pb
KPD7-474.7B	Paringa int. Shale	2689-2688	po nod	Somerville (Kal Apt)	50500	15650	-20	x	
KPD7-491	Paringa int. Shale	2689-2688	po nod	Somerville (Kal Apt)	50500	15675	-30	x	
KPD7-475.2	Paringa int. Shale	2689-2688	po nod	Somerville (Kal Apt)	50500	15650	-20	x	
KPD7-476A	Paringa int. Shale	2689-2688	po nod	Somerville (Kal Apt)	50500	15650	-20	x	
ORY-001	Paringa int. Shale	2689-2688	po nod	Super Pit	48645	19570	-450	x	
SE12-1435.5	Paringa int. Shale	2689-2688	po nod	~4 km S of Super Pit	41600	16900	-1100	x	
SE4-815.8	Black Flag Group	2681-2678	py nod	~2 km S of Super Pit	44000	18900	-200	x	

Sample	Ore type	Location	Northing	Easting	RL	Tr ace Elements	S iso	Pb iso
106765	Fimiston	Lake View mine, Super Pit	47900	19465	0	x		
106755	Mt. Charlotte	Flanagan Fault, Mt. Charlotte	N/A	N/A	N/A	x	x	x
700192	Fimiston	Super Pit (Trafalgar)	48290	19360	N/A	x		
700264	Fimiston	N/A	N/A	N/A	N/A	x	x	x
700265	Fimiston	N/A	N/A	N/A	N/A	x		
Trafalgar bx	Fimiston	Super Pit (Trafalgar)	N/A	N/A	N/A	x		
GMO-001	Fimiston	Super Pit, north end	49675	19655	-170	x		x
GMO-002	Fimiston	Super Pit, north end	49675	19655	-170	x	x	x
SE6-718.6	Mt. Charlotte	~3 km S of Super Pit	43000	17000	-400	x		

within the aforementioned euhedral pyrite in vein-proximal alteration selvages (primarily GMD units 7-9; Travis et al., 1971), with only minor amounts of native Au in the quartz veins themselves; overall, the average grade for the deposit is 4 g/t Au (Ridley and Mengler, 2000). Scheelite ($CaWO_4$) is a common accessory mineral in Mt. Charlotte ore (Ridley and Mengler, 2000; Brugger et al., 2002).

5.4 Sampling and Methods

Information for all samples used in this study is summarized in Table 5.1. A total of 25 rocks were collected from six different locations, including the Super Pit itself in east Kalgoorlie (16 samples), the borough of Somerville in west Kalgoorlie/Boulder (drill hole KPDDH007; 5 samples), one location near the Mt. Charlotte mine 3 km north of the Super Pit (1 sample), and three locations several km south of the Super Pit, which represent the three 'SE' (South End) drill holes sampled for this study (SE-4, SE-6, and SE-12; 3 samples). These historically significant holes were drilled by Western Mining Corporation over an 11-year period from 1952-1963, and are now stored in the Geological Survey of Western Australia's core library in Somerville, west Kalgoorlie. The collars for these holes are located roughly 2.5, 3.5, and 4.5 km south of the southern end of the Super Pit, respectively (Fig. 5.2A; Travis et al., 1971); cross-sections for the SE holes (after Travis et al., 1971, and Tripp, 2013) are shown in Fig. 5.3A-C.

At the Golden Mile, exposures of interflow shale near the top of the Paringa Basalt were sampled in a then-recently blasted area of the pit, between approximately 49500-49650 mN, 19600-19650 mE, and -170 mRL on the Oroya East mine grid (Fig. 5.2B). One other sample of Paringa interflow shale from the Super Pit does not appear on the inset map, as it was collected a few hundred meters to the south of the southern boundary of the inset map in Fig. 5.2B (48645 mN, 19570 mE, -450 mRL); its approximate position is marked in Fig. 5.2A with a yellow star and the name 'Oroya'. A Super Pit sample of Black Flag Group shale from the Chaffers area (BFB), immediately below the Golden Mile Fault (Fig. 5.2A), was also collected for this study. Outside the Super Pit approximately 3 km to the north, one sample of Kapai Slate (GMKS) was taken from recent diamond drill core; this drill hole was completed ~0.5 km SE of the Mt. Charlotte headframe, at approximately 52419 mN and 20381mE on the Oroya East mine grid (Fig. 5.2A). For other distal samples of the shales, drill core sections of Paringa interflow shale (SE-12) and Black Flag Group shale (SE-4 and SE-6) were investigated, and a much more recent drill hole, KPDDH007, completed in June 2013 and partially financed under the Geological Survey of Western Australia's Exploration Incentive Scheme (EIS), was sampled for Kapai Slate pyrite and Paringa interflow shale pyrrhotite.

Six samples of Fimiston ore and one sample of Mt. Charlotte ore were collected from various locations within the Super Pit (Fig. 5.2A-B). Three of the Fimiston samples (700192, 700264, and 700265) were loaned to CODES from the University of Western Australia as part of the OSNACA (Ore Samples Normalized to Average Crustal Abundance) research project. Location information for the OSNACA samples is exact for 700192 only (48290 mN, 19360 mE, Oroya East grid), but we have reason to believe that 700264 and 700265 are both Fimiston ore samples from the Western Lode System (S. Hagemann, pers. comm., 2013). Two other Fimiston samples (Trafalgar bx and GMO) were collected by the senior author during a visit to the Super Pit in May 2013, and the last Fimiston sample (106765) is from a small collection of Golden Mile samples housed at the University of Tasmania; this rock was taken from the Lake View mine (1000' level, 10138 cut and fill, 47900 mN 19465 mE, Oroya East grid). The Mount Charlotte samples come from two different areas: the first (106755) is from the Golden Mile collection housed at the University of Tasmania and was taken from the Flanagan Fault in the Mt. Charlotte mine, whereas the other Mt. Charlotte sample used for this study comes from SE-6.

Efforts were made to ensure that the surface samples collected were relatively fresh (i.e., below the base of complete oxidation). In both surface sampling and drill core collection, the focus was on black

shale containing visible pyrite nodules. Nodule diameter was not a discriminating factor for sampling, although geochemical analysis via SEM and/or LA-ICP-MS becomes more difficult with increase in nodule size (these techniques require small [i.e., less than 5 cm diameter] media). Super Pit samples of Black Flag Group, Paringa interflow shale, and ore material, plus sections of oriented drill core from all localities, were trimmed with a rock saw, and individual pyrite and pyrrhotite nodules were cut out from most of the rest of the rock, set in 25 mm diameter epoxy resin mounts, and polished on a 1 μm diamond lap wheel, with additional polishing on an alumina wheel (for shale matrix).

Five Super Pit Paringa interflow shale samples containing pyrite nodules (GMSP-003, GMSP-001, GMSP-008, GMSP-006, GMSP-009, BFB-003, and BFB-004A) and one Super Pit Paringa interflow shale sample containing pyrrhotite nodules (ORY-001) were chosen for detailed trace element, Pb isotope, and/or S isotope studies based on their size (up to 2.5 cm diameter) and generally exceptional degree of preserved zonation. Two samples of Black Flag Group pyrite nodules from the Super Pit (BFB-003 and -004A) and one pyrite nodule from the Kapai Slate ~3 km away from the Super Pit to the north (GMKS-002) were likewise analyzed. In addition to the nodules, we analyzed the five samples of pyritic Fimiston ore (106765, 700192, 700264, 700265, and Trafalgar bx), the two samples of pyrite-arsenopyrite Fimiston ore (GMO-001 and -002), and the two samples of pyritic Mt. Charlotte ore (106765, SE6-718.5) for trace element and/or Pb isotopic compositions. Outside the known ore zones to the north, west and south, two samples of Kapai Slate (GMKS-002 and KPD7-272A) and several samples of Paringa interflow shale and Black Flag Group from the 'SE' holes and KPDDH007 (see Table 5.1) were analyzed for trace elements.

Petrographic examination of all samples via optical microscope was followed up with SEM and LA-ICP-MS analyses; all analytical work was undertaken at the Central Science Laboratory (SEM) and at CODES (petrography; LA-ICP-MS), University of Tasmania. The laser methodology employed at CODES for trace element analysis of these samples is almost identical to that published in detail in Large et al. (2009) and Danyushevsky et al. (2011). We utilized a method containing 43 elements, of which 40 are quantifiable or semi-quantifiable using the UTas in-house STDGL2b2 standard glass (Danyushevsky et al., 2011), as well as the USGS basalt glass GSD-1G (Jochum et al., 2005) and in-house pyrite from the Huanzala deposit in Peru. Laser methodology for Pb isotopes is slightly different than that for trace elements, in that only the four Pb isotopes (^{204}Pb, ^{206}Pb, ^{207}Pb, and ^{208}Pb) plus a few other marker elements, such as ^{75}As, ^{202}Hg, and ^{197}Au, are analyzed. This is to maximize precision for Pb isotope measurements as well as to negate common isobaric interferences (e.g., ^{202}Hg on ^{204}Pb). Readers are referred to Meffre et al. (2008), Woodhead et al. (2009), and Steadman et al. (2013) for further details regarding elements chosen and instrumentation setup for Pb isotopes.

The SHRIMP-SI at the Australian National University (ANU) was utilized to determine concentrations of ^{32}S, ^{33}S and ^{34}S in both nodular and ore-stage pyrite samples. Due to the high rates of outgasing in sulfides and shales, and the sensitivity of the high-vacuum SHRIMP sample chamber to outgasing, composite mounts were created by placing small (≤5 mm) pieces of pyrite or pyritic shale from up to 6 samples in epoxy to create a single 25 mm diameter mount. All mounts were coated with 0.01 μm of gold prior to analysis in order to dissipate charge build up and provide approximately 10 kV of energy to ensure the ablated ions have the correct potential.

The SHRIMP analysis chamber was pumped down to less than 10^{-6} Pa prior to the start of an analysis session. Pre-ablation of the sample surface and sputtering of the SHRIMP spot for 120 s was completed for each measurement to eliminate any possible surface contamination. During the analysis phase, a 25 μm diameter primary Cs+ beam (10 keV) was focused on the unknown pyrite. The impact energy of the Cs^+ ions was held at 15 kV by holding the sample surface at -10 kV and accelerating the Cs^+ ions to +5 kV in the primary column. Each of the three S isotopes examined were analyzed with respective count rates of 630 MHz (^{32}S), 5 MHz (^{33}S), and 28 MHz (^{34}S). Every analysis records 10 cycles with 10 s of data acquisition in each cycle, and each S isotope was detected and measured using

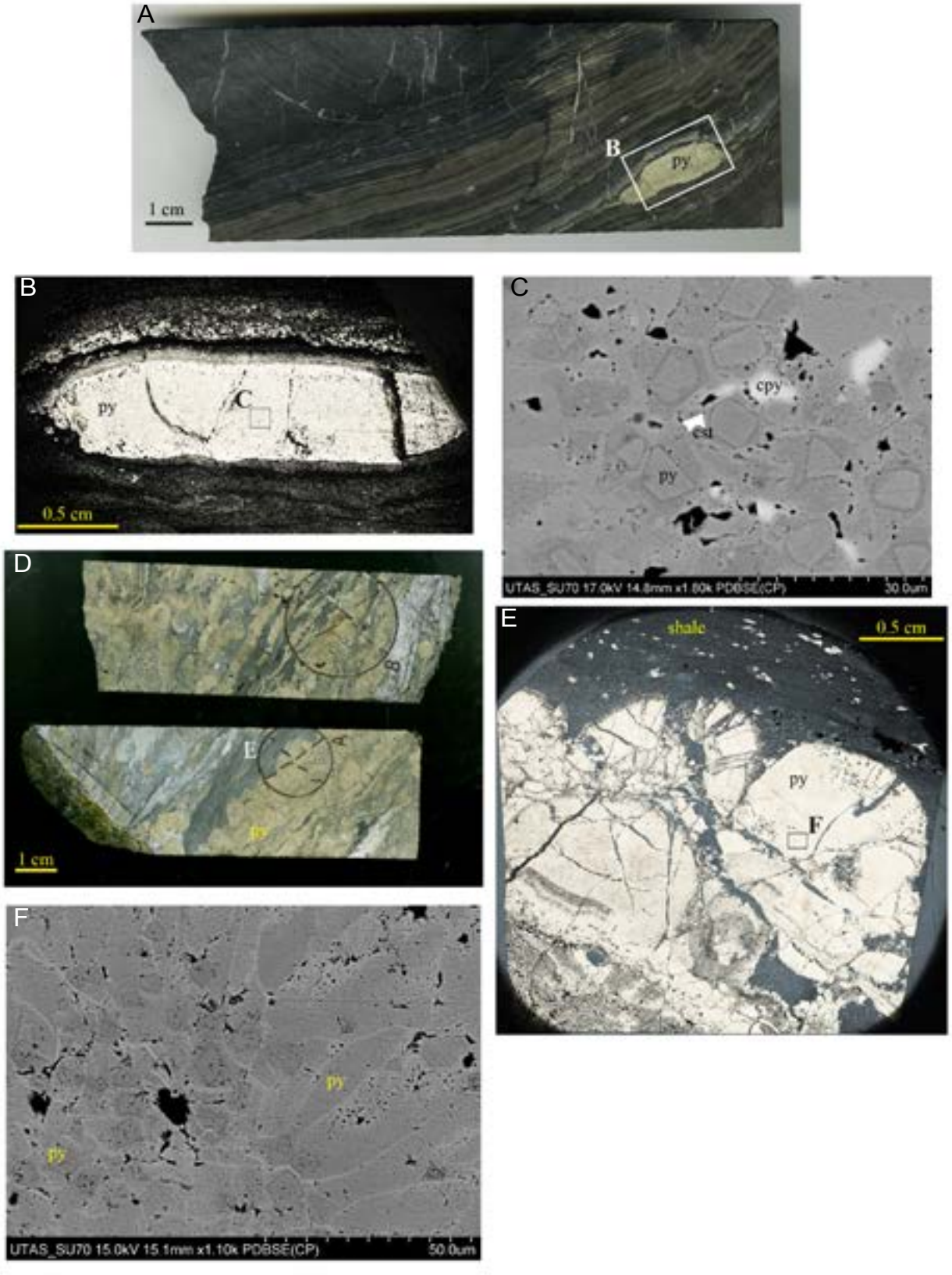

Fig. 5.4 Kapai Slate photos. A. Drill core of Kapai Slate from 0.5 km S of the Mt. Charlotte mine (core is 15 cm long, 4 cm wide). B. GMKS-002, a nodule from the Kapai Slate drill core in 'A'. Field of view is 2 cm. C. SEM image of the core of GMKS-002, showing zoned pyrite intergrown with chalcopyrite and cassiterite (bright phase in middle). D. Drill core sample of Kapai Slate from drill hole KPDDH007 (core pieces are 10 cm long and 4 cm wide). E. Photo mosaic of KPD7-272A, showing the intricate pyrite textures of the Kapai Slate. F. SEM image of the very fine-scale growth zonation in pyrite from KPD7-272A. Compare with that in 'C' from GMKS-002.

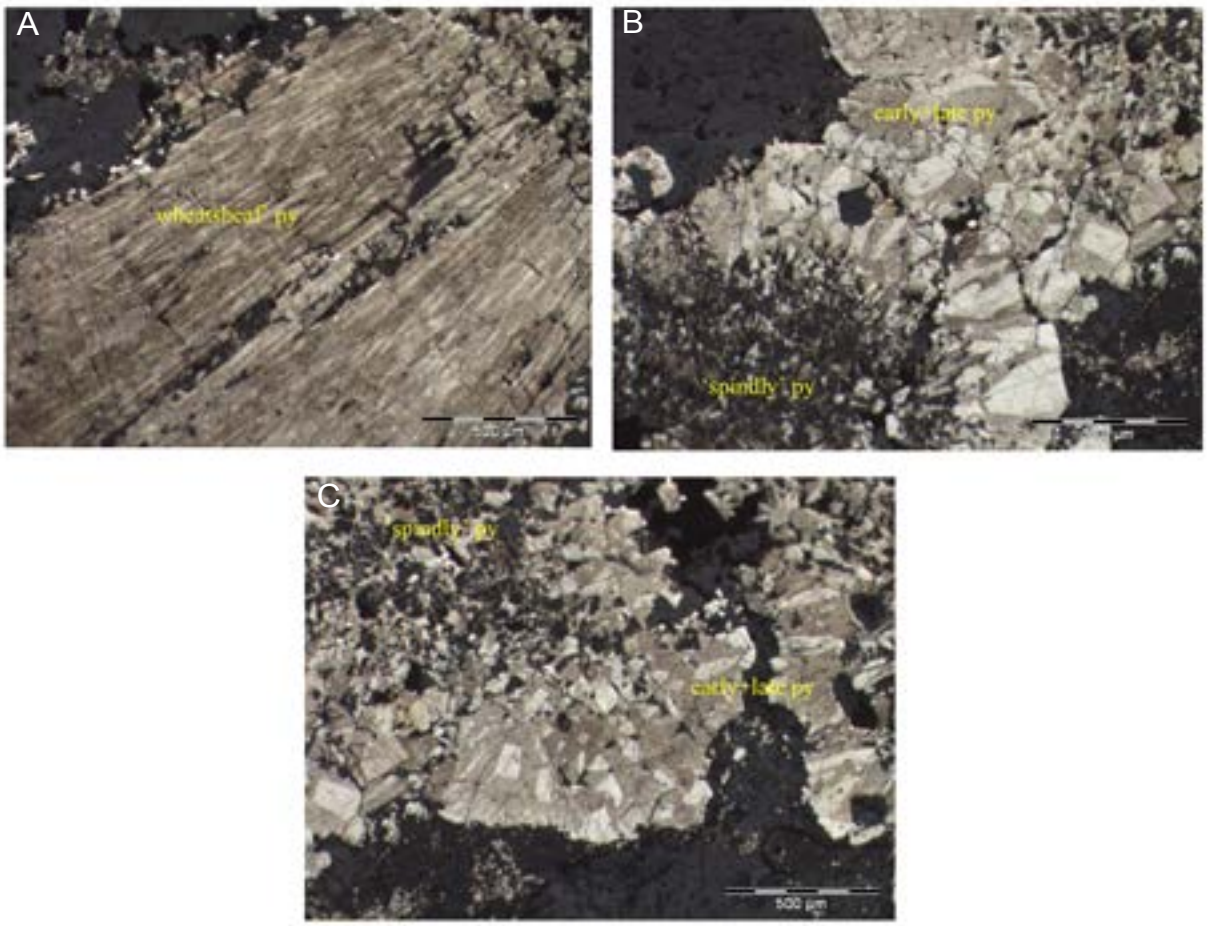

Fig. 5.5 Detailed photographs of etched pyrite in KPD7-272A, showing 'wheatsheaf' texture (A), as well as intergrowths of this early form and a later, more euhedral type which is less reactive to the acid etch (B and C). So-called 'spindly' pyrite can be seen in the lower left-hand portion of the photograph in B.

Faraday cups (Ireland et al., 2008). The standard materials, Balmat pyrite (Crowe and Vaughan, 1996; Williford et al., 2011) and an in-house pyrite from New Zealand ($\delta^{34}S$ ~4±0.1‰; $\Delta^{33}S$ = 0±0.2‰), were analyzed twice approximately every 7 analyses (~90 minutes). Typical errors on all analyses were 0.1‰ for $\delta^{34}S$ and 0.2‰ for $\Delta^{33}S$.

5.5 Results

5.5.1 Mineralogy and petrography of samples from the Kapai Slate, Paringa Interflow Shale, and Black Flag Group

Kapai Slate. Figure 5.4A shows Kapai Slate from north of the Super Pit (sample 'GMKS'), which is marked by thin beds of varying pyrite content along with a pyrite nodule in the lower right-hand corner of the photo. Pyrite nodules from this sample of Kapai Slate are spherical to ovoid and contain growth zones, though these are not readily visible either in hand sample or under the microscope. Figure 5.4B shows the ovoid nodule GMKS-002, which has a thin rim developed around an interior of mostly equigranular pyrite (intergrown with chalcopyrite). Around the nodule is a zone of very fine grained pyrite, which is then surrounded by shale matrix and another, coarser-grained variety of pyrite. Figure

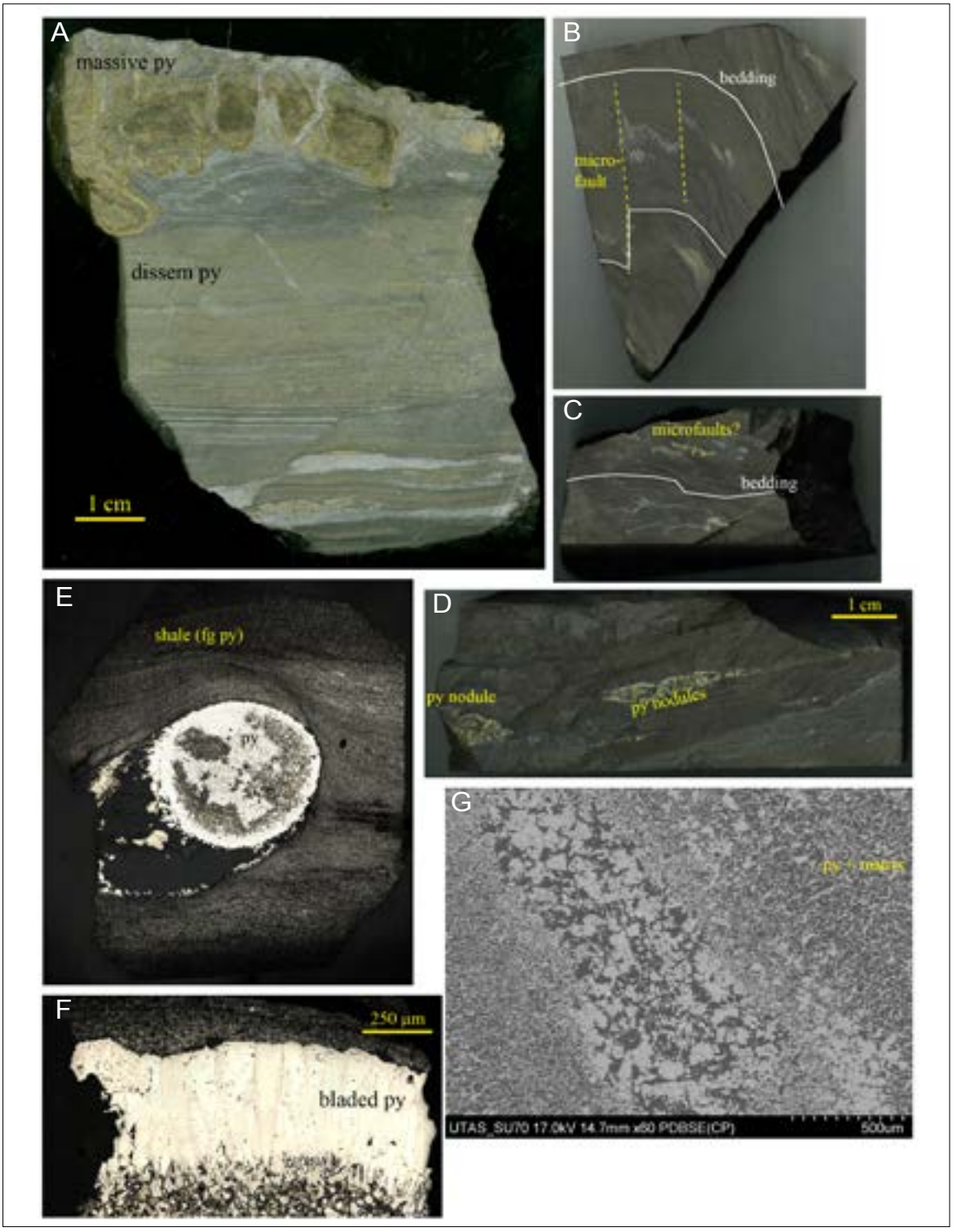

Fig. 5.6 Pyrite-rich Paringa interflow shale photos. A. Large (15 cm by 10 cm) hand sample of Paringa shale from the Super Pit (sample GMSP-009), showing both massive pyrite and fine laminations highlighted by pyrite. B. The next three photos are of the same rock, but each was taken at different angles. The rock is approximately 15 cm by 10 cm. The first photo is taken perpendicular to bedding, showing folds which have experienced mm-scale offset. C. Photo taken parallel to bedding. The cleavage is more noticeable in this photo. D. Photo again taken parallel to bedding, second face. Here, two (possibly three) pyrite nodules can be seen, parallel to bedding and deformed. E. GMSP-006, a pyrite nodule. Pressure shadows have developed on this nodule, which are filled by quartz and minor sulfides (pyrite, chalcopyrite, and sphalerite). A significant amount of the host rock is still attached; bedding (highlighted by fine-grained pyrite) deforms around the nodule. Field of view is 2 cm. F. Detail of the rim in GMSP-004, which clearly demonstrates the radiating nature of pyrite in the outermost rim of Paringa interflow shale nodules. The rim is 5 mm wide (i.e., from top to bottom). G. Detail of GMSP-002, showing the variety in nodule pyrite textures. The core of this nodule is silicate/carbonate-rich with coarse-grained pyrite, which is completely surrounded by a zone of intergrown pyrite 'spicules' and matrix. This texture is common in Paringa interflow shale pyrite nodules.

5.4C is an SEM image showing the internal pyrite texture of the pyrite nodule GMKS-002; note the multiple growth zones in the pyrite crystals (represented by different shades of gray), as well as the presence of chalcopyrite (gray-white) and cassiterite (SnO_2; bright white phase in middle of image).

Samples of Kapai Slate taken from KPDDH007 are characterized by semi-massive to massive pyrite mineralization (almost 100 vol. % pyrite in some areas) interspersed with carbonate-rich shale containing disseminated pyrite (Fig. 5.4D). The Kapai Slate interval in KPDDH007 contains a number of diverse pyrite textures, including 'wheat sheaf', 'feathery', and 'spindly' pyrite, (Fig. 5.4E, 5.5A-C). SEM imaging further highlights complex internal chemical zonation within these pyrites on the micro-scale, as evidenced by the alternating dark and light-colored growth zones in cross-sections of the 'feathery' pyrites (Fig. 5.4F); similar textures are present in GMKS-002 (Fig. 5.4C). The 'feathery' appearance of pyrite in sample KPD7-272A is also reminiscent of cone-in-cone structures reported by Guy et al. (2014) in pyrites from the West Rand Group in the Witwatersrand district of South Africa, which those authors interpreted as a typical diagenetic texture. Other pyrites in these samples overgrow the 'wheat sheaf', 'feathery', and 'spindly' pyrites, and these are typical euhedra with no apparent zonation. In the shale matrix to the massive/semi-massive pyrite layers, disseminated pyrite containing abundant matrix inclusions are present (Fig. 5.4E).

Paringa Basalt interflow shale. In both SE-12 and KPDDH007, the Paringa interflow shale is located at the top of a hyaloclastite within the Paringa Basalt, which presumably marks the cessation of Paringa Basalt volcanism. However, this geologic relationship is not preserved in our samples collected from the Super Pit due to the effects of blasting. Two samples of the Paringa Basalt interflow shale from the Super Pit are shown in Figure 5.6A-D, with photos in 'B', 'C', and 'D' being of the same rock but taken at different angles to bedding. The first sample contains a layer of massive pyrite at the top, with complex growth zones which has been brecciated, fractured and partially infilled with later pyrite and minor chalcopyrite, below which is thinly-bedded shale containing a high degree of fine-grained pyrite, giving the rock its brown color (Fig. 5.6A). Folded bedding planes in the second sample are offset by small faults with cm-scale displacement (Fig. 5.6B), and a spaced cleavage has developed at a relatively high angle to bedding (Fig. 5.6C). Small but coherent pyrite bodies (nodules?) are also cut by the foliation (Fig. 5.6B). In the third photo of this sample, looking perpendicular to bedding, three pyrite nodules are present (Fig. 5.6D).

The other images in Figure 5.6 are of pyrite nodules within the Paringa interflow shale samples from the Super Pit. In general, Paringa interflow shale pyrite nodules have an inner zone of silicate-carbonate matrix material which is completely surrounded by pyrite 'needles', or 'spindly' pyrite (Fig. 5.6I). In between this zone and the outermost rim is an area dominated by silicate-carbonate material with medium-grained pyrite, as well as significant chalcopyrite and sphalerite (Fig. 5.6E-F). The outer rims on the interflow shale nodules vary in size, but generally have a radiating texture, best seen in Figure 6h. These textures are similar to those reported by Falconer et al. (2006) and Guy et al. (2014), who posited marcasite precursors for the diagenetic pyrites they studied. On the other hand, Rickard (2012) maintains that bladed/columnar pyrite is a common diagenetic texture.

A second facies of the Paringa Basalt interflow shale contains brecciated, re-sedimented and deformed pyrrhotite nodules (Fig. 5.7A); Clout (1989) referred to this rock type as "pyrrhotite-rich hyaloclastite." The key difference between this sample and the other nodules previously described from this formation is that all of these nodules are pyrrhotite (with intergrown carbonates and silicates, which are the darker areas of the nodules). In this sample, there are two types of pyrrhotite defined by texture: the first (and presumably earliest) pyrrhotite has ubiquitous tiny (< 1 μm) gangue inclusions, whereas the later type is virtually devoid of gangue minerals. Figure 5.7C-D is also a pyrrhotite-rich rock from the Paringa interflow shale (i.e., black shale containing pyrite or pyrrhotite nodules), but this sample is from drill hole KPDDH007.

Paringa interflow shale from SE-12 is characterized by widespread pyrrhotite mineralization (Fig.

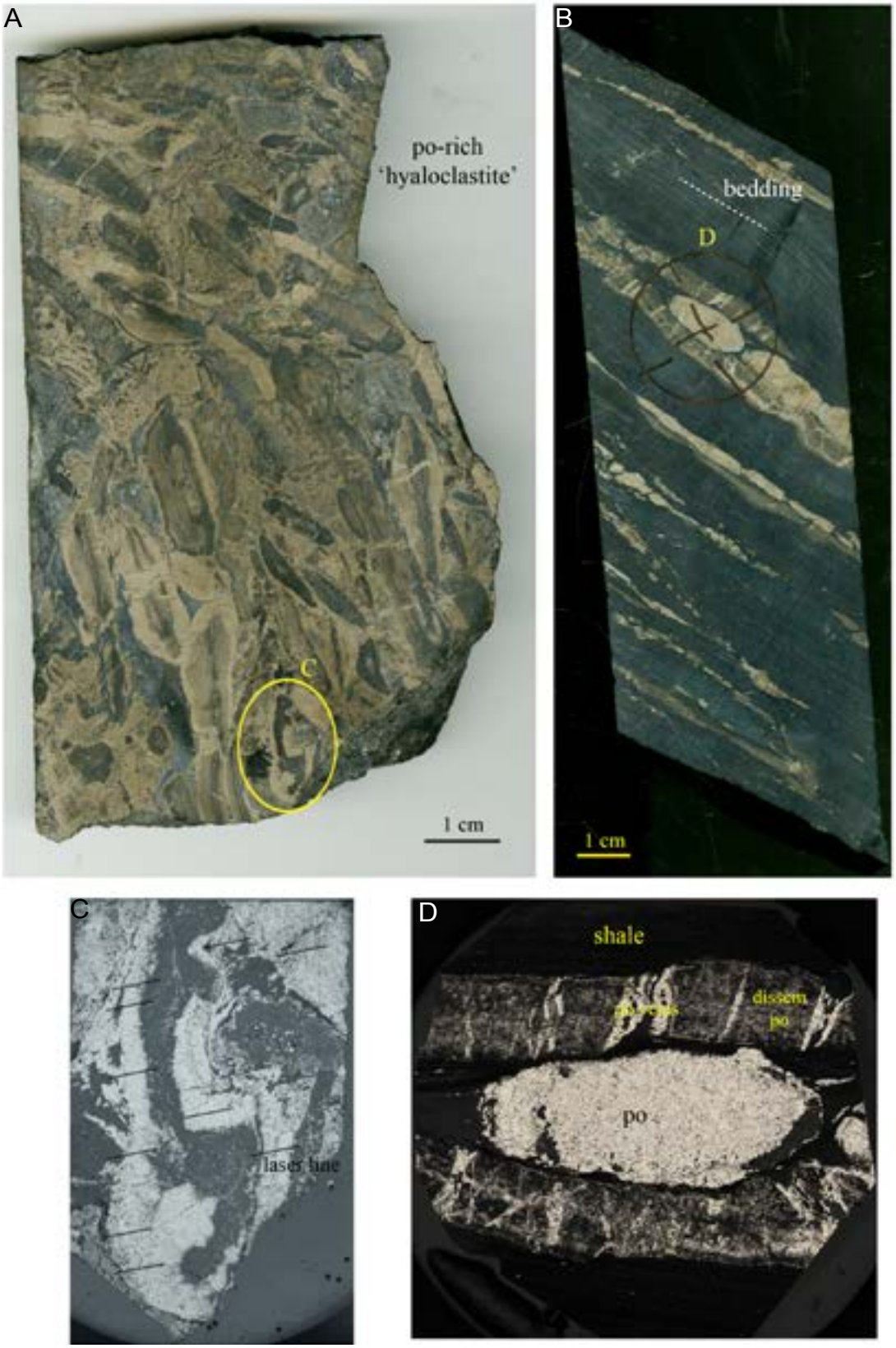

Fig. 5.7 Pyrrhotite-rich Paringa interflow shale, part I. A. Brecciated and re-sedimented pyrrhotite nodules. Sample comes from the Super Pit, a few hundred meters south of the pyrite-rich samples collected in the field. Size is 15 cm long by 8 cm wide. B) Black shale from drill hole KPDDH007, showing nodular pyrrhotite intimately associated with later forms of the same mineral. C) polished mount of nodule circled in 'A' (ORY). Black lines across sample are due to laser analyses. D) Polished mount of nodule circled in 'B' (KPD7-491).

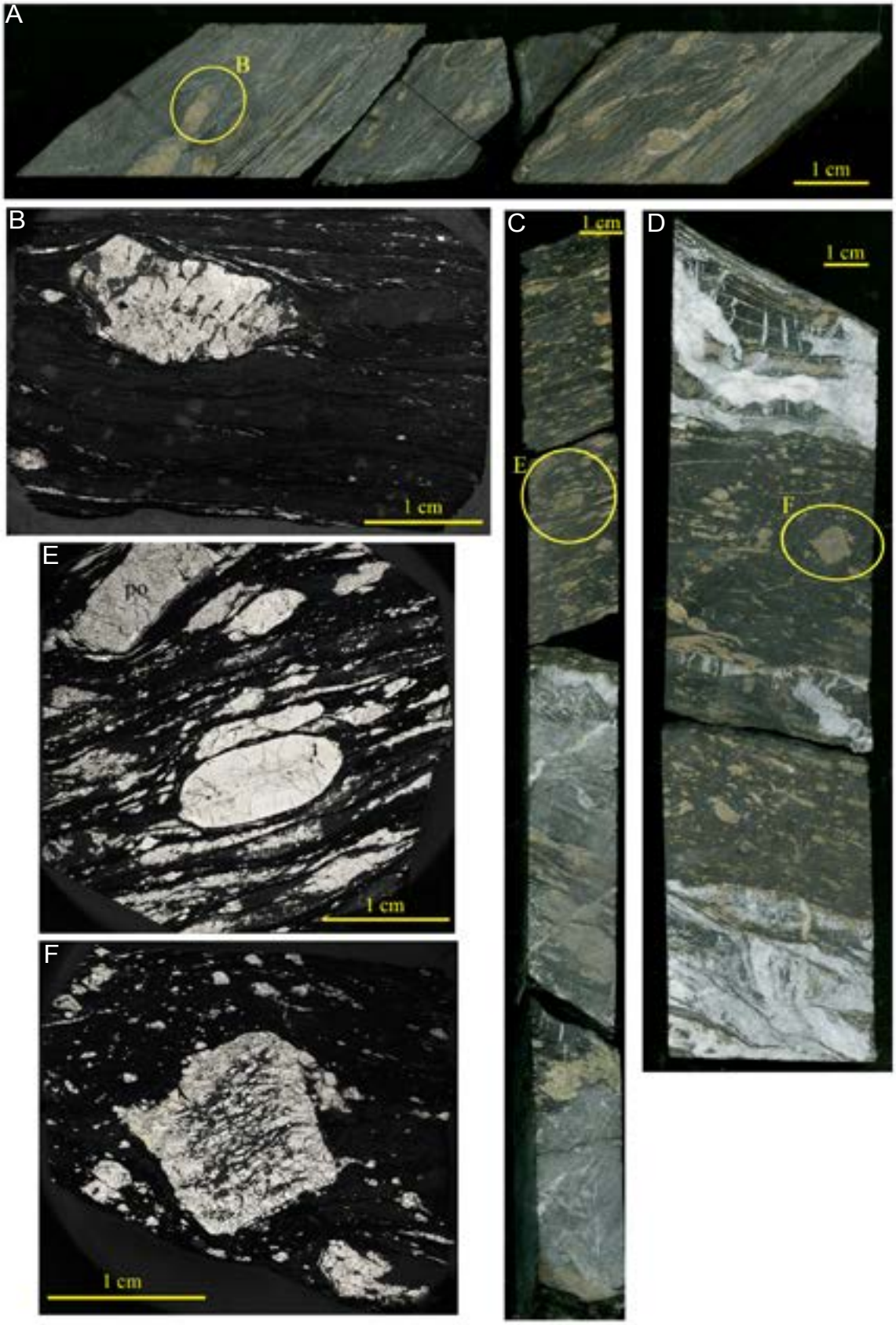
A
B
1 cm
B
1 cm
C
1 cm
E
D
1 cm
F
E
po
1 cm
F
1 cm

Fig. 5.8 (previous) Pyrrhotite-rich Paringa interflow shale, part II. A. Moderately deformed pyrrhotite-rich sample from SE-12 (SE12-1435.5). Sample is 9 cm long, 4 cm wide. B. Pyrrhotite nodule from SE12-1435.5, showing both the pyrrhotite nodule and the later pyrrhotite replacing it (the later pyrrhotite appears more reflective than the nodule due to a relative lack of gangue inclusions). Pyrrhotite 'streaks' highlight the foliation. Field of view is 1.5 cm. C. Quarter-cut drill core of pyrrhotite-rich Paringa interflow shale from KPDDH007, showing an abundance of pyrrhotite nodules and variation in lithology. The section is 25 cm long. D. Same unit from the same drill hole, again displaying a high percentage of pyrrhotite nodules. Quartz-carbonate veins cut through the unit and displace the nodules. Core sample is 12 cm by 4 cm. E. Polished mount of section in 'C', highlighting the ovoid nodule in the middle. Field of view is 2 cm. F. Polished mount of large pyrrhotite nodule in 'D', with an unusual diamond-shaped outline and abundant gangue inclusions (mostly carbonate). Field of view is 2 cm.

5.8A). Some of the pyrrhotite is in nodule form, and these nodules show evidence of post-depositional deformation (e.g., attenuation) and alteration (pyrrhotite veinlets cross-cutting the nodule; Fig. 5.8B). Pyrrhotite 'streaks' highlight the foliation (Fig. 5.8B). The pyrrhotite-rich Paringa interflow shale in KPDDH007 sits approximately 200 meters below the Kapai Slate interval; as in the example from SE-12, this horizon is dominated by pyrrhotite nodules and laminae with rare pyrite in silicate-rich shale (Fig. 5.8C-F). On the microscopic level, there are two types of pyrrhotite defined by texture, just as in the brecciated pyrrhotite nodule sample from within the deposit (Fig. 5.7A) and the Paringa interflow shale from SE-12: the earlier type is rich in minute (<1 μm) gangue inclusions, while the later variety is virtually gangue inclusion-free. The first pyrrhotite comprises the nodules and laminae, whereas the second pyrrhotite occupies the pressure shadows to these nodules and laminae.

Black Flag Group shale. Shale belonging to the Black Flag Group is not as sulfidic as the previous two formations, but its nodule abundance is among the highest of our sample set. Figure 5.9A is a photo of sample 'BFB' from the Chaffers region of the Super Pit; note that bedding deforms around the largest pyrite nodule. The photo in Figure 5.9B is of the large nodule in 5.9A, showing the ~1 cm-long rim and recrystallized (?) pyrite core. Growth textures are well-preserved in the rims; they are similar to the radiating-textured rims on pyrite nodules from the Paringa interflow shale (e.g., Fig. 5.6H), except that here, a significant component of very fine grained, non-sulfide 'matrix' material is intergrown with the pyrite. The Black Flag Group samples from SE 4 (SE4-821 and SE4-815.8) are characterized by large (~1 cm diameter), partially recrystallized pyrite nodules, as well as disseminated fine grained pyrite which has also been partially recrystallized (Fig. 5.9C-E).

5.5.2 Ore sample mineralogy and petrography

The sample designated 'Trafalgar bx' is from the Trafalgar area of the Super Pit, near the Golden Mile Fault, and comprises brecciated fragments of Golden Mile Dolerite partially replaced by banded ankerite (Fimiston stage 1; Clout, 1989) and rimmed by pyrite-tourmaline mineralization (Fimiston stage 2; Clout, 1989), all of which is cemented by chalcedonic quartz (Fimiston stage 3; Clout, 1989; Fig. 5.10A). The OSNACA samples 700192, 700264, and 700265 and the UTas sample 106765 (Fig. 5.10B-D) are all silicified GMD hosting pyrite cubes and pyritohedrons containing complex internal zonation, as revealed by SEM imaging (Fig. 5.10E). GMO-001 and GMO-002 come from the same rock, a polymictic breccia composed of dominantly Paringa Basalt clasts and lesser black shale clasts, the latter containing small pyrite euhedra; locally abundant arsenopyrite is present throughout the rock (Fig. 5.11A-B). This sample was collected from the northern end of the Super Pit in the Eastern Lode System, in the same area as pyrite nodule samples GMSP-003, -006, -008, and GMSP-009 (Fig. 5.2B). Pyrite in the GMO samples is generally one of two types: large (up to 5 mm diameter), inclusion-free euhedra, or small (~10 μm) disseminated crystals (Fig. 5.11B). Arsenopyrite is characteristically mm-scale euhedra containing inclusions of pyrite. The Mt. Charlotte samples 106755 and SE6-718.5 are both characterized by medium-grained (1-2 mm) pyrite euhedra hosted in ankerite-altered Golden Mile Dolerite (Figs. 5.11C and D).

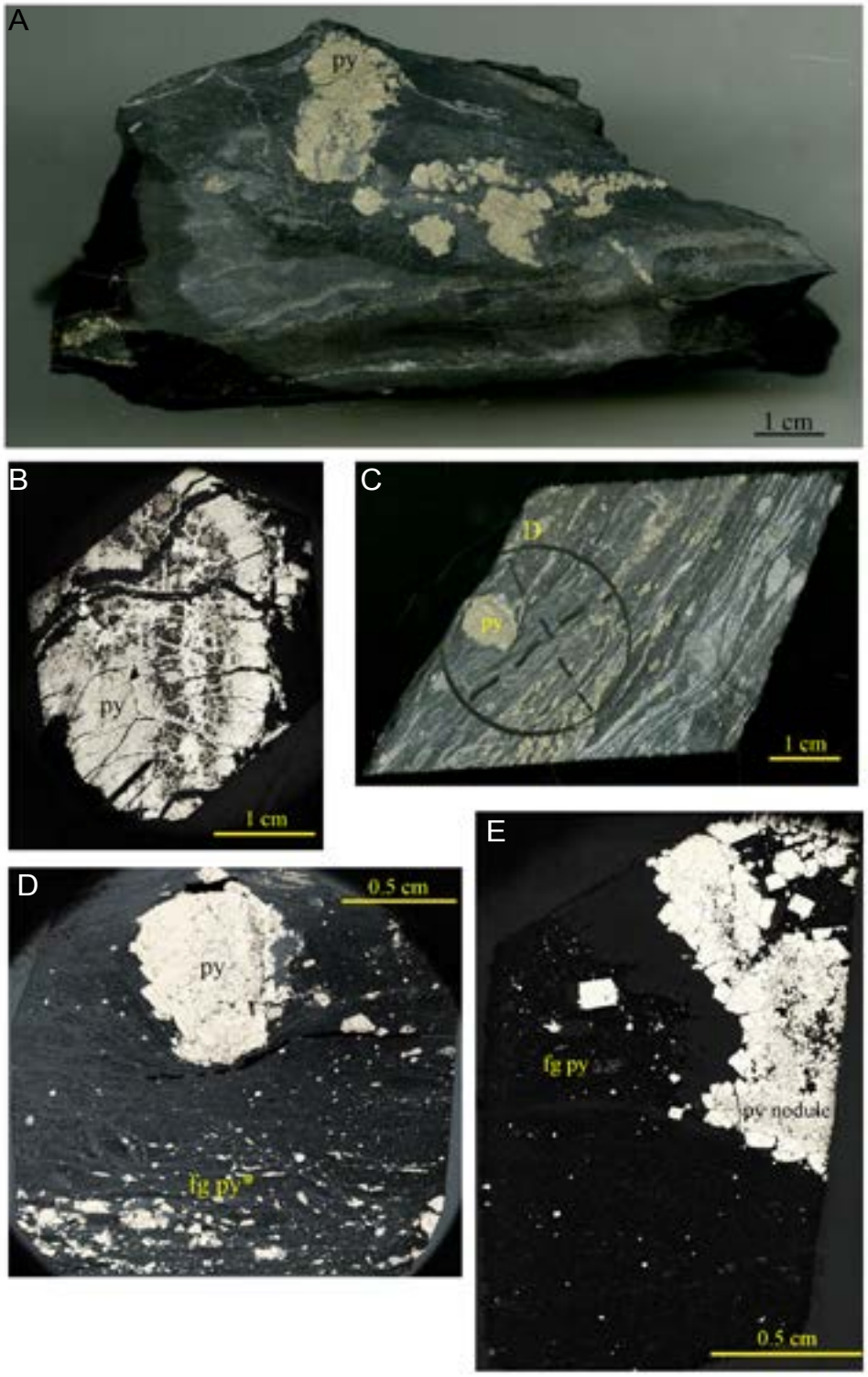

Fig. 5.9 Photos of shale and pyrite nodules from the Black Flag Group. A. Hand sample 'BFB' taken from the Chaffers area of the Super Pit (Fig. 5.2a), immediately below the Golden Mile Fault. The rock shown is 10 cm wide. B. Large (> 2 cm) pyrite nodule from BFB (BFB-003) with thick (~0.5 to 1 cm) rim and recrystallized pyrite core. Late sulfide-poor veins cut across the sample. C. Drill core sample of Black Flag Group shale from SE-4. Sample is 4 cm wide, 6 cm long. D. Polished mount of sample in 'C' (SE4-821), showing a large, recrystallized pyrite nodule with finer grained pyrite (fg py*) in the matrix which has also been recrystallized. Field of view is 2.5 cm. E. Part of another pyrite nodule from SE-4 (SE4-815.8), with attached shale matrix. Sample is 1 cm by 2.5 cm.

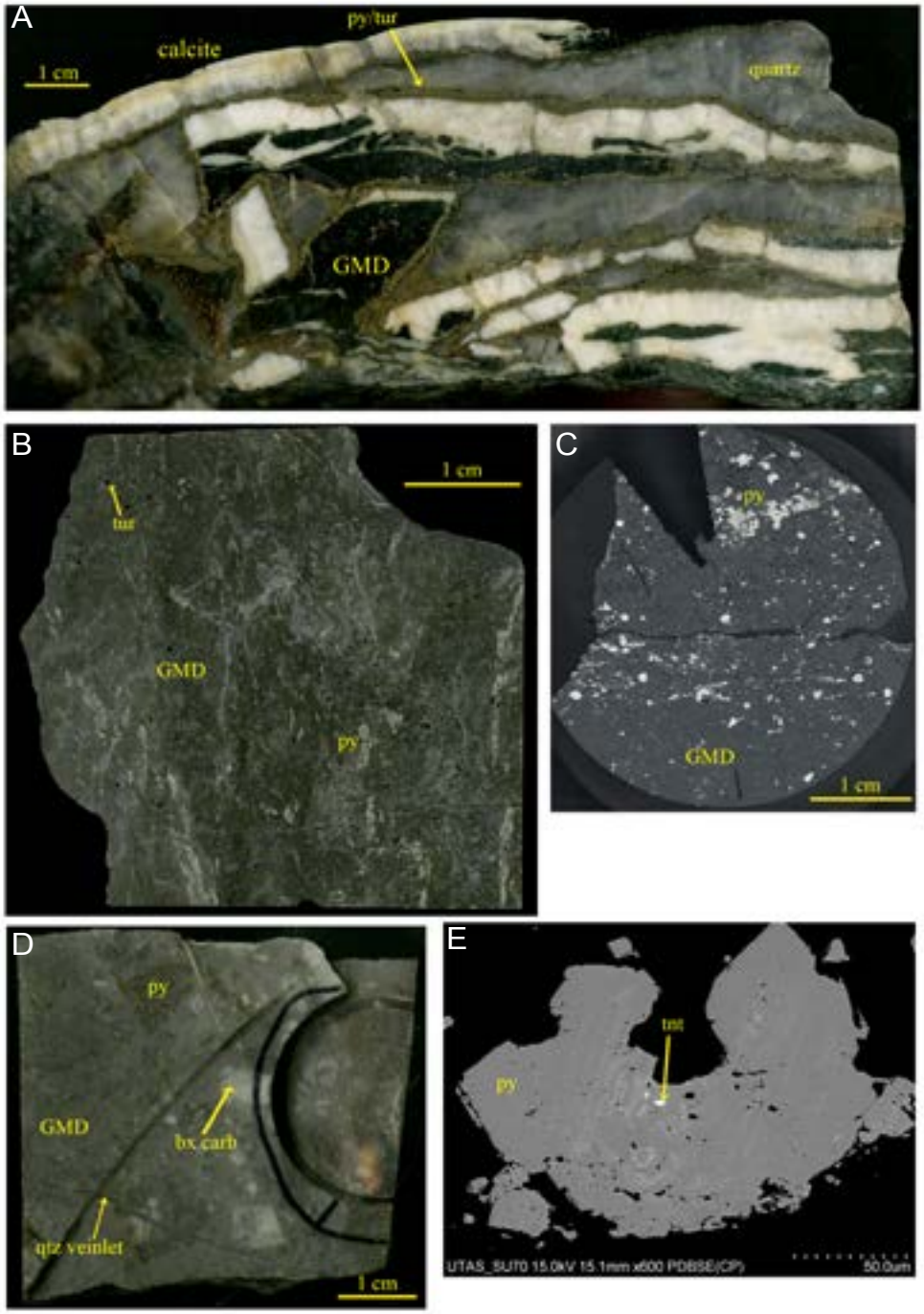

Fig. 5.10 Fimiston ore samples. A. Sample from the Trafalgar area of the Super Pit (Fig. 5.2a), displaying the three primary stages of the Fimiston event (Clout, 1989): Stage 1 is represented by banded calcite/ankerite replacing fragments of the Golden Mile Dolerite (dark green-black), while stage 2 is present as rims of pyrite±tourmaline on the altered GMD fragments. The matrix to this breccias sample is quartz (stage 3), which is in part chalcedonic. Sample is 17 cm long, 8 cm wide. B. Polished slab of typical siliceous Fimiston lode containing disseminations of pyrite and tourmaline (tur) in highly altered Golden Mile Dolerite. Thin, brecciated carbonate veins are also present. C. Polished mount of OSNACA (Ore Samples Normalized to Average Crustal Abundance) sample 700264, which, while not cut from the rock in 'B', was sampled from one very much like it. The rock has abundant pyrite, both as disseminated individual crystals and 'stringers' of fine-grained pyrite. Dots on the various pyrite crystals in the photo are laser analysis craters (for Pb isotopes). Field of view is 2.5 cm. D. Sample 700192, from the OSNACA suite. This rock is a brecciated and silicified piece of Golden Mile Dolerite. Fine-grained disseminated pyrite is present throughout, as is brecciated carbonate. Sample width is 5 cm. E. SEM image of a typical Fimiston-stage pyrite crystal, showing fine-scale growth zonation highlighted by changes in chemistry (here related to As content – thin, bright zones in image indicate high [> 10,000 ppm] As) and abundant inclusions, in this case tennantite (tnt), but in others, native gold and/or gold tellurides are present.

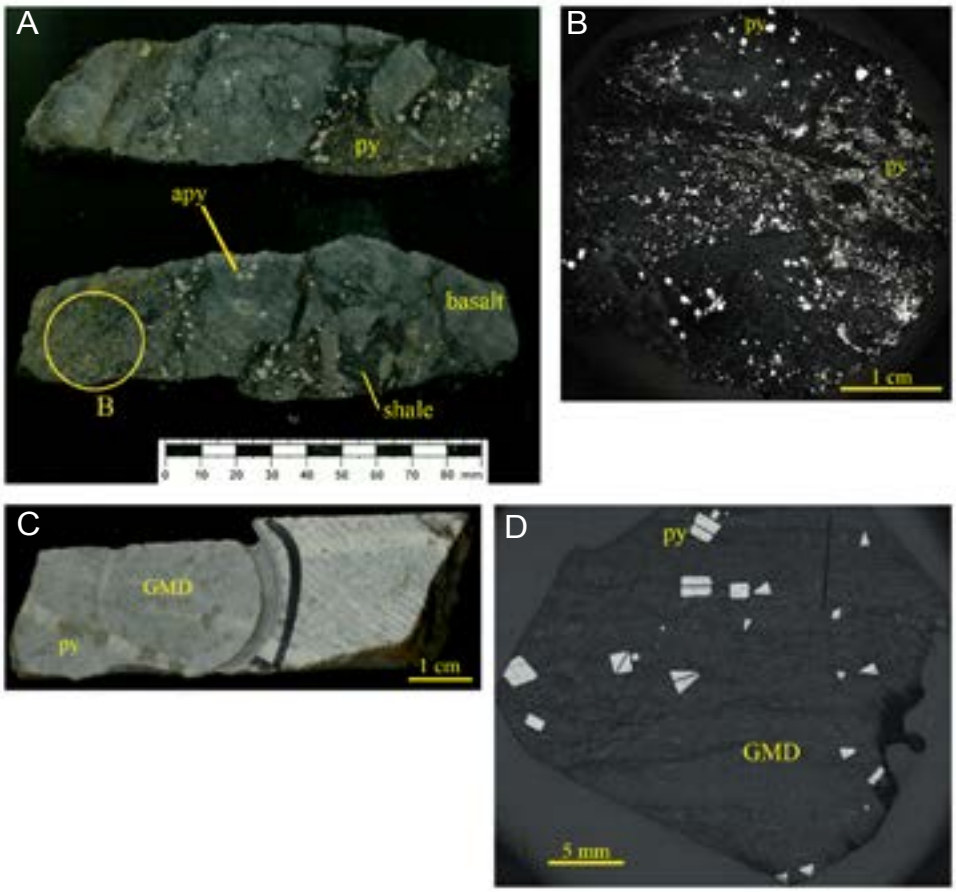

Fig. 5.11 Fimiston (continued) and Mt. Charlotte samples. A. Scan of two halves of GMO, a breccia composed primarily of Paringa Basalt and black shale clasts. The entire rock is mineralized with pyrite and arsenopyrite. B. Polished mount of GMO (GMO-002), showing abundant pyrite mineralization. Field of view is 2 cm. C. Quarter-cut drill core of carbonate-altered Golden Mile Dolerite (GMD) with Mt. Charlotte-style pyrite euhedra, drill hole SE-6. D. Polished mount of 106755, which is mineralized GMD (unit 8) from the Flanagan Fault zone at the underground Mount Charlotte mine. Lines across the pyrite crystals are laser burns (for Pb isotope analysis). Field of view is 2.5 cm.

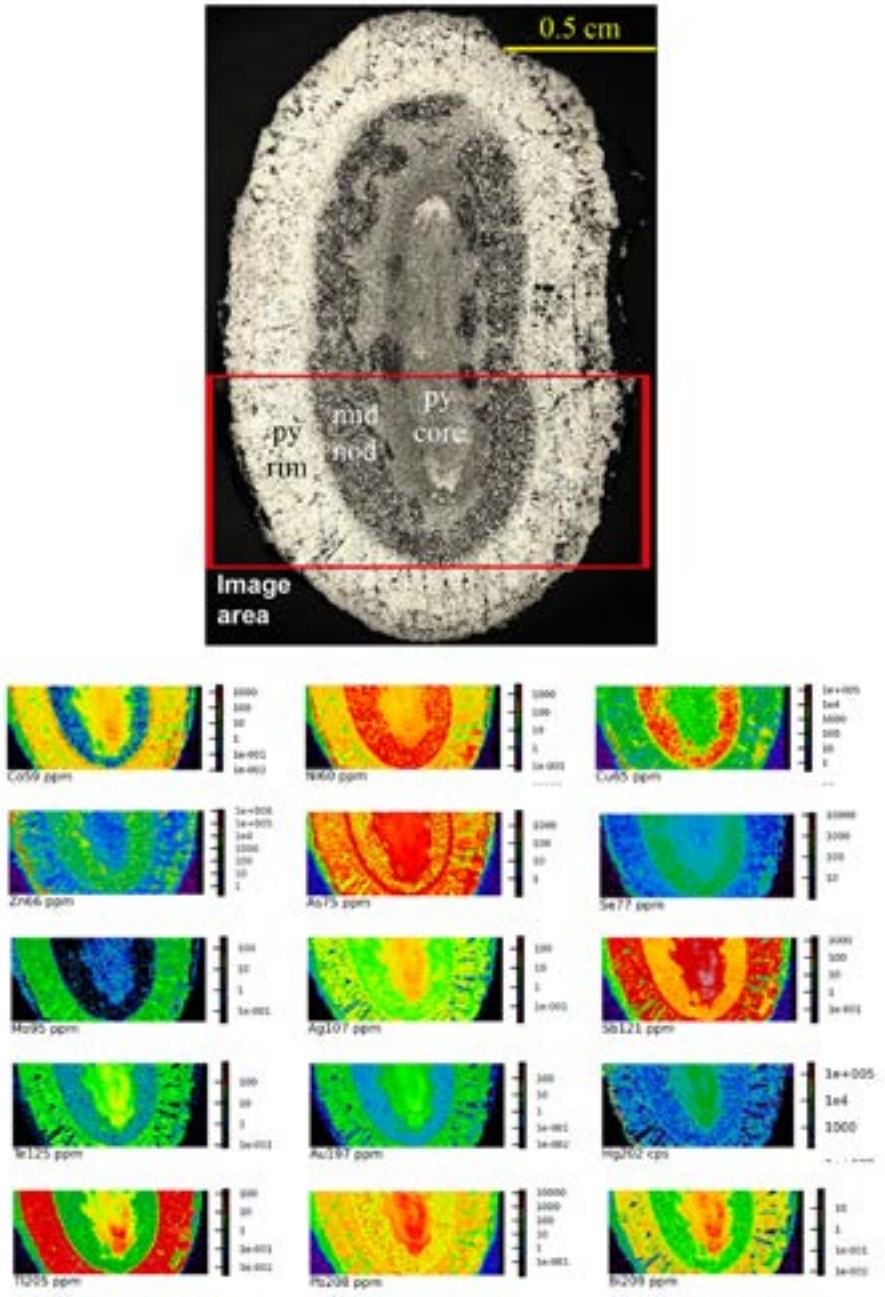

Fig. 5.12 GMSP-003 LA-ICP-MS trace element image. Pyrite in the cores to Paringa interflow shale pyrite nodules is enriched in Co, Ni, Cu, As, Mo, Ag, Sb, Te, Au, Hg, Tl, Pb, and Bi. Intermediate zones contain greater Ni, Cu, Zn, and Se relative to the core pyrite, partially due to a different pyrite type but also due to the presence of chalcopyrite and sphalerite. The outer pyrite rim is almost geochemically identical to the pyrite core, except that it has greater Mo and Tl but less Hg. The nodule is 2.5 cm long (from top to bottom of image).

5.5.3 LA-ICP-MS geochemical investigation - imaging of proximal samples

Paringa interflow shale nodule GMSP-003. This nodule is composed of at least four concentric pyrite-matrix or pyrite-only zones (Fig. 5.12). The matrix to the nodule is heterogeneous; minerals in these zones include quartz, white mica, chlorite, and Fe-carbonate. The innermost pyrite is characterized by fine 'spindle'-shaped pyrite crystals intergrown with mica and lesser carbonate. Enveloping this irregular, sausage-shaped area is a zone of pyrite-poor, carbonate-rich material that is itself overgrown by a thick (~2 mm) rim of almost pure pyrite (small amounts of chalcopyrite and sphalerite also occur in the outermost rim, along with rare silicates and carbonates). The pyrite in the outermost rim is bladed (cf. Fig. 5.6H).

One-fourth of this nodule, encompassing all visible growth zones, was mapped via LA-ICP-MS; results are shown in Figure 5.12. The most striking feature of GMSP-003 is the well-defined and concentric nature of the growth zones, to which the trace elements correspond: Cobalt, Ni, Cu, Zn, As, Mo, Ag, Sb, Te, Au, Tl, Pb, and Bi all co-vary with each other in the different pyrite types, with the exception of the pyrites in the relatively pyrite-poor zone inside the thick pyrite rim; these are apparently more enriched in Se and less enriched in all other trace elements than the other pyrite types (Fig. 5.13). Key trace elements include Au (3-4 ppm average, with small electrum inclusions within the inner pyrite core and outer pyrite rim), Te (30-40 ppm; ~10 times higher concentration than gold), Ag (30-40 ppm, same as Te), Sb (>1,000 ppm in the core of the nodule), Tl (maximum >50 ppm in the rim), Pb (>1,000 ppm in the core), and Bi (maximum 20-30 ppm). Abundant chalcopyrite and sphalerite inclusions are present, as evidenced by the high Cu and Zn zones (Fig. 5.12); in general, where these are plentiful, pyrite is less common.

Paringa interflow shale nodule GMSP-001. Like GMSP-003, GMSP-001 has an exterior rim of radiating pyrite, but this rim is much thinner than that of GMSP-003, and the interior growth zones of GMSP-001 are not as well-defined as in GMSP-003 (Fig. 5.13). Pyrite in the innermost zones has the 'spindle' shape seen in GMSP-003, but in the outer zones euhedral to subhedral pyrite is prevalent. The matrix to the innermost nodule is largely iron carbonate, with additional fine-grained silicates, especially in one small zone near the center of the nodule. This domain appears to post-date the thin rim of pyrite in the middle. On either end of the nodule, pressure shadows have developed, which are filled by sulfides (pyrite, chalcopyrite, and sphalerite) on one end.

Approximately half of this Paringa interflow shale nodule was imaged, and like GMSP-003, it has significant enrichments in Co, Ni, Cu, Zn, As, Mo, Ag, Sb, Te, Au, Hg, Tl, Pb, and Bi, all of which are covariant (Fig. 5.13). Also like GMSP-003, there are two zones of high Au-Te-Ag-As-Sb-Hg-Tl-Pb-Bi, separated by a 'moat' of pyrite and matrix that contain lower amounts of these elements but higher Se (100 ppm in middle vs. 50 ppm in core and rim). Molybdenum shows the same bimodal concentration differences as in GMSP-003 (i.e., high values in the rim, low values in the core), along with Tl and Hg, although this behavior is masked somewhat in the latter element due to the plethora of sphalerite inclusions, particularly in the rim zone (Fig. 5.13). Chalcopyrite is also abundant within the nodule, where it is intergrown with pyrite.

Of particular interest in this nodule is the thin but somewhat continuous zone of very high Ni (>100,000 ppm) and Sb (>200,000 ppm) concentrations. SEM investigations reveal the presence of ullmannite (NiSbS) intergrown with pyrite and chalcopyrite in these areas (Fig. 5.14A-D). Ullmannite is a sulfosalt that forms a series with Willyamite ([Co, Ni]SbS) and is also related to the minerals gersdorffite (NiAsS), paracostibite (CoSbS), and cobaltite (CoAsS). Selenium and As are also enriched in ullmannite from GMSP-001 relative to the nodule pyrite. Ullmannite has been reported from the Golden Mile previously by Golding (1978), specifically in Green Leader ore.

Pyrite in the GMSP-001 pressure shadow is enriched in Co (which is also zoned), Ni, and Se, but depleted in all other trace elements. Chalcopyrite in the pressure shadow contains low-level Ag (~10

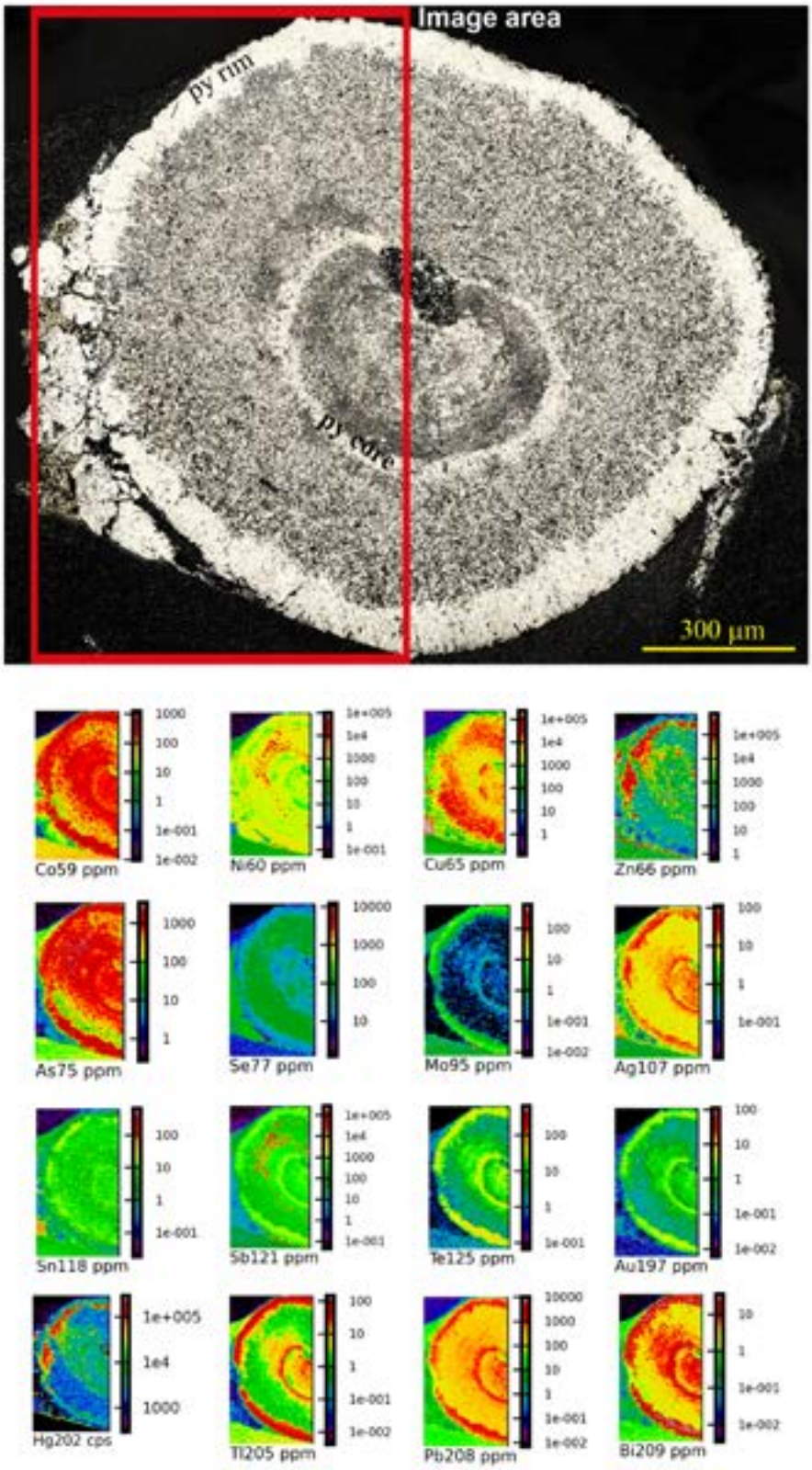

Fig. 5.13 Trace element image of GMSP-001. As this nodule is also from the Paringa interflow shale (like GMSP-003), the trace element contents and patterns are much the same, but there are a few differences. The biggest change between this nodule and GMSP-003 (Fig. 5.12) is the presence of ullmannite (NiSbS) in a crudely ovoid ring within the nodule. This nodule also contains more sphalerite inclusions, and has well-developed pressure shadows containing pyrite, chalcopyrite, and sphalerite. The pyrite in the pressure shadow has very different trace element characteristics from the nodular pyrite. Field of view is approximately 1.5 cm.

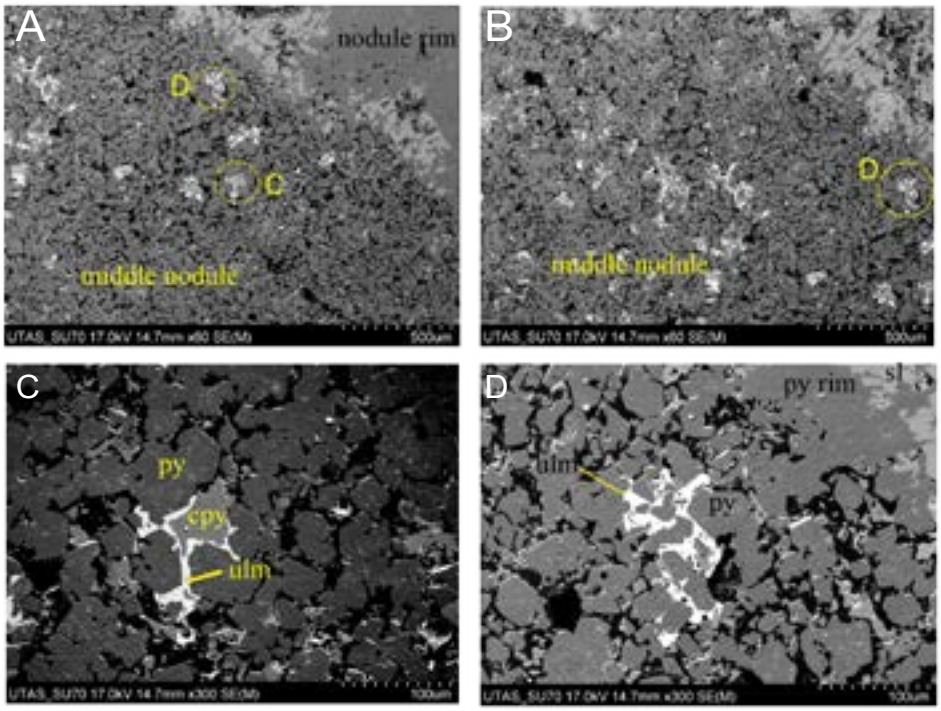

Fig. 5.14 Ullmannite (NiSbS) in GMSP-001. This sulfosalt is intergrown with pyrite, chalcopyrite, and the carbonate-silicate nodule matrix. In certain cases (see 'D'), the ullmanite appears to be replacing the pyrite euhedra/subhedra.

ppm), Sn (~50 ppm), and Au (~0.1 ppm).

Paringa interflow shale nodule GMSP-008. GMSP-008 (Fig. 5.15A-C) is not as complex as GMSP-003 or GMSP-001 (with respect to pyrite), but it nonetheless has internal and external diversity that the other two lack. On the rim of the nodule, a clear distinction between nodule pyrite and later coarse-grained pyrite is evident by the slight change in color and shape of the grains (Fig. 5.15B-C). Intergrown with this later pyrite are other sulfides (e.g., chalcopyrite, sphalerite, and rare arsenopyrite) and electrum (Fig. 5.15C). Approximately one-fourth of this nodule, plus a large portion of the pressure shadow and surrounding shale matrix, was imaged. This nodule is very much like GMSP-003 and GMSP-001 in trace element geochemistry, but the interior zone of trace element-rich pyrite in -003 and -001 is not present here. However, the outer rim is well developed, along with several grains of free gold associated with a later generation of Ni-rich pyrite in the pressure shadow; these gold grains are not present in GMSP-001, which, like GMSP-008, has pressure shadows containing a later generation of pyrite. Other sulfide phases in this nodule include chalcopyrite and sphalerite. Chalcopyrite is enriched in Se (50 ppm), and Sn (~100 ppm) relative to the nodular pyrite, whereas the pressure shadow pyrite is still more enriched in Se (~100 ppm). Mercury is present in the sphalerite, as well as in the nodule pyrite, but at lower levels. The shale matrix contains a high proportion of the pyrite-bound trace elements due to the presence of very small (<10 μm) pyrite crystals.

Black Flag nodule BFB-004A. As is shown here and below in the next image, there is a clear difference in trace element concentrations between nodules in the Paringa Basalt interflow shale and those in the Black Flag Group and Kapai Slate. A portion of the rim and 'core' of a Black Flag nodule was imaged (Fig. 5.16), and as with the previous nodules, this Black Flag nodule (particularly the rim zone) contains high Co (1,000-2,000 ppm), Ni (~1,000 ppm), Cu (~1,000 ppm), Zn (~50 ppm), As (500-1,000 ppm), Se (50-100 ppm), Mo (1-5 ppm), Ag (~5 ppm), Sn (2-3 ppm), Sb (~100 ppm), Te (20-30 ppm), Au (1-2

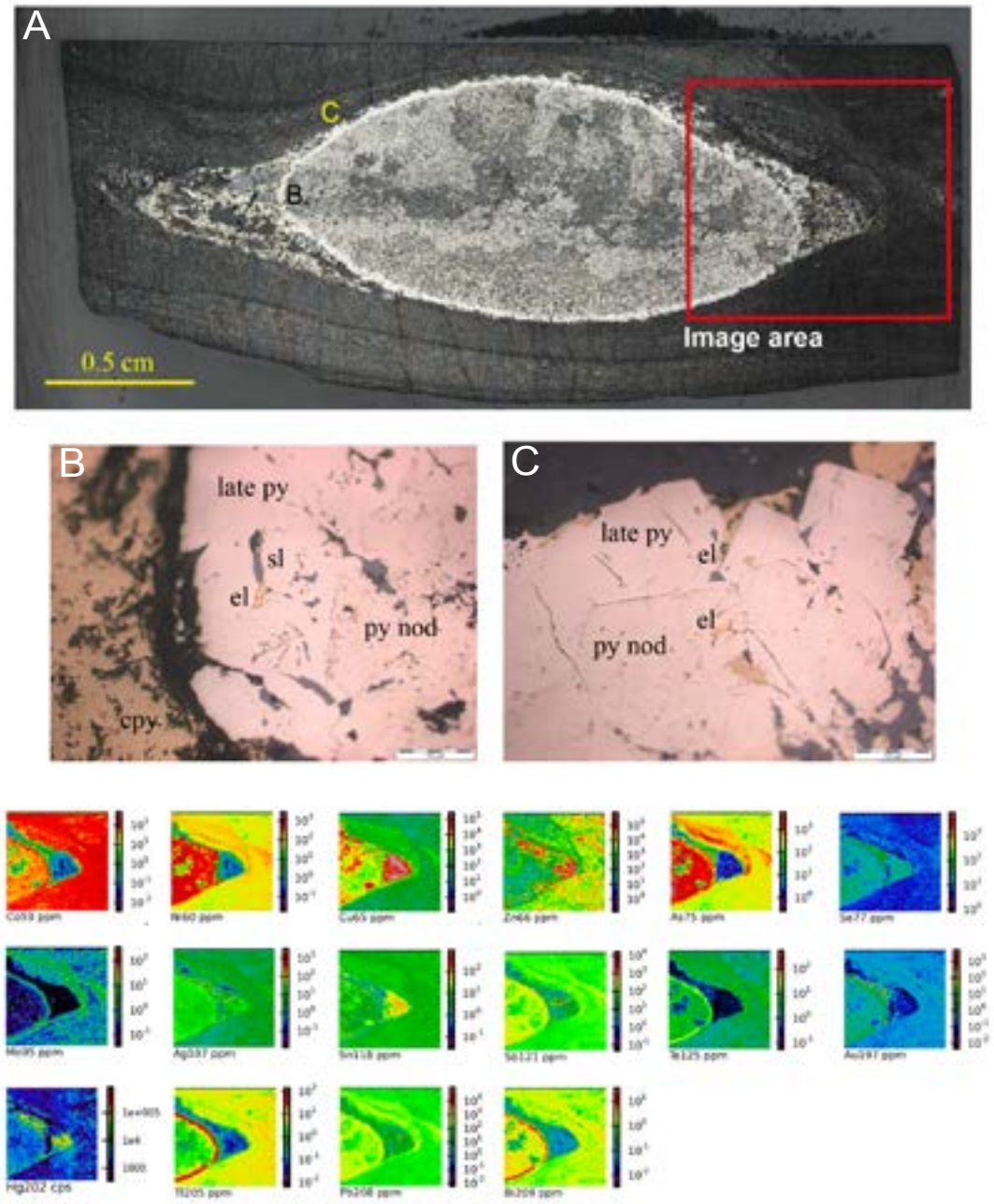

Fig. 5.15 LA-ICP-MS imaging, GMSP-008. A. The investigated pyrite nodule. Field of view is 3 cm. B. Photomicrograph showing the association of electrum with the later pyrite in the pressure shadows. Where the nodule rim has been fractured, electrum can be present (as in 'C'). Like the previous Paringa interflow shale nodules (Figs. 5.12 and 5.13), the outermost rim of this nodule is enriched in a large suite of trace elements (including Au, at around 5 ppm). However, the innermost zone of trace element-rich pyrite is not present here. The amount of chalcopyrite in the nodule is greater than GMSP-003 (Fig. 5.12) and GMSP-001 (Fig. 5.13); there is also more chalcopyrite in the pressure shadow. Electrum inclusions pepper the pressure-shadow pyrite; lastly, the fine-grained 'matrix' pyrite has a geochemical suite similar to that of the nodule rim.

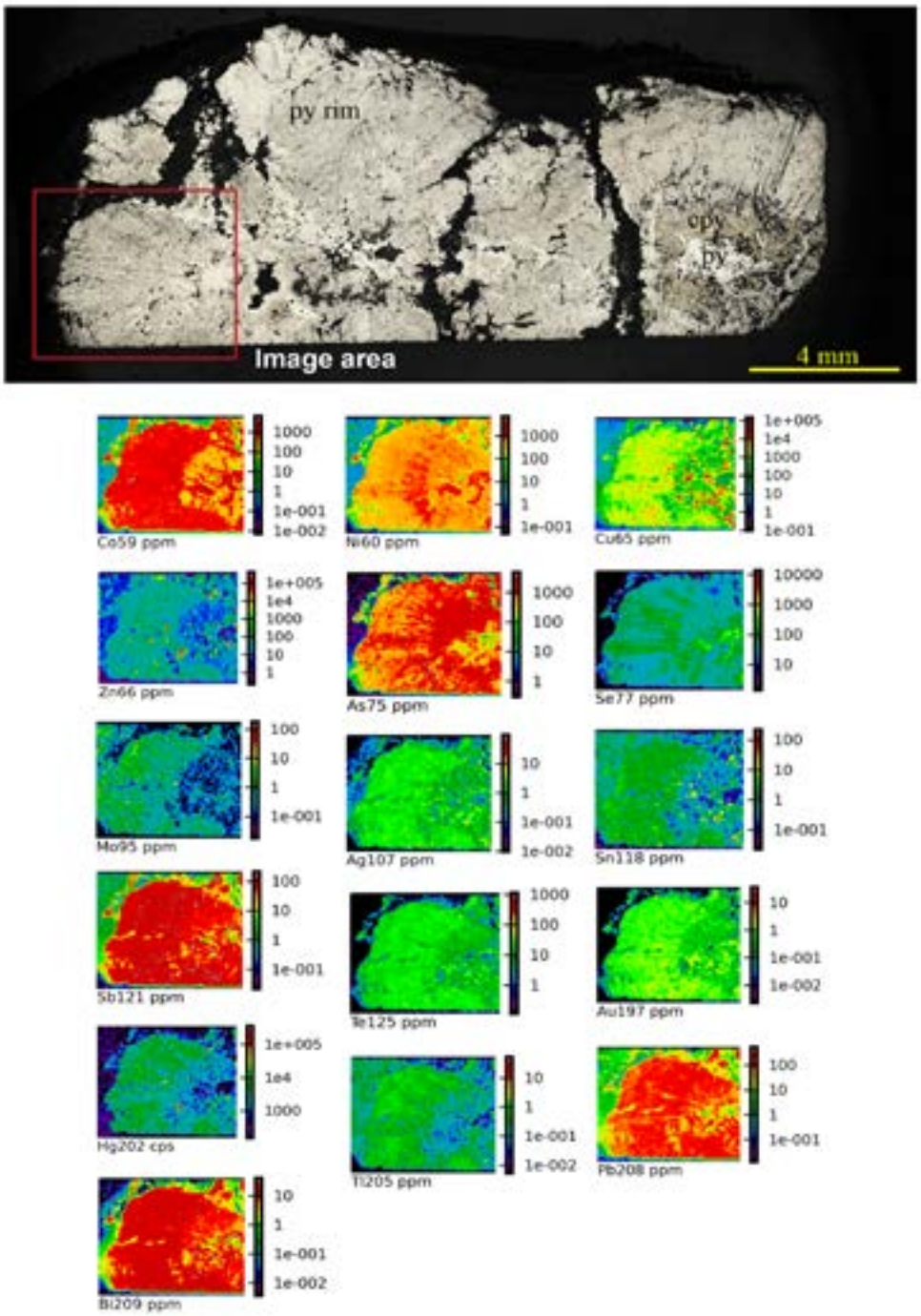

Fig. 5.16 LA-ICP-MS image of BFB-004A, a Black Flag pyrite nodule from the Super Pit. Trace elements (including Au) in BFB-004A display coherent patterns, as in all previous nodules (Figs. 5.12-5.15), and there is a difference in geochemistry between the rim and the core pyrites. Selenium, Ni, Co, and Mo are enriched in the (presumably) later pyrite. Field of view is 2 cm.

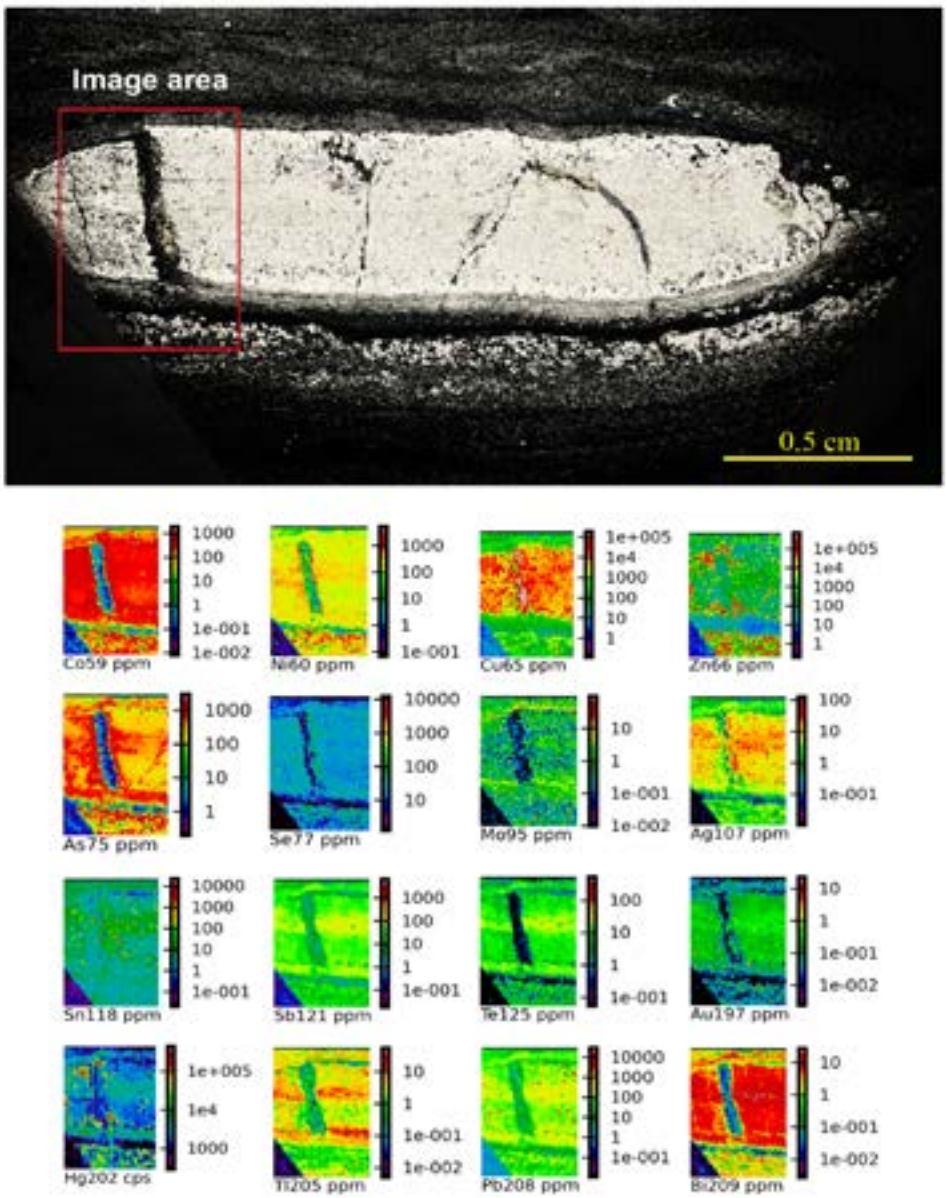

Fig. 5.17 LA-ICP-MS trace element imaging of GMKS-002, from the Kapai Slate. Disregarding the cross-cutting chalcopyrite-sphalerite vein, all trace elements present in this nodule display coherent patterns. The highest value of Au occurs in the core of the nodule (≤1 ppm), and As, Ag, Sb, Te, Tl, Pb, and Bi are likewise enriched with Au in the core.

ppm), Hg (~7,000 counts per second), Tl (0.5-1 ppm), Pb (100-200 ppm), and Bi (10-20 ppm). However, a key difference between this nodule and the previous ones is the far lower Au (≤1 ppm) content, although this element is co-variant with the others in the structure of BFB-004A, as with the previous nodules.

A second generation of pyrite is also present in this nodule; like the later pyrite generations in the Paringa interflow shale pyrite nodule images, the type here is enriched in Se (~1,000 ppm), Co (~5,000 ppm), and Ni (~5,000 ppm), but also has appreciable Bi (~50 ppm) and is relatively depleted in all other trace elements.

Kapai Slate nodule GMKS-002. One-fourth of this nodule was LA-ICP-MS imaged, covering all zones within the nodule plus the rim of fine-grained pyrite enveloping the nodule and some of the coarser pyrites in the matrix (Fig. 5.17). The nodule is characterized by a core enriched in Au-As-Ag-Te-Sb-Tl-Pb-Bi (Au ≤1 ppm), surrounded by a region relatively depleted in these same elements (Au ≤0.5 ppm). On the left side of the image, the nodule is cut by a chalcopyrite-sphalerite vein; chalcopyrite is also disseminated throughout the nodule as intergrowths with the nodular pyrite. The latter form of chalcopyrite commonly has minor intergrown cassiterite (see Fig. 5.4C). Immediately surrounding the nodule is a zone of tightly clustered, fine-grained (<1 μm) pyrite euhedra, and the trace element character of these pyrites is similar to the nodule core pyrite. The rim of the nodule is depleted in all trace elements relative to the core, except for Co (~500 ppm), Ni (~500 ppm), Se (~50 ppm), and perhaps Tl (~30 ppm).

5.5.4 LA-ICP-MS geochemical investigation - spot/line data on proximal and distal pyrite and pyrrhotite

Spot analyses of the several zones of GMSP-003 confirm the imaging results, with maximum Au values greater than 8 ppm in the innermost core of the nodule (Fig. 5.18A-B). Similar values characterize the early pyrite in GMSP-009 (Fig. 5.18A-B). When compared to the global sedimentary pyrite database of Large et al. (2013; 2014; Fig. 5.18B), the early pyrite types in GMSP-003 and GMSP-009 stand out as among the richest (in terms of Au and Te) from any locality or eon in the geologic record. Although spot measurements were not taken on the other imaged nodules, the laser imaging returns robust mean values, implying that the element concentrations displayed in Figs. 5.12-5.17 are trustworthy.

Early pyrite from the SE holes and KPDDH007 were analyzed via LA-ICP-MS in spot mode only. A total of 52 analyses on 2 samples containing early pyrite were collected, and the data reveal interesting geochemical trends (Fig. 5.18A-B). The early sedimentary pyrite from the Kapai Slate (KPD7-272A) is relatively enriched in Co, Ni, Cu, Ag, Sn, Sb, Te, Au, Tl, Pb, and Bi compared to background values (Table 5.2), and these numbers closely match those from the imaged Kapai Slate nodule GMKS-002 in Figure 5.17, considering the differences in laser spot size (which controls energy output and therefore element count rates) between the two analytical sessions. The nodule in GMKS-002 does have greater Te and Bi than the pyrite in KPD7-272A, but the Au, Ag, and Te contents of both samples are well below those of GMSP-003 and GMSP-009 (Table 5.2; Fig. 5.18A-B). In SE-4, as with the Kapai Slate from KPD7-272A, the Black Flag Group early pyrite from SE4-815.8 is enriched in Co, Ni, Cu, As, Ag, Sb, Te, Tl, Pb, and Bi relative to background values. The Black Flag nodule BFB-004A is likewise high in these elements, but is particularly high in Te, Bi, and Sb relative to SE4-815.8 (Table 5.2). However, apart from Te and Bi, the Au, Ag, and Sb values of both Black Flag samples are also significantly lower than those in GMSP-003 and -009.

Line data were also collected on the Super Pit Paringa interflow sample containing brecciated pyrrhotite nodules (Fig. 5.7A) for comparison of its trace element contents with the various pyrite nodules in the same formation. Pyrrhotite in this sample is high in Pb, Sb, Ag, Bi, and Te compared to background values, but is not Au-rich (average value of 0.07 ppm; Table 5.3). Laser and SEM data reveal the presence of ullmannite in this sample, just as in the Paringa interflow shale pyrite nodule GMSP-001 (Figs. 5.14-5.15), which results in very high Sb values for this sample (Table 5.3). Pyrrhotite from the

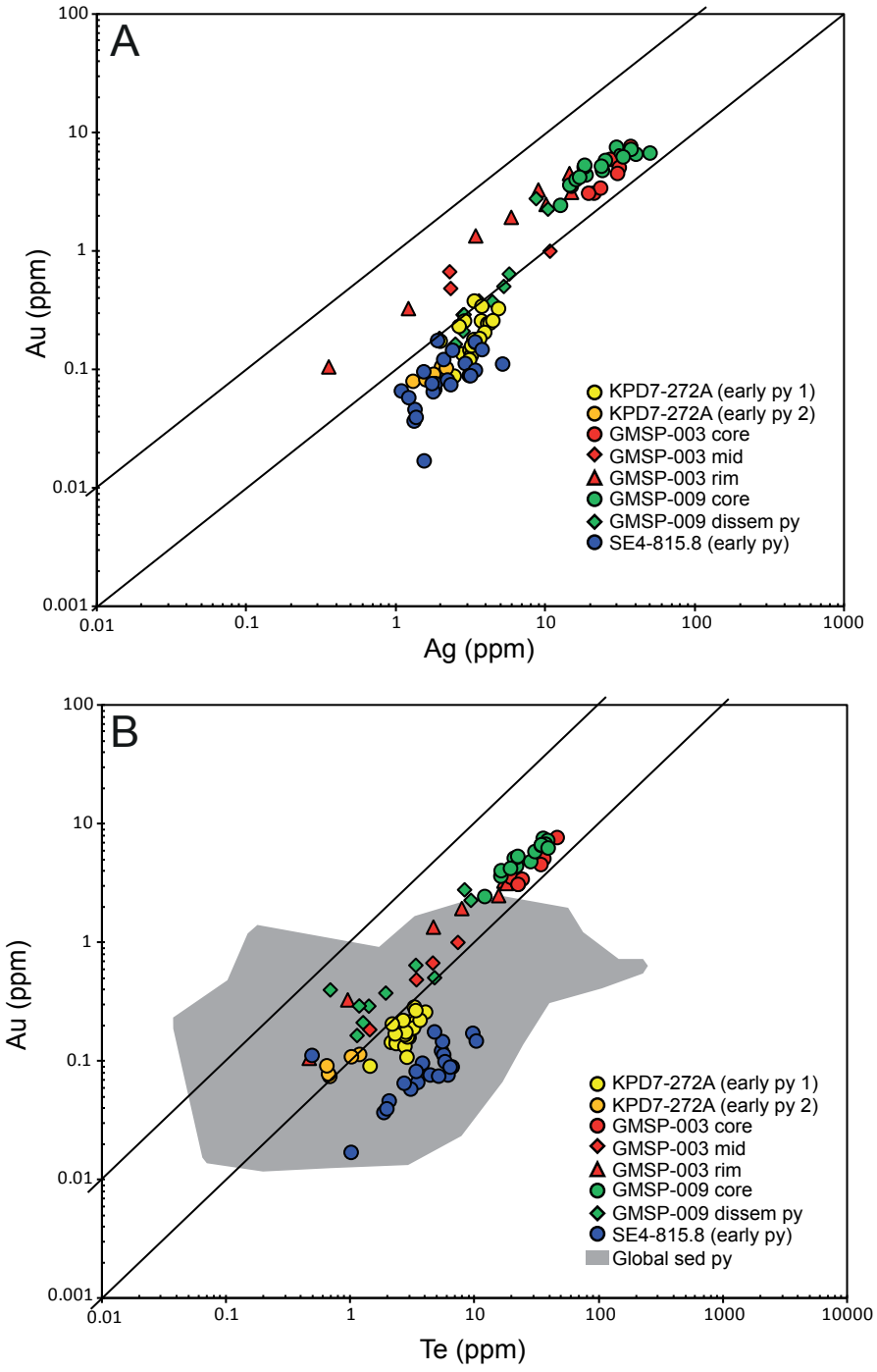

Fig. 5.18 LA-ICP-MS trace element spot analyses for sedimentary sulfides. A. Au vs. Ag for samples in the Kapai Slate, Paringa interflow shale, and Black Flag Group. The Paringa interflow shale samples clearly stand out from the Kapai and Black Flag samples. B. Similar relationships are present in Au vs. Te space, with the various pyrite zones in GMSP-003 (core, rim, and middle; all red symbols) and the early pyrite in GMSP-009 sitting at the high end of the global sedimentary pyrite database (gray field; from Large et al., 2013 and 2014), highlighting this formation's unusual geochemical character.

Table 5.2 Average trace element values (ppm) for early pyrite in Kapai Slate, Paringa Interflow Shale, and Black Flag Group

Kapai Slate	**Co**	**Ni**	**Cu**	**Zn**	**As**	**Se**	**Mo**	**Ag**	**Sn**	**Sb**	**Te**	**Au**	**Tl**	**Pb**	**Bi**
KPD7-272A py1	118.35	169.6	169.6	51.1	422.6	6.9	0.7	3.2	10.2	30.3	2.9	0.19	5.7	220	1.4
KPD7-272A py2	27.5	75.7	160.8	44	289.3	2.9	0.6	1.8	5	10.7	0.84	0.09	30.7	56.2	0.46
GMKS-002**	344.2	164.6	12961.8*	1121*	292	10.2	1.32	10.4*	123.8*	57.1	12.7	0.19	2.4	244.5	9.1
Paringa Int. Shale	**Co**	**Ni**	**Cu**	**Zn**	**As**	**Se**	**Mo**	**Ag**	**Sn**	**Sb**	**Te**	**Au**	**Tl**	**Pb**	**Bi**
GMSP-003 core	147.1	243.4	247	7.1	1193.2	24.1	0.66	25.5	2.6	802.2	30	4.6	18.8	779.4	8.9
GMSP-003 mid	199.1	324.4	5292*	42.1*	1708	28.8	0.34	4.3	2.2*	136.1	4.2	0.6	2.4	142.1	1.31
GMSP-003 rim	87.7	211.3	180.4	6.6	892.4	8.7	1.48	10.8	0.33	454	15.6	3.1	55	368	5.8
GMSP-009 early	205.6	280	348.2	1533.8*	1083.4	7.01	1.27	25.5	0.86	692.2	26.7	5.4	4.2	690.9	9
Black Flag Grp	**Co**	**Ni**	**Cu**	**Zn**	**As**	**Se**	**Mo**	**Ag**	**Sn**	**Sb**	**Te**	**Au**	**Tl**	**Pb**	**Bi**
SE4-815.8 early	389.2	472.5	172.9	190.6*	821.9	21.07	2.6*	2.3	0.71	31.5	4.5	0.09	4.1	235.8	6.4
BFB-004A**	1161.2	583.8	2016.4*	232.9*	1081.7	59.3	0.82	2.62	1.6	123.8	23.6	0.39	0.57	96.3	18.6

* = indicates artificially high values due to non-pyrite sulfide inclusions (i.e., cpy, sp, and mo)

** = reduced from individual image lines

Table 5.3 Average trace element values (ppm) for pyrrhotite in Paringa interflow shale

	Co	Ni	Cu	Zn	As	Se	Mo	Ag	Sn	Sb	Te	Au	Tl	Pb	Bi
KPD7-491 po nodule	878.7	1083.5	29.3	21.9	0.1	46.3	12.3	2.9	1.2	10.9	5.1	0.02	0.42	95	2.07
KPD7-491 po dissem	825.1	993.5	38264.2*	5833.8*	0.32	48.3	0.44	10	8.5	60	10	0.11	3.6	404.9*	15.1
KPD7-491 po vein	869.8	1096.9	3545.3*	23.3	0.11	44.1	0.14	2.8	2.2	7.2	3.8	0.03	0.5	75.1	2.4
ORY-001 po	384.6	739.5	465.1*	29.3	0.18	26.8	0.88	8.7	0.96	402.4*	5.9	0.07	0.58	457.6*	2.5
KPD7-475.2 po nodule	690.6	890.4	1.3	82.9*	0.82	40.7	2.18	4.1	2.96	24.1	8.2	0.04	0.68	429.4*	6.1
KPD7-476A po	480	1030.9	1.7	1.48	0.1	36.7	0.06	7.7	0.48	65.2	12.1	0.11	1.93	333	4
KPD7-474.7B early po	656.4	845.9	1.6	3.2	0.54	41.3	0.47	4.5	2.58	22.7	6	0.06	1.89	150.2	4
KPD7-474.7B po nodule	684.9	853.6	148*	3.3	0.27	52	0.39	8.2	1.25	75.4	22	0.11	2.2	410.5	15.5
KPD7-474.7B late po	686.3	760.7	10.9	8.2	0.37	48.1	0.03	1.1	0.62	0.89	0.7	0.002	0.13	27.2	0.95
SE12-1435.5 po nodule	248.5	665.7	2.9	2.7	N/A*	19.7	0.02	3.9	1.3	27.4	5.3	0.03	0.68	103	9.5
SE12-1435.5 late po	249.3	636.8	2.1	7.7	N/A*	20.2	0.04	0.2	1.2	0.95	0.3	0.007	0.03	3.3	0.53

* = indicates artificially high values due to non-pyrrhotite sulfide inclusions (i.e., cpy, sp, ulm, and gn)

N/A* = As not available due to apy analyses immediately prior to po analyses

distal samples, particularly from the Paringa interflow shale in KPDDH007, was also investigated. These pyrrhotite-rich Paringa interflow shale samples in KPDDH007 contain a distinct type of pyrrhotite, identifiable both petrographically and geochemically, which comprises the nodular form of this mineral in these samples. Like the pyrrhotite nodule-rich sample from the Golden Mile, this pyrrhotite is richer in certain trace elements, particularly in Ag, Sb, Te, Au, Tl, Pb, and Bi (Table 5.3), than its presumably later counterpart in the nodule pressure shadows. The same relationship holds for the pyrrhotite nodule in SE12-1435.5. The implications of these data are discussed below.

5.5.5 LA-ICP-MS geochemical investigation - spot data on ore samples

The trace element characteristics of Fimiston and Mount Charlotte ore pyrite also reveal several interesting trends (Fig. 5.19A-C). In terms of Au-Ag-Te, Fimiston pyrites are generally more enriched than Mt. Charlotte pyrites, though we note that individual Fimiston pyrites can have low Ag (0.3 ppm) and Au (0.3 ppm) values (Table 5.4). All Mt. Charlotte pyrites plot well below the Te:Au = 10 line, mostly due to the low Au content of these pyrites, whereas Fimiston pyrites generally have Te:Au ratios closer to 1. Fimiston pyrites are also generally richer in As than Mt. Charlotte pyrites, by nearly an order of magnitude on average (Table 5.4). Fimiston and Mount Charlotte pyrites show the greatest difference in Co, Ni, and As, as evidenced by the averages in Table 5.3. All analyzed pyrites from Fimiston ore contain < 100 ppm Se and variable by low (i.e., less than 300 ppm) Co content, whereas Mt. Charlotte pyrites are commonly higher in both Ni (≥ 200 ppm) and Co (over 500 ppm in some instances) than their Fimiston counterparts. However, the Co-Ni ratios of both Fimiston and Mt. Charlotte pyrites are generally >1.

In comparison to the pyrite nodule trace element data (Table 5.2), especially those from the Paringa interflow shale, the ore pyrites are significantly lower in Tl, Pb, and Bi without exception, whereas Fimiston pyrites are almost always higher in As and commonly higher in Au than all of the nodules (Table 5.4). Mount Charlotte pyrites are lower in almost every trace element category than the pyrite nodules. The pyrite nodules from the Paringa interflow shale (specifically the cores to those nodules) are also comparatively enriched in Sb by over an order of magnitude compared to the ore pyrites.

5.5.6 S isotope geochemistry

In-situ measurements of $\delta^{34}S$ and $\Delta^{33}S$ in the pyrite nodules and ore-related pyrite via SHRIMP (Fig. 5.20A) have revealed a complex and fascinating geochemical history. The $\Delta^{33}S$ ratio in particular has proved to be extremely valuable, as it demarks not only nodules from ore-related pyrite, but also nodules from each formation and intra-nodule isotopic variation. In $\Delta^{33}S$-$\delta^{34}S$ space, nearly all of the pyrite nodules plot in the right-hand quadrants (i.e., positive $\delta^{34}S$ and positive or negative $\Delta^{33}S$), while the ore-related pyrites define a trend of $\delta^{34}S$ compositions from -6 to +6 ‰ and narrow, near-zero $\Delta^{33}S$ values.

In general, the pyrite nodule cores have negative $\Delta^{33}S$ values, irrespective of which unit they are from (excepting Black Flag nodules), whereas the rims of all nodules have positive $\Delta^{33}S$ values (Fig. 5.20A). This is particularly evident in GMSP-003, from the Paringa interflow shale, which has the strongest $\Delta^{33}S$ signals, either positive or negative, of the entire sample set. Other pyrite types associated with the nodules (e.g., pressure shadow/recrystallized pyrite, disseminated fine-grained pyrite in the shale matrix, pyrite euhedra within the nodules) contain their own distinct $\Delta^{33}S$-$\delta^{34}S$ signals. We discuss these differences at length in the discussion section below.

5.5.7 Pb isotope geochemistry

Pyrite in eight nodules (GMSP-003, GMSP-001, GMKS-002, GMSP-008, GMSP-009, GMSP-006, BFB-004A, and BFB-003) one sample of pyritic Fimiston ore (700264), two samples of pyrite-arsenopyrite Fimiston ore (GMO-001 and GMO-002), and one sample of Mount Charlotte pyrite-bearing ore (106755) were analyzed for Pb isotopic composition via LA-ICP-MS at CODES, University

Table 5.4 Average trace element values (ppm) for Fimiston and Mount Charlotte ore pyrite

Fimiston	**Co**	**Ni**	**Cu**	**Zn**	**As**	**Se**	**Mo**	**Ag**	**Sn**	**Sb**	**Te**	**Au**	**Tl**	**Pb**	**Bi**
106765	206	165	366.7*	126.7*	2053.7	13	0.11	3.4	0.11	18.2	32.3	4.8	1.17	7.6	0.16
700192	121.2	61.2	268.3	82.2*	7459.7	14.3	1.9	26.3*	0.21	53.1	88.5*	47.1*	3.2	11.2	0.12
700264	223.7	117.1	892.2*	133.3	3757.9	7.7	36.9*	15.7	1.63	46.6	70.1*	45.4*	0.4	31.1	0.54
700265	110.2	8.5	14.3	4.9	1552.2	8.3	0.1	2.5	0.65	14.4	14.4	2.4	2.22	3.8	0.01
Trafalgar bx	81.5	60	477.3	36.4	364.7	26.1	0.63	3.3	0.08	16.4	0.43	0.36	0.33	42.8	0.08
GMO-002	90.7	410.2	75.3	714.6*	4300.6	9.6	0.31	0.67	0.25	13.7	0.97	3.6*	0.22	20.3	4.5
Mount Charlotte	**Co**	**Ni**	**Cu**	**Zn**	**As**	**Se**	**Mo**	**Ag**	**Sn**	**Sb**	**Te**	**Au**	**Tl**	**Pb**	**Bi**
106755	307	219	2.5	0.8	255.9	8.4	0.06	0.4	0.09	1.4	5	0.37	0.03	6.8	0.16
SE6-718.6	623.6	554.8	1.27	6.5	1303.8	4.2	0.07	0.11	0.16	0.87	3.2	0.11	0.01	2.6	0.19

* = indicates artificially high values due to Au-Ag telluride and non-pyrite sulfide inclusions (i.e., cpy, sp, and mo)

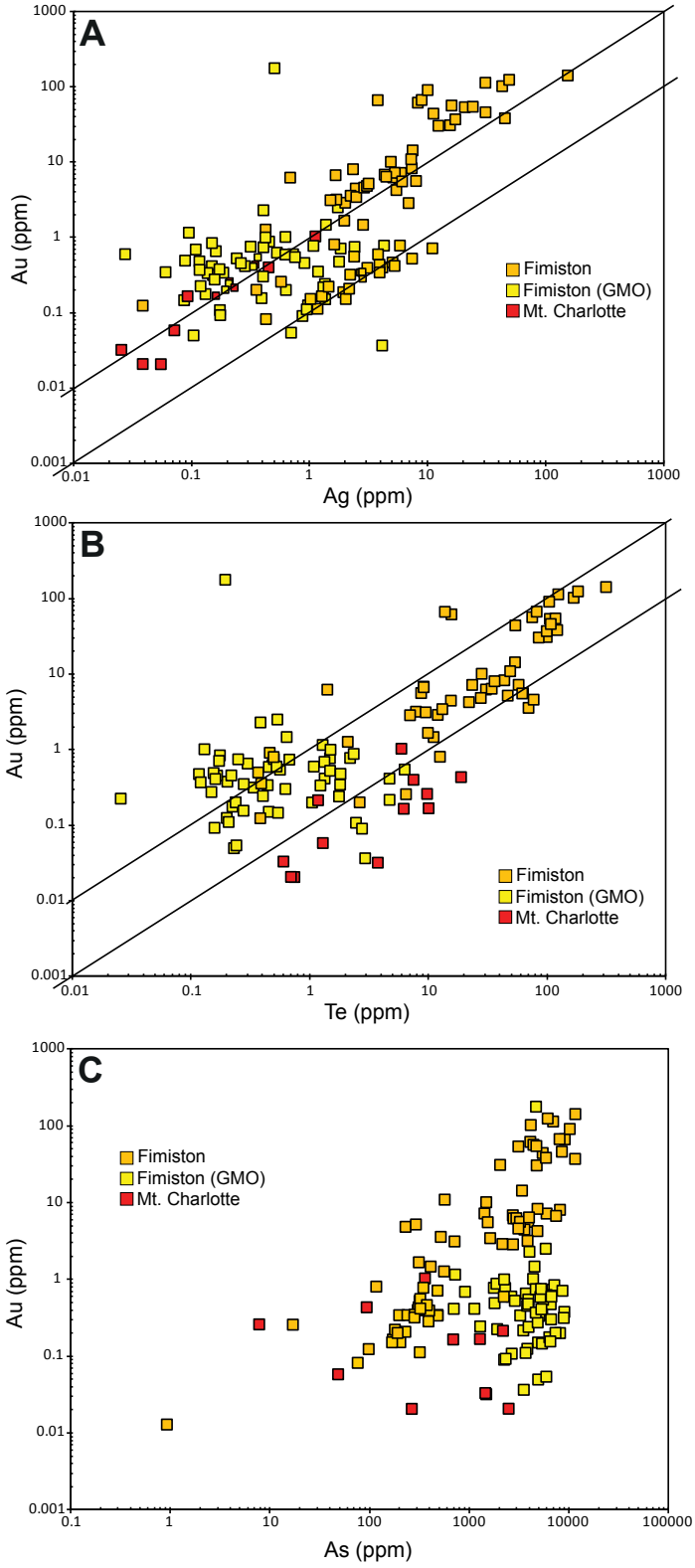

Fig. 5.19 Trace element spot analyses on ore pyrites. A. Au-Ag relationships in Fimiston and Mt. Charlotte-stage pyrites. Fimiston pyrites are characteristically higher in Au and Ag than Mt. Charlotte pyrites, though there is significant variation amongst the samples in our suite. For example, pyrites in 700192 and 700264 have Au concentrations commonly in excess of 10 ppm, whereas Au in the pyrite from the Trafalgar bx sample (Fig. 5.10a) is typically less than 2 ppm. That sample also has a Ag:Au ratio of ~10, similar to diagenetic pyrites globally (Large et al., 2014). Mount Charlotte-stage pyrites are universally lower in Au and Ag than Fimiston-stage pyrites. B. Au-Te diagram, showing similar characteristics to the Au-Ag plot. C. Au-As, which shows that Fimiston pyrites are generally more As-rich than their Mt. Charlotte-stage counterparts.

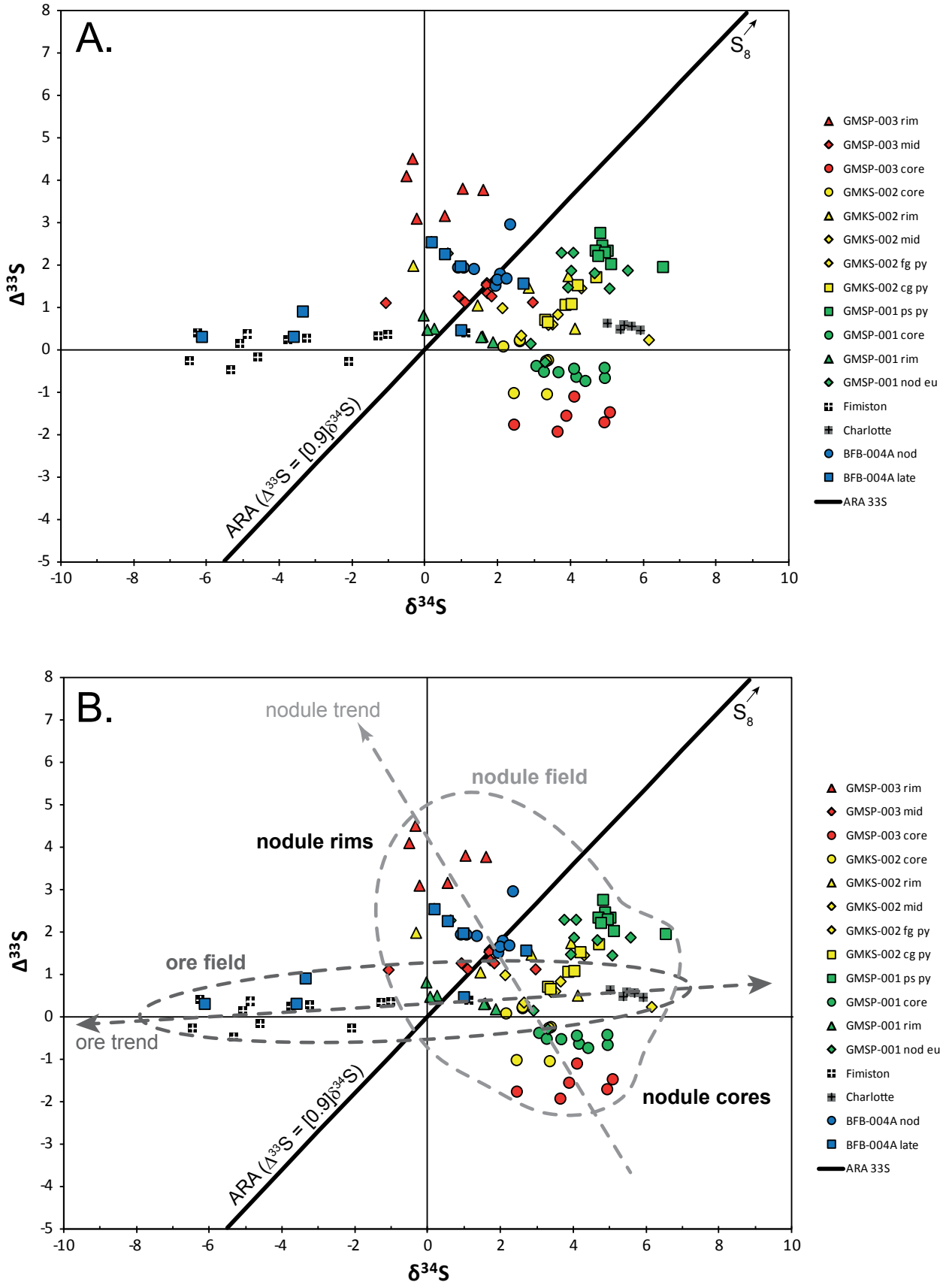

Fig. 5.20 Sulfur isotopes of the pyrite nodules and ore-stage pyrites. See text for discussion. ARA = Archean Reference Array (Guy et al., 2014).

of Tasmania. Although this technique is less precise than solution mass spectrometry, the small (≤100 μm) spatial resolution enables the primary Pb composition to be determined without contamination from late stage ingress or contributions from in-situ U decay of detrital phases. Analyses were grouped according to the amount of radiogenic Pb present and the measured U/Pb ratios; those with the highest amount of radiogenic Pb and high U/Pb ratios were rejected from the data set in order to achieve an MSWD of less than 2 (similar to that on the secondary standards; Table 5.5).

In Pb isotopic space, most samples plot on or above an upper-crustal growth curve with higher μ ($^{238}U/^{204}Pb$) than the crustal average of 9.74 (Stacey and Kramers, 1975), similar to previous studies on the Pb isotopic composition of rocks and minerals in the Eastern Goldfields Superterrane (e.g., Browning et al., 1987; McNaughton et al., 1993; McNaughton and Groves, 1996). Both the ore and nodule leads define trends at specific ages (Fig. 5.21A). Furthermore, the Pb in the Kapai Slate nodule has an older model age than the Pb in the Paringa Basalt interflow shale nodules, which generally have older model ages than the Black Flag nodules; likewise, the ore-stage pyrite in 700264 (Fimiston-style mineralization) has a model age within error of Paringa interflow shale nodules GMSP-003, GMSP-001, and GMSP-008, whereas Mt. Charlotte-style pyrite plots within error of the Black Flag nodules BFB-003 and BFB-004A (note: the errors on sample 106755 are quite high due to a low number of analyses). GMO-002 and GMO-001 (pyrite-arsenopyrite Fimiston mineralization) have distinctly younger model ages than all other samples.

A curious feature of these samples, particularly in the ore pyrites, is the presence of distinct isotopic zones within single crystals. For example, certain pyrites in 106755 have outer domains containing radiogenic $^{207}Pb/^{206}Pb$ ratios that transition to inner regions where the $^{207}Pb/^{206}Pb$ ratio is much less radiogenic. Figure 5.22 illustrates this pattern: the laser analytical line begins in pyrite with $^{207}Pb/^{206}Pb$ = 0.89, but as the beam crosses the middle of the grain, the $^{207}Pb/^{206}Pb$ ratio shifts to 1.07, where it holds steady until reaching the end of the pyrite grain and the $^{207}Pb/^{206}Pb$ ratio falls back down to around 0.88. This isotopic heterogeneity has been reported by past researchers (e.g., McNaughton et al., 1993), but to the best of our knowledge, the spatial resolution necessary to capture this phenomenon has not been available before.

The Jaguar pyrite standard (Woodhead et al., 2009), from the Archean Jaguar VHMS deposit in the Kurnalpi Terrane of the Eastern Goldfields Superterrane (Belford, 2010), was analyzed in the same analytical run as the Golden Mile nodules as a secondary standard and is plotted for comparison. Error ellipses for the ore pyrites are slightly larger than most of the nodule error ellipses due to either lower Pb content (<10 ppm), the presence of small monazite or xenotime inclusions (i.e., high U and/or Th, leading to greater scatter in the $^{207}Pb/^{206}Pb$ ratio), or a combination of these factors.

5.6 Discussion

5.6.1 Implications of the trace element and S isotope data of the pyrite nodules and the ore pyrites

As the above petrographic and trace element data show, pyrite (and pyrrhotite) nodules from the Kapai Slate, the Paringa Basalt interflow shale, and the Black Flag Group shale reveal complex geochemical histories involving multiple stages of precipitation and fluctuating physicochemical characteristics of the fluids from which they formed. The trace element data for each nodule in each formation track along with the petrographic textures (i.e., certain zones are more or less enriched in some elements relative to concentrations of the same element in certain other zones within the nodule), but of even greater interest is the fact that the S isotope data behave similarly, at least in part. The latter dataset provides a stronger case for the tight relationship between texture and geochemical makeup in these nodules by virtue of the behavior of the minor S isotopes (^{33}S, in this instance), which do not appear to have been greatly affected by post-depositional metamorphism.

Table 5.5 Average Pb isotope compositions for nodular and ore pyrite

Sample	207/206	±1s	206/204	±1s	207/204	±1s
106755	1.0693	0.0038	13.814	0.102	14.835	0.084
700264	1.0776	0.0006	13.664	0.020	14.733	0.023
BFB-003	1.0697	0.0008	13.786	0.029	14.741	0.022
BFB-004A	1.0755	0.0008	13.845	0.020	14.889	0.020
GMKS-002	1.0808	0.0010	13.566	0.017	14.652	0.015
GMO-001	1.0652	0.0016	14.010	0.017	14.917	0.019
GMO-002	1.0682	0.0015	13.942	0.021	14.874	0.020
GMSP-001	1.0784	0.0006	13.702	0.007	14.789	0.010
GMSP-003	1.0792	0.0008	13.693	0.019	14.773	0.014
GMSP-006	1.0740	0.0018	13.817	0.023	14.838	0.032
GMSP-008	1.0831	0.0011	13.709	0.015	14.841	0.014
GMSP-009	1.0738	0.0006	13.709	0.019	14.723	0.014
Jaguar	1.0890	0.0011	13.347	0.016	14.540	0.024

The major isotopes of S (^{32}S and ^{34}S) have been used for decades to decipher S sources in sulfides and sulfates and to ascertain the redox state of the fluids that precipitated them (e.g., Ohmoto, 1972; Ohomoto and Rye, 1979), but within the last 10-15 years, the minor S isotopes (^{33}S and ^{36}S) have come to the fore following the discovery of non-zero $\Delta^{33}S$ (commonly referred to as mass-independent fractionation of sulfur, or MIF-S) in Archean sulfides by Farquhar et al. (2000). This apparently unique feature of Archean sulfides makes S isotopic studies particularly powerful for researchers investigating S sources and fluid-atmosphere redox states in this part of the geologic record.

The $\Delta^{33}S$ data presented in Fig. 5.20A and 5.20B show that S sources for the nodules are not the same as S sources in the ore-stage pyrites (note the different trends in the data). The trend with a high negative slope in the nodular data is similar to a trend in multiple pyrite datasets from the Archean Kapvaal Craton of southern Africa (Kamber and Whitehouse, 2007; Philippot et al., 2012; Roerdink et al., 2013), which is thought to have formed either by oxidation of SO_2 associated with felsic volcanism (Philippot et al., 2012) or by local, biologically-mediated redox processes occurring in the sediments during pyrite formation (Kamber and Whitehouse, 2007; Roerdink et al., 2013). Given that the nodular pyrite samples in this study are from interflow shales associated with basalt, and that the pyrite apparently formed during marine sedimentation, it is not unreasonable to expect sulfur contributions from both seawater sulfate and volcanic sulfur (as elemental S_8). We therefore favor a model similar to those of Kamber and Whitehouse (2007) and Roerdink et al. (2013), whereby bacterial reduction of oceanic SO_4^{2-} was responsible for the formation of pyrite in the cores of Kapai and Paringa interflow shale nodules, and we invoke the same process for the rims, except there, the bacteria acted on elemental S_8 alone or a mixture of SO_4^{2-} and S_8. These data suggest that the Kapai Slate and Paringa interflow shale nodules started forming at or close to the sediment-water interface, where access to seawater would be least impeded, but as sedimentation (and nodule growth) continued on the seafloor, the direct seawater sulfate supply was eventually cut off, leaving the nodules with access to pore water S alone.

The Black Flag sample BFB-004A does not follow the general pattern of the Kapai and Paringa interflow shale nodules, which may signal a change in either S source or redox conditions in the atmosphere and/or ocean during the formation of these nodules. We do note that the $\delta^{34}S$-$\Delta^{33}S$ values of the late pyrite in BFB-004A (Fig. 5.20A) might represent an overprint of pre-existing pyrite by hydrothermal fluids related to the creation of Fimiston-stage ore, or these pyrites may actually be Fimiston-stage pyrites which have nucleated on the pre-existing pyrite nodule. We further note that while no other

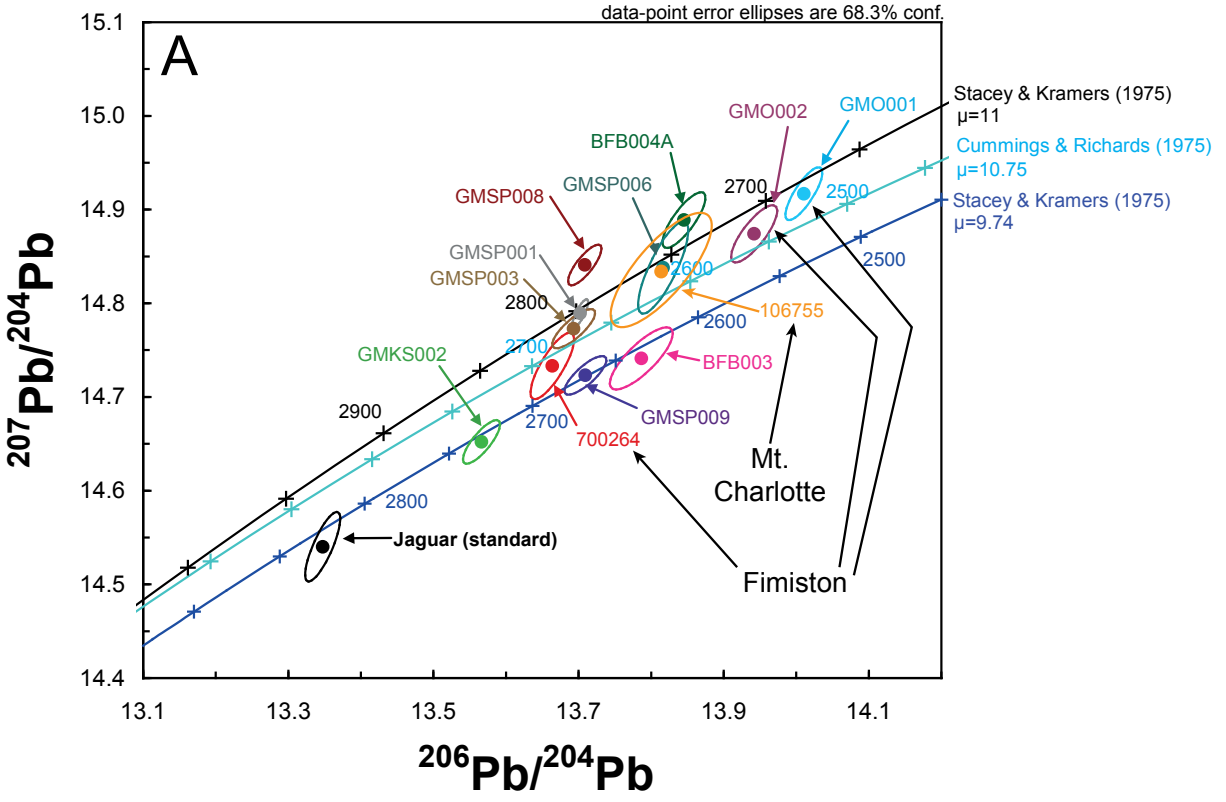
data-point error ellipses are 68.3% conf.
A
Stacey & Kramers (1975) μ=11
Cummings & Richards (1975) μ=10.75
Stacey & Kramers (1975) μ=9.74
GMO002
GMO001
BFB004A
GMSP008
GMSP006
GMSP001
GMSP003
GMKS002
BFB003
GMSP009
700264
106755
Mt. Charlotte
Fimiston
Jaguar (standard)
2700
2500
2600
2800
2900
15.1
15.0
14.9
14.8
14.7
14.6
14.5
14.4
13.1
13.3
13.5
13.7
13.9
14.1
207Pb/204Pb
206Pb/204Pb

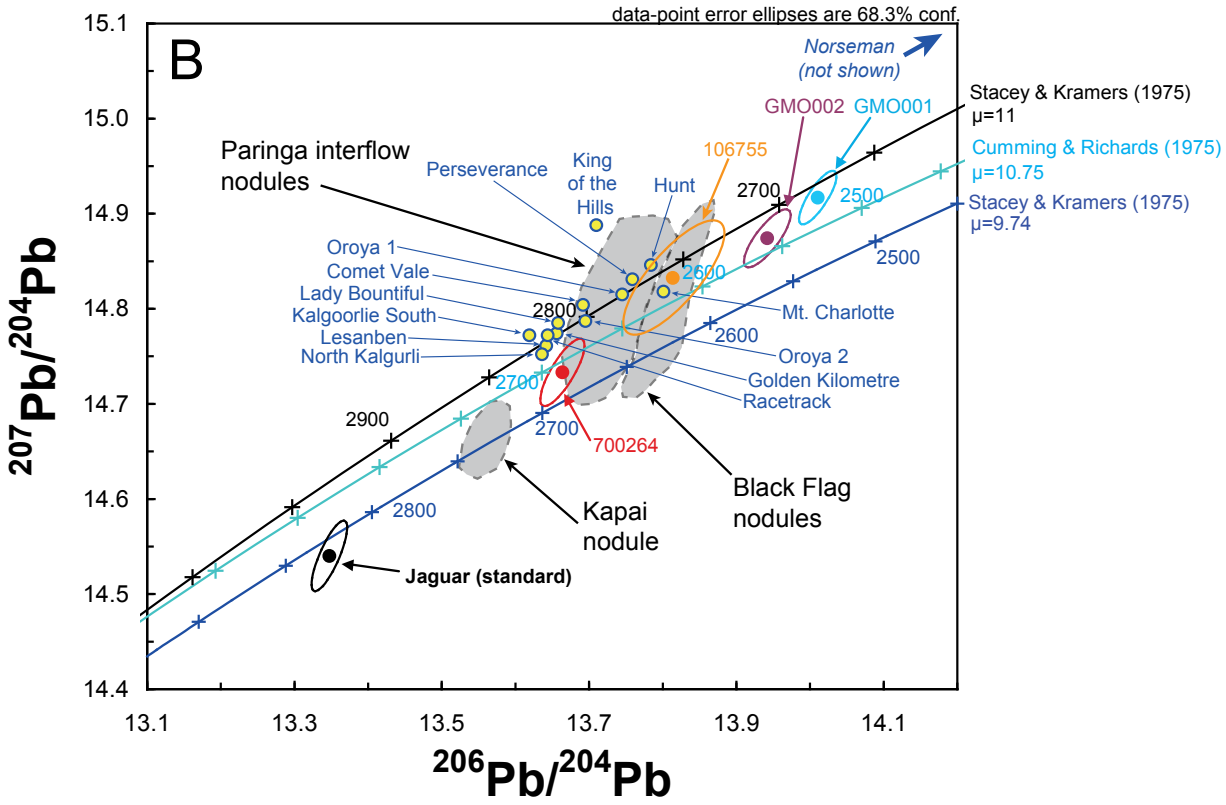
data-point error ellipses are 68.3% conf.
B
Norseman (not shown)
Stacey & Kramers (1975) μ=11
Cumming & Richards (1975) μ=10.75
Stacey & Kramers (1975) μ=9.74
Paringa interflow nodules
Perseverance
King of the Hills
Hunt
106755
GMO002
GMO001
Oroya 1
Comet Vale
Lady Bountiful
Kalgoorlie South
Lesanben
North Kalgurli
Mt. Charlotte
Oroya 2
Golden Kilometre
Racetrack
700264
Kapai nodule
Black Flag nodules
Jaguar (standard)
2700
2500
2600
2800
2900
15.1
15.0
14.9
14.8
14.7
14.6
14.5
14.4
13.1
13.3
13.5
13.7
13.9
14.1
207Pb/204Pb
206Pb/204Pb

Fig. 5.21 (opposite) Pb isotope geochemistry of pyrite nodules and pyrite ore. A. $^{207}Pb/^{204}Pb$ vs. $^{206}Pb/^{204}Pb$ diagram. The pyrite nodules define three separate trends on upper-crustal growth curves (in order of stratigraphy), whereas the three ore samples are more scattered. The pyrite nodule from the Kapai Slate (GMKS-002) has the least radiogenic composition, followed by the Paringa interflow shale population, which is then followed by the two Black Flag nodules. Ore sample 700264 plots on the same trend as the Paringa nodules, whereas GMO-001 and GMO-002 are much more radiogenic and plot by themselves on the far end of the plot. B. Our data combined with historical data from Browning et al. (1987) and McNaughton et al. (1993). Most of the ore sulfide data (galena, except for Oroya 1 and Oroya 2 [altaite] and Mt. Charlotte [pyrite]) plot between the Paringa nodule and Black Flag nodule fields, which is also where 700264 and 106755 fall. However, other Eastern Goldfields deposits have very radiogenic Pb (e.g., Norseman); these are not shown on this plot.

nodule in our sample set has such distinct isotopic zonation as GMSP-003, the others appear to have similar trends but their signals are muted (e.g., GMSP-001). This is likely due to different conditions locally around each nodule at the time of the formation of the rims, particularly in the Paringa interflow shale.

As for the ore pyrites, several pieces of information can be gleaned from the S isotope and trace element data. First, while there is a clear difference in the $\delta^{34}S$ signals of Fimiston and Mt. Charlotte pyrite, known from the literature (Phillips et al., 1986a, b; 1988; Cameron and Hattori, 1987; Clout, 1989; Hodkiewicz et al., 2009), there is very little spread between them in $\Delta^{33}S$ space. Furthermore, the nearly flat trend defined by the Fimiston and Mt. Charlotte pyrites in Figure 5.20 is close to the mass-dependent fractionation (i.e., non-atmospheric S) array, which is characterized by a large range in $\delta^{34}S$ but an essentially homogeneous $\Delta^{33}S$ range of ~0±0.2‰ (Ono et al., 2003). The two datasets together suggest that the S source for both types of ore pyrite was likely non-photolytic oceanic sulfate, and that biogenic reduction of this sulfate to sulfide was the primary method of pyrite formation. Hattori and Cameron's (1986) $\delta^{34}S$ data on anhydrite from Fimiston-stage veins, along with Clout's (1989) $\delta^{34}S$ data on the same, lend further support to our model, as evidenced by this mineral's $\delta^{34}S$-enriched values (+12 to +18‰). However, whereas the Fimiston pyrites likely formed in an open, relatively oxygen-rich system (wide range of mostly negative $\delta^{34}S$), the pyrites of Mt. Charlotte appear to have formed under more reducing and sulfate-limited conditions, as evidenced by their $\delta^{34}S$ values (restricted range and $\delta^{34}S>0$‰). These interpretations are consistent with past studies on the S isotopes of Fimiston- and Mt. Charlotte-stage pyrite and Fimiston-stage anhydrite (e.g., Clout, 1989), but others (e.g., Phillips et al., 1986; Evans et al., 2006) have advanced a different interpretation of these data, based primarily on thermodynamic modeling, that invokes hematite creation at the expense of primary titanomagnetite in the Golden Mile Dolerite as a critical factor for the creation of sulfate in Fimiston-stage ore zones. This idea, while theoretically possible, does not rule out the possibility of fluid mixing (or boiling and phase separation) as the main factor controlling Fimiston-stage mineralization, as discussed in Clout (1989). One possible way to resolve this issue is to analyze $\Delta^{33}S$ and $\Delta^{36}S$ in early anhydrite from Fimiston-stage ore samples to ascertain the presence of MIF-S, whereby the preservation of the MIF-S signal would be strong evidence that the early anhydrite formed from seawater (Crowe et al., 2014; Paris et al., 2014; Zhelezinskaia et al., 2014)..

In terms of trace elements, Fimiston pyrites are nearly always higher in As than either sedimentary pyrites or Mt. Charlotte pyrites, whereas Mt. Charlotte pyrites are typically higher in Ni and Co (but lower in As) than either of the other two categories. Since the most likely source for As in an orogenic environment is sedimentary rocks (Tomkins, 2010; Pitcairn et al., 2014), we therefore posit that the Fimiston ore event derived a greater proportion of its metal budget from a sedimentary source, likely at moderate depth below the paleosurface (3-4 km, i.e., below the pyrite-pyrrhotite transition zone). On the other hand, the higher Ni and Co in Mt. Charlotte pyrites suggests that they precipitated from a hotter (and likely deeper) fluid than either Fimiston-stage or sedimentary pyrites, consistent with past research on the geochemistry of Mt. Charlotte-stage ore fluids (e.g., Clout, 1989). This may indicate a fluid and metal source largely devoid of sedimentary material, i.e., a magmatic source, but this model is

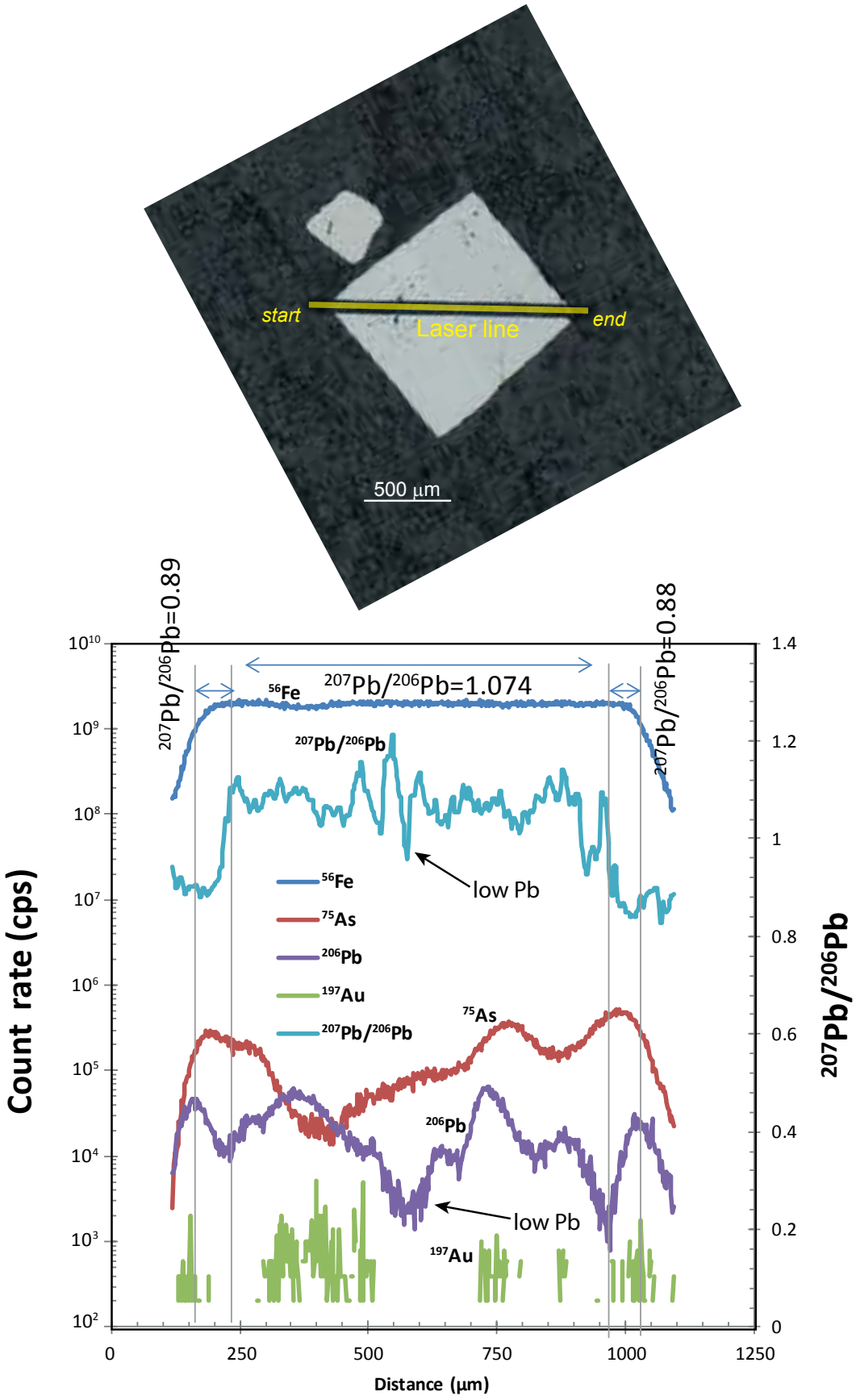

Fig. 5.22 Laser line showing Pb isotope zonation in a single pyrite grain from Mount Charlotte (sample 106755).

difficult to reconcile with the $\delta^{34}S$ > 0‰ S isotope data described above.

The other features of the ore pyrites are their strong trace element heterogeneity (differences of over 5 orders of magnitude), even within the same grain, which is far greater than that in the sedimentary pyrites (and pyrrhotites); and their lower overall trace element budget (compared to the nodules), consistent with previous work on ore-stage pyrites from this deposit (Phillips et al., 1986; 1988) and pyrites of multiple generations in other orogenic gold districts (Large et al., 2007; 2009; 2013).

5.6.2 Origin of the Paringa interflow shale pyrrhotite nodules

There are two possible origins for the pyrrhotite nodules in the Paringa interflow shale: one, they are diagenetic; or two, they are metamorphosed pyrite nodules. Diagenetic pyrrhotite is rare even in modern sediments (Larrasoaña et al., 2007), and no previous study has documented diagenetic pyrrhotite in Archean metasediments. However, its formation this early in the sedimentary cycle may have been more common at Neoarchean-Paleoproterozoic times than currently thought. For example, at the Paleoproterozoic Homestake orogenic gold deposit (USA), the unit underlying the ore host BIF contains a facies of pyrrhotite-rich black shale very similar in texture to that in the Paringa interflow shale from KPDDH007 and SE-12, although the Homestake example has experienced considerably more deformation and metamorphism (Steadman et al., accepted pending revisions). Like the pyrrhotite nodules in the Paringa interflow shale, the Homestake early pyrrhotite is distinguished from the later, metamorphic pyrrhotite by the presence of tiny, ubiquitous gangue inclusions. Furthermore, the early pyrrhotite at Homestake appears to be partially consumed by the later pyrrhotite. This textural distinction is mirrored by the trace element systematics, which show that the early pyrrhotite is orders-of-magnitude more enriched in Ag, Sb, Te, Tl, Pb, and Bi than the later pyrrhotite.

The Homestake example is weakly compelling on its own, but its similarities to the Paringa interflow shale examples are more difficult to explain apart from an appeal to a situation in which certain unique geochemical conditions (i.e., very low fO_2, high aH_2S, and high dissolved Fe^{2+}) were met in the water column and/or the sedimentary pile prior to (or perhaps during) lithification on the Neoarchean seafloor. These data underscore the apparent fact that the Neoarchean ocean in the vicinity of the Golden Mile (and quite likely most of the Eastern Goldfields) may have been a dynamic environment which fostered the flourishing of microbial life (and thus the creation of diverse iron sulfides) in the water column, on the seafloor, and in the sediments.

On the other hand, if these pyrrhotite nodules were originally pyrite, as in the Paringa interflow shale samples from the Super Pit, this would provide very strong evidence to the argument that the trace element concentrations in the pyrite nodules at present are essentially unchanged from the formation of the nodules. This is because pyrite commonly loses much of its trace element inventory during the general metamorphic reaction $FeS_2 + T + P + H_2O \Rightarrow Fe_{1-x}S + H_2S + O_2$ (Large et al., 2011; Thomas et al., 2011; Tomkins, 2010; 2013), and pyrrhotite is generally a poor host for most pyrite-bound trace elements, especially As and Au. This would also further highlight the unique nature of the Paringa interflow shale, as distinct from the Kapai Slate or shales in the Black Flag Group, which do not appear to be as strongly anomalous in the key ore-forming elements.

5.6.3 Pb isotope systematics of nodular and ore sulfides

Previous Pb isotope studies of individual sulfide minerals and whole-rock samples from the Kalgoorlie Terrane of the Eastern Goldfields Superterrane have defined a triangular array on a $^{207}Pb/^{204}Pb$ vs. $^{206}Pb/^{204}Pb$ diagram (McNaughton et al., 1993; McNaughton and Groves, 1996; McCuaig and Kerrich, 1998). Individual Pb isotope analyses from a single locality can vary significantly, even if two samples of the same unit (or two minerals from one sample) are analyzed. Furthermore, as we have shown here, even individual sulfide grains can have differences of up to 10% in $^{207}Pb/^{206}Pb$ ratios between growth zones. Therefore, caution must be employed when interpreting Pb isotope results in

this gold province.

The Pb isotope data in Figure 5.21A clearly demonstrate that there are at least two sources of Pb in the pyrite nodules and ore pyrites, one with $^{206}Pb/^{204}Pb$ ratios of 13.6-13.7 and another with ratios of 13.9-14.0. Although we cannot say with certainty that the nodules formed before the Fimiston ore bodies on Pb isotope evidence alone, it is remarkable that the Pb isotope systematics of the nodules obey the stratigraphic order (with one exception): the Kapai Slate nodule GMKS-002 is less radiogenic (older) than the Paringa Basalt interflow shale nodules, which are mostly less radiogenic than the Black Flag nodules (GMSP-006 overlaps with BFB-003, but its error bars are also the highest of the sample set). This gives us confidence that the nodules and the ore-stage pyrites can be resolved from one another, at least for some of the formations (i.e., the Kapai Slate) and ore pyrite types (GMO-001 and 002). The fact that our Pb-Pb model age for the Kapai Slate (~2730 Ma, based on Stacey and Kramers growth curve with $\mu = 9.74$) is not the same as the published depositional age (2692 ± 4 Ma; Claoué-Long et al., 1988) is not a concern, as Pb-Pb dating of sulfides (particularly by laser ablation) is never as accurate and precise as U-Pb dating of zircon. Furthermore, these data also do not support a model of Golden Mile formation that invokes an uncontaminated mantle-derived fluid, as such a fluid would precipitate pyrite with significantly lower $^{207}Pb/^{204}Pb$ and $^{206}Pb/^{204}Pb$ ratios than the nodule and ore pyrites have; these hypothetical pyrites would in turn plot on a lower-μ growth curve (i.e., closer to the Jaguar pyrite, and the Teutonic Bore galena of McNaughton et al., 1993). Previous research (e.g., McNaughton et al., 1993) also sought to establish a direct link between Mesoarchean granitoids ~5 km below the current surface and the gold deposits of this region, based upon the structural geometry of the province and the systematic Pb isotope record of initial radiogenic Pb in the ore pyrites over the entire region. These authors proposed that a significant body of fluid containing radiogenic Pb was tapped from the deep crust at 2630 Ma by crustal-scale faults and transported to the various sites of deposition along the ~100 km-long Menzies-Kalgoorlie-Kambalda shear zone. We do not accept the 'one-shot' 2630 Ma timing proposed in their model, as based on our work, there are multiple events at slightly different times, consistent with field observations of the geology of the Golden Mile deposit. However, we do acknowledge that the Mesoarchean granitoids may have contributed some Pb to the sulfides in Kalgoorlie and elsewhere in the Eastern Goldfields (i.e., GMO-001 and GMO-002).

The 'anomalously' old Pb in ore sample 700264 is intriguing, given that this sample is ore (Fimiston-stage), yet it overlaps with the Paringa interflow shale pyrite nodules. Historic data from several gold deposits in the Eastern Goldfields (Browning et al., 1987; McNaughton et al., 1993) also have similar ratios to ore sample 700264, the Paringa nodules, and/or the Black Flag nodules (Fig. 5.21B), i.e., they have relatively unradiogenic Pb (note: some other gold deposits in the Eastern Goldfields have very radiogenic Pb compositions [e.g., Norseman], which are not shown on our diagram, but these ratios may be due to post-ore processes, i.e., metamorphism). The trend defined by 700264, GMSP-003, GMSP-001, and GMSP-008 (possibly GMSP-009 also) is evidence of this: these samples arguably have the same Pb, and one explanation why the nodules plot at higher μ values than the ore pyrites might be because the nodules are situated in black shale, a lithology known to be enriched in U relative to average continental crust. The same cannot be said of GMO-001 and GMO-002, which are much more radiogenic than the rest of the data. These samples are more akin to those from Norseman, which is in higher metamorphic grade terrain (amphibolite facies; McCuaig and Kerrich, 1998). In summary, our Pb isotope data support a diagenetic interpretation for the origin of the nodules, and also suggest that many of the Fimiston lodes (and perhaps Mt. Charlotte quartz vein stockworks) have Pb from greenstone sequences that contained thin, highly sulfidic interflow sedimentary rocks.

5.6.4 Differentiating shale formations at the Golden Mile and elswhere in the Eastern Goldfields based upon pyrite nodule textures and geochemistry

Each of the three shale formations in this study contains pyrite and pyrrhotite nodules with textures that

appear to be unique to the unit. This relationship has implications for regional stratigraphic correlation in the Eastern Goldfields Superterrane. Interestingly, pyrite nodules with nearly identical textures and similar geochemical patterns to the Paringa interflow shale, Black Flag Group shale, and Kapai Slate nodules were described from the Lucky Bay gold prospect, 70 km to the SSE of Kalgoorlie, by Steadman et al. (2013). There is also black shale with pyrite nodules at the Nimbus Ag-Zn-Pb deposit, ~15 k E of the Super Pit.

An interesting (and perhaps key) feature of the pyrite nodule geochemistry is the drastic difference in Au and Ag content between nodules in the three formations. While the Kapai Slate and Black Flag Group shale nodules have modest Au concentrations of ~0.1-1 ppm and Ag concentrations of ~1-10 ppm, the Paringa interflow shale nodules have over half an order of magnitude more Au (max ~8 ppm) and nearly as much more Ag (max 30 ppm). All of these concentrations range from on par with, to well above, the average Au concentration of 0.17 ppm for sedimentary pyrite globally (Large et al., 2013). As demonstrated above (see '5.5 - Results'), these concentrations have not been affected by later hydrothermal processes that enriched the Golden Mile with Au and other metals (that is, they owe their origin to an earlier, sedimentary/diagenetic process). This leads to a call for investigation into the cause of such large fluctuations in trace metal concentrations over short time intervals (5-10 million years), especially as this is a time in Earth's history when the atmosphere and ocean are thought to have been almost universally reducing with respect to oxygen. Recent research suggests these changes in trace element composition might be related to fluctuating ocean water chemistry with time: Large et al. (2014) documented the rise and fall of multiple trace elements in sedimentary pyrites at specific times in Earth's history, from 3500 Ma to the present. They attribute the dynamic increase of pyrite-bound trace elements (such as Mo, Se, and Cu) to rising oxygen levels and associated biological productivity in the ocean.

Alternatively, the high amount of Au, particularly in the Paringa interflow shale pyrite nodules, might reflect local controls on the enrichment of the water column (i.e., the presence of voluminous basalt and komatiite). Other black shale localities in the Eastern Goldfields Superterrane need to be reevaluated in light of these data in order for the characteristics of the Kapai Slate, Paringa interflow shale, and Black Flag Group identified here to be more completely defined.

5.6 Conclusions

Quantitative LA-ICP-MS trace element analyses, Pb isotope ratios, and in-situ S isotope measurements, of diagenetic pyrite and pyrrhotite nodules from several black shale units in and along strike from the giant Golden Mile Au-Ag-Te deposit and the immediately surrounding region reveal multiple stages of Au, Te, and As enrichment during sedimentation and volcanism at ca. 2700-2680 Ma (i.e., before the first ore event – Fimiston – at ≤ 2650 Ma) in a constantly changing oceanic and atmospheric environment. These data show that the syn-sedimentary/diagenetic trace element and S isotope signature of sulfides can be preserved through not only mild metamorphism and deformation, but also periodically intense, long-lived hydrothermal alteration. While some of the ore-stage pyrites (particularly those from the Fimiston event) contain trace element patterns reminiscent of the sedimentary pyrites, their zonation and trace metal budgets do not fully match those of the sedimentary pyrites, and furthermore, the S sources of the ore-stage and sedimentary pyrites are different (especially in terms of $\Delta^{33}S$). The data presented in this study also suggest a need for further research on the volcanic/sedimentary history and geochemical complexity of early sulfides in ore districts, as they potentially hold a great deal of vital geologic information.

Chapter 6

Relating black shale sulfide geochemistry to ore source and mineralogy in BIF-hosted (and greenstone-hosted) gold deposits: a LA-ICP-MS study

6.1 Introduction

The source of gold in orogenic gold deposits remains unresolved: on the one hand, there are those who believe that the gold now contained in a typical orogenic (either greenstone-hosted or sediment-hosted) gold deposit was originally located much deeper than the current near-surface environment, in either the lower crust or the upper mantle (Groves, 1993; Groves et al., 1998; Goldfarb et al., 2001; 2005; Hronsky et al., 2012; Phillips and Powell, 2010). This model (see Fig. 6.1A) is generally accepted as the one that best accounts for the regional architecture and geochemical nature of these deposits. On the other hand, some geologists think that the gold source or sources are upper-crustal materials, ostensibly much closer to the deposit than the lower crust or upper mantle. One upper-crustal rock type in particular has received much attention in the last 10 years: carbonaceous and pyritic black shale, or mudstone. This lithology is known to have high amounts of certain metals that are keys to the formation of a sediment-hosted or greenstone-hosted orogenic gold deposit, such as Au, As, Ag, Te, and Sb (Buryak, 1982; Ketris and Yudovitch, 2009; Large et al., 2011; Tomkins 2010, 2013; Pasava et al., 2013). Furthermore, there are many orogenic gold districts around the world that have black shales in or around the mine area, such as Sukhoi Log (Russia; Large et al., 2007; Meffre et al., 2008), Bendigo (Australia; Large et al., 2009; Thomas et al., 2011), Kumtor (Kyrgyzstan; Large et al., 2011), Spanish Mountain (Canada; Large et al., 2009), the Quadrilátero Ferrífero (Brazil; Ribero-Rodrigues et al., 2007; Vial et al., 2007), Betze-Post, Rodeo, and Goldstrike in the north Carlin Trend (USA; Large et al., 2009; 2011), Muruntau (Uzbekistan; Pasava et al., 2013), and the Witwatersrand goldfields (South Africa; Large et al., 2013).

Two other sediment (specifically banded iron formation, or BIF)-hosted gold districts, Homestake (USA) and Randalls (Australia), also contain carbonaceous and sulfidic black shale, but these have not previously been studied in any detail. The Homestake deposit, situated in the northern Black Hills, is currently the world's largest BIF-hosted gold district, despite being closed for over a decade, with a global resource of almost 41 Moz (~1300 t) Au in nearly 30 separate (but closely spaced and largely strata-bound) ore bodies, all of which was mined at an average grade of 8 g/t (Caddey et al., 1991). The Randalls district comprises three separate deposits (Santa-Craze, Maxwells, and Cock-Eyed Bob) at different locations along the same folded BIF horizon in the southern Eastern Goldfields Superterrane, a part of the Archean-Proterozoic Yilgarn Craton. The total gold endowment of the three deposits is ~0.6 Moz at 3 g/t, which, while significantly less than Homestake, is more typical of BIF-hosted gold deposits around the world (see chapter 4). Black shale forms part of the stratigraphic footwall to the ore-bearing BIF at the Homestake deposit, whereas the same rock type is much farther removed from

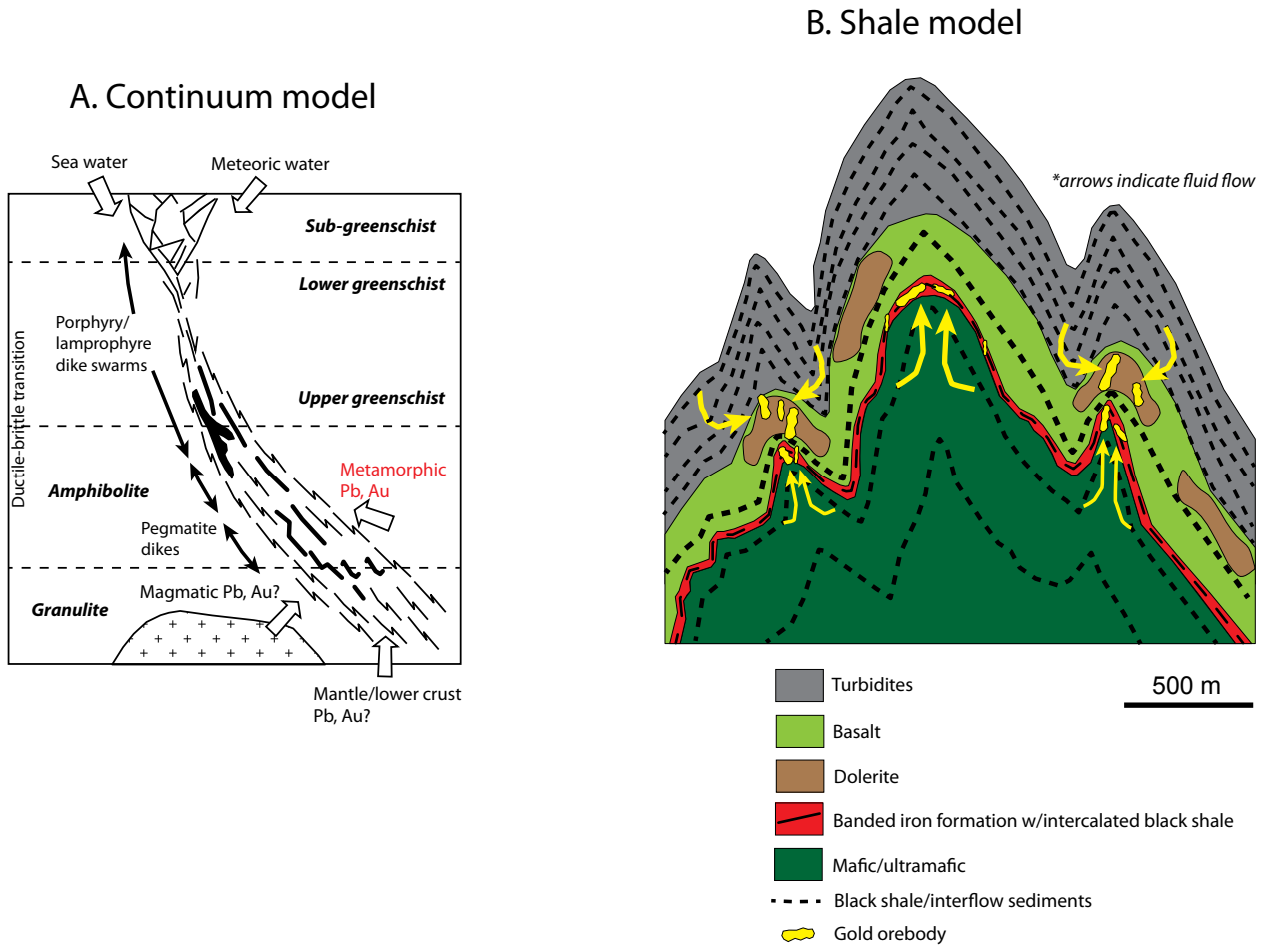

Fig. 6.1 A. Continuum/metamorphic model for orogenic gold deposits (redrawn after Phillips and Powell, 2009). This model proposes that orogenic gold resources can form over a large section of the crust at varying temperatures and pressures, but the metal source for all of these is one or a combination of mantle/lower crust, magma, or metamorphosed middle crust. Fluids for orogenic gold deposits, according to the model, can be metamorphic, meteoric, or oceanic in origin. **B**. A 'shale' model for orogenic gold deposits, whereby black shales (either as thin interflow sediments within mafic volcanic packages or as thicker constituents of turbidite sequences) are tapped at least for metals during metamorphism (if not fluids). In this respect, there is considerable overlap between the model here proposed and that in 'A': sedimentary rocks metamorphosed to the amphibolite facies undergo widespread devolatilization, and in those which have a significant budget of sedimentary pyrite, the fludis produced can contain vast amounts of ore-forming metals (e.g., Au, As, Ag, Te, and Pb).

the Randalls deposits, existing at depth (> 3.5 km) beneath the Randalls basin and outcropping ~10 km WSW of Cock-Eyed Bob, at Lucky Bay (adjacent to the alkaline Lake Randell). The work done at Randalls/Lucky Bay was extended to include the world-famous and giant (~65 Moz, or 2100 t) Golden Mile greenstone-hosted gold deposit, primarily because of its relatively close position to Randalls/Lucky Bay (~60 km to the NNW) and the general similarity in stratigraphy between the two areas.

The geochemical nature of sedimentary and ore-related pyrite and associated sulfides in these study areas were investigated using laser ablation inductively-coupled plasma mass spectrometry (LA-ICP-MS), with additional research by whole-rock XRF and sulfide textural characterization via optical and scanning electron microscopy. Lead isotopes of the sulfides were also measured via LA-ICP-MS to ascertain the ages of the various sulfide generations both in the sediments and in the ore zone (Golden Mile only). This work has led to a better understanding of the trace element character of sulfides in and around BIF-hosted gold deposits, and has also placed constraints on the timing of gold introduction and its source(s) in the sediment-hosted (and greenstone-hosted) orogenic gold deposit classification scheme at large.

6.2 Homestake

The Homestake mine was developed around the Homestake Formation, a carbonate-facies (siderite-ankerite) banded iron formation (BIF) that has been folded, metamorphosed, and structurally disrupted (Fig. 4.1b). Stratigraphically beneath this unit lies the Poorman Formation, the upper part of which contains pyritic black shale (Fig. 4.1c). The Homestake ore bodies are long, narrow shoots focused primarily in the BIF, though the ore does transgress the BIF-black shale contact in certain areas (see Fig. 3 in Morelli et al., 2010).

The black shale at Homestake belongs to the Ross member of the Poorman Formation. Examples of the sulfidic nature of the Ross member are shown in Figure 4.2. Metamorphic grade varies across the mine, from amphibolite facies in the east to greenschist in the west (the metamorphic isograds are broadly zoned around Proterozoic granite intrusions). Therefore, Poorman samples from the eastern portions of the mine are predominately pyrrhotite-bearing with late, retrograde metamorphic pyrite, whereas samples from the western mine area are mainly pyrite, as maximum metamorphic temperatures apparently did not exceed pyrite stability (although these pyrites were recrystallized to a substantial degree). Pyrite (and pyrrhotite) from both the western and eastern mine areas were analyzed for trace element contents and characteristics.

Two forms of early pyrite occur in the upper Poorman Formation: disseminated euhedra (including aggregates of these euhedra into anhedral shapes) and nodules, which are predominantly round. Figure 4.6 and 4.7 show two laser images, one for each py1 form analyzed. In Figure 4.7, the anhedral mass of early pyrite is partially overgrown by a rim of later (presumably metamorphic) pyrite, termed py2, while in Figure 4.6, the nodule has pressure shadows that are mostly filled with pyrrhotite (some metamorphic pyrite is present as well). Both types contain an abundance of trace elements, most notably Au (~0.5 ppm), As (1000-10,000 ppm), and Ag (~10 ppm) but also Co (~100 ppm), Ni (100-500 ppm), Cu (100-500 ppm), Se (~50 ppm), Mo (10-50 ppm), Sb (50-100 ppm), Te (10-20 ppm), Hg (1000 counts per second), Tl (0.5-5 ppm), Pb (~100 ppm), and Bi (~10 ppm). The Pb and S isotope characteristics of these pyrites indicate that the trace elements are essentially indigenous; however, the Pb in these pyrites is significantly disturbed by later thermotectonic events.

Chapter 4 details the amount of Au, As, Ag, and Te that could be produced (theoretically) from a given volume of upper Poorman Formation (black shale). The Homestake deposit contained nearly 1300 t Au, and if the upper Poorman Formation was the sole metal source, a volume of at least 12 km^3 would be required, which is well within the known extent of the upper Poorman. Few researchers have suggested that the upper Poorman could be a source of metals for Homestake; most 'syngeneticists' have suggested that Au was already present in the Homestake Formation (siderite-ankerite BIF) before deformation and metamorphism commenced (Rye and Rye, 1974; Redden and DeWitt, 2008). The bulk of research on Homestake focuses on the late Paleoproterozoic Harney Peak-type granitic intrusions as potential fluid (and metal) sources (e.g., Frei et al., 2009). A fourth possible source, rarely mentioned in the literature, is the thick (>1 km) mafic package of the lower Poorman Formation, originally pillow basalt but now metamorphosed to amphibolite. Tomkins (2010) modeled the S source potential of mafic greenstones and found them to be insufficient in terms of metal concentration ability; the ore-forming process would have to be ultra-efficient in order to create a deposit sourced entirely from mafic metavolcanics. Morelli et al. (2010) analyzed Re and Os in ore-stage arsenopyrite, and concluded that none of the metasedimentary or metavolcanic units that comprise Homestake could have been the Re and Os source (and, by extension, the Au source). Rather, they appealed to a mantle origin for these metals. However, the fact that black shale is widely recognized as a sink for many ore-forming metals (including Au and As), and the intimate association between this rock type and the ore host BIF at Homestake, leads to a plausible scenario in which early stage (syn-sedimentary to diagenetic) pyrite

in the upper Poorman Formation releases its metal budget (plus S) during metamorphic conversion to pyrrhotite, and through-going metamorphic and/or magmatic fluids transfer these metals to structural sites of low pressure, where they precipitate in the BIF as native gold, pyrrhotite, and arsenopyrite (Fig. 6.1B).

6.3 Randalls and Lucky Bay

The Santa Claus member BIF of the Belches Supersequence at the Randalls deposits (Cock-Eyed Bob, Maxwells, and Santa-Craze) is essentially laminated oxide-facies (magnetite-dominant) iron formation, which has been altered to pyrrhotite- and arsenopyrite-dominant BIF in ore zones (Fig. 3.3). The unit consists of alternating mm-scale laminations of magnetite and quartz, with cm-thick intervals of mudstone (now massive chlorite). In ore zones, pyrrhotite replaces the magnetite but preserves the original laminae, while arsenopyrite also replaces magnetite but obliterates primary textures. Free gold is associated with both pyrrhotite and arsenopyrite (Figs 3.5, 3.9), but also with magnetite (not shown).

Pyritic black shale at Lucky Bay is thought to be correlative with the Black Flag Group, a widespread volcano-sedimentary unit in the Eastern Goldfields, based on detrital U-Pb zircon geochronology (Steadman et al., 2013). This unit contains several large (≤ 1 cm) pyrite nodules (Fig. 2.4) interpreted by Steadman et al. (2013) to have grown during early diagenesis; all of them have experienced low-grade (lower greenschist facies) metamorphism and deformation, leading to the development of pressure shadows and renewed pyrite-sulfide growth on the margins of the nodules (Fig. 2.4). Textures within the nodules appear to be essentially unchanged.

Figures 2.10, 2.11, and 2.12 illustrate the trace-element systematics of the several pyrite nodule types from Lucky Bay; all nodules are enriched in Au (0.5-2 ppm), Ag (10-30 ppm), As (1000-5000 ppm), Te (20-50 ppm), Sb (100-200 ppm), Hg (1000 cps), Pb (1000-5000 ppm), and Bi (10-50 ppm). The Randalls BIF pyrrhotite and arsenopyrite are significantly less enriched in Au, Ag, As, Hg, Pb, and Bi, but can have higher Te (up to 500 ppm in arsenopyrite; Fig. 3.10) and Mo (up to 100 ppm in arsenopyrite; Fig. 3.11). Lead and S isotopes of the nodules support the early diagenesis interpretation

Unlike the BIF-black shale relationships at Homestake, the present-day ore host BIF at Randalls is far removed from any black shale, being surrounded by thousands of meters of turbidites. However, at depth beneath the basin (i.e., greater than 3 km) is the Black Flag Group, which outcrops in the Lucky Bay area. Given that this unit is folded under the Belches Sequence by a syncline, it is theoretically possible that sedimentary pyrite in black shale of the Black Flag Group contributed some of its metal budget to the ore zones at Cock-Eyed Bob, Maxwells, and Santa-Craze. The total amount of known gold in the Randalls BIF district is < 1 Moz (< 50 t), so the required volume of source rock at Randalls is orders of magnitude smaller that what is needed for Homestake. Calculations in Chapter 3 show that a sedimentary succession at least 500 m thick (containing perhaps 20-25 %, or 100 m, of black shale), could account for the amount of gold in the three Randalls deposits, not to mention As. This is well within the total thickness of the Black Flag Group, indicating that this sequence should be considered a source of metals for these deposits.

6.4 Golden Mile

Gold orebodies at Kalgoorlie are predominantly one of two types: Fimiston-style (also called Golden Mile-style) lodes and Mount Charlotte-style quartz vein stockworks. Fimiston lodes are pipe-shaped shoots contained within carbonate- and sericite-altered dolerite; they are commonly V-rich (vanadium-rich mica) and Te-rich (nearly 20 different tellurides have been reported from the deposit) and can have abundant free gold; the V-rich lodes are commonly green in color due to the amount of V in the rocks ; such ore is called 'Green Leader' mineralization. The Mount Charlotte quartz-vein stockworks are

characterized by large, coarse-grained quartz and flat-sided vein geometries, with the veins containing free gold and the proximal haloes to those veins containing sulfides (predominantly pyrite). The primary host lithology in both cases is the Golden Mile Dolerite, but some gold also occurs in the underlying Paringa Basalt and the overlying Black Flag Group.

Pyritic black shale similar in many respects to that from Lucky Bay occurs at the Golden Mile deposit in three distinct units: the Kapai Slate, Oroya Shale (informal name) and the Black Flag Group shale. These three lithologies comprise only a small percentage of the total rock volume at the Golden Mile, but all three formations contain diagenetic pyrite nodules, some of which have very similar internal and external textures to the Lucky Bay nodules; Figures 5.4-5.9 display examples of nodules from these units.

Several examples of each pyrite nodule type was imaged, and results are shown in Figures 5.12, 5.13, and 5.15-5.17. The amount of trace elements in a given Golden Mile pyrite nodule depends on which formation the nodule comes from: Oroya Shale nodules have the highest overall trace element concentrations, followed by Kapai Slate and then Black Flag nodules, which have roughly the same levels of trace elements (except for Ag, which is an order of magnitude higher in the Kapai nodules). The Oroya Shale nodules also have among the highest gold contents of any sedimentary pyrite in the world (Fig. 5.18), which is an interesting fact given this formation's proximity to the Golden Mile ore bodies in both space and time.

The size of the Golden Mile's metal endowment seemingly rules out a sedimentary source alone, given how thin the three shale units are (maximum 30 m) and their apparently restricted extent. However, the pyrite nodules here are very gold-rich (especially those belonging to the Oroya Shale), and under the right conditions, significant amounts of gold could be produced from relatively small volumes of rock. Several different rock types exist in and around the deposit, and as discussed in Chapter 5, any one of these (or a combination) may have played a role in forming the Golden Mile. The most likely scenario is one involving pyritic black shales, mafic-felsic porphyritic intrusions, and basalt/komatiite flows, all being accessed by different fluids at various times in multiple (but closely spaced) locations, culminating in one of the biggest single gold deposits in the world (Fig. 6.1B).

6.5 Conclusions

The laser results from Homestake, Lucky Bay/Randalls, and the Golden Mile show that the trace element signature of early (syn-sedimentary to early diagenetic) pyrites are rich in ore-forming elements, particularly Au, As, Ag, Te, Sb, Hg, Pb, and Bi. Furthermore, the data from Homestake and the Golden Mile indicate that this signal can be preserved through at least moderate deformation and metamorphism, even though the early pyrite can be recrystallized to a substantial degree (i.e., Homestake). These data have wide-ranging implications for the understanding of hydrothermal systems in ore environments, and also add new information to existing exploration models of orogenic gold deposit formation (both sediment-hosted and greenstone-hosted), which will help geologists search more effectively for new orogenic gold resources.

References

Agangi, A., Hoffman, A., and Wohlgemuth-Ueberwasser, C.C., 2013. Pyrite zoning as a record of mineralization in the Ventersdorp Contact Reef, Witwatersrand Basin, South Africa. *Economic Geology* 108, 1243–1272.

Andrianjakavah, P., Salvi, S., Béziat, D., Guillaume, D., Rakotondrazafy, M., and Moine, B., 2007. Textural and fluid inclusion constraints on the origin of the banded-iron-formation-hosted gold deposits at Maetvatanana, central Madagascar. *Mineralium Deposita* 42, 385–398.

Anhaeusser, C.R., 1976. Archean metallogeny in Southern Africa. *Economic Geology* 71, 16–43.

Arias, D., Corretgé, L.G., and Villa, L., 1998. A new source of isotopically heavy sulphur in lode-gold deposits of NW Spain: A batch volatilization process in the conversion of pyrite to pyrrhotite by contact metamorphism. *Terra Nova* 10, 136–138.

Ayres, D.E., 1972. Genesis of iron-bearing minerals in banded iron formation mesobands in the Dales Gorge member, Hamersley Group, Western Australia. *Economic Geology* 67, 1214–1233.

Bajwah, Z., Seccombe, P., and Offler, R., 1987, Trace element distribution, Co:Ni ratios and genesis of the Big Cadia iron-copper deposit, New South Wales, Australia. *Mineralium Deposita* 22, 292-300.

Baker, J., Peate, D., Waight, T., and Meyzen, C., 2004. Lead isotopic analysis of standards and samples using a Pb-207-Pb-204 double spike and thallium to correct for mass bias with a double-focusing MC-ICP-MS. *Chemical Geology* 211, 275–303.

Bardoux, M., 2013. Early Paleoproterozoic sediment-hosted gold of the Birimian and Guiana Shields. FUTORES (Future Understanding of Tectonics, Ores, Resources, Environment, and Sustainability) Conference, Townsville, Australia, 2-5 June 2013, Proceedings.

Barley, M.E., Brown, S.J.A., Krapež, B., and Kositcin, N., 2008. Physical volcanology and geochemistry of a Late Archaean volcanic arc: Kurnalpi and Gindalbie Terranes, Eastern Goldfields Superterrane, Western Australia. *Precambrian Research* 161, 53–76.

Barley, M.E., Krapež, B., Groves, D.I., and Kerrich, R., 1998. The late Archaean bonanza: metallogenic and environmental consequences of the interaction between mantle plumes, lithospheric tectonics, and global cyclicity. *Precambrian Research* 91, 65–90.

Bartram, G.D., 1969, Wall rock alteration associated with auriferous lodes at Kalgoorlie. Unpublished PhD thesis, Perth, Australia, University of Western Australia.

Bateman, R., and Hagemann, S., 2004. Gold mineralisation throughout about 45 Ma of Archaean orogenesis: protracted flux of gold in the Golden Mile, Yilgarn craton, Western Australia. *Mineralium Deposita* 39, 536–559.

Bavinton, O.A., 1981. The nature of sulfidic metasediments at Kambalda and their broad relationships with associated ultramafic rocks and nickel ores. *Economic Geology* 76, 1606–1628.

Bavinton, O.A., and Keays, R.R., 1978, Precious metal values from interflow sedimentary rocks from the komatiite sequence at Kambalda, Western Australia. *Geochimica et Cosmochimica Acta* 42, 1151-1163.

Bekker, A., and Eriksson, K.A., 2003, A Paleoproterozoic drowned carbonate platform on the southeastern margin of the Wyoming Craton: a record of the Kenorland breakup. *Precambrian Research* 120, 327-364.

Bekker, A., Barley, M.E., Fiorentini, M.L., Rouxel, O.J., Rumble, D., and Beresford, S.W., 2009. Atmospheric sulfur in Archean komatiite-hosted nickel deposits. *Science* 326, 1086–1089.

Bekker, A., Kahru, J.A., Eriksson, K.A., and Kaufman, A.J., 2003, Chemostratigraphy of Paleoproterozoic carbonate successions of the Wyoming Craton: tectonic forcing of biogeochemical change? *Precambrian Research* 120, 279-325.

Bekker, A., Slack, J.F., Planavsky, N., Krapež, B., Hofmann, A., Konhauser, K.O., and Rouxel, O.J., 2010. Iron Formation: The sedimentary product of a complex interplay among mantle, tectonic, oceanic, and biospheric processes.*Economic Geology* 105, 467–508.

Belford, S., 2010. Genetic and chemical characterisation of the host succession to the Archean Jaguar VHMS deposit.Unpublished PhD thesis, Hobart, Australia, University of Tasmania, 258 p.

Berry, A.J., Danyushevsky, L.V., O'Neill, H.C., Newville, M., and Sutton, S.R., 2008. Oxidation state of iron in komatiite melt inclusions indicates hot Archaean mantle. *Nature* 455, 960–963.

Biczok, J., Hollings, P., Klipfel, P., Heaman, L., Maas, R., Hamilton, M., Kamo, S., and Friedman, R., 2012. Geochronology of the North Caribou greenstone belt, Superior Province, Canada: Implications for tectonic history and gold mineralization at the Musselwhite mine. *Precambrian Research* 192–195, 209–230.

Black, L.P., and Gulson, B.L., 1978. The age of the Mud Tank Carbonatite, Strangways Range, Northern Territory.*Journal of Australian Geology and Geophysics* 3, 227–232.

Black, L.P., Kamos, L., Allen, C.M., Aleinkoff, J.N., Davis, D.W., Korsch, R.J., and Foudoulis, C., 2003. TEMORA 1: a new zircon standard for Phanerozoic U-Pb geochronology. *Chemical Geology* 200, 155–170.

Blewett, R.S., Czarnota, K., Henson, P.A., 2010. Structural-event framework for the eastern Yilgarn Craton, Western Australia, and its implications for orogenic gold. *Precambrian Research* 183, 203–229.

Bornhorst, T.J., and Williams, W.C., 2013. The Mesoproterozoic Copperwood sedimentary rock-hosted stratiform copper deposit, Upper Peninsula, Michigan. *Economic Geology* 108, 1325–1346.

Boulter, C.A., Fotios, M.G., and Phillips, G.N., 1987. The Golden Mile, Kalgoorlie: A giant gold deposit localized in ductile shear zones by structurally induced infiltration of an auriferous metamorphic fluid. *Economic Geology* 82, 1661–1678.

Browning, P., Groves, D.I., Blockley, J.G., and Rosman, K.J.R., 1987. Lead isotope constraints on the age and source of gold mineralization in the Archean Yilgarn block, Western Australia. *Economic Geology* 82, 971–986.

Brugger, J., Maas, R., Lahaye, Y., McRae, C., Ghaderi, M., Costa, S., Lambert, D., Bateman, R., and Prince, K., 2002, Origin of Nd-Pb-Sr isotopic variations in single scheelite grains from Archaean gold deposits, Western Australia. *Chemical Geology* 182, 203-225.

Bryan, S.E., Allen, C.M., Holcombe, R.J., and Fielding, C.R., 2004. U-Pb zircon geochronology of Late Devonian to Early Carboniferous extension-related silicic volcanism in the northern New England Fold Belt. *Australian Journal of Earth Sciences* 51, 645–664.

Bullis, H.R., Hureau, R.A., and Penner, B.D., 1994. Distribution of gold and sulfides at Lupin, Northwest Territories *Economic Geology* 89, 1217–1227.

Buryak, V.A., 1982. Metamorphism and ore formation. Moscow, Nedra Press, 256 p. (in Russian).

Caddey, S.W., Bachman, R.L., Campbell, T.J., Reid, R.R., and Otto, R.P., 1991. The Homestake gold mine, an early Proterozoic iron-formation-hosted gold deposit, Lawrence County, South Dakota. *United States Geological Survey Bulletin* 1857-J, 67 p.

Cameron, E.M., and Hattori, K., 1987, Archean gold mineralization and oxidized hydrothermal fluids. *Economic Geology* 82, 1177-1191.

Campbell, I.H., and Hill, R.I., 1988. A two-stage model for the formation of the granite-greenstone terrains of the Kalgoorlie-Norseman area, Western Australia. *Earth and Planetary Science Letters* 90, 11–25.

Campbell, I.H., Ballard, J.R., Palin, J. Michael, Allen, C., and Faunes, A., 2006. U-Pb zircon geochronology of granitic rocks from Chuquicamata-El Abra porphyry copper belt of northern Chile: Excimer laser ablation ICP-MS analysis. *Economic Geology* 101, 1327–1344.

Cathelineau, M., Boiron, M-C., Holliger, P., Marion, P., and Denis, M., 1989. Gold in arsenopyrites: Crystal chemistry, location and state, physical and chemical conditions of deposition. *Economic Geology Monograph* 6, 328–341.

Champion, D.C., and Cassidy, K.F., 2007. An overview of the Yilgarn Craton and its crustal evolution. In: Bierlein, F.P., and Knox-Robinson, C.M., (eds.), *Proceedings of Geo-conferences (WA) Inc. Kalgoorlie '07 Conference, Kalgoorlie, Western Australia*, 13–35.

Chang, Z., Large, R.R., and Maslennikov, V., 2008. Sulfur isotopes in sediment-hosted orogenic gold deposits: Evidence for an early timing and a seawater sulfur source. *Geology* 36, 971–974.

Chinn, W., 1969. Structural and mineralogical studies of the Homestake mine, Lead, South Dakota. Unpublished PhD thesis, Berkeley, California, University of California, 190 p.

Claoué-Long, J.C., Compston, W., and Cowden, A., 1988. The age of the Kambalda greenstones resolved by ion-microprobe: Implications for Archaean dating methods. *Earth and Planetary Science Letters* 89, 239–259.

Clout, J.M.F., 1989, Structural and isotopic studies of the Golden Mile gold-telluride deposit, Kalgoorlie, WA: Unpublished PhD thesis, Melbourne, Australia, Monash University, 352 p.

Clout, J.M.F., Cleghorn, J.H., and Eaton, P.C., 1990. Geology of the Kalgoorlie Gold Field. *Australian Institute of Mining and Metallurgy Monograph* 14, 411–431.

Connolly, J.P., 1927. Tertiary mineralization of the northern Black Hills. *South Dakota School of Mines Bulletin* 15, 130 p.

Cooke, D.R., and Simmons, S.F., 2000, Characteristics and genesis of epithermal gold deposits. *Reviews in Economic Geology* 13, 245-278.

Corkhill, C.L., and Vaughan, D.J., 2009. Arsenopyrite oxidation – A review. *Applied Geochemistry* 24, 2342–2361.

Craig, J.R., and Solberg, T.N., 1999, Compositional zoning in ore minerals at the Craig mine, Sudbury, Ontario, Canada. *The Canadian Mineralogist* 37, 1163–1176.

Craig, J.R., and Vokes, F.M., 1993. The metamorphism of pyrite and pyritic ores: an overview. *Mineralogical Magazine* 57, 3–18.

Crowe, D.E., and Vaughan, R.G., 1996. Characterization and use of isotopically homogeneous standards for in situ laser microprobe analysis of $^{34}S/^{32}S$ ratios. *American Mineralogist* 81, 187–193.

Crowe, S.A., Paris, G., Katsev, S., Jones, C., Kim, S-T., Zerkle, A.L., Nomosatryo, S., Fowle, D.A., Adkins, J.F., Sessions, A.L., Farquhar, J., and Canfield, D.E., 2014, Sulfate was a trace constituent of Archean seawater. *Science* 346, 735-739.

Cumming, G.L., and Richards, J.R., 1975. Ore lead isotope ratios in a continuously changing earth. *Earth and Planetary Science Letters* 28, 155–171.

Czarnota, K., Champion, D.C., Goscombe, B., Blewett, R.S., Cassidy, K.F., Henson, P.A., and Groenewald, P.B., 2010. Geodynamics of the eastern Yilgarn Craton. *Precambrian Research* 183, 175–202.

Dahl, P.S., Hamilton, M.A., Jercinovic, M.J., Terry, M.P., Williams, M. L., and Frei, R., 2005. Comparative isotopic and chemical geochronometry of monazite, with implications for U-Th-Pb dating by electron microprobe: An example from metamorphic rocks of the eastern Wyoming Craton (U.S.A.). *American Mineralogist* 90, 619–638.

Dahl, P.S., Hamilton, M.A., Wooden, J.L., Foland, K.A., Frei, R., McCombs, J.A., and Holm, D.K., 2006. 2480 Ma mafic magmatism in the northern Black Hills, South Dakota: A new link connecting the Wyoming and Superior cratons. *Canadian Journal of Earth Sciences* 43, 1579–1600.

Danyushevsky, L.V., Robinson, P., Gilbert, S., Norman, M., Large, R., McGoldrick, P., and Shelley, M., 2011. Routine quantitative multi-element analysis of sulphide minerals by laser ablation ICP-MS: Standard development and consideration of matrix effects. *Geochemistry: Exploration, Environment, Analysis* 11, 51–60.

Deol, S., Deb, M., Large, R.R., and Gilbert, S., 2012. LA-ICPMS and EPMA studies of pyrite, arsenopyrite, and loellingite from the Bhukia-Jagpura gold prospect, southern Rajasthan, India: Implications for ore genesis and gold remobilization. *Chemical Geology* 326–327, 72–87.

Dobbe, R.T.M., 1991. Ullmannite, cobaltian ullmannite, and willyamite from Tunaberg, Bergslagen, central Sweden. *The Canadian Mineralogist* 29, 199–205.

Dugdale, A.L., Wilson, C.J.L., Leader, L.D., Robinson, J.A., and Dugdale, L.J., 2009. Carbonate spots: understanding the relationship to gold mineralization in central Victoria, southeastern Australia. *Mineralium Deposita* 44, 205–219.

Dunphy, J.M., Fletcher, I.R., Cassidy, K.F., and Champion, D.C., 2003. Compilation of SHRIMP U-Pb geochronological data, Yilgarn Craton, Western Australia 2001–2002. *Geoscience Australia Record* 2003/15, 139.

Dupuis, C., Beaudoin, G., 2011. Discriminant diagrams for iron oxide trace element fingerprinting of mineral deposits. *Mineralium Deposita* 46, 319–335.

Evans, K.A., Phillips, G.N., and Powell, R., 2006, Rock-buffering of auriferous fluids in altered rocks associated with the Golden Mile-style mineralization, Kalgoorlie gold field, Western Australia: *Economic Geology*, v. 101, p. 805-817.

Falconer, D.M., Craw, D., Youngson, J.H, and Faure, K., 2006, Gold and sulphide minerals in Tertiary quartz pebble conglomerate gold placers, Southland, New Zealand. *Ore Geology Reviews* 28, 525-545.

Farquhar, J., Bao, H., and Thiemens, M., 2000, Atmospheric influence of Earth's earliest sulfur cycle. *Science* 289, 756-758.

Fiorentini, M., Beresford, S., Barley, M., Duuring, P., Bekker, A., Rosengren, N., Cas, R., and Hronsky, J., 2012. District to camp controls on the genesis of komatiite-hosted nickel sulfide deposits, Agnew-Wiluna greenstone belt, Western Australia: Insights from multiple sulfur isotopes. *Economic Geology* 107, 781–796.

Frei, R., Dahl, P.S., Frandsson, M.M., Jansen, L.A., Hansen, T.R., Terry, M.P., and Frei, K.M., 2009. Lead-isotope and trace-element geochemistry of Paleoproterozoic metasedimentary rocks in the Lead and Rochford basins (Black Hills, South Dakota, USA): Implications for genetic models, mineralization ages, and sources of leads in the Homestake gold deposit. *Precambrian Research* 172, 1–24.

Fripp, R.E.P., 1976. Stratabound gold deposits in Archean banded iron-formation, Rhodesia. *Economic Geology* 71, 58–75.

Fyon, J.A., Crocket, J.H., and Schwarcz, H.P., 1986. The Carshaw and Malga iron-formation-hosted gold deposits of the Timmins area, in Colvine, A.C., ed., Geology of Gold in Ontario: Toronto. *Ontario Geological Survey, Miscellaneous Paper* 110, 98–110.

Gaboury, D., 2013. Does gold in orogenic deposits come from pyrite in deeply buried carbon-rich sediments?: Insights from volatiles in fluid inclusions. *Geology* 41, 1207–1210.

Gauthier, L., Hagemann, S., and Robert, F., 2004, Architecture and timing of gold mineralisation at the Golden Mile gold deposit, Kalgoorlie, Western Australia: Unpublished report, pp. 95, http://www.ga.gov.au/corporate_data/68023/68023.pdf.

Gauthier, L., Hagemann, S., and Robert, F., 2008, Paragenesis of Fimiston-style lodes at the Golden Mile, Kalgoorlie, Western Australia: Unpublished poster, http://www.ga.gov.au/corporate_data/68045/68045.pdf.

Geusebroek, P.A., and Duke, N.A., 2004. An update on the geology of the Lupin gold mine, Nunavut, Canada. *Exploration Mining Geology* 13, 1–13.

Glasson, M.J., and Keays, R.R., 1978. Gold mobilization during cleavage development in sedimentary rocks from the auriferous slate belt of central Victoria, Australia: Some important boundary conditions. *Economic Geology* 73, 496–511.

Goldfarb, R.J., Baker, T., Dubé, B., Groves, D.I., Hart, C.J.R., and Gosselin, P., 2005. Distribution, character, and genesis of gold deposits in metamorphic terranes. *Economic Geology 100th Anniversary Volume,* 407–450.

Goldfarb, R.J., Groves, D.I., and Gardoll, S., 2001. Orogenic gold and geologic time: a global synthesis. *Ore Geology Reviews* 18, 1–75.

Goldhaber, M.B., 2003, Sulfur-rich sediments, *in* Mackenzie, F.T. ed., *Treatise on Geochemistry*, 1st edition, 257-288.

Golding, L.Y., 1978. Mineralogy, geochemistry and origin of the Kalgoorlie gold deposits, Western Australia. Unpublished PhD thesis, Melbourne, Australia, University of Melbourne.

Golding, L.Y., 1985. The nature of the Golden Mile Dolerite south-east of Kalgoorlie, Western Australia. *Australian Journal of Earth Sciences* 32, 55–63.

Golding, L.Y., and Keays, R.R., 1981. Problems of ore genesis at Kalgoorlie. Fifth Australian Geological Convention ("Sediments Through the Ages"), Perth. *Geological Society of Australia Abstracts* 3, 70 p.

Goscombe, B., Blewett, R.S., Czarnota, K., Groenewald, P.B., and Maas, R., 2009. Metamorphic evolution and integrated terrane analysis of the eastern Yilgarn Craton: Rationale, methods, outcomes, and interpretation. *Geoscience Australia Record* 2009/23, 281.

Gregory, D.D., 2014, Trace element contents of sedimentary pyrite. Unpublished PhD thesis, Hobart, Australia, University of Tasmania.

Gregory, D.D., Large, R.R., Halpin, J.A., Lounejeva-Baturina, E., Lyons, T.W., Wu, S., Sack, P.J., Chappaz, A., Maslennikov, V.V., and Bull, S.W., 2015, Trace element content of background sedimentary pyrite in black shales. *Economic Geology* 110, in press.

Gross, G.A., 1980. A classification of iron formations based on depositional environments. *Canadian Mineralogist* 18, 215–222.

Groves, D.I., 1993. The crustal continuum model for late-Archaean lode-gold deposits of the Yilgarn Block, Western Australia. *Mineralium Deposita* 28, 366–374.

Groves, D.I., Goldfarb, R.J., Gebre-Mariam, M., Hagemann, S.G., and Robert, F., 1998. Orogenic gold deposits: A proposed classification in the context of their crustal distribution and relationship to other gold deposit types. *Ore Geology Reviews* 13, 7–27.

Groves, D.I., Goldfarb, R.J., Robert, F., and Hart, C.J.R., 2003. Gold deposits in metamorphic belts: Overview of current understanding, outstanding problems, future research, and exploration significance. *Economic Geology* 98, 1–29.

Groves, D.I., Golding, S.D., Rock, N.M.S., Barley, M.E., and McNaughton, N.J., 1988. Archaean carbon reservoirs and their relevance to the fluid source for gold deposits. *Nature* 331, 254–257.

Groves, D.I., Phillips, G.N., Falconer, L.J., Houstoun, S.M., Ho, S.E., Browning, P., Dahl, N., and McNaughton, N.J., 1987, Evidence for an epigenetic origin for BIF-hosted gold deposits in greenstone belts of the Yilgarn block, Western Australia. *Geology Department & University Extension, University of Western Australia, Publication* 11, 167–179.

Groves, D.I., Phillips, G.N., Ho, S.E., Houstoun, S.M., and Standing, C.A., 1987, Craton-scale distribution of Archean greenstone

gold deposits: Predictive capacity of the metamorphic model. *Economic Geology* 82, 2045–2058.
Gu, L., and McClay, K.R., 1992, Pyrite deformation in stratiform lead-zinc deposits of the Canadian Cordillera. *Mineralium Deposita* 27, 169–181.
Guillong, M., Kuhn, H-R., and Günther, D., 2003. Application of a particle-separation device to reduce inductively-coupled plasma-enhanced elemental fractionation in laser-ablation inductively coupled plasma-mass spectrometry. *Spectrochimica Acta Part B*, 58, 211–220.
Gustafson, J.K., 1933, Metamorphism and hydrothermal alteration of the Homestake gold-bearing formation. *Economic Geology* 28, 123–162.
Gustafson, J.K., and Miller, J.S., 1937, Kalgoorlie geology re-interpreted. *Proceedings of the Australian Institute of Mining and Metallurgy* 106, 93–125.
Guy, B.M., Beukes, N.J., and Gutzmer, J., 2011. Paleoenvironmental controls on the texture and chemical composition of pyrite from non-conglomeratic sedimentary rocks of the Mesoarchean Witwatersrand Supergroup, South Africa. *South African Journal of Geology* 113, 195–228.
Guy, B.M., Ono, S., Gutzmer, J., Lin, Y., and Beukes, N.J., 2014, Sulfur sources of sedimentary "buckshot" pyrite in the auriferous conglomerates of the Mesoarchean Witwatersrand and Ventersdorp Supergroups, Kapvaal Craton, South Africa. *Mineralium Deposita* 49, doi: 10.1007/s00126-014-0518-3.
Hammond, N.Q., and Moore, J.M., 2006, Archaean lode gold mineralisation in banded iron formation at the Kalahari Goldridge deposit, Kraapian greenstone belt, South Africa. *Mineralium Deposita* 41, 483–503.
Hark, J.S., 2009, Zircon, monazite, and xenotime as provenance indicators in selected Precambrian crystalline rocks, Black Hills uplift, South Dakota. Unpublished M.S. thesis, Kent, Ohio, Kent State University, 153 p.
Harris, A.E., Allen, C.M., Bryan, S.E., Campbell, I.H., Holcombe, R.J., Palin, and Michael, J., 2004. ELA-ICP-MS U-Pb zircon geochronology of regional volcanism hosting the Bajo de la Alumbrera Cu-Au deposit: Implications for porphyry-related mineralization. *Mineralium Deposita* 39, 46–67.
Hattori, K., and Cameron, E.M., 1986, Archean magmatic sulphate. *Nature* 319, 45-47.
Hergt J.M., Preston, P., Bright, R.M.J., and Phillips, G.N., 2000, Differentiated mafic sills in the Yandal greenstone belt. *AIG Bulletin* 32, 55-67.
Hodkiewicz, P.F., Groves, D.I., Davidson, G.J., Weinberg, R.F., and Hagemann, S.G., 2009. Influence of structural setting on sulphur isotopes in Archean orogenic gold deposits, Eastern Goldfields Province, Yilgarn, Western Australia. *Mineralium Deposita* 44, 129–150.
Hosted, J.O., and Wright, L.B., 1923, Geology of the Homestake ore-bodies and the Lead area of South Dakota. *Engineering and Mining Journal* 115, 793–799, 836–843.
Hronsky, J.M.A., Groves, D.I., Loucks, R.R., and Begg, G.C., 2012, A unified model for gold mineralisation in accretionary orogens and implications for regional-scale exploration targeting methods. *Mineralium Deposita* 47, 339–358.
Hutchinson, R.W., 1976, Lode gold deposits: The case for volcanogenic distribution, in Pacific Northwest Mining and Metals Conference, Portland, Oregon, 1975, Proceedings. Salem, Oregon, Department of Geology and Mineral Industries.
Ireland, T.R., Clement, S., Compston, W., Foster, J.J., Holden, P., Jenkins, B., Lanc, P., Schram, N., and Williams, I.S., 2008, Development of SHRIMP. *Australian Journal of Earth Sciences* 55, 937-954.
Jackson, S.E., Pearson, N.J., Griffin, W.L., and Belousova, E.A., 2004. The application of laser ablation-inductively coupled plasma-mass spectrometry to in-situ U-Pb zircon geochronology. *Chemical Geology* 211, 47–69.
James, H.L., 1954, Sedimentary facies of iron-formation. *Economic Geology* 49, 235–293.
Jarosewich, E., Nelen, J.A., Norberg, J.A., 1980. Reference samples for electron microprobe analysis. *Geostandards Newsletter* 4, 43–47.
Jochum, K.P., Wilson, S.A., Abouchami, W., Marghaleray, A., Chmeleff, J., Eisenhauer, A., Hegner, E., Iaccheri, L.M., Kieffer, B., Krause, J., McDonough, W.F., Mertz-Kraus, R., Raczek, I., Rudnick, R.L., Scholz, D., Steinhoefel, G., Stoll, B., Stracke, A., Tonarini, S., Weis, D., Weis, U., and Woodhead, J.D., 2005, GSD-1G and MPI-DING reference glasses for in situ and bulk isotopic determination. *Geostandards and Geoanalytical Research* 35, 193-226.
Jowett, E.C., Roth, T., Rydzewski, A., Oszczepalski, S., 1991. "Background" $\delta^{34}S$ values of Kupferschiefer sulphides in Poland: Pyrite-marcasite nodules. *Mineralium Deposita* 26, 89–98.
Jowitt, S.M., and Keays, R.R., 2012, Shale-hosted Ni-(Cu-PGE) mineralisation: a global overview. *Applied Earth Science* 120, 187-197.
Kamber, B.S., and Whitehouse, M.J., 2007, Micro-scale sulphur isotope evidence for sulphur cycling in the late Archean shallow ocean. *Geobiology* 5, 5-17.
Kaufman, A.J., Johnston, D.T., Farquhar, J., Masterson, A.L., Lyons, T.W., Bates, S., Anbar, A.D., Arnold, G.L., Garvin, J., and Buick, R., 2007, Late Archean biospheric oxygenation and atmospheric evolution. *Science* 317, 1900–1903.
Keays, R.R., 1983, Archaean gold deposits and their source rocks: The upper mantle connection. *Gold '82, Amsterdam, Proceedings*, 17–51.
Keays, R.R., 1995, The role of komatiitic and picritic magmatism and S-saturation in the formation of ore deposits. *Lithos* 34, 1–18.
Kerswill, J.A., 1993, Models for iron-formation-hosted gold deposits, *in* Kirkham, R.V., Sinclair, W.D., Thorpe, R.I., and Duke, J.M., eds., *Mineral Deposit Modeling* (Geological Association of Canada Special Paper 40), 171-199.
Kerswill, J.A., 1996, Iron-formation-hosted stratabound gold, *in* Eckstrand, O.R., Sinclair, W.D., and Thorpe, R.I., eds., *Geology of Canadian Mineral Deposit Types* (*Geology of Canada* 8, 367-382).
Ketris, M.P., and Yudovitch, Y.E., 2009, Estimation of Clarkes for carbonaceous bioliths: World averages for trace element contents in black shales and coals. *International Journal of Coal Geology* 78, 135–148.
Klein, C., 1973. Changes in mineral assemblages with metamorphism of some banded iron-formations. *Economic Geology* 68, 1075–1088.
Kolb, J., Hellman, A., Rogers, A., Sindern, S., Vennemann, T., Böttcher, M.E., and Meyer, F.M., 2004. The role of a transcrustal shear zone in orogenic gold mineralization at the Ajjanahalli mine, Dharwar Craton, south India. *Economic Geology* 99, 743–759.

Konhauser, K.O., Pecoits, E., Lalonde, S.V., Papineau, D., Nisbet, E.G., Barley, M.E., Arndt, N.T., Zhanle, K., and Kamber, B.S., 2009. Oceanic nickel depletion and a methanogen famine before the Great Oxidation Event. *Nature* 458, 750–753.

Kositcin, N., Brown, S.J.A., Barley, M.E., Krapež, B., Cassidy, K.F., and Champion, D.C., 2008. SHRIMP U-Pb age constraints on the late Archaean tectonostratigraphic architecture of the Eastern Goldfields Superterrane, Yilgarn Craton, Western Australia. Precambrian Research, 161, 5–33.

Krapež, B., and Hand, J.L., 2008. Late-Archaean deep-marine volcaniclastic sedimentation in an arc-related basin: The Kalgoorlie Sequence of the Eastern Goldfields Superterrane, Yilgarn Craton, Western Australia. *Precambrian Research* 161, 89–113.

Krapež, B., Barley, M.E., and Brown, S.J.A., 2008. Late Archaean synorogenic basins of the Eastern Goldfields Superterrane, Yilgarn Craton, Western Australia Part I. Kalgoorlie and Gindalbie Terranes. *Precambrian Research* 161, 135–153.

Krapež, B., Barley, M.E., and Pickard, A.L., 2003, Hydrothermal and resedimented origins of the precursor sediments to banded iron formation: Sedimentological evidence from the Early Palaeoproterozoic Brockman Supersequence of Western Australia. *Sedimentology* 50, 979–1011.

Krapež, B., Brown, S.J.A., Hand, J., Barley, M.E., and Cas, R.A.F., 2000. Age constraints on recycled crustal and supracrustal sources of Archaean metasedimentary sequences, Eastern Goldfields Province, Western Australia: evidence from SHRIMP zircon dating. *Tectonophysics* 322, 89–133.

Krapež, B., Hand, J.L., 2008. Late Archaean deep-marine volcaniclastic sedimentation in an arc-related basin: The Kalgoorlie Sequence of the Eastern Goldfields Superterrane, Yilgarn Craton, Western Australia. *Precambrian Research* 161, 89–113.

Krapež, B., and Pickard, A., 2010. Detrital-zircon age-spectra for Late Archaean synorogenic basins of the Eastern Goldfields Superterrane, Western Australia. *Precambrian Research* 178, 91–118.

Krapež, B., Standing, J.G., Brown, S.J.A., and Barley, M.E., 2008. Late Archeaen synorogenic basins of the Eastern Goldfields Superterrane, Yilgarn Craton, Western Australia Part II. Kurnalpi Terrane. *Precambrian Research* 161, 154–182.

Krogstad, E.J., Walker, R.K., Nabelek, P.I., and Russ-Nabelek, C., 1993, Lead isotopic evidence for mixed sources of Proterozoic granites and pegmatites, Black Hills, South Dakota, USA. *Geochimica Et Cosmochimica Acta* 57, 4677-4685.

Larcombe, C.O.G., 1912, The geology of Kalgoorlie. *Australasian Institute of Mining and Engineering Transactions* 14, 1-327.

Large, R.R., 2010. Evidence for a two-stage process in the genesis of sediment-hosted gold-arsenic deposits, in Deb., M., and Goldfarb, R.J., eds., *Gold Metallogeny: India and Beyond*. London, Alpha Science International Ltd., 309 p.

Large, R.R., Bull, S.W., and Maslennikov, V.V., 2011. A carbonaceous sedimentary source-rock model for Carlin-type and orogenic gold deposits. *Economic Geology* 106, 331–358.

Large R.R., Danyushevsky, L., Hollit, C., Maslennikov, V., Meffre, S., Gilbert, S., Bull, S., Scott, R., Emsbo, P., Thomas, H., Singh, B., and Foster, J., 2009. Gold and trace element zonation in pyrite using a laser imaging technique: Implications for the timing of gold in orogenic and Carlin-style sediment-hosted gold deposits. *Economic Geology* 104, 635–668.

Large, R.R., Halpin, J.A., Danyushevsky, L.V, Maslennikov, V.V., Bull, S.W., Long, J.A., Gregory, D., Lounejeva, E., Lyons, T.W., Sack, P., McGoldrick, P., and Calver, C.R., 2014, Trace Element Content of Sedimentary Pyrite as a New Proxy for Deep-Time Ocean-Atmosphere Evolution. *Earth and Planetary Science Letters* 389, 209-220.

Large, R.R., Maslennikov, V.V., and Bull, S.W., 2011. A carbonaceous sedimentary source-rock model for Carlin-type and orogenic gold deposits. *Economic Geology* 106, 331–358.

Large, R.R., Maslennikov, V.V., Robert, F., Danyushevsky, L., and Chang, Z., 2007. Multistage sedimentary and metamorphic origin of pyrite and gold in the giant Sukhoi Log deposit, Lena gold province, Russia. *Economic Geology* 102, 1233–1267.

Large, R.R., Meffre, S., Burnett, R., Guy, B., Bull, S., Gilbert, S., Goemann, K., and Danyushevsky, L., 2013. Evidence for an intrabasinal source and multiple concentration processes in the formation of the Carbon Leader Reef, Witwatersrand Supergroup, South Africa. *Economic Geology* 108, 1215–1241.

Larrasoaña, J.C., Roberts, A.P., Musgrave, R.J., Gràcia, E., Piñero, E., Vega, M., and Martínez-Ruiz, F., 2007, Diagenetic griegite and pyrrhotite formation in gas hydrate marine sedimentary systems. *Earth and Planetary Science Letters* 261, 350-366.

Lehner, S.W., Busek, P.R., McDonough, W.F., and Ash, R.D., 2008. Siderophile element distribution in metal-sulfide nodules from EH3 Sahara 97072. *Meteoritics and Planetary Science (Abstract)* 43, 5275, p. A85.

Lindgren, W., 1906, Metasomatic processes in the gold deposits of Western Australia. *Economic Geology* 1, 530-544.

Longerich, H.P., Jackson, S.E., and Günther, D., 1996. Laser ablation inductively coupled mass spectrometric transient signal data acquisition and analyte concentration calculation. *Journal of Analytical Atomic Spectrometry* 11, 899–904.

Ludwig, K.R., 2003. Users manual for Isoplot/Ex version 3.00: A geochronology toolkit for Microsoft Excel. *Berkeley Geochronology Center Special Publication* 4. Berkeley, CA, USA.

Macdonald, A.J., 1983. The iron formation-gold association: Evidence from Geraldton area, in Colvine, A.C. (ed.), The geology of gold in Ontario. *Ontario Geological Survey Miscellaneous Paper* 110, 75–83.

Macdonald, A.J., and Fyon, J.A., 1986. Sulphidation – the key to gold mineralization in banded iron formation, in *Gold '86: an international symposium on the geology of gold deposits*. Toronto, Ontario Geological Survey, 96–97.

Marin-Carbonne, J., Rollion-Bard, C., Bekker, A., Rouxel, O., Agangi, A., Cavalazzi, B., Wohlgemuth-Ueberwasser,C.C., Hofmann, A., McKeegan, K.D., 2014, Coupled Fe and S isotope variations in pyrite nodules from Archean shale. *Earth and Planetary Science Letters* 392, 67-79.

McCuaig, T.C., and Kerrich, R., 1998. P-T-t-deformation-fluid characteristics of lode gold deposits: evidence from alteration systematics. *Ore Geology Reviews* 12, 381–453.

McNaughton, N.J., and Groves, D.I., 1996. A review of Pb-isotope constraints on the genesis of lode-gold deposits in the Yilgarn craton, Western Australia. *Journal of the Royal Society of Western Australia* 79, 123–129.

McNaughton, N.J., Groves, D.I., and Witt, W.K., 1993. The source of lead in Archaean lode gold deposits of the Menzies-Kalgoorlie-Kambalda region, Yilgarn Block, Western Australia. *Mineralium Deposita* 28, 495–502.

McNaughton, N.J., Mueller, A., and Groves, D.I., 2005. The age of the giant Golden Mile deposit, Kalgoorlie, Western Australia: Ion-microprobe zircon and monazite U-Pb geochronology of a synmineralization lamprophyre dike. *Economic Geology* 100, 1427–1440.

Meffre, S., Large, R.R., Scott, R., Woodhead, J., Chang, Z., Gilbert, S.E., Danyushevsky, L.V., Maslennikov, V., and Hergt, J.M., 2008. Age and pyrite Pb-isotopic composition of the giant Sukhoi Log sediment-hosted gold deposit, Russia. *Geochimica et Cosmochimica Acta* 72, 2377–2391.

Melezhik, V.A., Filippov, M.M., and Romashkin, A.E., 2004, A giant Palaeoproterozoic deposit of shungite in NW Russia: genesis and practical applications. *Ore Geology Reviews* 24, 135-154.

Melezhik, V.A., Grinenko, L.N., and Fallick, A.E., 1998. 2000-Ma sulphide concretions from the 'Productive' Formation of the Pechenga Greenstone Belt, NW Russia: Genetic history based on morphological and isotopic evidence. *Chemical Geology* 148, 61–94.

Melezhik, V.A., Huhma, H., Condon, D.J., Fallick, A.E., and Whitehouse, M.J., 2007, Temporal constraints on the Paleoproterozoic Lomagundi-Jatuli carbon isotopic event: Geology, v. 35, p. 655-658.

Morelli, R., Creaser, R.A., Seltmann, R., Stuart, F.M., Selby, D., and Graupner, T., 2007. Age and source constraints for the giant Muruntau gold deposit, Uzbekistan, from coupled Re-Os-He isotopes in arsenopyrite. *Geology* 35, 795–798.

Morelli, R.M., Bell, C.C., Creaser, R.A., and Simonetti, A., 2010. Constraints on the genesis of gold mineralization at the Homestake gold deposit, Black Hills, South Dakota, from rhenium-osmium sulfide geochronology. *Mineralium Deposita* 45, 461–480.

Morey, A.A., Tomkins, A.G., Bierlien, F.P., Weinberg, R.F., and Davidson, G.J., 2008. Bimodal distribution of gold in pyrite and arsenopyrite: Examples from the Archean Boorara and Bardoc shear systems, Yilgarn Craton, Western Australia. *Economic Geology* 103, 599–614.

Morris, R.C., 1980. A textural and mineralogical study of the relationship of iron ore to banded iron-formation in the Hamersley Iron Province of Western Australia. *Economic Geology* 75, 184–209.

Mueller, A.G., 1997. The Nevoria gold skarn deposit in Archean iron-formation, Southern Cross Greenstone Belt, Western Australia: I. Tectonic setting, petrography, and classification. *Economic Geology* 92, 181–209.

Mueller, A.G., 2007. Copper-gold endoskarns and high-Mg monzodiorite-tonalite intrusions at Mt. Shea, Kalgoorlie, Australia: implications for gold-pyrite-tennantite mineralization in the Golden Mile. *Mineralium Deposita* 42, 737–769.

Mueller, A.G., and McNaughton, N.J., 2000. U-Pb ages constraining batholiths emplacement, contact metamorphism, and the formation of gold and W-Mo skarns in the Southern Cross area, Yilgarn Craton, Western Australia. *Economic Geology* 95, 1231–1257.

Mueller, A.G., and Muhling, J.R., 2013. Silver-rich telluride mineralization at Mount Charlotte and Au-Ag zonation in the giant Golden Mile deposit, Kalgoorlie, Western Australia. *Mineralium Deposita* 48, 295–311.

Mueller, A.G., Harris, L.B., and Lungan, A., 1988. Structural control of greenstone-hosted gold mineralization by transcurrent shearing: A new interpretation of the Kalgoorlie mining district, Western Australia. *Ore Geology Reviews* 3, 359–387.

Mueller, A.G., Lawrance, L.M., Muhling, J., and Pooley, G.D., 2012. Mineralogy and PTX relationships of the Archean Hannan South Au-Cu (Co-Bi) deposit, Kalgoorlie, Western Australia: Thermodynamic constraints on the formation of a zoned intrusion-related skarn. *Economic Geology* 107, 1–24.

Mueller, A.G., Nemchin, A.A., and Frei, R., 2004. The Nevoria gold skarn deposit, Southern Cross Greenstone Belt, Western Australia: II. Pressure-temperature-time path and relationship to postorogenic granites. *Economic Geology* 99, 453–478.

Nadoll, P., Mauk, J.L., Hayes, T.S., Koenig, A.E., and Box, S.E., 2012. Geochemistry of magnetite from hydrothermal ore deposits and host rocks of the Mesoproterozoic Belt Supergroup, United States. *Economic Geology* 107, 1275–1292.

Nelson, D.R., 1995. Compilation of SHRIMP U-Pb zircon geochronology data, 1994, Perth, Western Australia, Western *Australia Geological Survey Record* 1995/3, 244 pp.

Neumayr, P., Walshe, J., Hagemann, S., Petersen, K., Roache, A., Frikken, P., Horn, L., and Halley, S., 2008. Oxidized and reduced mineral assemblages in greenstone belt rocks of the St. Ives gold camp, Western Australia: Vectors to high-grade ore bodies in Archaean gold deposits? *Mineralium Deposita* 43, 363–371.

Newton, P.G.N., Smith, B., Bolger, C., and Holmes, R., 1998. Randalls gold deposits. In: Berkman, D.A., and Mackenzie, D.H., (Eds.), *Geology of Australian and Papua New Guinean Mineral Deposits*. Melbourne, The Australian Institute of Mining and Metallurgy, 225–232.

Nickel, E.H., 1977, Mineralogy of the "green leader" gold ore at Kalgoorlie, Western Australia. *Proceedings of the Australasian Institute of Mining and Metallurgy* 263, 9-13.

Nixon, D.G., Hesford, C., Fitzgerald, M., and Lister, G., 2014, Relative timing of gold mineralization within the Kalgoorlie camp. *Gold'14 at Kalgoorlie*, Extended Abstracts, 97-99.

Noble, J.A., 1950. Ore mineralization in the Homestake gold mine, Lead, South Dakota. *Geological Society of America Bulletin* 61, 221–252.

Ohmoto, H., 1972. Systematics of sulfur and carbon isotopes in hydrothermal ore deposits. *Economic Geology* 67, 551–578.

Ohmoto, H., and Rye, R.O., 1979. Isotopes of sulfur and carbon, in Barnes, H.L., (ed.), *Geochemistry of hydrothermal ore deposits*. Wiley, New York, 517–612.

Ono, S., Eigenbrode, J.L., Pavlov, A.A., Karecha, P., Rumble III, D., Kasting, J.F., and Freeman, K.H., 2003. New insights into Archean sulfur cycle from mass-independent sulfur isotope records from the Hamersley Basin, Australia. *Earth and Planetary Science Letters* 213, 15–30.

Paige, S., 1913. Pre-Cambrian structure of the northern Black Hills, South Dakota, and its bearing on the origin of the Homestake ore body. *Geological Society of America Bulletin* 24, 293–300.

Paige, S., 1923. The geology of the Homestake mine. *Economic Geology,*18, 205–237.

Paige, S., 1924. Geology of the region around Lead, South Dakota. *United States Geological Survey Bulletin* 765, 56 p.

Painter, M.G.M., and Groenewald, P.B., 2001. Geology of the Mount Belches 1:100,000 sheet, Western Australia Geological Survey, 1:100,000 Geological Series Explanatory Notes, pp. 38.

Palin, J.M., and Xu, Y., 2000. Gilt by association? Origins of pyritic gold ores in the Victory mesothermal gold deposit, Western Australia. *Economic Geology* 95, 1627–1634.

Paris, G., Adkins, J.F., Sessions, A.L., Webb, S.M., and Fischer, W.W., 2014, Neoarchean carbonate-associated sulfate records positive $\Delta^{33}S$ anomalies. *Science* 346, 739-741.

Partridge, M.A., Golding, S.D., Baublys, K.A., and Young, E., 2008. Pyrite paragenesis and multiple sulfur isotope distribution in late Archean and early Paleoproterozoic Hamersley Basin sediments. *Earth and Planetary Science Letters* 272, 41–49.

Pasava, J., Frimmel, H., Vymazalova, A., Dobes, P., Jukov, A.V., and Koneev, R.I., 2013. A two-stage evolution model for the Amantaytau orogenic-type gold deposit in Uzbekistan. *Mineralium Deposita* 48, 825–840.

Paton, C., Woodhead, J.D., Hellstrom, J.C., Hergt, J.M., Grieg, A., Maas, R., 2010. Improved laser ablation U-Pb zircon geochronology through robust down-hole fractionation correction. *Geochemistry, Geophysics, Geosystems* 11, Q0AA06, doi: 10.1029/2009GC002618.

Pawley, M.J., Wingate, M.T.D., Kirkland, C.L., Wyche, S., Hall, C.E., Romano, S.S., and Doublier, M.P., 2012. Adding pieces to the puzzle: episodic crustal growth and a new terrane in the northeast Yilgarn Craton, Western Australia. *Australian Journal of Earth Sciences* 59, 603–623.

Pecoits, E., Gingras, M.K., Barley, M.E., Kappler, A., Posth, N.R., and Konhauser, K.O., 2009. Petrography and geochemistry of the Dales Gorge banded iron formation: Paragenetic sequence, source and implications for palaeo-ocean chemistry. *Precambrian Research* 172, 163–187.

Philippot, P., van Zuilen, M., and Rollion-Bard, C., 2012, Variations in atmospheric sulphur chemistry on early Earth linked to volcanic activity. *Nature Geoscience* 5, 668-674.

Phillips, G.N., 1986. Geology and alteration in the Golden Mile, Kalgoorlie. *Economic Geology* 81, 779–808.

Phillips, G.N., and Groves, D.I., 1983. The nature of Archaean gold fluids as deduced from gold deposits in Western Australia. *Geological Society of Australia Journal* 30, 25–39.

Phillips, G.N., and Powell, R., 2009. Formation of gold deposits: Review and evaluation of the continuum model. *Earth-Science Reviews* 94, 1–21.

Phillips, G.N., and Powell, R., 2010. Formation of gold deposits: A metamorphic devolatilization model. *Journal of Metamorphic Geology* 28, 689–718.

Phillips, G.N., Groves, D.I., Amaro, D., Hallbauer, D.K., and Fotios, M.G., 1988, Morphology and trace element compositions of pyrites from Kalgoorlie gold deposits: Sensitive indicators of syndeformational fluid regimes and depositional processes: Geology Department and University Extension, University of Western Australia Publication 12, 217-226.

Phillips, G.N., Groves, D.I., Hallbauer, D.K., Fotios, M.G., and Amaro, D., 1986, Pyrite morphology and composition as a reflection of gold mineralization style, Kalgoorlie, Western Australia [abs.]: Geocongress 1986, Johannesburg, South Africa.

Phillips, G.N., Groves, D.I., Neall, F.B., Donnelly, T.H., and Lambert, I.B., 1986, Anomalous S isotope compositions in the Golden Mile, Kalgoorlie. *Economic Geology* 81, 2008-2015.

Phillips, G.N., Groves, D.I., and Kerrich, R., 1996. Factors in the formation of the giant Kalgoorlie gold deposit. *Ore Geology Reviews* 10, 295–317.

Phillips, G.N., Groves, D.I., and Martyn, J.E., 1984. An epigenetic origin for Archean banded iron-formation-hosted gold deposits. *Economic Geology* 79, 162–171.

Pitcairn, I., Teagle, D., and Craw, D., 2014, Metabasalts as sources of metals in orogenic gold deposits. *Mineralium Deposita* 49, DOI 10.1007/s00126-014-0547-y.

Pitcairn, I.K., Teagle, D.A.H., Craw, D., Olivo, G.R., Kerrich, R., and Brewer, T.S., 2006. Sources of metals and fluids in orogenic gold deposits: Insights from the Otago and Alpine schists, New Zealand. *Economic Geology* 101, 1525–1546.

Qian, G., Brugger, J., Skinner, W.M., Chen, G., and Pring, A., 2010. An experimental study of the mechanism of the replacement of magnetite by pyrite up to 300˚C. *Geochimica et Cosmochimica Acta* 74, 5610–5630.

Ramdohr, P., 1969. *The Ore Minerals and their Intergrowths*. Oxford, Pergamon Press, 1174 p.

Redden, J.A., and DeWitt, E., 2008. Maps showing geology, structure, and geophysics of the central Black Hills, South Dakota. *United States Geological Survey Scientific Investigations Map 2777*, 48 p.

Redden, J.A., Peterman, Z.E., Zartman, R.E., and DeWitt, E., 1990. U-Th-Pb geochronology and preliminary interpretation of Precambrian tectonic events in the Black Hills, South Dakota, in Lewry, J.F., and Stauffer, M.R., eds., The Early Proterozoic Trans-Hudson Orogen of North America. *Geological Association of Canada Special Paper* 37, 229–251.

Reich, M., Kesler, S.E., Utsunomiya, S., Palenik, C.S., Chryssoulis, S.L., and Ewing, R., 2005. Solubility of gold in arsenian pyrite. *Geochimica et Cosmochimica Acta* 69, 2781–2796.

Reimann, C., and de Caritat, P., 1998. *Chemical elements in the environment: Fact sheets for the geochemist and environmental scientist*. Berlin, Springer, 398 p.

Ribero-Rodrigues, L.C., de Oliveira, C.G., and Friedrich, G., 2007. The Archean BIF-hosted Cuíaba gold deposit, Quadrilátero Ferrífero, Minas Gerias, Brazil. *Ore Geology Reviews* 32, 543–570.

Rickard, D.T., 2012, Sulfidic sediments and sedimentary rocks. *Developments in Sedimentology* 65, 801 p.

Rickard, D.T., 2014, The sedimentary sulfur system: Biogeochemistry and evolution through time, *in* Holland, H.D., and Turekian, K.K., eds., *Treatise on Geochemistry*, 2nd edition: Amsterdam, Elsevier 9, 267-326.

Ridley, J.R., and Mengler, F., 2000, Lithological and structural controls on the form and setting of vein stockwork orebodies at the Mount Charlotte gold deposit, Kalgoorlie. *Economic Geology* 95, 85-98.

Robert, F., Poulsen, K.H., Cassidy, K.F., and Hodgson, C.J., 2005, Gold metallogeny of the Yilgarn and Superior Cratons. *Economic Geology 100th Anniversary Volume*, 1001-1031.

Roberts, F.I., Witt, W.K., and Westaway J., 2004. Gold mineralization in the Edjudina-Kanowna region, Eastern Goldfields, Western Australia. *Western Australia Geological Survey Report* 90, 263 p.

Robinson, B.W., and Kasakabe, M., 1975. Quantitative preparation of SO_2 for $^{34}S/^{32}S$ analyses from sulphides by combustion with cuprous oxide. *Analytical Chemistry* 47, 1179–1181.

Roerdink, D.L., Mason, P.R.D., Whitehouse, M.J., and Reimer, T., 2013, High-resolution quadruple sulfur isotope analyses of 3.2

Ga pyrite from the Barberton Greenstone Belt in South Africa reveal distinct environmental controls on sulfide isotopic arrays. *Geochimica et Cosmochimica Acta* 117, 203-215.

Rubin, A.E., 1993. Magnetite-sulfide chondrules and nodules in CK carbonaceous chondrites; implications for the timing of CK oxidation. *Meteoritics* 28, 130–135.

Rye, D.M., and Rye, R.O., 1974. Homestake gold mine, South Dakota: I. Stable isotope studies. *Economic Geology* 69, 293–317.

Rye, D.M., Doe, B.R., and Delevaux, M. H., 1974. Homestake gold mine, South Dakota: II. Lead isotopes, mineralization ages, and source of lead in ores of the northern Black Hills. *Economic Geology* 69, 814–822.

Sack, P.J., Berry, R.F., Meffre, S., Falloon, T.J., Gemmell, J. Bruce, and Friedman, R.F., 2011. In situ location and U-Pb dating of small zircon grains in igneous rocks using laser ablation-inductively coupled plasma-quadrupole mass spectrometry. *Geology, Geophysics, Geosystems* 12, Q0AA14, doi:10.1029/2010GC003405.

Scantlebury, G.M., 1983. The characteristics and origin of the gold lodes in and around the Brownhill Syncline, Golden Mile, Western Australia. Unpublished BSc Honours thesis, Perth, University of Western Australia.

Schandl, E.S., and Gorton, M.P., 2000. Sb-enriched ultramafic lamprophyre in the Hemlo Au-Mo deposit of the Superior Province, Canada: Evidence for post-Archean Sb mobility. *European Journal of Mineralogy* 12, 625–637.

Scott, K.M., Radford, N.W., Hough, R.M., and Reddy, S.M., 2011, Rutile compositions in the Kalgoorlie goldfields and their implications for exploration. *Australian Journal of Earth Sciences* 58, 803-812.

Shackleton, J.M., Spry, P.G., and Bateman, R., 2003. Telluride mineralogy of the Golden Mile deposit, Kalgoorlie, Western Australia. *Canadian Mineralogist* 41, 1503–1524.

Sharwood, W.J., 1911. Analysis of some rocks and minerals from the Homestake mine, Lead, South Dakota. *Economic Geology* 6, 729–789.

Simmons, S.F., White, N.C., and John, D.A., 2005, Geologic characteristics of epithermal precious and base metal deposits. *Economic Geology 100th Anniversary Volume*, 485-522.

Singoyi, B., Danyushevsky, L., Davidson, G.J., Large, R., and Zaw, K., 2006. Determination of trace elements in magnetites from hydrothermal deposits using the LA ICP-MS technique. SEG Keystone Conference, Denver, USA: CD-ROM.

Siva Siddaiah, N., and Rajamani, V., 1989. The geologic setting, mineralogy, geochemistry, and genesis of gold deposits in the Archean Kolar schist belt, India. *Economic Geology* 84, 2155–2172.

Siva Siddaiah, N., Hanson, G.N., and Rajamani, V., 1994. Rare earth element evidence for syngenetic origin of an Archean stratiform gold sulfide deposit, Kolar Schist Belt, south India. *Economic Geology* 89, 1552–1566.

Squire, R.J., Allen, C.M., Cas, R.A.F., Campbell, I.H., Blewett, R.S., and Nemchin, A.A., 2010. Two cycles of voluminous pyroclastic volcanism and sedimentation related to episodic granite emplacement during the late Archean: Eastern Yilgarn Craton, Western Australia. *Precambrian Research* 183, 251–274.

Stacey, J.S., and Kramers, J.D., 1975. Approximation of terrestrial lead isotope evolution by a two-stage model. *Earth and Planetary Science Letters* 26, 207–221.

Steadman, J.A., 2015. Banded iron formations, pyritic black shales, and gold deposits: a re-evaluation. Unpublished PhD thesis, Hobart, Australia, University of Tasmania.

Steadman, J.A., Large, R.R., Davidson, G.J., Bull, S.W., Thompson, J., Ireland, T.R., and Holden, P., 2014, Paragenesis and composition of ore minerals in the Randalls BIF-hosted gold deposits, Yilgarn Craton, Western Australia: Implications for the timing of deposit formation and constraints on gold sources. *Precambrian Research* 234, 110-132.

Steadman, J.A., Large, R.R., Meffre, S., and Bull, S.W., 2013. Age, origin, and significance of nodular sulfides in 2680 Ma carbonaceous black shale of the Eastern Goldfields Superterrane, Yilgarn Craton, Western Australia. *Precambrian Research* 230, 227–247.

Steadman, J.A., Large, R.R., Meffre, S., Olin, P.H., Danyshevsky, L.V., Gregory, D.D., Belousov, I., Lounejeva, E., Ireland, T.R., and Holden, P., 2015, Syn-Sedimentary to Early Diagenetic Gold in Black Shale-Hosted Pyrite Nodules at the Golden Mile Deposit, Kalgoorlie, Western Australia. *Economic Geology* 110, in press.

Stillwell, F.L., 1931. The occurrence of telluride minerals at Kalgoorlie. *Proceedings of the Australian Institue of Mining and Metallurgy* 84, 115–190.

Strauss, H., 4 Ga of seawater evolution: Evidence from the sulfur isotopic composition of sulfate, *in* Amend, J.P., Edwards, K.J., and Lyons, T.W., eds., Sulfur biogeochemistry - past and present: *Geological Society of America Special Paper 379*, 195-205.

Strauss, H., and Scheiber, J., 1990. A sulfur isotope study of pyrite genesis: The mid-Proterozoic Newland formation, Belt Supergroup, Montana. *Geochimica et Cosmochimica Acta* 54, 197–204.

Sung, Y.-H., Brugger, J., Ciobanu, C.L., Pring, A., Skinner, W., and Nugus, M., 2009. Invisible gold in arsenian pyrite and arsenopyrite from a multistage Archaean gold deposit: Sunrise Dam, Eastern Goldfields Province, Western Australia. *Mineralium Deposita* 44, 765–791.

Swager, C.P., 1997. Tectono-stratigraphy of late Archaean greenstone terranes in the southern Eastern Goldfields, Western Australia. *Precambrian Research* 83, 11–42.

Swager, C.P., Witt, W.K., Griffin, T.J., Ahmat, A.L., Hunter, W.M., McGoldrick, P.J., and Wyche, S., 1992. Late Archaean granite-greenstones of the Kalgoorlie Terrane, Yilgarn Craton, Western Australia. *Geology Department and University Extension Services, University of Western Australia Publication* 22, 107–122.

Thomas, H.V., Large, R.R., Bull, S.W., Maslennikov, V., Berry, R.F., Fraser, R., Froud, S., and Moye, R., 2011. Pyrite and pyrrhotite textures and composition in sediments, laminated quartz veins, and reefs at Bendigo gold mine, Australia: insights for ore genesis. *Economic Geology* 106, 1–31.

Tomich, S.A., 1952, Some structural aspects of Kalgoorlie. *Proceedings of the Australasian Institute of Mining and Metallurgy* 164, 45-76.

Tomich, S.A., 1959, The Oroya Shoot and its relationship to other flatly plunging ore pipes at Kalgoorlie. *Proceedings of the Australasian Institute of Mining and Metallurgy* 190, 113-124.

Tomich, S.A., 1974. A new look at Kalgoorlie Golden Mile geology. *Proceedings of the Australasian Institute of Mining and Metallurgy* 251, 27–35.

Tomich, S.A., 1976. Further thoughts on the application of the volcanogenic theory to the Golden Mile ores at Kalgoorlie. *Proceedings of the Australasian Institute of Mining and Metallurgy* 258, 19–29.

Tomich, S.A., 1986, An outline of the economic geology of Kalgoorlie, Western Australia. *South African Journal of Geology* 89, 35-55.

Tomkins, A.G., 2010. Windows of metamorphic sulfur liberation in the crust: implications for gold deposit genesis. *Geochimica et Cosmochimica Acta* 74, 3246–3259.

Tomkins, A.G., 2013. A biogeochemical influence on the secular distribution of orogenic gold. *Economic Geology* 108, 193–197.

Travis, G.A., and Woodall, R., 1975, reply to Tomich, S.A., 1974, 'A new look at Kalgoorlie Golden Mile geology'. *Proceedings of the Australasian Institute of Mining and Metallurgy* 256, 33-36.

Travis, G.A., Woodall, R., and Bartram, G.D., 1971. The geology of the Kalgoorlie Goldfield. Symposium on Archaean rocks, Perth, 1970. *Geological Society of Australia Special Publication* 3, 175–190.

Tripp, G., 2013, Stratigraphy and structure in the Neoarchean of the Kalgoorlie district, Australia: Critical controls on greenstone-hosted gold deposits: Unpublished PhD thesis, James Cook University, Townsville, Australia, 773 p.

Vial, D.S., Abreu, G.C., Schubert, G., and Ribero-Rodrigues, L.C., 2007. Smaller gold deposits in the Archean Rio das Velhas greenstone belt, Quadrilátero Ferrífero, Brazil. *Ore Geology Reviews* 32, 651–673.

Vielreicher, N.M., Groves, D.I., Snee, L.W., Fletcher, I.R., and McNaughton, N.J., 2010. Broad synchroneity of three gold mineralization styles in the Kalgoorlie gold field: SHRIMP, U-Pb, and $^{39}Ar/^{40}Ar$ geochronological evidence. *Economic Geology* 105, 187–227.

Wagner, T., Boyce, A.J., Jonsson, E., and Fallick, A.E., 2004. Laser microprobe sulphur isotope analysis of arsenopyrite: Experimental calibration and application to the Boliden Au-Cu-As massive sulphide deposit. *Ore Geology Reviews* 25, 311–325.

Wagner, T., Klemd, R., Wenzel, T., and Mattsson, B., 2007. Gold upgrading in metamorphosed massive sulfide deposits: Direct evidence from laser-ablation—inductively coupled plasma—mass spectrometry analysis of invisible gold. *Geology* 35, 775–778.

Weidenbeck, M., Alle, P., Corfu, F., Griffin, W.L., Meier, M., Oberli, F., Vonquandt, A., Roddick, J.C., and Spiegel, W., 1995. Three natural zircon standards for U-Th-Pb, Lu-Hf, trace element, and REE analyses. *Geostandards Newsletter* 19, 1–23.

Weisberg, M.K., Connolly, H.C., Ebel, D.S., and Kimura, M., 2006. Sulfide-metal nodules in EH3 chondrites. *Meteoritics and Planetary Science (Abstract) 41*, 5317, A186.

White, R.W., Powell, R., and Phillips, G.N., 2003, A mineral equilibria study of the hydrothermal alteration in mafic greenschist facies rocks at Kalgoorlie, Western Australia. *Journal of Metamorphic Geology* 21, 455-468.

Williford, K.H., van Kranendonk, M.J., Ushikubo, T., Kozdon, R., and Valley, J.W., 2011. Constraining atmospheric oxygen and seawater sulfate concentrations during Paleoproterozoic glaciations: in situ sulfur three-isotope microanalysis of pyrite from the Turee Creek Group, Western Australia. *Geochimica et Cosmochimica Acta* 75, 5686–5705.

Woodall, R.W., 1965, Structure of the Kalgoorlie Goldfield, in McAndrew, J. (ed.), *Geology of Australian Ore Deposits*, 2nd edition: 8th Commonwealth Mining and Metallurgy Conference, Melbourne, Australia, 71-79.

Woodhead, J., Hergt, J., Meffre, S., Large, R.R., Danyushevsky, L., and Gilbert, S., 2009. In situ Pb isotope analysis of pyrite by laser ablation (multi-collector and quadrupole) ICPMS. *Chemical Geology* 232, 344–354.

Zhelezinskaia, I., Kaufman, A.J., Farquhar, J., and Cliff, J., 2014, Large sulfur isotope fractionations associated with Neoarchean microbial sulfate reduction. *Science* 346, 742-744.

Chapter 8

Appendices

8.1 Homestake appendices

8.1.1 Detrital zircon geochronology

Three samples of sandstone from the Ellison Formation were selected for detrital zircon U-Pb geochronology. The first, sample 19776-3054, is a dark gray silty sandstone comprising ~50 % well-rounded quartz grains (up to 1 mm) and ~50 % mica (i.e., chlorite and biotite). The second sample (DBM911C-8624) is a light gray, medium-grained turbiditic sandstone with 1–2 % lithic fragments and accessory sulfides. The third sample (19776-3955) is a heterogeneous mudstone-sandstone-siltstone interval, where each lithology is contained in discrete, cm-thick beds. All three rocks are deformed, as evidenced by a penetrative cleavage in mudstone intervals, the fractured nature of the quartz grains, and mica-defined foliation; in addition, garnet has partially or totally replaced mudstone fragments in samples 19776-3054 and 19776-3955, indicating that metamorphic temperatures reached the garnet zone (lower amphibolite facies). Samples were crushed and milled at CODES, using a hydraulic crusher fitted with tungsten carbide plates and a chrome steel mill (5–10 seconds mill time). The milled material was panned for zircons, and the recovered zircons were set in epoxy. Once the epoxy had hardened, the mounts were washed in an ultrasonic bath, dried for 12 hours, and placed in a sealed vacuum chamber until the day of analyses.

Instrumentation for U-Pb geochronology at CODES consists of a Resonetics M50 ablation cell, capable of holding 20 samples, and a Coherent 193 nm ArF gas-charged excimer laser microprobe, coupled to an Agilent 7500 cs quadrupole ICP-MS. Zircon standards used in the analysis runs included 91500 (primary; Weidenbeck et al., 1995), TEMORA 1 (secondary; Black et al., 2003), GJ1 (Jackson et al., 2004), and Mud Tank (Black and Gulson, 1978). Reported ages are $^{207}Pb/^{206}Pb$ ages with no corrections for common Pb (except where specified). Data reduction was performed using the Isoplot software (Ludwig, 2003) and following the guidelines set forth in Black et al. (2003) and Paton et al. (2010).

8.1.1.1 U-Pb geochronology - results

The zircons from all three Ellison Formation samples (n = 120) display varying degrees of Pb loss due to varying intensities of metamictization. Thus, on concordia diagrams, the zircons plot in a 'shotgun' array, with few grains actually falling on concordia (Fig. 8.1A–C). Individual zircons can have very old ages, as far back as ~3400 Ma, consistent with previous work (McCombs et al., 2004; Hark, 2009). The youngest populations in all three samples are Neoarchean (2860–2680 Ma), with no Paleoproterozoic zircons present. Similar detrital zircon patterns were reported by Hark (2009) for another, older Paleoproterozoic siliciclastic succession in the northern Black Hills (see 'Discussion' below).

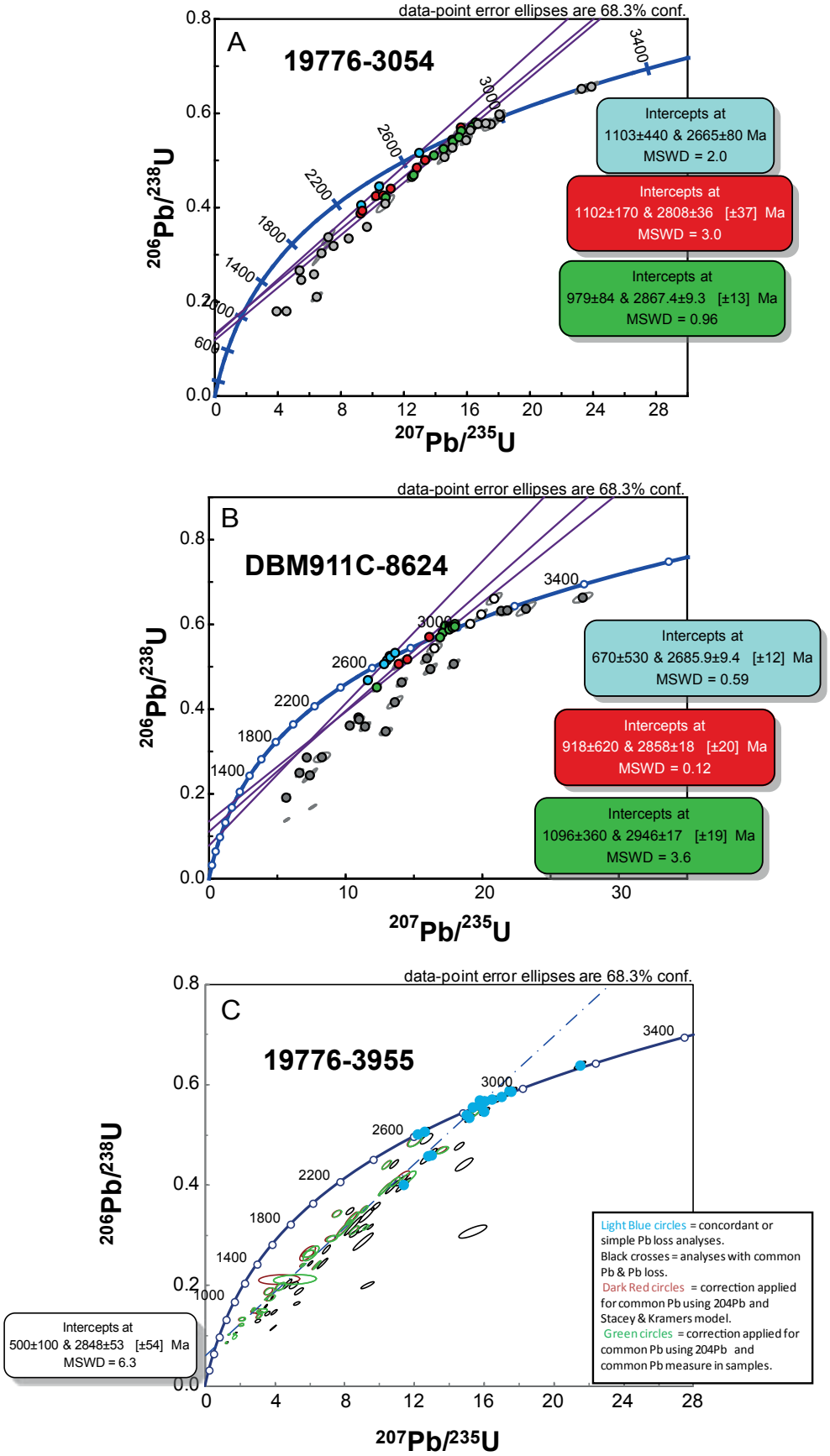

Figure 8.1 Concordia plots for zircons from three Ellison Formation samples. **A**. Sample 19776-3054. **B**. Sample DBM911C-8254. **C**. Sample 19776-3955. All three samples display similar patterns, in that the zircon populations have experienced widespread Pb loss, apparently in the late Neoproterozoic or early Paleozoic, and the detritus sources are all Archean, despite an assumed depositional age of ~1975 Ma (Redden et al., 1990).

8.1.1.2 U-Pb zircon geochronology - discussion

8.1.1.2.1 Comparison of Ellison Formation detrital zircon U-Pb ages with other Black Hills age dates

Detrital zircon geochronology has not yet been published for any Precambrian sedimentary successions in the Black Hills. Various mafic and felsic plutonic and volcanic units, on the other hand, have been directly dated by more than one age-dating technique: Redden et al. (1990) published TIMS U-Pb in zircon dates for several units across the Black Hills, including the Ellison Formation at the Homestake mine. These authors determined a $^{207}Pb/^{206}Pb$ age of 1974 ± 8 Ma (1σ?) for a boulder of 'felsic metatuff', which is interpreted to be a crystallization age for the metatuff and also provides a minimum age for the Homestake Formation. Dahl et al. (2006) used U-Pb in magmatic titanite and zircon from the Blue Draw Metagabbro to obtain a $^{207}Pb/^{206}Pb$ age of 2480 ± 6 Ma (2σ) for that unit, which they interpreted as the crystallization age and the onset of rifting between the Wyoming and Superior Cratons. Frei et al. (2009) quoted a U-Pb in zircon crystallization age of 2012 ± 3 Ma (2σ) for a gabbroic sill ~10 km SSE of Nemo (Bogus Jim Sill; Hark, 2009) that, according to these authors, is the intrusive equivalent of the lower Poorman Formation (Yates member), a massive body of mafic to ultramafic volcanics (now amphibolites) in the Homestake mine. This age also provides a maximum age for the Homestake Formation.

The detrital zircon $^{207}Pb/^{206}Pb$ ages determined in this study reveal that the clastic sediments in the Homestake deposit did not receive detritus from any Paleoproterozoic crustal material that may have been exposed at the time of deposition. A detrital zircon study of the Paleoproterozoic Box Elder Creek Formation by Hark (2009) came to similar conclusions. The Ellison and Box Elder Creek Formations are separated not only by distance (~10 km at present) but also time: the latter formation is believed to have been deposited between 2560–2480 Ma, based on cross-cutting relationships with the Blue Draw Metagabbro (2480 Ma; Dahl et al., 2006) and the Little Elk Granite (2560 Ma; McCombs et al., 2004). By contrast, the Ellison Formation is bracketed by the ~1974 Ma felsic metatuff of Redden et al. (1990) and the supposed temporal equivalence of the Bogus Jim Sill (~2012 Ma; Hark, 2009) and the lower Poorman Formation (Yates member). Nevertheless, the apparent 500 million year gap in deposition between these two formations, and the multiple thermotectonic events in the Black Hills during this time (Dahl et al., 2006), did not effect changes in provenance for this region of the Wyoming Craton, implying that the Craton was tectonically stable throughout this period, at least in the interior regions.

The timing of Pb loss in the Ellison Formation zircon populations is peculiar, as ages of 500–1000 Ma correspond to no known magmatic, hydrothermal, or tectonic event in this region of the Black Hills Province or the Wyoming Craton at large. A comprehensive study of detrital zircons in the Bighorn Basin, ~350 km to the west and thus closer to the core of the Wyoming Craton, also revealed geologically recent episodes of zircon Pb loss (ca. 50 Ma), but these were interpreted to result from magmatism associated with the emplacement of the Absaroka volcanic province in present-day NW Wyoming (May et al., 2013). These authors also dated a sample of Neoarchean mafic gneiss from the Bighorn-Beartooth magmatic complex, which yielded abundant zircon (~100 grains) but nearly all these grains were severely metamict, as our zircons from the Ellison Formation were. What is more, May et al. (2013) discovered a good negative correlation between U content in zircon and the degree of discordance seen in each grain (i.e., the higher the U, the more discordant the zircon). Our work shows a very similar pattern (Fig. 4.20), and we interpret this correlation to be the result of Pb loss. The study of May et al. (2013), our work, and the works of Hark (2009) and Ghosh (2009) show quite clearly that zircons from metaigneous and metasedimentary rocks across the Wyoming Craton have strongly disturbed Pb, but still yield valuable geologic information about the history of this part of Laurentia, including geologically reasonable age dates of some igneous formations.

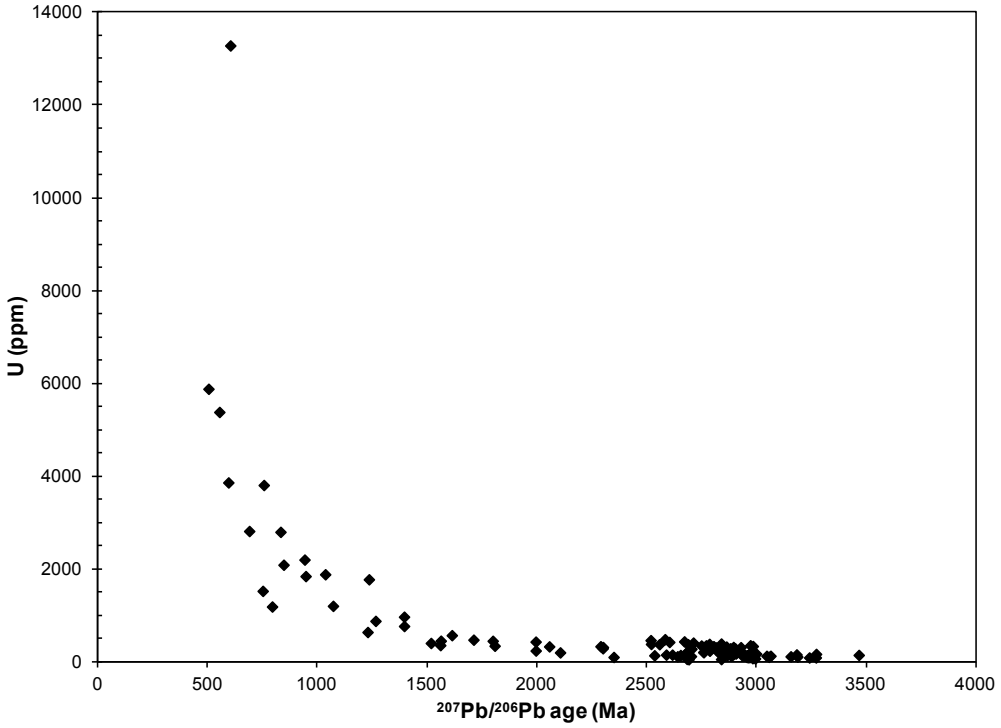

Figure 8.2 U vs. age in detrital zircons. As uranium content increases within a zircon crystal, its apparent age decreases exponentially. We believe this to be a function of Pb loss. Similar data were reported from the Bighorn Basin (central Wyoming Craton) by May et al. (2013).

8.1.1.3 U-Pb zircon geochronology - conclusions

Our data on detrital zircons in the Ellison Formation highlight the difficulties associated with U-Pb geochronology of igneous and sedimentary units in the Black Hills and the broader Wyoming Craton, bolstering the conclusions of previous works and calling for more rigorous searching of suitable candidates to improve the time scale of this important Archean-Proterozoic province.

8.2.1 Whole-rock XRF geochemistry

Thirty samples of upper Poorman Formation (Ross member), representing several sedimentological facies within the Ross member, were submitted to ALS Chemex, Brisbane, Australia, for 48-element (including minor and trace elements) solution ICP-MS analysis via four-acid digestion, as well as total C by LECO. Detection limits for major elements (including C) was 0.01%; for minor elements, detection limits varied, but generally 0.5 ppm was the cutoff. Trace element detection limits were 0.05 ppm.

8.2.1.1 Whole-rock XRF data - results

Whole-rock analysis of 30 Ross member samples reveals that organic carbon content (C_{org}) ranges widely (0.05 to 26.9 wt. %; Table 8.1), and nearly all samples are enriched in the redox-sensitive trace element suite (V-Mo-Se-Ni-Ag-Zn-Cu; cf. Large et al., 2009; 2011). Furthermore, the elements Mo, Au, and Re show positive correlations with C_{org}, while Al correlates negatively with C_{org} (Fig. 8.2A–E). Barium and Sn show good positive correlations with Al.

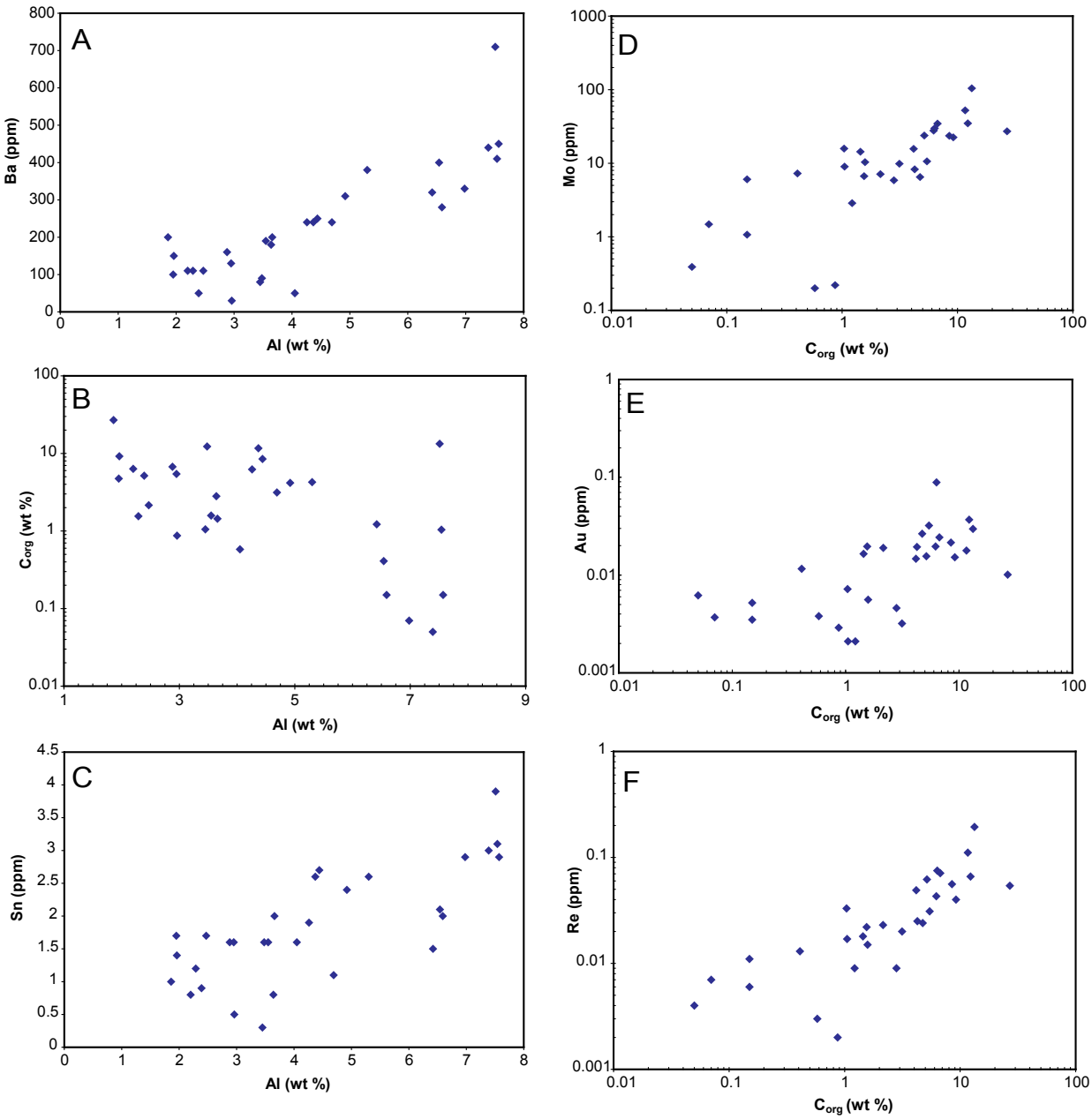

Figure 8.3 Whole-rock data. **A**. Ba vs. Al. **B**. C_{org} (organic C) vs. Al. **C**. Sn vs. Al. **D**. Mo vs. C_{org}. **E**. Au vs. C_{org}. **F**. Re vs. C_{org}.

Table 8.1 Whole-rock analyses of selected upper Poorman Formation samples

Sample	Ag	Al	As	Ba	Be	Bi	Ca	Cd	Ce	Co	Cr	Cs	Cu	Fe	Ga	Ge	Hf	In	K
	ppm	%	ppm	ppm	ppm	ppm	%	ppm	ppm	ppm	ppm	ppm	ppm	%	ppm	ppm	ppm	ppm	%
HS 009-3	1.29	1.96	5.5	150	0.44	0.76	3.57	0.94	23.2	47.7	30	0.33	362	22.4	5.83	0.39	0.3	0.044	0.47
HS 011	0.43	1.86	10.1	200	0.52	0.27	6.63	0.63	10.95	23.7	86	1.02	118	8.97	7.44	0.18	0.2	0.032	0.76
HS 012	2.08	7.51	9.8	710	3.32	1.83	0.47	5.1	71.3	64.7	137	2.51	235	18.2	32.5	0.41	0.7	0.168	2.96
HS 013	2.97	3.48	10.9	90	1.35	4.02	0.38	1.62	13.95	52.4	83	2.73	379	26.8	13.5	0.44	0.4	0.062	1.22
HS 014	1.44	2.39	29.7	50	0.93	0.84	0.9	2.32	22.7	194	59	0.7	376	26.3	8.35	0.42	0.3	0.073	0.94
HS 017-B	3.09	2.2	12.2	110	1.12	1.29	0.18	6.01	16.85	79.4	44	0.66	409	26.6	7.9	0.42	0.2	0.11	0.85
HS 022-7	0.61	7.39	449	440	3.04	0.26	1.2	0.15	96.7	32.2	50	6.86	197.5	9.55	20.2	0.28	2.3	0.068	3.75
HS 024-2	1.31	2.29	1.4	110	0.89	0.69	2.63	3.18	48.6	45.4	36	0.54	344	14.65	8.53	0.27	0.7	0.064	1.04
HS 025	1.47	2.47	1.4	110	1.15	0.58	2.97	2.11	61.2	97.9	39	2.09	308	15.8	8.89	0.32	1	0.044	1.18
HS 026-4	1.38	4.37	3.3	240	2.64	0.94	5.74	9.33	50.6	12.4	102	1.67	120	10.4	13.8	0.25	1.4	0.145	2.2
HS 027-4	1.28	2.88	8.3	160	1.81	0.46	3.01	7.19	26.4	173.5	64	0.98	137.5	12.3	9.27	0.24	0.9	0.105	1.48
HS 029-2	1.4	3.66	1.4	200	1.99	0.63	3.3	1.7	55.7	48.2	63	2.08	222	14.2	12.05	0.28	1.2	0.048	1.8
HS 030	1.36	4.26	6.5	240	1.75	0.39	7.41	2.76	28.6	44	88	4.57	129	10.75	12.75	0.22	1.1	0.066	2.01
HS 031	2.88	4.92	9.1	310	2.4	2.41	2.65	5.03	158	42.2	66	5.18	245	9.77	16.25	0.33	4.3	0.105	2.37
HS 032	1.96	5.3	6.2	380	2.59	0.66	1.02	0.61	92.4	50	52	3.8	317	11.3	16.25	0.27	1.5	0.057	2.5
HS 034	0.31	3.45	9	80	0.85	1.01	10.4	2.1	23.5	31	59	5.74	86.1	2.62	9.67	0.12	0.7	0.04	1.84
HS 036-3	0.95	4.44	34.4	250	2.49	0.39	1.01	5.46	47.8	40.7	92	5.3	153	9.53	14.7	0.23	2.2	0.11	2.24
HS 037	0.8	7.57	1.1	450	4.28	0.35	0.29	0.56	100.5	39.8	58	3.97	167.5	6.28	22.2	0.23	3.8	0.076	3.9
HS 038	0.18	6.98	0.6	330	2.44	0.51	0.3	0.12	87.4	39.8	52	7.53	86	7.64	19.9	0.21	3.2	0.072	3.41
HS 039	0.15	6.59	0.4	280	2.13	0.53	1.01	0.2	79.2	37.4	49	9.69	61.4	9.51	18.75	0.24	3	0.067	2.56
HS 040	0.81	3.55	2.9	190	2.24	0.14	3.73	1.2	42.5	37.3	69	2.06	362	10.05	10.65	0.23	1.7	0.033	1.73
HS 043	1.33	2.95	142.5	130	1.75	0.99	2.04	0.13	73.5	96.8	31	2.84	66.6	14.9	10.2	0.36	1.7	0.031	1.45
HS 050	0.05	2.96	0.4	30	0.51	0.14	0.51	0.06	22.4	29	27	0.94	13.7	13.85	9.04	0.2	0.2	0.039	0.23
HS 051	0.15	4.05	4.7	50	0.64	0.42	0.6	0.08	55	27.2	39	2	49.3	16	12.85	0.25	0.4	0.046	0.46
HS 052	0.49	6.42	8.2	320	1.89	0.15	4.44	0.9	50.7	24.7	101	6.5	70.8	3.38	17.8	0.16	1.1	0.059	3.06
HS 053	0.88	3.64	1.9	180	1.09	0.34	8.47	0.74	30.5	26.8	63	1.28	125	5.12	10.1	0.15	0.8	0.037	1.62
HS 054	0.65	4.69	13.3	240	1.45	0.23	5.96	1.3	39	33.7	77	2.33	102	3.83	13.65	0.14	0.8	0.058	2.25
HS 063	0.11	6.54	5	400	2.4	0.39	0.59	0.54	86.1	33.3	60	7.88	68.4	10.15	20.7	0.24	3.4	0.085	3.14
HS 064	0.88	1.95	126	100	1.26	0.52	1.61	0.32	52.6	111.5	31	3.94	246	14.3	7.66	0.31	1	0.038	1.05
HS 067	0.97	7.54	29.2	410	2.77	0.66	0.64	1.89	99.8	41.5	112	10.15	160.5	4.77	24.9	0.22	1.3	0.097	3.79

Table 8.1 Whole-rock analyses of selected upper Poorman Formation samples - cont.

Sample	La	Li	Mg	Mn	Mo	Na	Nb	Ni	P	Pb	Rb	Re	S	Sb	Sc	Se	Sn	Sr	Ta
	ppm	ppm	%	ppm	ppm	%	ppm	ppm	ppm	ppm	ppm	ppm	%	ppm	ppm	ppm	ppm	ppm	ppm
HS 009-3	10.9	2.7	2.05	782	22.5	0.81	0.8	338	180	46.6	14.9	0.04	14.7	5.76	11.4	14	1.4	263	0.17
HS 011	5.4	5.2	3.91	1420	27.2	0.25	1.2	126	330	19.3	24.1	0.054	2.77	2.39	12.8	3	1	312	0.13
HS 012	41.6	27	1.12	128	104.5	1.03	1.7	246	290	83.7	109	0.194	11.95	15.6	35.8	13	3.9	415	0.16
HS 013	7	13.2	0.86	116	34.9	0.93	1.2	406	60	134	61.1	0.066	18	23.4	15.1	22	1.6	228	0.16
HS 014	12.1	6.9	0.71	257	23.8	0.56	1.1	351	210	31.4	38.4	0.062	19	3.91	9.4	21	0.9	129	0.26
HS 017-B	9.3	5.2	0.3	55	29.8	0.33	0.8	319	80	76	34.1	0.075	16.05	14.3	8.6	17	0.8	58.3	0.19
HS 022-7	51	59.2	2.79	4470	0.39	0.39	4.9	60.9	310	12.7	197.5	0.004	3.96	1.92	12.9	4	3	47	0.28
HS 024-2	30.2	11.1	1.7	8570	6.68	0.28	6.6	114	670	36.6	42.2	0.022	6.7	4.54	6.7	8	1.2	67.4	0.26
HS 025	37.8	16.4	1.67	6900	7.1	0.31	13.2	115.5	1520	27.3	59.4	0.023	9.85	5.48	7.4	10	1.7	79.9	0.37
HS 026-4	36.7	28.8	3.22	5780	52.3	0.05	7.1	81.4	350	51	90.4	0.111	5.14	9.38	15.6	6	2.6	138	0.31
HS 027-4	19.4	22.3	1.81	3070	34.6	0.04	2.9	96.8	140	43.6	63.9	0.071	9.36	7.34	10.3	8	1.6	71.6	0.28
HS 029-2	41.6	29.2	2.08	3490	14.35	0.07	3.2	129	300	70.5	87	0.018	6.85	3.64	10.8	10	2	79.3	0.29
HS 030	17.3	33.4	5.15	7570	27.8	0.11	29.4	65.8	250	26.3	106	0.043	7.02	3.47	13.9	7	1.9	102	0.6
HS 031	92.3	39.4	1.91	2100	15.7	0.1	10.2	81.1	6610	143.5	133.5	0.049	5.19	4.97	13.2	8	2.4	50.1	1.07
HS 032	50.2	31.4	1.23	996	8.27	0.09	3	93.4	3280	29.4	126	0.025	6.11	4.25	11.6	6	2.6	29.7	0.23
HS 034	14.2	19.9	6.76	501	9.01	0.05	1.4	50.1	200	2.2	108	0.017	1.44	0.17	11.5	3	0.3	63.4	0.22
HS 036-3	32.4	49.6	1.37	819	23.6	0.05	3.4	130.5	1600	22	117.5	0.056	6.35	8.2	14	8	2.7	73.5	0.29
HS 037	52.9	53	1.37	268	6.04	0.29	7.8	62.8	450	26.4	180	0.011	4.29	2.02	14.5	4	2.9	46.2	0.56
HS 038	46.3	48.1	1.73	3250	1.48	0.67	12.5	38.4	370	7.3	180	0.007	2	0.58	13.5	2	2.9	43.9	0.97
HS 039	41.9	54.5	1.94	5630	1.07	0.57	11.6	36.4	870	8.9	163.5	0.006	1.76	0.65	12.6	2	2	64.7	0.85
HS 040	29.7	26.1	2.64	2350	10.35	0.05	3	115.5	380	7.8	74	0.015	7.3	2.49	9.7	9	1.6	129.5	0.31
HS 043	40.7	21.9	0.69	1120	10.6	0.27	5.6	111.5	7440	71.2	71.5	0.031	15.65	26.5	7.9	13	1.6	88.8	0.48
HS 050	11.9	25.2	2.57	6340	0.22	<0.01	5.3	16.1	250	6.2	15.4	0.002	0.1	0.46	6.3	<1	0.5	15.8	0.45
HS 051	29.1	33.2	3.14	7550	0.2	0.01	9.9	27.3	320	19.9	30.3	0.003	0.31	0.52	8.9	1	1.6	19.3	0.7
HS 052	29.8	55.3	3.45	1330	2.87	0.26	5.3	47.5	200	8.3	160.5	0.009	1.71	2.92	14.4	3	1.5	52.4	0.38
HS 053	17.5	20.7	4.93	2660	5.87	0.22	1.8	54.4	130	13.1	68.5	0.009	2.55	3.26	8	5	0.8	83.4	0.19
HS 054	22.1	36.7	3.72	1260	9.84	0.13	3.9	55.6	190	10.4	103.5	0.02	2.04	2.2	11.2	4	1.1	63.6	0.37
HS 063	46.1	68.7	2.29	9620	7.27	0.94	14.1	47.7	400	8.3	170.5	0.013	1.21	0.49	16.5	2	2.1	50.4	1.02
HS 064	31.5	21.2	1.12	1850	6.49	0.11	5.6	103	2370	32.5	63	0.024	14.2	10.95	6.3	13	1.7	59.4	0.49
HS 067	54.7	87.2	1.97	130	15.85	0.3	6.5	96.5	230	23.2	217	0.033	3	4.57	20.3	7	3.1	21.7	0.47

Table 8.1 Whole-rock analyses of selected upper Poorman Formation samples - cont.

Sample	Te	Th	Ti	Tl	U	V	W	Y	Zn	Zr	$C_{organic}$	Au
	ppm	ppm	%	ppm	ppm	ppm	ppm	ppm	ppm	ppm	%	ppm
HS 009-3	0.55	3.4	0.031	1.18	10.2	143	201	4.1	289	14.6	9.2	0.0152
HS 011	0.24	1.1	0.063	1.14	2.9	328	105.5	4.6	181	6.6	26.9	0.0101
HS 012	0.73	15	0.154	5.81	44.8	1020	55.7	8.5	1310	27.3	13.3	0.0297
HS 013	1.63	5.6	0.068	4.98	22.7	371	134.5	4.7	422	14.9	12.3	0.0369
HS 014	0.79	4.5	0.051	1.86	12.3	271	313	6.5	594	10.4	5.16	0.0156
HS 017-B	0.85	4.5	0.041	2.28	16.3	283	264	3.3	1380	6.5	6.33	0.0888
HS 022-7	0.34	17.9	0.188	1.73	3.7	92	131	6.9	115	75.6	0.05	0.0062
HS 024-2	0.73	4.3	0.058	0.68	4.1	103	254	8.1	610	31.7	1.55	0.0196
HS 025	0.87	4.6	0.075	0.94	4.7	107	280	11.7	402	64	2.15	0.019
HS 026-4	0.93	7.3	0.138	1.6	26.9	482	59.6	9.6	1600	60	11.65	0.0178
HS 027-4	0.75	4.5	0.082	1.17	14.6	370	201	5.9	1240	36.5	6.72	0.0243
HS 029-2	0.7	7.1	0.096	0.92	6.5	140	245	8	322	47.5	1.44	0.0165
HS 030	0.45	6.7	0.155	1.39	12.7	235	134	6.3	419	42.8	6.22	0.0196
HS 031	0.91	15.4	0.107	1.6	12.3	204	273	30	712	163	4.17	0.0147
HS 032	0.65	11.9	0.092	1.49	9	137	218	14.3	119	52.6	4.26	0.0194
HS 034	0.24	4.9	0.091	1.16	6.3	139	211	17.1	219	27.2	1.05	0.0021
HS 036-3	0.6	8.3	0.102	2.35	15.3	385	183	12.7	1070	84.7	8.49	0.0215
HS 037	0.2	17.1	0.199	1.94	6.3	103	251	11	160	132.5	0.15	0.0035
HS 038	0.24	15.9	0.242	1.06	4.1	80	189	8.8	142	108	0.07	0.0037
HS 039	0.24	14.3	0.222	1.37	4.3	77	156	12.4	114	106	0.15	0.0052
HS 040	0.26	6.5	0.094	2.76	5.7	117	225	9.1	202	65.6	1.58	0.0056
HS 043	1.69	5.7	0.064	2.31	9.8	128	460	34.4	29	82.1	5.44	0.0321
HS 050	0.07	6	0.112	0.12	1.3	37	161.5	3.2	64	9.6	0.87	0.0029
HS 051	0.2	9.4	0.207	0.21	1.7	53	106.5	4.1	91	17.7	0.58	0.0038
HS 052	0.15	10.5	0.165	1.74	4.2	133	102	5.7	141	43	1.22	0.0021
HS 053	0.25	5.9	0.075	0.66	2.8	76	103	5.9	117	24.8	2.81	0.0046
HS 054	0.22	8.4	0.134	0.98	5.9	163	159	6.3	190	28.8	3.14	0.0032
HS 063	0.27	13.4	0.446	1.06	3.1	113	93.3	11.4	165	124	0.41	0.0116
HS 064	0.88	3.9	0.051	1.44	5.6	101	460	15.7	69	45.9	4.74	0.0265
HS 067	0.42	16.7	0.206	2.85	10.9	222	135	8.1	254	48.7	1.04	0.0072

8.2.1.2 Whole-rock data - Discussion

The negative correlation between Al and C_{org} indicates that C_{org} is not contained within detrital clay particles (cf. Large et al., 2011), but likely represents the remains of bacteria that lived at or near the sediment-water interface. Barium and Sn, on the other hand, do correlate positively with Al, which is expected given the common incorporation of these elements into micas and feldspars at trace levels. The good positive correlation between Au, Mo, Re, and C_{org} suggests that these metals (along with Zn, Ni, and Cu) were adsorbed onto organic matter during sedimentation, a key early process for the formation of sediment-hosted gold deposits (Large et al., 2007, 2009, 2011; Tomkins, 2013).

8.3.1 LA-ICP-MS imaging of pyrite, pyrrhotite, and arsenopyrite from the Poorman and Homestake Formations

HS 045 (MA-93-2). Eight kilometers northwest of the Homestake mine, near the town of Maitland, a series of exploration holes were drilled from the surface down to depths greater than 2 km. Several of the drill holes intersected distal equivalents of the mine stratigraphy (i.e., Poorman, Homestake, and Ellison Formations), including the carbonaceous and sulfidic shale of the Ross member. Pyrite in the Ross member from drill hole MA-93-2 is recrystallized, but conversion to pyrrhotite is minimal, unlike other Ross member samples from the Homestake mine. Similar to image 1, there is a nodule-like form of pyrite present (labeled 'py1' in Fig. 8.4) containing abundant gangue inclusions. The py1 'nodule' is partially enveloped by subhedral-euhedral, inclusion-free pyrite ('py2'). The trace element characteristics of py1 are similar to those in the nodule pyrite from image 1, with high Co (50–100 ppm), Ni (50–100 ppm), Cu (50–100 ppm), As (~5,000 ppm), Mo (5–10 ppm), Ag (5–10 ppm), Sb (10–50 ppm), Au (0.1–0.5 ppm), Hg (~1000 cps), Tl (~5 ppm), Pb (50–100 ppm), and Bi (1–5 ppm). Spikes in the Cu image likely indicate the presence of small chalcopyrite inclusions, as in Figure 4.6, along with similar patterns in the Pb image (galena inclusions). Py2 is again similar in nature to the later pyrite surrounding the nodule in Figure 4.6, being enriched only in Co (500–1000 ppm), Ni (500–100 ppm), and As (500–1000 ppm).

Image 3: HS 032A-3 (DDH 19600). Within this sample, at least two different pyrite-pyrrhotite associations are preserved. Whereas the pyrrhotite associated with both pyrites is geochemically identical (e.g., high Ni; below-detection Co; low Ag, Sb, Pb, and Bi), the small pyrite crystal in this image (Fig. 8.5) has drastically different geochemical hallmarks than that in the following image (see below). The Co-Ni-Cu-Zn-As-Ag-Sb-Te-Au-Pb-Bi±Se signature in this pyrite is akin to the pyrites in Figures 4.6 and 8.4, except that As content in this pyrite (~100 ppm) is lower than the previous two by more than an order of magnitude. Mercury is also not present in this pyrite, as in the others.

Image 5: HS 067 (DDH 19776). Figure 8.6 shows an image of coexisting pyrite and pyrrhotite in a carbonaceous siltstone from drill hole 19776, and as with pyrrhotite in the previous two images (Figs 8.9, 4.10), pyrrhotite in this sample has below detection Co and As, but retained Ni (~2000 ppm), Se (~50 ppm), Ag (~10 ppm), Sb (~10 ppm), Pb (50–100 ppm), and Bi (1–5 ppm) from the preexisting pyrite. The pyrite cube in this image has at least two generations, defined by an early, 'spongy' core with a euhedral, inclusion-free rim. The core contains the signature Co-Ni-Se-As-Ag-Mo±Au, while the rim has more As and Co but roughly equivalent amounts of Ni to the core.

Image 6: HS 060 (DDH 19600, Homestake Formation). A common mineralogical feature of the Homestake Formation is disseminated pyrrhotite, which along with pyrrhotite veins and arsenopyrite megacrysts comprise the bulk of the sulfide budget in this unit. This style of pyrrhotite is enriched in Co (100–200 ppm), Ni (100–500 ppm), and Se (~100 ppm), and also has low amounts of Ag (0.1–0.5 ppm), Pb (~1 ppm), and Bi (~0.1 ppm; Fig. 8.7). Gold and As are both below detection (< 0.01 ppm).

Image 7: 16233. Unlike arsenopyrite from most gold deposits (Cathelineau et al., 1989; Morey et al., 2008; Agangi et al., 2013; Steadman et al., 2014), the arsenopyrite crystals at Homestake are generally poor in trace elements. Sample 16233 is a chlorite-rich Homestake BIF from the 11 Ledge ore body, containing prograde garnet mantled by arsenopyrite euhedra. A map covering several intergrown crystals is shown in Figure 8.8. Arsenopyrite in this rock is characterized by elevated Co (1000 ppm in the cores, 5000 ppm on the rims), Ni (500 ppm in the rims), Sb (100 ppm in the cores, 50 ppm in the rims), and Bi (50 ppm in the cores). Gold content is negligible (< 0.01 ppm).

Image 8: 16229. Sample 16229 is arsenopyrite-rich gold ore from 11 Ledge, characterized by cm-scale arsenopyrite megacrysts in a chlorite-quartz matrix. Figure 8.9 reveals that arsenopyrite in this ore type is similar to the more disseminated arsenopyrite in 16233, except that arsenopyrite in this image lacks the Co-Ni-enriched rims and shows no distinct zonation. Bismuth is more enriched in this

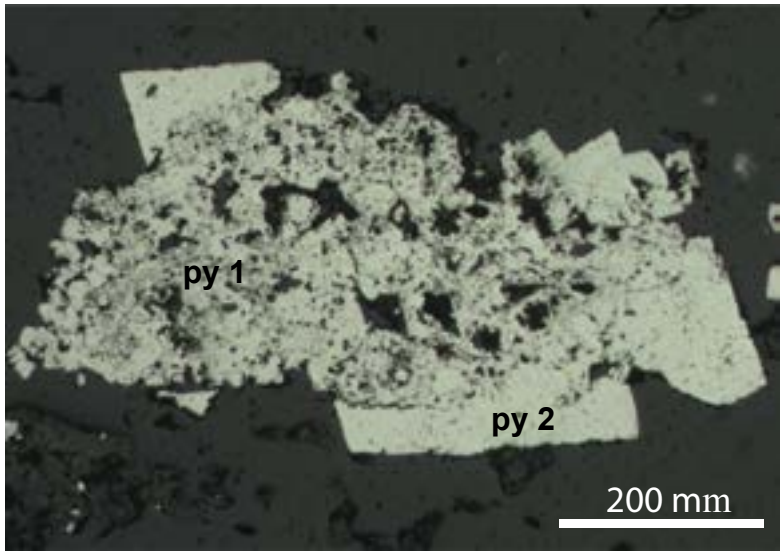

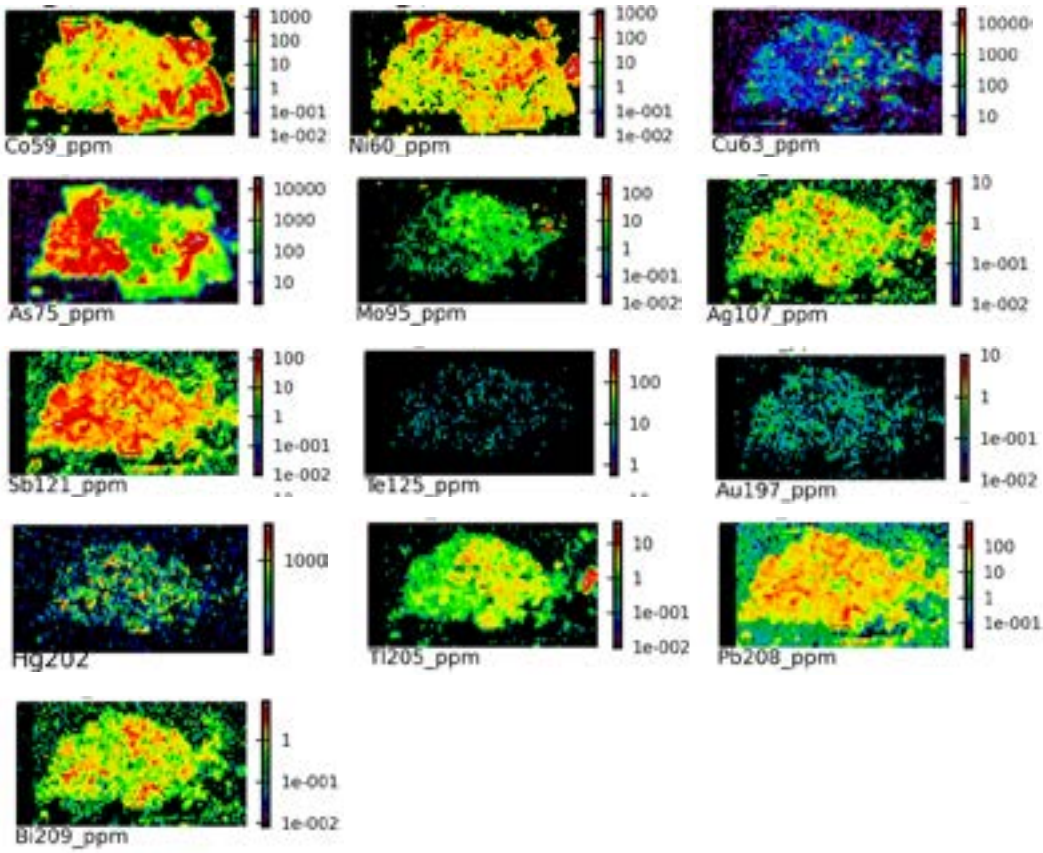

Figure 8.4 Upper Poorman Formation black shales from the Maitland area (5 km NW of Homestake) contain multi-generational Precambrian pyrite, same as upper Poorman black shales from within the mine. The earlier generation has a trace element signature similar to that of 19776-1842 (Fig. 4.7), which formed during diagenesis, whereas the later pyrite is enriched in Co, Ni, and As only, a signature indicative of hydrothermal or metamorphic pyrite.

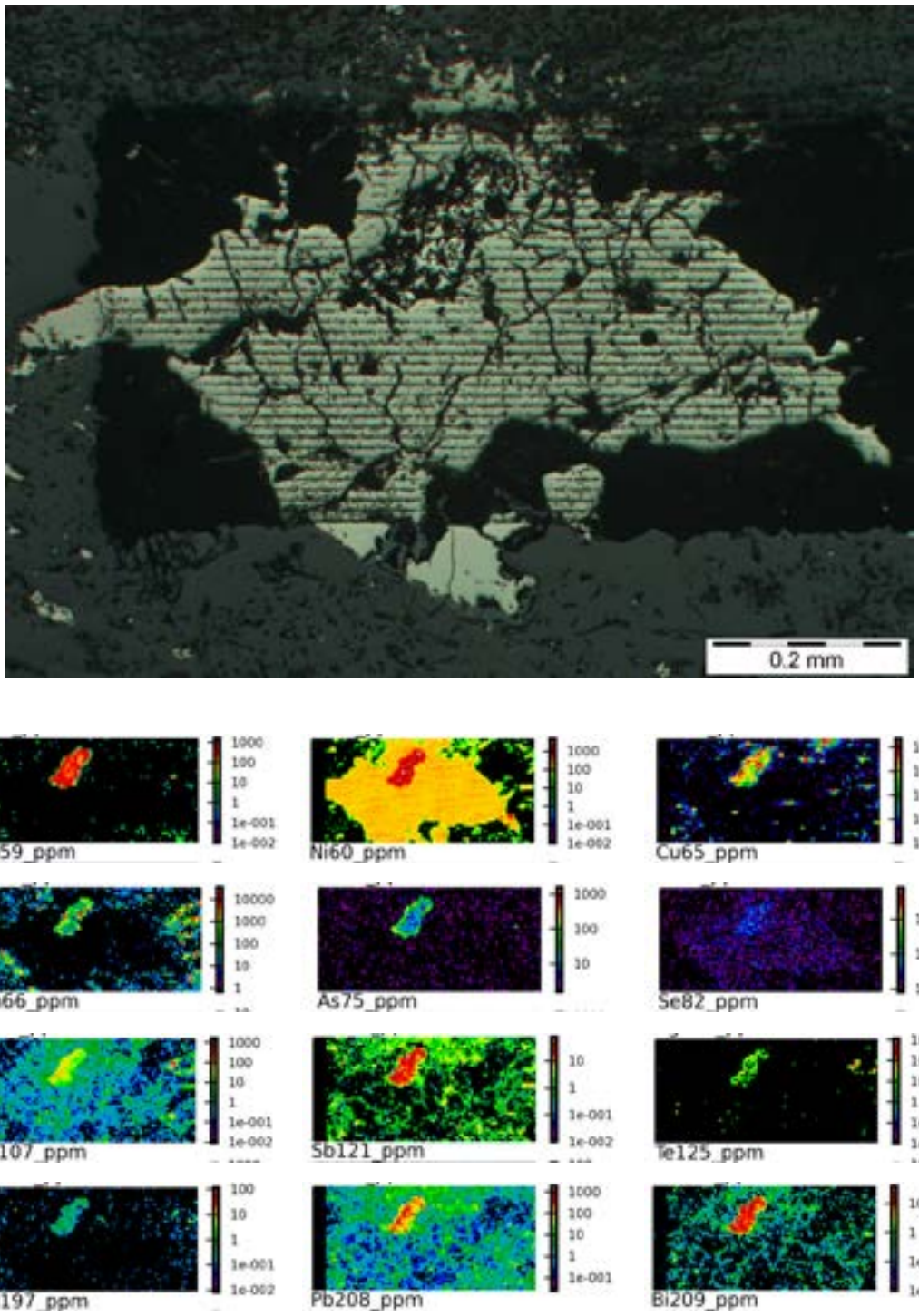

Figure 8.5 Third Precambrian pyrite map and first pyrrhotite map (HS 032A-3, small py in po). This sample is from drill hole 19600, and as with samples from 19776, much of the original pyrite in this lithology has been converted to pyrrhotite, but small remnants of the original pyrite apparently remain. A ratty pyrite 'core' to a large pyrrhotite crystal was imaged, and the trace element signature is surprisingly similar to the signature in pyrites from Figures 4.7 and 4.8.

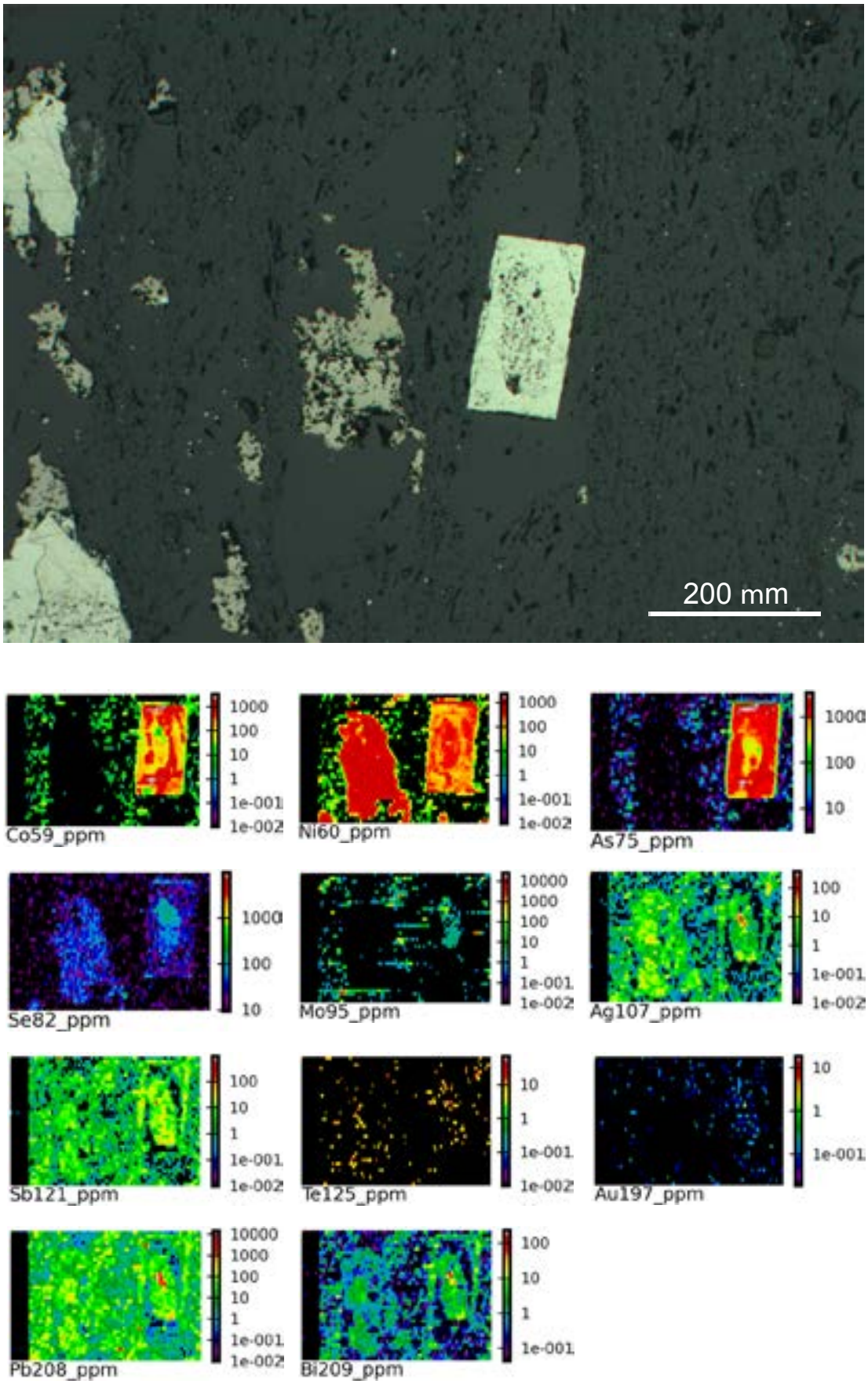

Figure 8.6 Disseminated pyrite and pyrrhotite in thin-bedded gray/black shale from the upper Poorman Formation (sample HS 067). Despite the different mode of occurrence, the two sulfide types show very similar trace element geochemistry to the pyrite-pyrrhotite association in Figure 10, where pyrite grew at the expense of pyrrhotite. Such a paragenesis does not seem to explain what is observed here, but Co diffusion from pyrrhotite to pyrite appears to have been in operation.

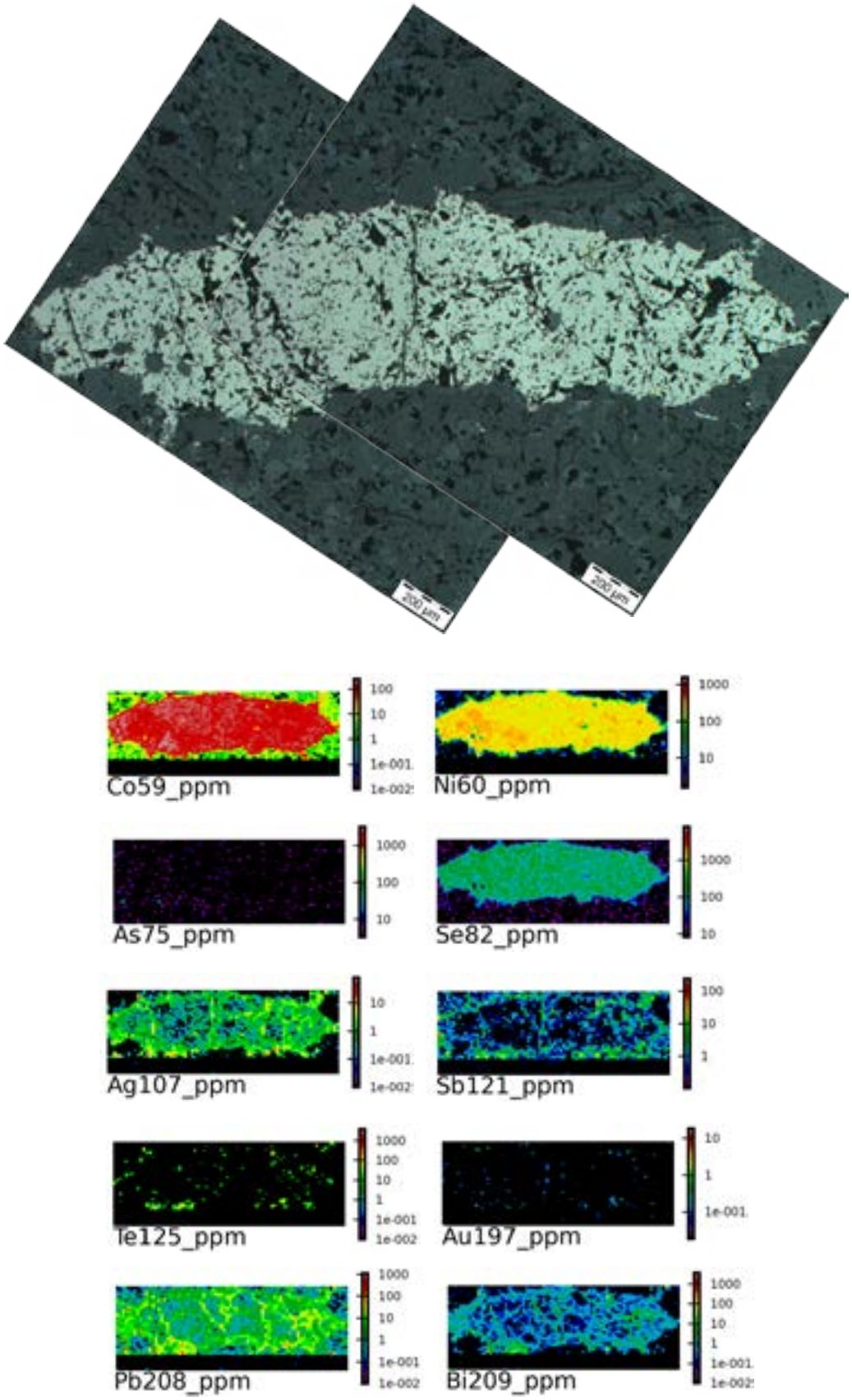

Figure 8.7 Disseminated pyrrhotite in the Homestake Formation (HS 060B.. This is the most common form of pyrrhotite occurrence in the Homestake Formation; understanding its trace element character is therefore beneficial. Unlike the pyrrhotite from the sulfidic interflow sediments and black shales of the upper Poorman Formation, pyrrhotite in the Homestake Formation is enriched in Co as well as Ni, Se, and low Ag, Pb, and Bi. However, this form of pyrrhotite, like all such in this study, contains below-detection As and Au.

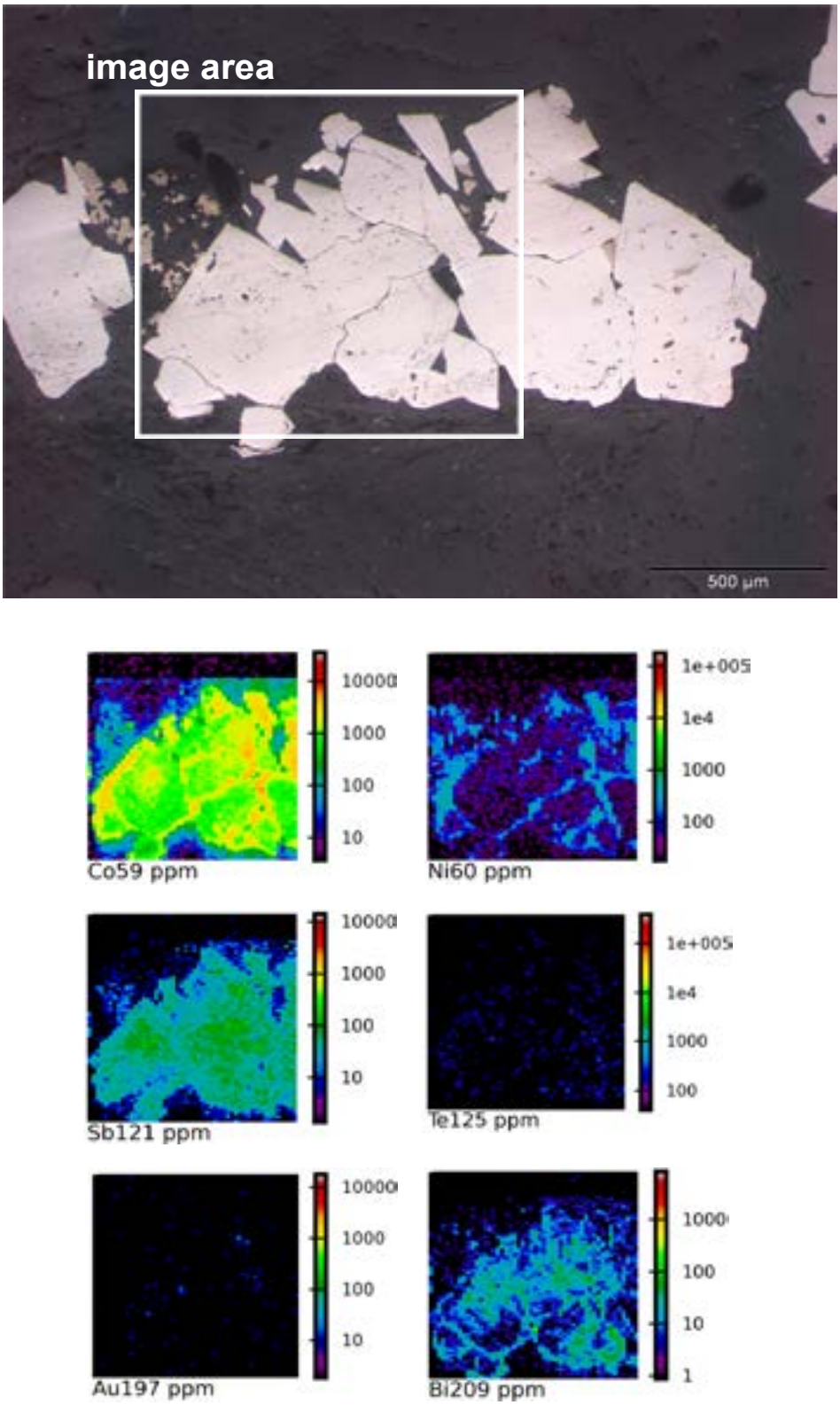

Figure 8.8 Homestake Formation arsenopyrite (sample 16233). Arsenopyrite in chlorite-rich sections of the Homestake Formation are relatively barren in trace elements, compared to the sedimentary pyrite in the figures above, as well as the pyrrhotite. However, some bimodal distribution is seen in Co, Ni, and Sb. Gold and Te are below detection, although faint Te enrichment is present in the outer rims of the crystals.

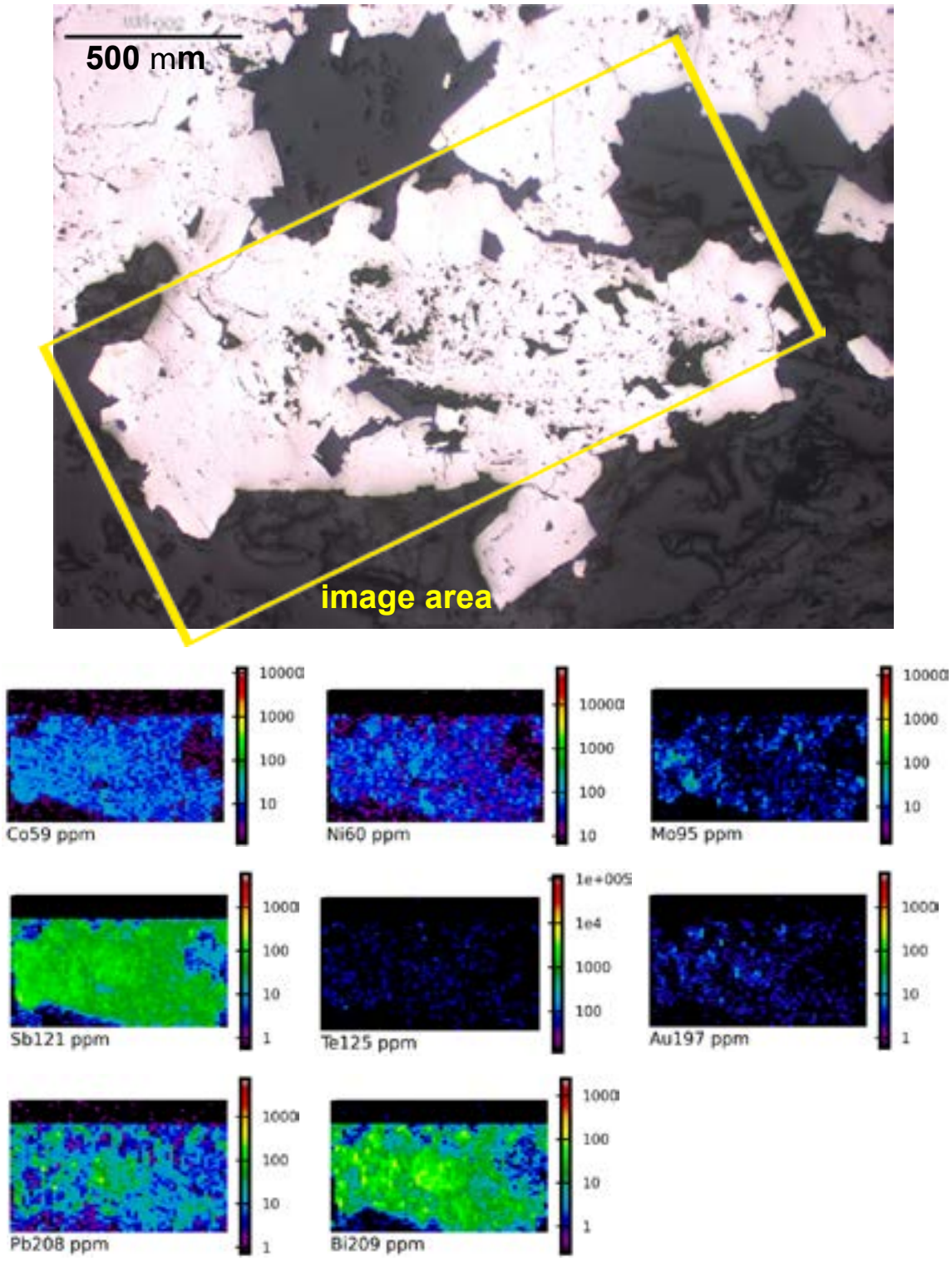

Figure 8.9 Homestake Formation arsenopyrite (sample 16229). This sample is a heavily arsenopyrite-altered BIF, where individual arsenopyrite crystals are routinely >1 cm in diameter. Again, the trace element content of this arsenopyrite is low, and there is even less zonation in this type than in the type shown in Figure 4.13 (Pb and Bi seem to show some zonation). Gold is noticeably absent from both arsenopyrite types, indicating that most gold in the deposit is not bound within the structure of sulfide minerals, as at other sediment-hosted gold deposits.

arsenopyrite than in the former (100 ppm vs. 50 ppm), while Pb is enriched in the core (generally 50 ppm, but up to 500 ppm locally). Gold (up to 10 ppm) and Te (~50 ppm) are slightly more enriched in this arsenopyrite than in the previous image, but like the other trace elements in this image, no distinct zonation is present.

8.4.1 Paleogene (Eocene) pyrite – LA-ICP-MS imaging

Image 1: DML-88-3_1114 (DDH DML-88-3). Coarse grained (>2 mm) euhedral pyrite occurs on the contact of Tertiary rhyolite and carbonate-rich siltstone (now phyllite) of the upper Poorman Formation in drill hole DML-88-3, which was drilled in the deeper levels of the Main Ledge ore body. These pyrites are characterized by high Ag (10–50 ppm), Sb (100–500 ppm), and Pb (100–1000 ppm) above background, with lesser As (100–500 ppm; Fig. 8.10). Other elements, such as Co, Ni, and Au, but also As, are more enriched in the rims than in the cores of these pyrites. Gold in particular shows a stark contrast, being virtually nonexistent in the pyrite until the outermost rim (5–20 ppm Au), where Co (50–100 ppm), Ni (200–300 ppm), and As (up to 5000 ppm) also increase. Interestingly, Te is not present at levels above the detection limit in this pyrite.

Image 2: 24286-500B (DDH 24286). The Eocene rhyolite dikes that intrude the Paleoproterozoic stratigraphy at Homestake are mineralized with pyrite and accessory galena, sphalerite, and chalcopyrite. Pyrite in these rhyolites is commonly in the form of sub-millimeter cubes, but larger examples exist in cross-cutting carbonate veins. A laser image of one of these small cubes (adjacent to anhedral, gangue inclusion-rich pyrite) shows that they are significantly enriched above background in Ag (20–200 ppm), Sb (30–300 ppm), and Pb (100–10,000 ppm), with enrichment in Au as well (one area near the middle of the grain contains ~20 ppm gold; Fig. 8.11). Cobalt, Ni, Cu, As, Mo, and Bi are also elevated above background. In contrast, the enveloping gangue inclusion-rich pyrite is comparatively barren in trace elements, containing above-background amounts of Se (~50 ppm) and Bi (~50 ppm) only.

8.4.1.1 Gold in rhyolite-hosted pyrites – remobilized Precambrian ore, or something more?

LA-ICP-MS imaging of pyrite hosted in Eocene rhyolite dikes throughout the Homestake mine has revealed that these sulfides contain gold at significant levels above background (see Figs 8.10 and 8.11). Although LA-ICP-MS technology was not available to the early 20th century geologists who worked on the Homestake deposit, many of them believed the orebodies were genetically related to the rhyolite intrusions (e.g., Noble, 1950); the presence of gold in these pyrites is therefore intriguing and seems to lend some validation to their case. On the other hand, Homestake geologists in the latter 20th century, having access to greater amounts of underground exposure and better technology, discounted the earlier magmatic-hydrothermal theory and concluded that the gold in and around the margins of the rhyolite dikes was mostly remobilized Precambrian ore (e.g., Rye et al., 1974; Caddey et al., 1991). We generally support the conclusions of the latter researchers, but we also acknowledge that there may have been an epithermal-style mineralization that added some gold to the system.

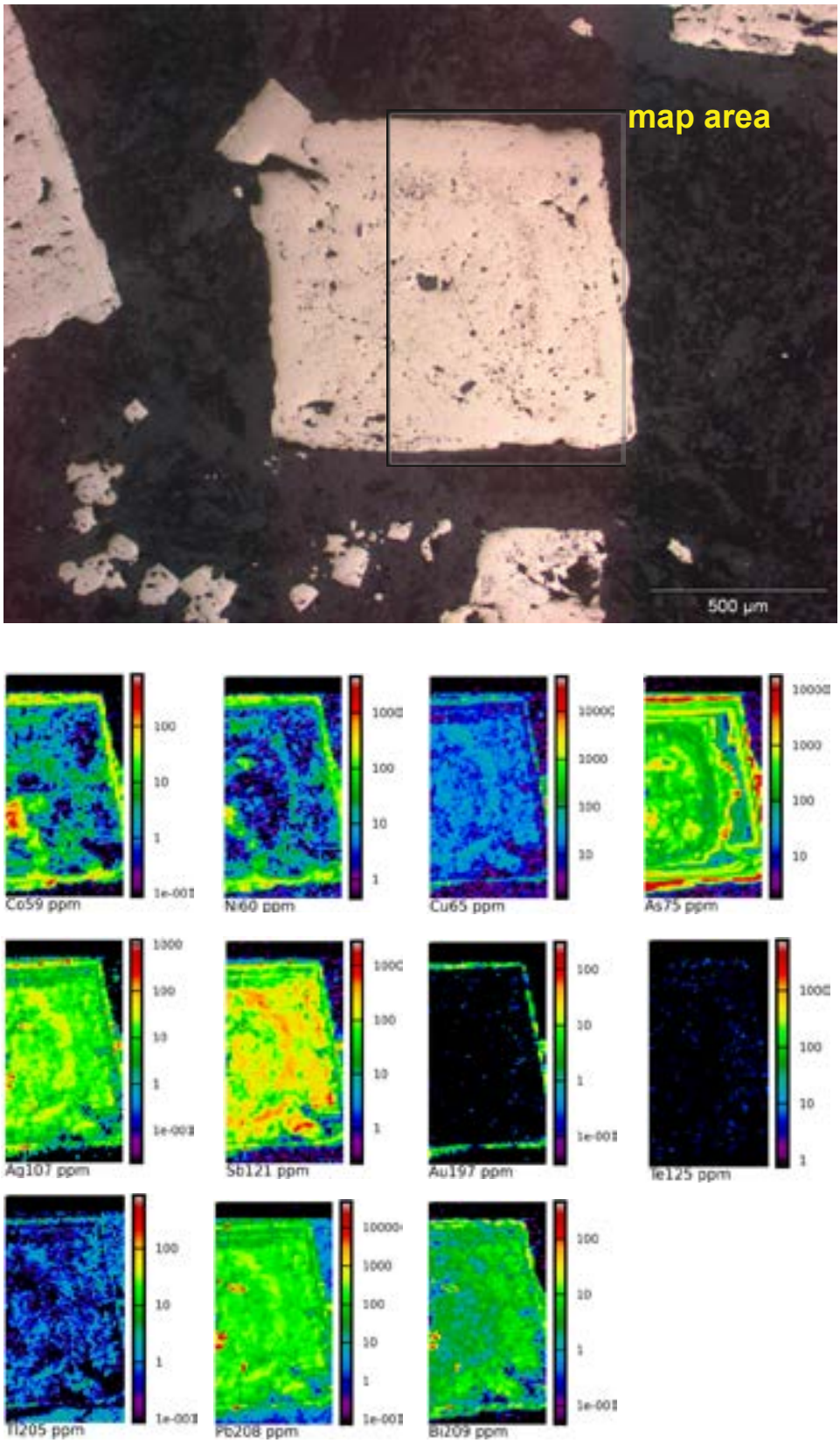

Figure 8.10 Tertiary pyrite 1 (DML883-1114). There are several types of pyrite that formed during Eocene alkalic magmatism in and around the Homestake mine. For the purposes of comparing Precambrian vs. Tertiary pyrite at Homestake, two pyrites representing common types were imaged. The first, shown here, is enriched in many trace elements, but a noticeable difference between it and all other Precambrian pyrites is the concentration of Au (and other elements) in the outermost rim.

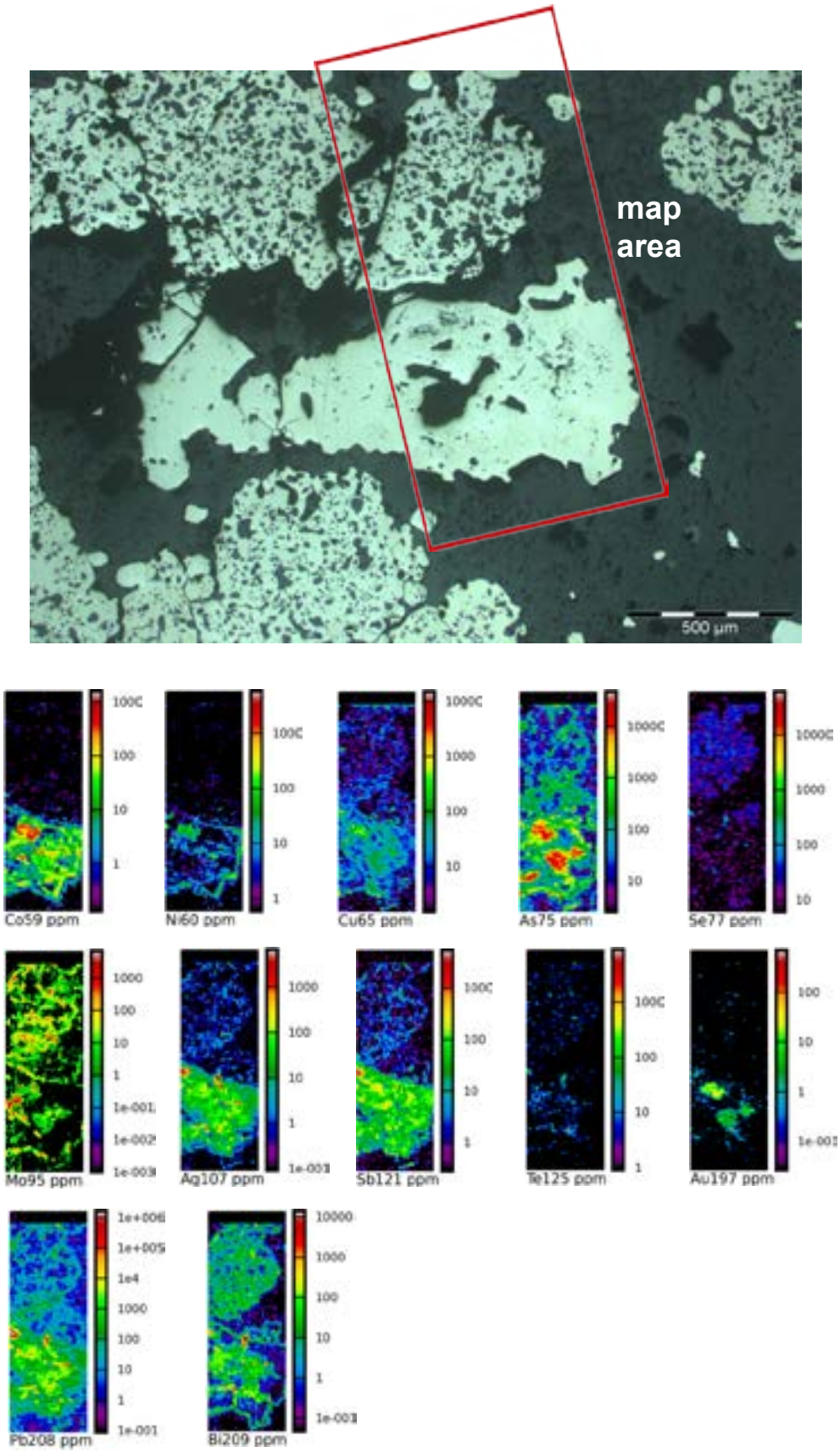

Figure 8.11 Tertiary pyrite 2 (24286-500B). Rhyolite dikes within the mine contain several percent pyrite, in the form of micron-scale cubes and anhedral masses. One of the latter was imaged, and the results show that there is a stark geochemical difference between the inclusion-rich, anhedral rim pyrite and the inclusion-poor, subhedral pyrite. Gold is concentration in patches within the 'core' pyrite, reaching levels of ~20 ppm.

8.5.1 Lead isotopes in Poorman Formation sedimentary and metamorphic pyrite

In-situ Pb isotope LA-ICP-MS spot analyses of pyrite from the upper Poorman Formation reveal at least two generations of Pb in a given grain (Fig. 8.12). Furthermore, Pb isotope analyses from the py1 (core) portions of upper Poorman pyrites have consistently older model ages than analyses from the rims (py2). The distribution of these pyrite leads is shown quite clearly in a LA-ICP-MS image of pyrite from sample HS 043 (Fig. 8.12B): while the core of this pyrite grain (py1) has abundant Pb (~1000 ppm), the rim (py2) contains minimal Pb (~1 ppm), and only where it has been fractured and infilled by ostensibly remobilized Pb. A laser spot was drilled in the matrix to these pyrite crystals, and that data point is plotted on Figure 8.12A for reference, as are Rye et al.'s (1974) galena data from Homestake BIF-gold ore samples and Frei et al.'s (2009) K-feldspar data from the Harney Peak granite. When compared with these other Pb sources, the upper Poorman pyrites contain less radiogenic Pb than the shale matrix, but more radiogenic Pb than the ore-stage galenas and granite Pb.

8.5.1.1 Pyrite Pb isotopes - discussion

While Pb loss has clearly affected zircons in the mine stratigraphy at Homestake, as well as the rest of the Wyoming craton (see above), a similar phenomenon seems to have occurred in sulfides of the upper Poorman Formation. The average $^{207}Pb/^{206}Pb$ ratio for all upper Poorman 'pyrite 1' pyrites analyzed is 0.89, which corresponds to Neoproterozoic model ages (i.e., ~800 Ma). Given the presumed depositional age of ~2000 Ma for the Poorman Formation, and the Pb loss history of zircons from the Ellison Formation, we conclude that the same late Paleoproterozoic thermotectonic processes which reset the U-Pb ratios of most Black Hills zircons (via Pb loss) also altered the original Pb isotopic compositions of early Paleoproterozoic pyrite. The metamorphic/deformational regime of 1750–1650 Ma may have added significant amounts of radiogenic Pb to the pyrites via fractures (e.g., Fig. 8.12B); this Pb would have mingled with preexisting Pb (model age = 2000 Ma?), resulting in new model ages significantly younger than the depositional age. A second possible influence on the current Pb isotopic composition of the upper Poorman pyrites is the widespread alkalic magmatism of 60–50 Ma in the Black Hills, manifest at Homestake as predominantly rhyolitic dikes in the Poorman and Homestake Formations; this event also crystallized new pyrite. This episode, like the Paleoproterozoic thermotectonism, would have added radiogenic Pb to the system, potentially re-setting the Pb-Pb model ages even further up the growth curve from the 2000 Ma depositional age (also the original model age?). Whatever the history, the fact remains that a reliable Pb-Pb model age for syn-sedimentary or early diagenetic pyrite in the upper Poorman Formation cannot be obtained using LA-ICP-MS techniques, and given the younger-than-expected model ages of ore-stage galenas and Harney Peak feldspars (Fig. 8.12A), perhaps no technique currently available is able to measure the 'original' Pb isotopic compositions of Pb-bearing minerals in the Black Hills.

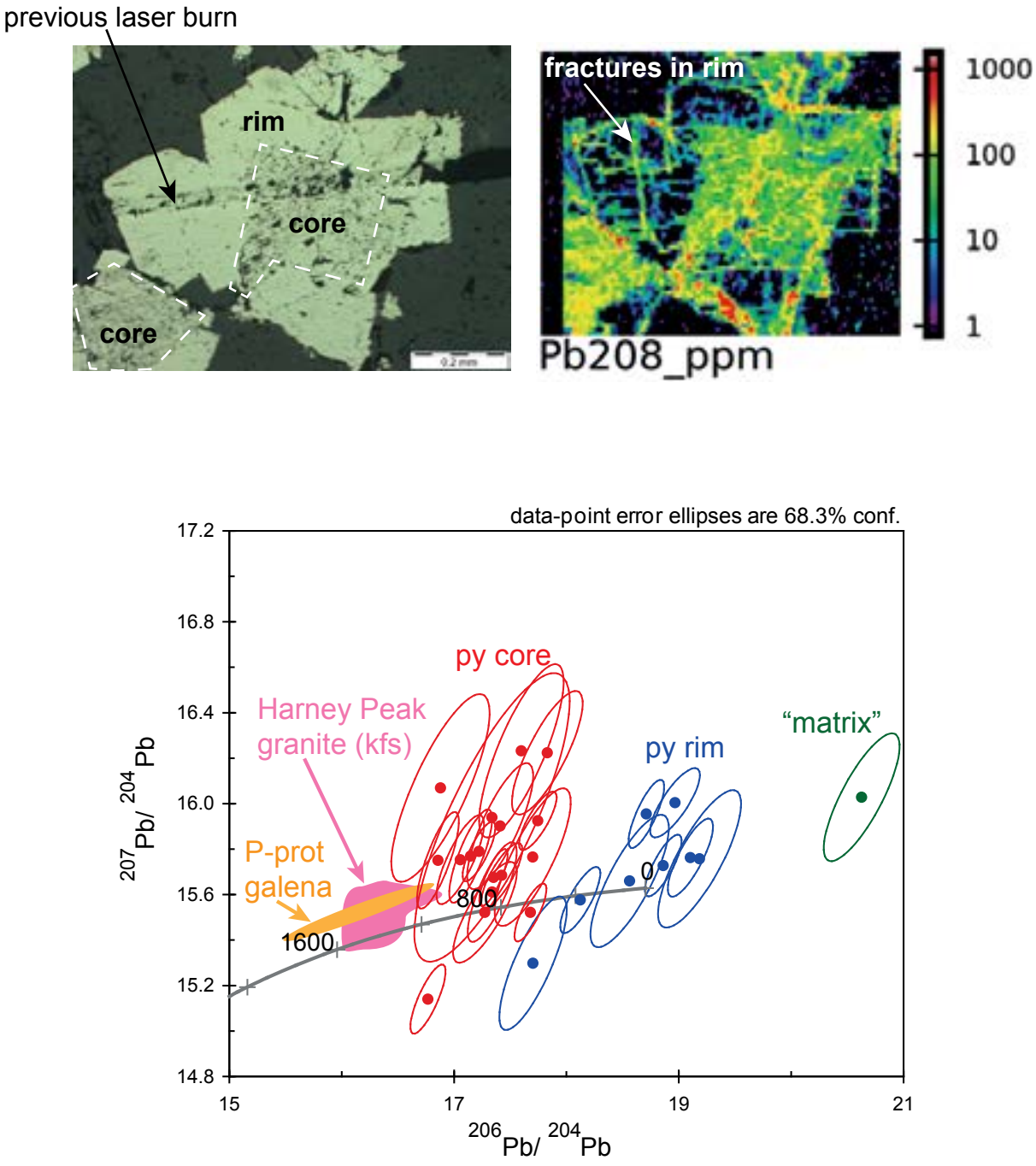

Figure 8.12 Pb isotopes. The sedimentary pyrites contain sufficient Pb to conduct Pb isotopic studies via LA-ICP-MS. Lead isotope systematics in the Black Hills (and greater Wyoming Craton) are complex due to modification by intense thermotectonism during the late Paleoproterozoic and also the Tertiary magmatic-hydrothermal events. Any original Pb in the earliest pyrite generation has been contaminated by highly radiogenic Pb, leading to geologically unreasonable model Pb-Pb ages for py1.